UNIVERSITÉ DE STRASBOURG

ÉCOLE DOCTORALE - PHYSIQUE ET CHIMIE PHYSIQUE

Institut Charles Sadron, UPR22, CNRS

THÈSE présentée par :

Alireza KAVAND

Soutenue prévue le : **4 Décembre 2019**

pour obtenir le grade de : **Docteur de l'université de Strasbourg**

Discipline/ Spécialité : Science des polymères

Development of a theranostic platform based on hyperbranched polymers grafted onto upconversion nanoparticles for the delivery of 5-fluorouracil

THÈSE dirigée par :

M. SERRA Christophe	Professeur, Université de Strasbourg
M. VANDAMME Thierry	Professeur, Université de Strasbourg

RAPPORTEURS :

Mme MINGOTAUD Anne-Françoise	Directeur de recherche, CNRS - IMRCP, Toulouse
M. KOEHLER Michael	Professeur, Université technologique d'Ilmenau (Allemagne)

Examinatrice :

Mme MILLOT Nadine	Professeur, Université de Bourgogne

Membres invités :

Mme CHAN-SENG Delphine	Chargé de recherche HDR, CNRS - ICS-Strasbourg
M. ANTON Nicolas	Maître de conférences HDR, Université de Strasbourg

To my wife

Acknowledgements

First and foremost I would like to express my sincere gratitude to my supervisors Prof. Christophe Serra and Dr. Delphine Chan-Seng for encouraging and supporting me from first day I arrived to Strasbourg until today. Thank you for all of your advice and guidance and your patience during three years. I would like to say that I can not imagine this milestone without your help. I am also thankful to Prof. Thierry Vandamme and Dr. Nicolas Anton for nice contribution and support for improving this work.

My special thanks to Jury committee, Dr. Anne Françoise Mingotaud, Prof. Michael Kohler, Prof. Nadine Millot. Thank you for all of your advice and suggestion for improving my manuscript.

I would like to thank to the CMP group technical staff for serious support, especially, Laurence Oswald for all of technical advices and trainings in lab and I thank to Alexandre Collard.

The assistance of members of the characterization platforms at ICS is appreciatively acknowledged; especially, Dr. Mélanie Legros, Catherine Foussat, Catherine Saettel Herr, Christian Blanck, Dr. Marc Schmutz for TGA, DLS, SEC and TEM analysis. Thank you for all of your kind support, contribution and valuable discussion during three years.

I would also like to thank all my group members and lab colleagues in CMP group and all roommates for your great contribution.

I thank the CNRS, the University of Strasbourg and physics and chemistry-physics doctoral school for financial support of my PhD study.

Finally, I would like to thank my wife, Marziyeh, for her understanding, her patience and endless love.

Best regards,

Alireza Kavand

Table of Contents

Résumé de la thèse

1. Introduction

La théranostique est un domaine prometteur en nanomédecine qui vise à combiner la thérapie et le diagnostic en un vecteur unique. Ce vecteur doit avoir le rôle de cargo pour transporter et délivrer un principe actif, mais aussi avoir des capacités d'imagerie permettant le suivi de ce vecteur. Diverses approches ont été explorées pour le développement de vecteurs pour la théranostique incluant des systèmes basés sur des sondes luminescentes (par exemple, BOPIDY et la porphyrine) ainsi que des nanoparticules (par exemple, les quantum dots, les particules d'oxyde de fer, d'or et de silice). Récemment, les particules à conversion photonique ascendante (*upconversion nanoparticles*, UCNPs) ont émergé comme de bons candidats pour la bioimagerie et la théranostique car ces nanoparticules inorganiques peuvent convertir une lumière d'excitation dans le proche infrarouge en une lumière d'émission dans le visible.

L'objectif de ce projet doctoral était de préparer des polymères linéaires et hyperramifiés à base de méthacrylamide de *N*-(2-hydroxypropyle) (HPMA) par polymérisation radicalaire contrôlée par transfert de chaine réversible par addition-fragmentation (RAFT) depuis la surface des UCNPs pour la théranostique. Les polymères hyperramifiés (HBPs) ont en effet attirés l'attention dans le domaine du développement des systèmes de délivrance de principes actifs en raison des cavités internes de leur structure globulaire qui peuvent être utilisées pour encapsuler des principes actifs, mais aussi du grand nombre de groupements fonctionnels présents à leur périphérie permettant d'introduire des ligands pour la délivrance de principes actifs ciblés. Ce projet doctoral (Figure 1) s'est donc intéressé à 1) la synthèse d'UCNPs à base de nanocristaux de $NaYF_4$:Yb^{3+},Er^{3+} en étudiant notamment leur transition de phase, 2) la modification de surface de ces UCNPs pour la croissance de polymères linéaires et hyperramifiés depuis leur surface et

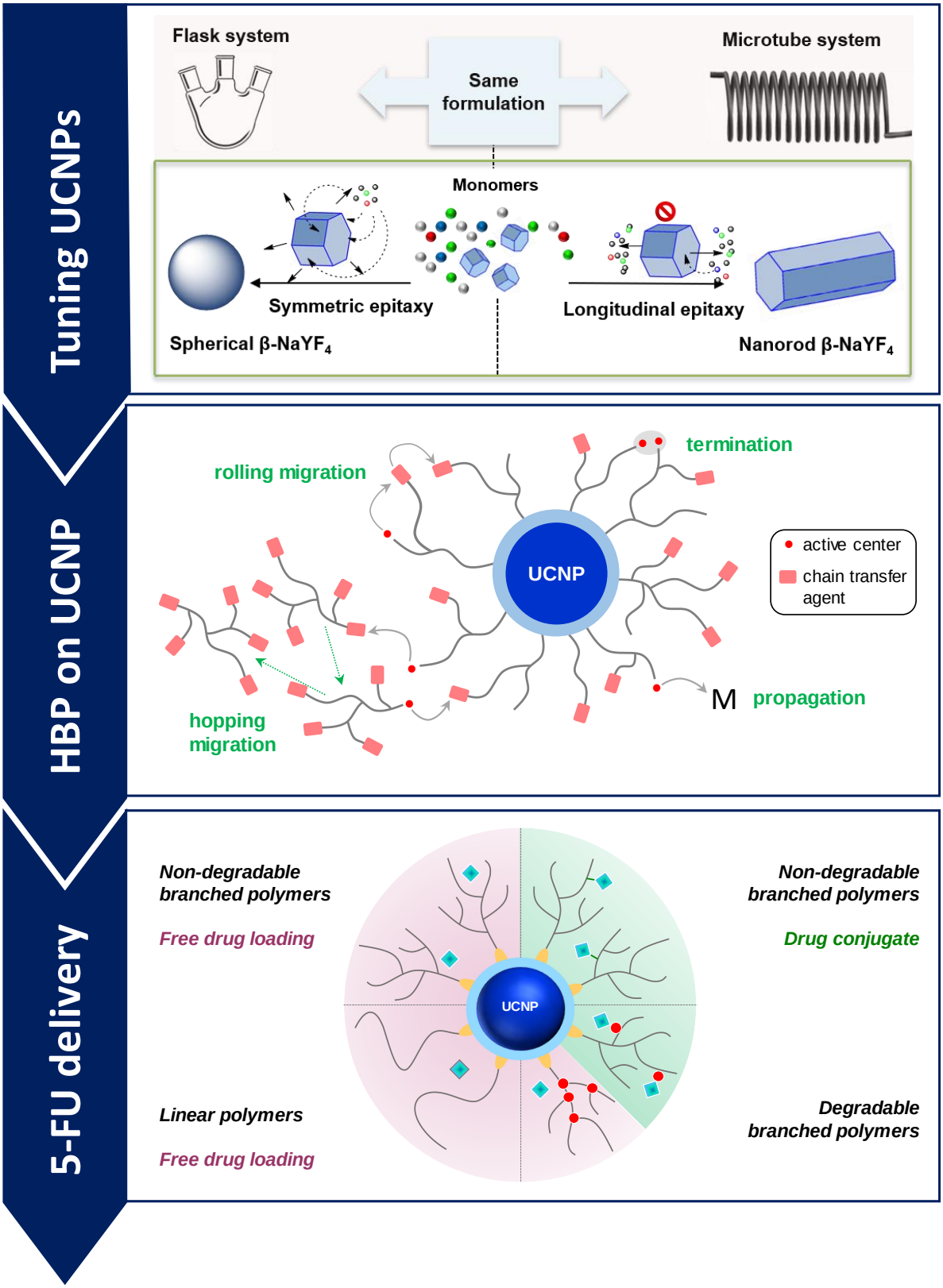

Figure 1. Description globale du projet doctoral : de la synthèse d'UCNPs de forme, taille et phase contrôlées à la croissance d'HBPs depuis leur surface pour le design de nanohybrides pour la délivrance de 5-fluorouracil (5-FU).

3) le design de nanoobjets à base d'UCNPs et de polymères hyperramifiés pour la théranostique.

2. Résultats et discussion

2.1. Synthèse et étude de la transition de phase de nanocristaux de $NaYF_4:Yb^{3+},Er^{3+}$

Cette partie du projet porta sur une nouvelle méthode pour contrôler la taille et la forme des nanocristaux de conversion ascendante. L'objectif de cette partie était d'étudier l'effet du réacteur sur la croissance des nanocristaux. Les UCNPs ont été synthétisées selon une méthode de coprécipitation utilisant différents types de réacteurs pour le post traitement thermique à haute température (~ 300°C), tels qu'un ballon à fond rond ou des microtubes de diamètres internes et de longueurs variables. Compte tenu de la clairance corporelle des nanoparticules et de la sensibilité à l'imagerie, les nanocristaux de très petite taille sont privilégiés comme sondes de contraste pour des applications biomédicales. Par ailleurs, il est possible de modifier les propriétés de surface des UCNPs de tailles supérieures à 10 nm pour en faire des nanocarriers pour l'administration de médicaments. L'objectif de cette partie était donc de contrôler la taille et la forme des UCNPs afin d'obtenir des tailles ultra petites jusqu'à 100 nm. La modification du procédé de traitement thermique a été plus particulièrement étudiée pour obtenir des UCNPs ultra petites monodisperses. Pour cela, des microtubes en acier inoxydable de diamètres internes et de longueurs différents ont été utilisés pour l'étape du traitement thermique, et les résultats ont été comparés à ceux obtenus avec la méthode standard en utilisant un simple ballon à fond rond. On a constaté que la taille et les propriétés des UCNPs étaient influencées par le type de réacteur thermique (ballon ou microtube). Par exemple, les nanocristaux avaient un taux de croissance modéré dans les microtubes malgré un excellent transfert de chaleur. En outre, les nanocristaux avaient tendance à se développer sous la forme anisotrope de nanobatônnets contrairement à ceux sphériques obtenus avec le réacteur ballon. Ainsi, cette étude a mis en évidence l'effet tangible de la nature du réacteur sur la taille et la forme des nanocristaux. Des nanocristaux présentant différentes phases, largeurs, diamètres et formes (bâtonnet, ovoïdes) ont été synthétisés pour une formulation unique. La Figure 2 montre les images TEM de nanocristaux de $NaYF_4:Yb^{3+},Er^{3+}$ qui ont été synthétisés dans des microtubes de différents diamètres internes. La stratégie développée au cours de ce projet peut être étendue à d'autres nanocristaux ou à d'autres formulations, et travailler en flux continu serait une autre

excellente perspective.

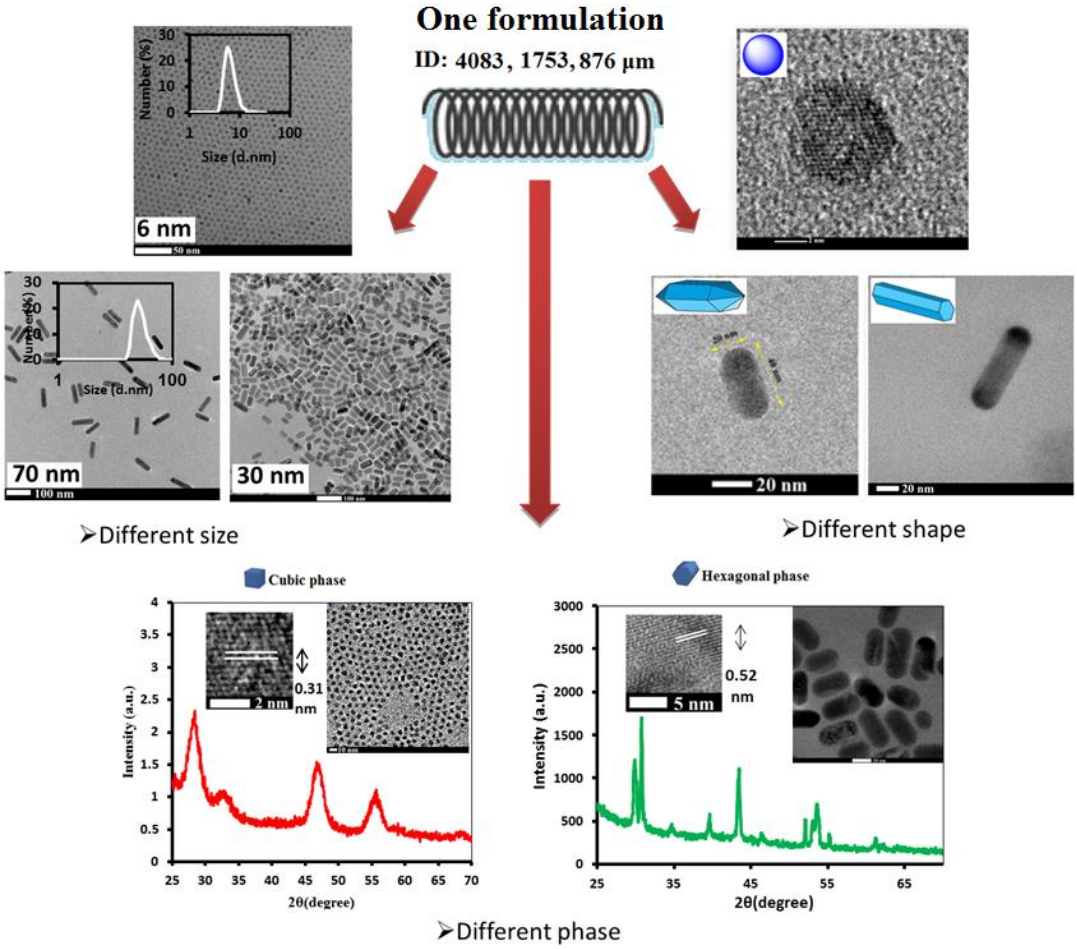

Figure 2. UCNPs, préparés dans différents microtubes, présentant diverses tailles, formes et phases.

2.2. Synthèse de polymères linéaires et hyperramifiés depuis la surface d'UCNPs

La préparation de polymères greffés à la surface de nanoparticules peut être abordée de deux façons : 1) couplage de polymères avec des groupements réactifs présents à la surface des nanoparticules ou 2) polymérisation du monomère depuis la surface des nanoparticules. Le choix s'est porté sur la deuxième approche car elle permet un meilleur contrôle du degré de fonctionnalisation. Le poly(méthacrylamide de *N*-(2-hydroxypropyle)) répondant aux critères de biocompatibilité et de solubilité dans l'eau nécessaire pour une application biomédicale et étant largement étudié pour la délivrance de principes actifs, le choix s'est porté sur le méthacrylamide de *N*-(2-hydroxypropyle) comme monomère.

La première étape a été de modifier la surface des UCNPs pour introduire un point d'ancrage permettant la polymérisation du monomère depuis leur surface. La modification de la surface

de ces particules a été réalisée en deux étapes en adaptant des protocoles décrits dans la littérature : 1) formation d'une écorce de silice possédant des fonctions amines à la surface et 2) couplage d'un agent de transfert de type RAFT par réaction d'amidification. L'agent de transfert à la surface des UCNPs a alors permis de faire croitre les chaines linéaires de poly(méthacrylamide de *N*-(2-hydroxypropyle)) (poly(HPMA)) depuis la surface des UCNPs (UCNP@polyHPMA). En réalisant la copolymérisation du méthacrylamide de *N*-(2-hydroxypropyle) en présence d'un transmère (molécule pouvant avoir simultanément le rôle de monomère et d'agent de transfert, Figure 3), des polymères hyperramifiés ont été également obtenus à la surface d'UCNPs (UCNP@HBP) par polymérisation vinylique auto-condensante (*self-condensing vinyl polymerization*, SCVP).

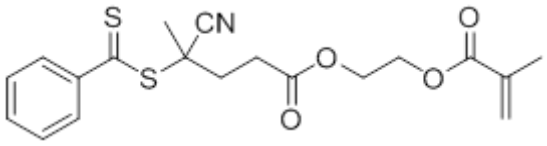

Figure 3. Structure du 2-(methacryloyloxy)ethyl 4-cyano-4-(phenylcarbonothioylthio)pentanoate utilisé comme transmère.

L'effet du taux de greffage en agent de transfert à la surface des UCNPs et du rapport molaire entre HPMA et le transmère sur les propriétés du polymère hyperramifié greffé à la surface des UCNPs a été étudié. A noter qu'en raison du mécanisme de la polymérisation radicalaire contrôlée de type RAFT, le polymère est formé simultanément à la surface des UCNPs et en solution. Les polymères hyperramifiés greffés sur les UCNPs ont été clivés de la surface des UCNPs pour les caractériser (Figure 4). La masse molaire des polymères a été obtenue par chromatographie d'exclusion stérique (SEC) en utilisant un mélange acétonitrile/eau (40/60) comme éluent. Il a été observé que le polymère formé à la surface des UCNPs a une masse molaire plus élevée que celui formé en solution ainsi qu'une dispersité (Đ) plus élevée. De plus, les résultats obtenus suggèrent que plus le taux de greffage en agent de transfert est élevé, plus la masse molaire du polymère hyperramifié est élevée.

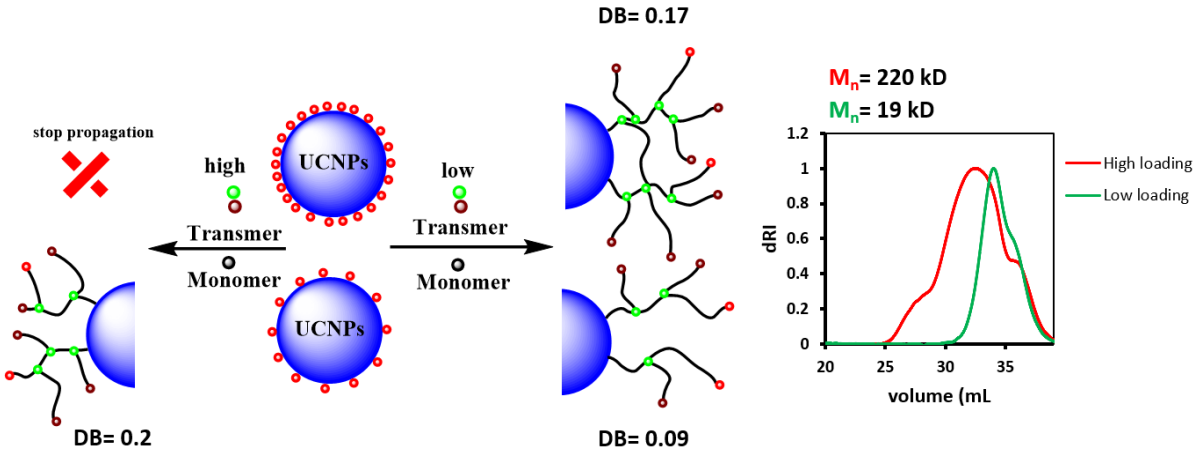

Figure 4. Effet du taux de greffage de l'agent de transfert de type RAFT (taux de greffage élevé en haut et faible en bas) et du rapport molaire entre le monomère (HPMA) et le transmère ([HMPA]:[transmère] élevé à gauche et faible à droite) sur le degré de ramification (DB) et la masse molaire des polymères hyperramifiés greffés sur des UCNPs.

Le taux de ramification (DB) des polymères hyperramifiés a été déterminé en combinant les résultats obtenus par analyse thermogravimétrique et spectroscopie UV-visible. Il a été observé que le DB augmentait avec le taux de greffage en agent de transfert à la surface des UCNPs ainsi qu'avec un rapport transmère sur monomère élevé. Lorsque le taux de greffage en agent de transfert et le rapport transmère sur monomère sont simultanément élevés, la croissance des chaines de polymères était fortement affectée probablement en raison des réactions de terminaison qui sont accrues dans ces conditions où la concentration en radicaux est élevée. De plus, en raison du mécanisme de la polymérisation radicalaire contrôlée de type RAFT et du fait que la polymérisation soit réalisée depuis une surface, un phénomène de retardation de la polymérisation a été observé. Plus le taux de greffage et la proportion en transmère sont élevés, plus le phénomène de retardation sera important. En effet, pour un système avec un haut taux de greffage, le nombre de moles d'unité de répétition d'HPMA par gramme d'UCNP était de : 3,2 mol pour un polymère linéaire, 1,3 mol pour un polymère hyperramifié avec un rapport [HPMA]:[transmère] de 200:1 et 0,24 mol pour un polymère hyperramifié avec un rapport [HPMA]:[transmère] de 200:2.

Ces résultats ont conduit à la conclusion les réactions affectant la croissance des chaines de polymères, telles que les réactions de terminaison et de transfert, sont plus prononcées en

raison de 1) la préparation d'un polymère hyperramifié induisant l'augmentation du nombre de chaines actives, 2) la croissance de polymère depuis la surface de nanoparticules induisant une concentration locale en chaines actives plus élevée, et 3) le mécanisme de transfert dégénératif de la polymérisation RAFT depuis une surface conduisant à des phénomènes de transfert de l'agent de transfert de type RAFT présent à l'extrémité des chaines des polymères (*hopping* entre des chaines en croissance à la surface des nanoparticules et en solution, et *rolling* entre chaines présentes à la surface d'UCNPs, Figure 5).

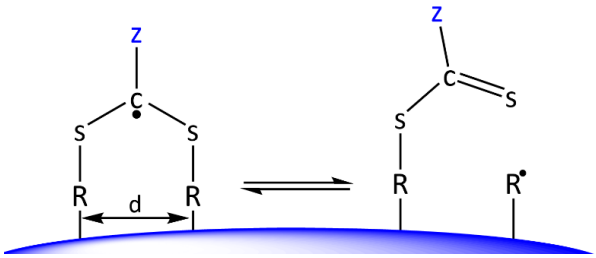

Figure 5. Mécanisme de retardation à la surface des nanoparticules pour la polymérisation radicalaire contrôlée de type RAFT liée à la faible distance d entre deux agents de transfert.

2.3. Modulation de la structure de polymères hyperramifiés greffés à la surface d'UCNPs pour la théranostique

Les polymères hyperramifiés greffés sur des UCNPs ont été étudiés pour encapsuler et relarguer un principe actif. 5-Fluorouracile (5-FU), un antimétabolite utilisé pour traiter différents types de cancer, a été utilisé comme principe actif modèle. Malheureusement, en raison de sa courte durée de vie et de sa faible spécificité entre les cellules saines et cancéreuses, 5-FU a une faible biodisponibilité et peut avoir des effets secondaires comme la diarrhée et une décoloration de la peau. Pour surmonter ces limitations, 5-FU a été encapsulé dans la couronne de polymères greffée sur des UCNPs. L'encapsulation de 5-FU dans une couronne de polymères hyperramifiée était plus efficace que pour son homologue linéaire (c.-à-d. 3,0 contre 1,5% de 5-FU encapsulé dans la couronne de polymères hyperramifiés et linéaires respectivement pour une exposition de ces nanoobjets à la même concentration en 5-FU). Le relargage de 5-FU de la couronne de polymères hyperramifiées était cependant rapide (60% dans les trois premières heures) dans des conditions physiologiques (pH 7,4 à 37 °C).

Afin d'éviter un relargage trop rapide de 5-FU, le principe actif a été conjugué au polymère hyperramifié greffé sur les UCNPs. 5-FU a été modifié afin d'introduire une fonction acide

carboxylique permettant sa conjugaison avec les fonctions alcool des unités de répétition d'HPMA (Schéma 1). La conjugaison de 5-FU par réaction d'amidification sur le polymère a permis d'augmenter la concentration en 5-FU sur ces nanoobjets (11,8% au lieu de 3,0% pour une encapsulation non covalente) et d'observer un relargage plus lent de 5-FU (60% en 20 jours).

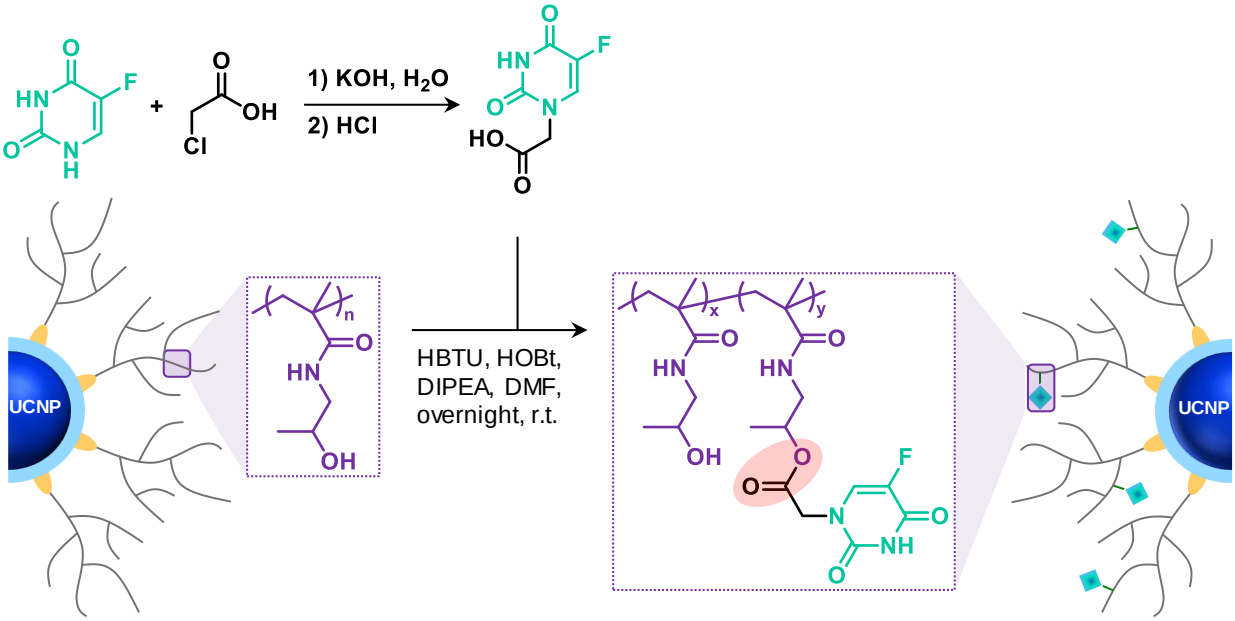

Schéma 1. Modification de 5-FU et sa conjugaison aux polymère hyperramifiés greffés sur des UCNPs.

Afin de mieux contrôler le relargage de 5-FU, l'utilisation de polymères ayant des points de ramification clivables sous l'effet d'un stimulus a été considérée. Deux stimuli ont été choisis en introduisant soit une liaison sensible aux réactions d'oxydation-réduction, ici un pont disulfure, soit une séquence peptidique (GLFL par exemple) clivable en présence d'une enzyme comme la cathepsine. A cet effet, des transmères possédant ces groupements clivables ont été synthétisés (Figure 6). Le transmère avec un pont disulfure a été synthétisé en suivant un protocole décrit dans la littérature. Celui sensible à la cathepsine a été préparé par synthèse peptidique en phase solide pour obtenir la séquence GLFG suivi d'une réaction d'amidification sur résine avec l'agent de transfert de type RAFT. Après clivage de la résine, l'extrémité acide carboxylique de la séquence peptidique a été couplée avec le méthacrylate de 2-hydroxylethyle par réaction d'estérification. L'insertion de ces transmères a été réalisée comme précédemment par copolymérisation avec le HPMA en présence d'UCNPs possédant

des agents de transfert de type RAFT à leur surface. La dégradation des polymères hyperramifiés ayant des points de ramification clivable en présence d'un réducteur, ici le dithiothréitol (DTT), a été étudiée et confirmée par analyse thermogravimétrique et diffusion de la lumière dynamique. L'étude pour les polymères sensibles aux enzymes est en cours.

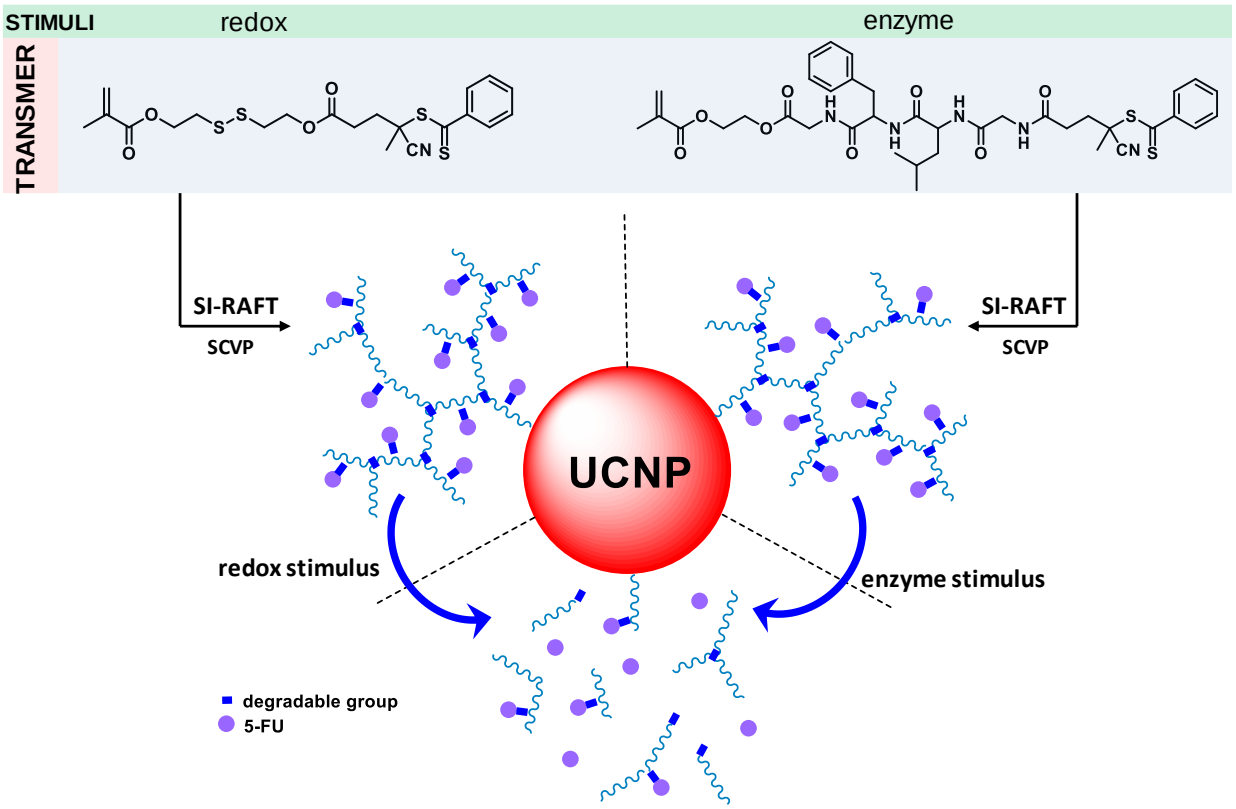

Figure 6. 5-FU conjugué à des polymères hyperramifiés dégradables par voie redox ou enzymatique greffés sur des UCNPs.

3. Conclusion

La théranostique est un domaine en essor en biomédecine en raison de son habilité à combiner le diagnostic et la thérapie en un même vecteur. L'approche employée lors de mon projet doctoral combine les propriétés luminescentes des UCNPs et la capacité des polymères à encapsuler un principe actif de façon covalente ou non.

Ce projet doctoral a conduit au développement et/ou approfondissement de différentes compétences : 1) synthèse de nanoparticules inorganiques dans des microtubes permettant de moduler la taille, la forme et la phase en fonction de différents paramètres opératoires, 2) la synthèse de nouveaux monomères et transmères en combinant la chimie organique et la synthèse peptidique en phase solide, 3) la préparation de polymères linéaires et

hyperramifiés par polymérisation radicalaire contrôlée de type RAFT depuis la surface des nanoparticules, 4) l'étude de l'encapsulation covalente et non covalente ainsi que le relargage de molécules modèles, et 5) l'étude de polymères répondant à un stimulus en terme de dégradation.

General introduction

Theranostics is a promising field in nanomedicine aiming at combining therapy and diagnostic on the same carrier or vector. this carrier will transport a therapeutic agent (e.g. drugs and sensitizers) at the targeted site for the treatment of a disease but also should exhibit some abilities for imaging to monitor this carrier. Various approaches have been explored to develop vectors for theranostics including systems based on luminescent probes (e.g. BOPIDY and porphyrin) along with nanoparticles (e.g. iron oxide, gold and silica nanoparticles, quantum dots). Recently, upconversion nanoparticles (UCNPs) have emerged as good candidates for bioimaging and theranostics as these inorganic nanoparticles convert an excitation light in the near infrared (NIR) into an emission light in the visible. The objective of this doctoral project was to prepare linear and hyperbranched poly(*N*-(2-hydroxypropyl) methacrylamide) by reversible addition-fragmentation chain transfer (RAFT) polymerization from the surface of UCNPs. Hyperbranched polymers (HBPs) have attracted the attention in the field of drug delivery due to their internal cavities of these globular structures that have been used to encapsulate drugs, but also the high number of functional groups at the periphery permitting to introduce ligands to promote targeted drug delivery. This thesis will be composed of one bibliographic chapter and three chapters describing the results obtained during my PhD as depicting in Figure I.1.

Chapter 1 will provide an overview on hyperbranched polymers and upconversion nanoparticles. In a first part, the features of hyperbranched polymers will be provided highlighting the different approaches to synthesize hyperbranched polymers and their functionalization with ligands for targeted drug delivery. In a second part, upconversion nanoparticles will be discussed including their composition, the approaches to synthesize them, and their surface modification using various methods.

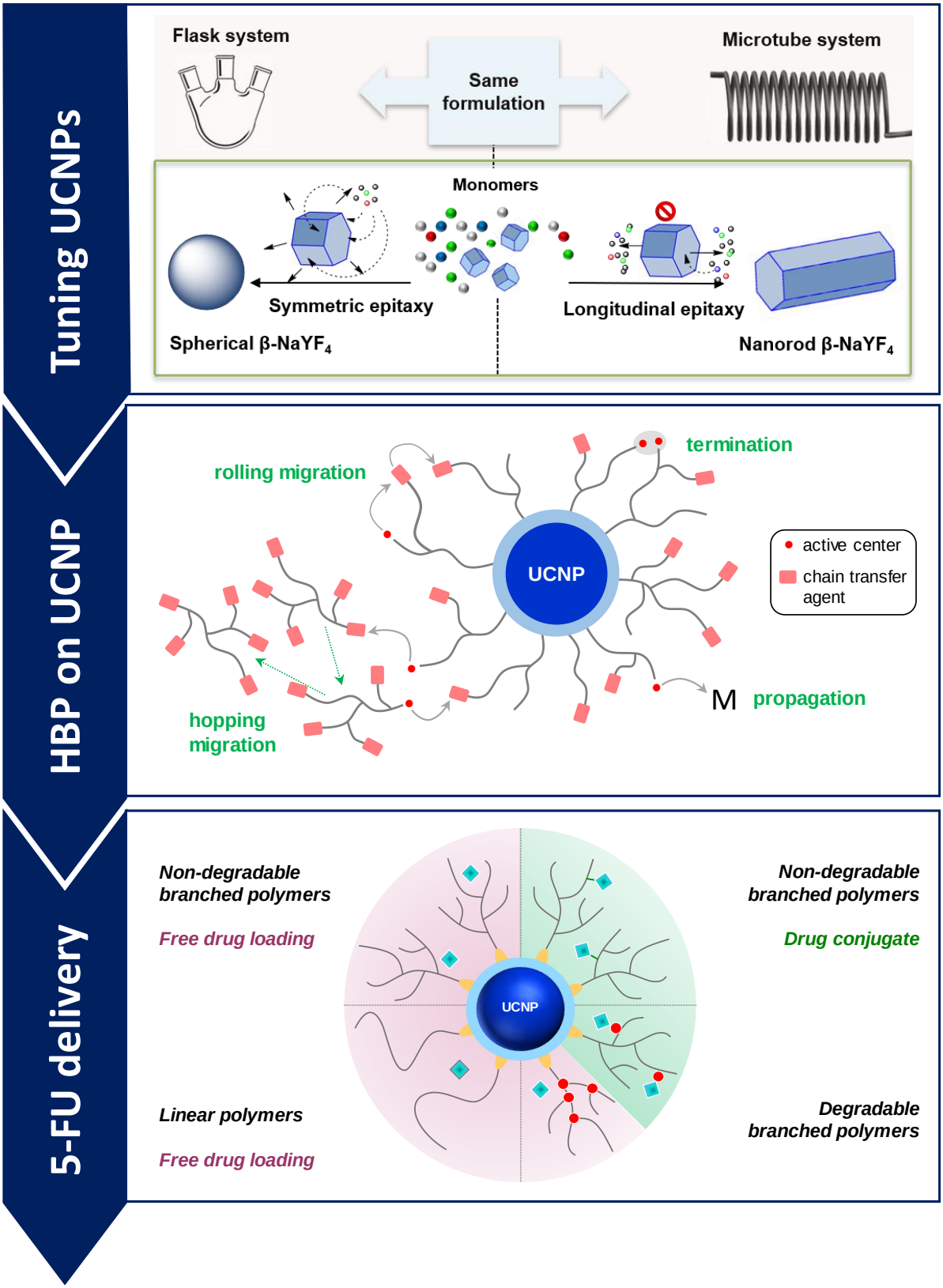

Figure I.1. From the synthesis of UCNPs of controlled shape, size and phase to the growth of HBPs of their surface to design nanohybrids for the delivery of 5-fluorouracil (5-FU).

Chapter 2 will focus on the synthesis of UCNPs based on $NaYF_4$:Yb^{3+},Er^{3+} nanocrystals via co-precipitation method involving nucleation and heat treatment steps. The main objective was to investigate the effect of the reactor used (round-bottom flask vs microtube) on the growth of nanocrystals to control their size and shape. Stainless steel microtubes with different inner diameters were used for the heat treatment step. The size and properties of UCNPs were influenced by the type of reactor used for the heat treatment step. The shape of the resultant nanocrystals from the round-bottom flask was spherical with slight inconstancies in size (2-5 nm) at different temperatures. Using microtubes, nanocrystals had a moderate rate of growth despite a homogeneous heat transfer and had a tendency to growth in anisotropic shape like nanorod. Nanocrystals with various widths, diameters, shapes (e.g. rod, oval), and presenting a single-phase were synthesized using the same formulation, but tuning the diameter of microtubes and the temperature. This study emphasized the nature of the reactor used as a new parameter having a tangible effect on the size and shape of nanocrystals.

Chapter 3 will describe the modification of spherical UCNPs to prepare hyperbranched poly(*N*-(2-hydroxypropyl) methacrylamide)s at their surface. The surface of UCNPs was first modified with a RAFT chain transfer agent to promote the growth of HBPs from the surface of UCNPs by self-condensing vinyl RAFT copolymerization in the presence of a methacrylate-based transmer. The study included the investigation of the effect of the grafting density in RAFT chain transfer agent at the surface of UCNPs and the concentration in transmer. This work highlighted the challenges of the system that were attributed to the increasing number of propagating chains and the surface-initiated RAFT polymerization enhancing chain-breaking reactions including termination and transfer reactions.

Chapter 4 will emphasize the results of this work on tuning the composition of the hyperbranched polymer grafted on UCNPs to aim at delivering 5-fluorouracil (5-FU). The encapsulation of 5-FU in the HBP grafted on UCNPs was low even though it was higher than when a linear polymer was used, while burst release was observed. To enhance the system, 5-FU was conjugated to the hydroxyl groups present on the repeat units of the polymer through ester linkages affording a more sustained release of 5-FU. Stimuli-responsive transmers were also synthesized and used to introduce branching points degradable upon exposure to either a reducing agent or an enzyme to promote triggered drug delivery.

CHAPTER 1: Hyperbranched polymers and upconversion nanoparticles for theranostics

Preface

HBPs have gained attention for the development of drug delivery systems due to the presence of internal cavities in their three-dimensional globular structure that can be used to encapsulate drugs and a large number of terminal functional groups, which can be decorated with a variety of functional moieties such as ligands for targeted drug delivery. On the other hand, lanthanide-doped upconversion nanoparticles (UCNPs) represent a new promising class of materials that may find a large variety of applications in different fields owing to unique properties such as high photostability, low cytotoxicity, efficient emission and long luminescence lifetimes. In this project, our purpose was the preparation for nanohybrid materials based on hyperbranched polymers and UCNPs. Therefore, in this bibliography chapter in a first part, hyperbranched polymers will be introduced. Their general synthesis methods and their potential for drug delivery will be reviewed. In the second part of this chapter, UCNPs and their several synthesis approaches will be presented. Finally, general methods for the modification of those type of nanomaterials will be introduced.

1. Hyperbranched polymers for drug delivery

1.1. Introduction

The developments in macromolecular engineering have led to the expansion of polymer topologies available. Among them, dendritic macromolecules mimic the branching of trees and possess attractive features such as high degree of branching units, high density of terminal functional groups, and their nanometric size. Dendritic macromolecules can be subdivided into dendrimers, hyperbranched polymers, and dendronized polymers. While dendrimers are characterized by a perfect regular structure and unimolecularity, hyperbranched polymers are highly and randomly branched macromolecules, and dendronized polymers consist in dendrons attached as side chains to a linear polymer backbone.

Hyperbranched polymers (HBPs) have like dendrimers a three-dimensional globular structure that have attracted the attention from both academia and industry. The advantages of these polymers (Figure 1.1) as compared to linear polymers are their low intrinsic viscosity, low tendency to chain entanglements, smaller hydrodynamic radius, good solubility and high degree of branching (DB) leading to a high number of terminal functional groups ranging from hydroxy groups to amines [1–3]. When compared to dendrimers, their structures are irregular with dendritic, linear and terminal units randomly distributed, and their synthesis leads to macromolecules with broad molecular weight distributions. However, HBPs can be easily synthesized in a one-pot reaction and thus are more cost efficient as compared to the multi-step approach for the dendrimers requiring a purification step after each coupling reaction [4]. Furthermore, due to their higher steric hindrance, dendrimers may be more challenging to functionalize than HBPs [5,6].

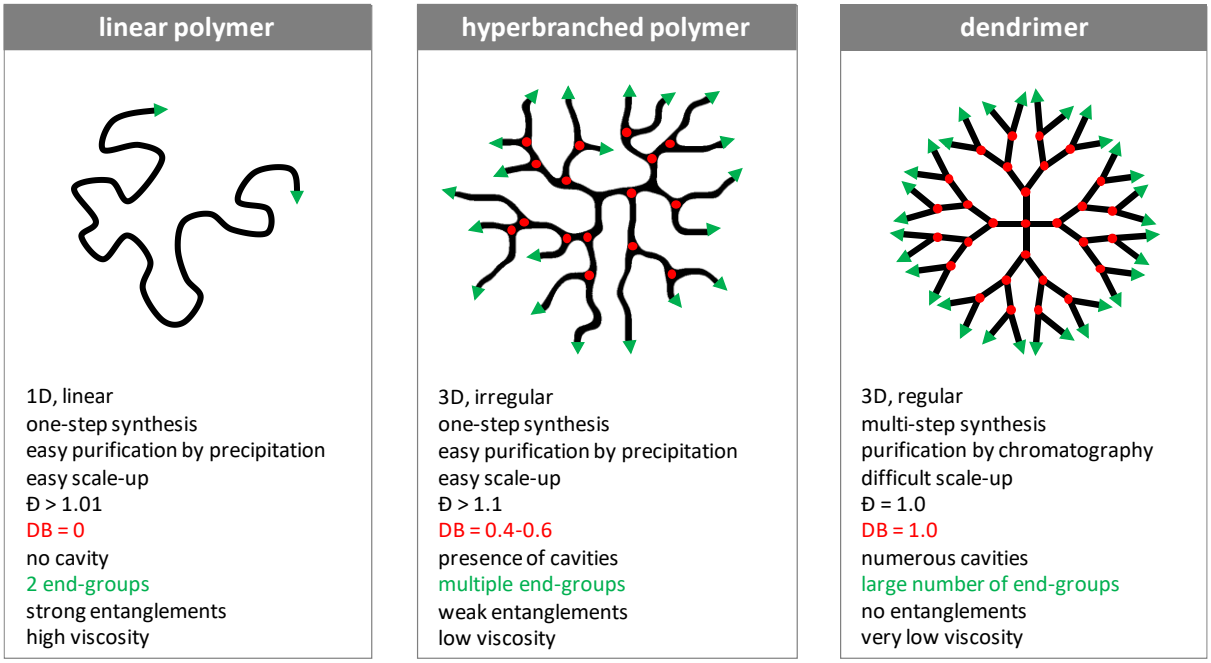

Figure 1.1. Comparison of HBPs with linear polymers and dendrimers.

HBPs have potential applications in optical, electronic and magnetic materials, coatings, additives, supramolecular chemistry, and biomedicine [7]. Their features are especially interesting for the development of nanocarriers in the field of drug delivery. The composition of HBPs is tunable at the branching, linear, and terminal units offering a significant degree of freedom in the design of nanocarriers for drug delivery. These units can be chosen to be responsive to one or multiple stimuli (*e.g.* pH [8–11], temperature [12–15], redox [16–18], light [19–22], magnetic field [23], enzyme [24–26]) to induce a change in conformation of the polymer chain or its degradation to trigger drug release [27]. Their globular three-dimensional structures lead to the formation of internal cavities that can be used to encapsulate small-molecule drugs (less than 900 g mol^{-1}), *e.g.* doxorubicin (DOX) and paclitaxel (PTX) for cancer treatment, and radioisotopes, *e.g.* ^{99m}Tc, ^{131}I, and ^{125}I, for diagnostic purposes. Furthermore, the high density of functional groups at the periphery of HBPs can be exploited to introduce functionalities on HBPs such as effective contrast agent probes for magnetic resonance imaging [28–31] or targeting groups to promote the specific accumulation of drug carriers at the targeted site also known as targeted drug delivery. In this section, we propose to provide an overview of the different synthesis strategies to obtain HBPs and their potential as drug delivery systems.

1.2. Synthesis strategies to prepare hyperbranched polymers

Various synthesis strategies have been used to prepare HBPs and have been reviewed in details in previous reviews [27,32–38]. This section does not aim at providing the reader a comprehensive overview of all the syntheses used to obtain HBPs, but pointing the main synthesis strategies developed and their general concept. The two main routes consider the use of either a pair of monomers or a single monomer with orthogonal functions to prepare HBPs (Figure 1.2). As compared to the single monomer route, the monomer-pair route has a stronger tendency to intramolecular cyclization leading to the formation of (multi)cyclic species [39–41]. The degree of branching can be tuned for the polymerizations conducted through a chain-growth method by changing the ratio between the monomers leading to linear units (monomers with one vinyl group) and those creating branching points (monomers possessing multiple vinyl groups in Section 1.2.1.2 and inimers in Section 1.2.2.2). These strategies have been extended to non-covalent interactions such as electrostatic interaction, hydrophobic interaction, and hydrogen-bonding interaction through both synthesis routes (monomer-pair and single monomer methodology) [22,42–44].

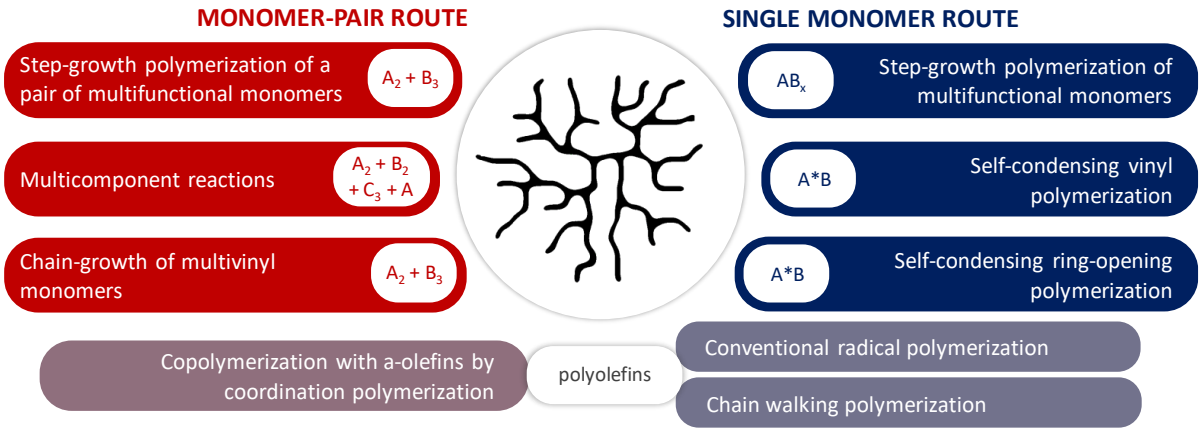

Figure 1.2. Main synthesis routes to prepare HBPs.

1.2.1. Monomer-pair route

1.2.1.1. Step-growth copolymerization of A_2 and B_3 monomers

The $A_2 + B_3$ system (*i.e.* using two monomers with one bearing two identical functional groups A and the other one three identical functional groups B) is attractive as it can be used to produce HBPs in large scales through a one-pot synthesis. The choice of the groups A and B is

dictated by the selective reactivity of the functional groups A with the functional groups B and their reactivity should be the same for the monomers and the functional groups present on the polymers. A large variety of A and B functional groups have been used, which includes those commonly used for step-growth polymerizations, such as hydroxyl groups with epoxides to prepare hyperbranched aliphatic polyethers [45], and anhydrides with amines to prepare hyperbranched polyimides [46,47], but also click chemistry such as azide with alkyne groups involved in copper-assisted alkyne-azide cycloaddition (CuAAC) reactions [48,49]. The control of the degree of branching is achieved by controlling the feed ratio and introducing a linear component. However, the A_2 + B_3 system generally suffers from a tendency to gelation and intramolecular cyclization.

The minimization of gelation can be afforded by quenching the polymerization before the gel point, conducting the polymerization in dilute solution, or introducing monofunctional end-capping reagents [50]. Another interesting approach, known as couple-monomer approach, is based on the use of monomer pairs with functional groups of non-equal reactivity [51]. B_3 is replaced by CB_2, for which the functional groups B and B' can both react with A, but do not have the same reactivity. An AB_2 intermediate is rapidly formed at the early stage of the polymerization, which then undergoes further propagation leading to the formation of HBPs. The first example of this approach was introduced by Yan *et al.* using 1-(2-aminoethyl)piperazine as CB_2 in the presence of divinyl sulfone as A_2 to prepare hyperbranched poly(sulfone-amine)s [51]. This approach has been extended to other functionalities (*e.g.* A_2 + CB_2 such as dithiols with propargyl acrylate forming as AB_2 intermediate a molecule bearing one thiol and one alkyne by thiol-ene reaction and leading to HBPs by thiol-yne reaction [52]). The use of other asymmetric monomers (*e.g.* AD + CB_2 such as methacryloyl chloride with 2-amino-2-methyl-1,3-propanediol forming as AB_2 intermediate by the reaction of the acid chloride with the amine followed by Michael addition of the methacrylate on the hydroxyl groups [53]).

The stepwise reaction between the A and B functional groups is random and each step can lead to either the growth of the polymer or a reaction of intramolecular cyclization. The presence of this side reaction affects the structure of the polymer obtained leading to truncated polymer topologies with a more limited number of terminal functional groups. The choice of monomers used can influence the extent of intramolecular cyclization reactions. For example, Ban *et al.* have investigated A_2 monomers with different spacing units between the

two terminal alkyne groups [49]. By increasing the rigidity (*i.e.* phenyl groups *vs.* alkyl chains) and decreasing the length (hexyl *vs.* dodecyl groups) of the spacing units, intramolecular cyclization reactions are diminished. Besides the choice of the monomers, the feed ratio between A_2 and B_3 strongly affect the intramolecular cyclization reactions. Using a feed ratio far from the stoichiometry in functional groups A and B limits the side reactions [54]. Furthermore, conducting the polymerization in dilute solution enhances the number of intramolecular cyclization reactions. Unal *et al.* have demonstrated that the melt polymerization of A_2 and B_3 monomers leads to highly branched polyesters without significant intramolecular cyclization reactions [55].

With the recent developments in multi-component reactions such as Ugi and Passerini reactions [56], the one-pot preparation of HBPs has been extended to the use of three or more monomers [57,58]. Deng *et al.* have reported the synthesis of HBPs by ABC-type Passerini reaction using hexanedioic acid (A_2), hexane-1,6-dial (B_2), 1,6-diisocyanohexane (C_2) and 10-undecenoic acid (A) [57]. The control of the total amount of A groups used for the polymerization and the ratio between A_2 and A is critical to avoid gelation and prepare HBPs. Similarly, Zhang *et al.* have conducted a multi-component reaction using propargyl amine, *N*-acethomocysteine thiolactone, diethylenetriamine in the presence of CuCl and *p*-toluenesulfonyl azide to produce HBPs [58].

1.2.1.2. Chain-growth polymerization of multivinyl monomers

Similarly, the $A_2 + B_x$ system has been adapted to chain growth polymerizations through the use of multivinyl monomers. Usually, multifunctional comonomers (B_x, *e.g.* divinylbenzene consisting in two difunctional groups corresponding to B_4) are used as crosslinking agents for the chain growth polymerization of vinyl monomers (A_2) allowing the formation of polymer networks using a small amount of this comonomer. Gelation can be retarded by using thiols as free radical chain transfer agents, but thiols need to be introduced at least in equimolar quantity relative to the multifunctional comonomer [59], and the polymerization has to be conducted in dilute solution [60] to obtain HBPs. The degree of branching can be increased by increasing the polymerization temperature and the amount of multifunctional comonomer [60,61]. The structure of the multifunctional comonomer affects the polymerization. For example, the two vinyl groups of divinylbenzene do not have the same reactivity (*i.e.* formation first of polymer chains with pendent vinyl groups followed by their reaction to form branching points) facilitating the formation of HBPs [60], while polymer gelation is more

challenging to inhibit using oligo(ethylene glycol) dimethacrylate, and ethylene glycol diacrylate is a poor branching agent [62].

This strategy has been extended to polymerization in dispersed media (*i.e.* suspension [63] and emulsion [64] polymerizations) and controlled radical polymerization such as atom transfer radical polymerization (ATRP) [65] and reversible addition-fragmentation chain transfer (RAFT) polymerization [66]. Among the controlled radical polymerization techniques catalytic chain transfer polymerization involving low-spin cobalt(II) complexes (usually cobaloximes) as chain transfer agents has attracted the attention to prepare HBPs using multifunctional monomers [67]. This technique permits the synthesis of HBPs with a minimal amount of chain transfer agent as compared to thiols and can be also performed in dispersed media [68]. Furthermore, HBPs with well-defined topology [69] (*i.e.* degree of branching and molecular weight) and functionalities (*i.e.* vinyl groups as terminal units that can be used for post-polymerization functionalization [70]) can be synthesized.

1.2.2. Single monomer route

1.2.2.1. Step-growth polymerization of AB_x monomers

The random polymerization of AB_x monomers bearing one reactive group A and multiple reactive groups B with $x \geq 2$ affording highly branched polymers without gelation considering the intramolecular reactions negligible has been predicted by Flory [71]. For AB_2 monomers, if both B groups have reacted with A groups of other AB_2 monomers a branching point is created, while a linear unit is obtained when only one of the two B groups is consumed. The resulting HBPs contain one A terminal group and (n+1) B terminal groups for n AB_2 monomers involved in the polymerization ((x-1)n+1 for AB_x monomers). AB_x monomers including not only AB_2, but also AB_3 [72–74], AB_4 [74,75], AB_6 [74] and AB_8 [75] have been used to prepare HBPs in an one-pot synthesis using different types of functionalities such as trimethylsiloxy groups with acid chlorides for the preparation of hyperbranched aromatic polyesters, protected isocyanates with hydroxyl groups to synthesize hyperbranched polyurethanes [76], cyclopentadienones with alkyne groups affording hyperbranched polyphenylenes through Diels-Alder reaction [77].

Extremely broad molecular weight distributions of these HBPs are expected at high conversions of A groups by enumeration of all the possible configurations [78]. The experimental dispersity of HBPs obtained from AB_x monomers is larger than the one of linear polymers from AB monomers, but smaller than the calculated ones. To obtain HBPs having

narrower molecular weight distributions, few strategies have been proposed: use of multifunctional cores (B_x) for the polymerization of AB_2 monomers that can be enhanced by a slow addition of AB_2 into a dilute solution of B_x [79,80], but also the selection of monomers with functional groups having different reactivities if present on the monomer or polymer [81–84].

This route has been combined with controlled radical polymerization to control the topology of HBPs. For example, Zhu *et al.* have reported the synthesis of V- and Y-type AB_2 monomers [85]. The V-type AB_2 monomer consists of an aromatic core with one alkyne and two bromides as A and B groups respectively, while the Y-type AB_2 monomer possesses one bromide and two alkynes. ATRP is performed from the bromo terminal groups followed by CuAAC reaction after modification of the bromides into azide groups to obtain HBPs with different branching patterns.

1.2.2.2. Self-condensing polymerization

Self-condensing vinyl polymerization (SCVP) was introduced by Fréchet using a vinyl monomer bearing a group able to initiate the polymerization of vinyl groups, known as inimer standing for *ini*tiating mono*mer* (A*B), that can be assimilated to the AB_2 system where the vinyl group behaves as a difunctional group equivalent to B_2, and the initiating group A* as the group A [86]. In this work, the inimer 3-(1-chloroethyl)ethenylbenzene is polymerized in the presence of $SnCl_4$ and tetrabutylammonium bromide. While the kinetics at the beginning of the polymerization is slow, the evolution of the molecular weight over time increases exponentially. The high dispersity of the obtained HBPs is attributed to the complex mechanism of polymer growth as each inimer can lead to the formation of different species. The A* group of A*B can initiate the polymerization by attacking the B group on another A*B inimer leading to a dimer possessing a vinyl group (B), an initiating group (A*) and an active center (b*) resulting from the attack on the double bond. The addition of the next A*B can thus occur either through the addition of its A* group on the B group of another A*B or the attack of either its A* or b* group on the double bond of another A*B.

Besides cationic polymerization, SCVP has been extended to anionic and radical polymerizations with a preference for living and controlled polymerizations to minimize crosslinking reactions and thus gelation of the reaction mixture. Due to the high reactivity of carbanions, the preparation of inimers containing a vinyl group and an anionic initiator is difficult, requiring the formation of the inimer to be formed *in situ* [87]. With the

developments of group transfer polymerization inimers with a silylketene acetal group that can be activated by nucleophilic catalysts to initiate the polymerization have been synthesized and used for the preparation of HBPs [88,89]. In a similar manner than SCVP, A*B inimers have been developed for self-condensing anionic or cationic ring-opening polymerization of cyclic epoxides [90,91], oxetanes [92], lactones [93] and phosphates [94]. The inimer usually consists of a hydroxyl group as the initiating species (A*) and a ring (B) acting as the difunctional group. For example, hyperbranched polyethers have been prepared by addition of the hydroxyl (A*) group from glycidol onto the epoxide (B) of another one leading to the formation of an additional alkoxide (b*) that can also promote nucleophilic propagation. One of the potential side reactions is intramolecular cyclization.

The three main controlled radical polymerization techniques (*i.e.* nitroxide-mediated polymerization (NMP), ATRP, and RAFT polymerizations) have been investigated to synthesize HBPs by SCVP. Two approaches have been employed to prepare HBPs by NMP. Alkoxyamine-functionalized styrenes [95] have been used as inimers affording HBPs with terminal alkoxyamines, while polymerizable nitroxides (styrene and methacrylate bearing a nitroxide) lead to HBPs with alkoxyamines at the branching points [96,97]. For the latter case, the branching points can be thermolytically degraded. Due to some limitations of NMP [98] such as slow polymerization kinetics, limited control over the homopolymerization of methacrylates and lower commercial availability of nitroxides and alkoxyamines, this controlled radical polymerization technique has been less extensively investigated as compared to ATRP and RAFT polymerizations. For ATRP, inimers derived from styrene and (meth)acrylates with an alkyl halide, either bromide or chloride, have been employed. Using a too high concentration in copper catalyst lead to gelation due to the formation of a high concentration in radicals promoting termination reactions by bimolecular couplings [99]. The preparation of HBPs is strongly affected by the temperature and the choice of the ligand, which dictates the ability of radicals either to propagate or deactivate into the dormant species and consequently the topology of HBPs obtained, *i.e.* ratio between linear and branching units [100,101]. RAFT polymerization uses A*B transmer (contraction of chain *trans*fer agent and mono*mer*) based on dithioester compounds, acting as chain transfer agents, functionalized with a vinyl group (styrene, (meth)acrylate, (meth)acrylamide, vinyl acetate) [102]. The vinyl group introduced either on the R-group attached to the sulfur of the dithioester or on the Z-group next to the thioketone of the chain transfer agent leads to the

positioning of the chain transfer agent either as terminal groups or at the branching points of HBPs respectively. Recently, organotellurium-mediated radical polymerization has been explored to prepare HBPs using a vinyl telluride possessing a hierarchical reactivity (*i.e.* the telluride cannot initiate by itself, but once the vinyl group has been activated, it participates to the polymerization creating branching points) in the presence of acrylates and an organotellurium chain transfer agent [103].

1.2.3. Case of branched polyolefins

Low-density polyethylene is commonly produced by radical polymerization under high temperature and high pressure leading to branched structures due to inter- and intramolecular chain transfer reactions [104], while high-density polyethylene with a low content of branching is prepared by coordination polymerization. Late transition metal homogeneous catalysts such as $Me_2Si(\eta^5\text{-}C_5Me_4)(\eta^1\text{-}N\text{-}tBu)TiCl_2$ have been used to copolymerize ethylene with a low amount of long α-olefins to prepare polyethylene with well-defined branches [105,106]. The development of catalysts for coordination polymerization has been explored to synthesize branched polyethylenes. For example, Barnhart *et al.* have proposed the use of a tandem catalyst system consisting in $[(\eta^5\text{-}C_5Me_4)SiMe_2(\eta^1\text{-}NCMe_3)TiCl_2$ promoting the polymerization of ethylene and 1-alkenes and $[C_5H_5B\text{-}Ph]_2ZrCl_2$ producing 1-alkene *in situ* [107]. Guan *et al.* have introduced the concept of chain walking polymerization to prepare hyperbranched polyethylenes [108,109] through the use of Pd-diimine catalysts, mechanism identified by Johnson *et al.* [110]. The ethylene-dissociated state of the catalyst can yield either the trapping of new ethylene monomer leading to chain growth or β-hydride elimination and isomerization inducing chain migration and formation of branching units. Other catalysts such as catalysts based on nickel [110] and zirconium [111] can also induce *in situ* formation of olefin-terminated oligomers via β-hydride elimination.

1.3. Hyperbranched polymers and passive targeted drug delivery

Targeted drug delivery systems have been developed to optimize their pharmacokinetics aiming at a targeted localization in the body. Nanosized carriers loaded with the drug can circulate in the bloodstream and accumulate preferentially at the tumor by the enhanced permeability and retention effect (EPR) [112–114]. This passive targeting is promoted by a prolonged circulation in the bloodstream and the differences existing between tumoral and healthy tissues such as higher vasculature and larger gap junctions between endothelial cells

of tumors (up to 1 μm). While very small carriers are rapidly cleared by the kidneys (*i.e.* threshold of renal clearance for nanoobjects with a hydrodynamic diameter of 6 nm) [115–117] and large ones accumulated mainly in the liver and spleen (greater than few hundreds of nanometers) [118], nanocarriers with a diameter between 20 and 200 nm can extravasate easily in tumor tissues [119].

As the size of drug carriers has a critical role in promoting low accumulation in healthy tissue and high accumulation in tumor tissue via the EPR effect, this parameter should be considered when designing polymers as drug delivery systems. Polymers of various topologies including HBPs [120,121] have been explored as drug carriers (Figure 1.3). Usually, HBPs of high molecular weight can be relatively easily synthesized reaching a reasonable size (>10 nm) to passively target tumors by EPR effect [122], while dendrimers with a number of generation higher than five are difficult to prepare due to steric hindrance affording nanostructures with a hydrodynamic diameter lower than 10 nm that are thus not suitable for passive targeting [123]. However, unimolecular HBPs of low molecular weight will have a small size and cannot be used for size-related passive targeting at the tumor via EPR effect as they can be easily removed by renal excretion or through bypassing filtration by the spleen [124]. Despite this limiting feature for drug delivery, their small size (less than 10 nm) has been exploited for other biomedical applications such as bioimaging reducing the toxicity of radioisotopes and facilitating their elimination through urine and feces [125,126]. The self-assembly of HBPs into multimolecular nanostructures has been considered to increase the size of nanocarriers [127–132]. Son *et al.* have reported the synthesis of hyperbranched polyglycerol monofunctionalized with spiropyran [133]. As hydrophobic spiropyran is known to undergo reversible photochromism at 250-380 nm forming the corresponding water-soluble merocyanine species, these spiropyran-functionalized hyperbranched polyglycerol self-assemble into micelles and disassemble upon UV irradiation. Pyrene has been encapsulated into these micelles, released upon irradiation at 254 nm and partially reloaded into micelles upon irradiation at 620 nm. Besides controlling the size, drug loading can be increased as compared to unimolecular nanostructures [131], but also the loading of large drugs such as enzymes and proteins is more efficient [134,135].

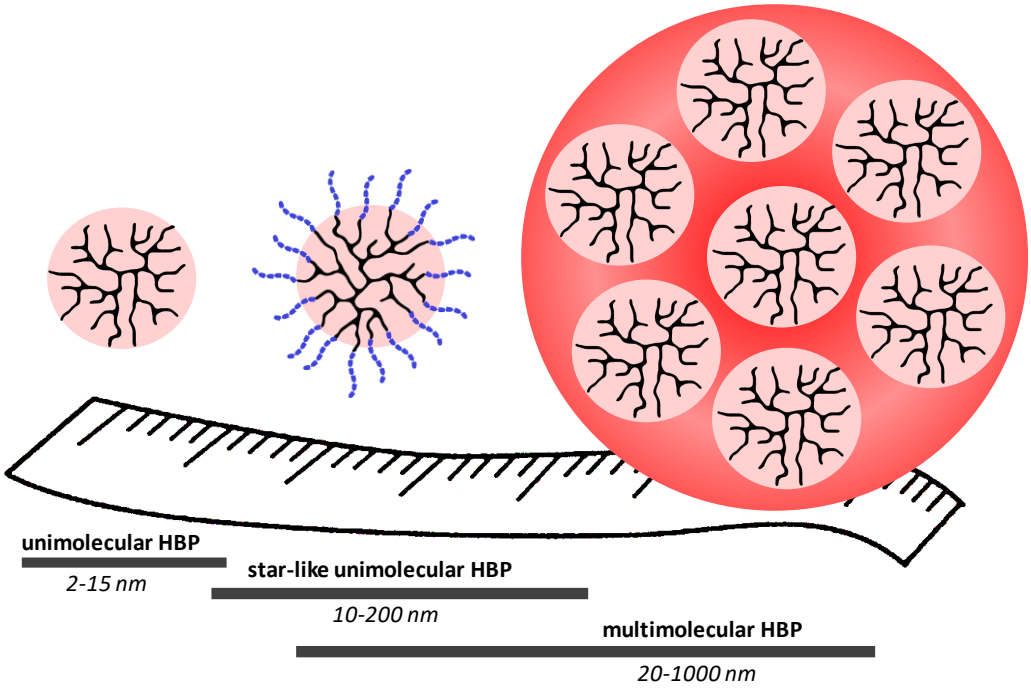

Figure 1.3. HBP nanostructures and their relative sizes.

Like dendrimers, HBPs form cavities that can be used to encapsulate cargos of different sizes [136] including small chemotherapeutic drugs such as DOX [137,138], camptothecin (CPT) [139,140], cisplatin [141–143], and 5-fluorouracil (5-FU) [144]. For example, Wu *et al.* have investigated hyperbranched polyglycerol and its ability to encapsulate and deliver a guest molecule [144]. HBP labeled with carboxyfluorescein (green light emission) entrapping chlorin e6 (red emission light) shows the co-localization of chlorin e6 and the HBP by confocal fluorescence microscopy in the cytoplasm of MGC-803 cells confirming the ability of the HBP to act as a carrier. The study of Rhodamine B-encapsulated in this HBP by nuclear magnetic resonance spectroscopy seems to indicate that Rhodamine B is entrapped by electrostatic interactions between the xanthene ring of Rhodamine B and ether linkages of the hyperbranched polyglycerol. Larger drugs such as DNA [145–148] and siRNA [149–151] form complexes with unimolecular HBPs by electrostatic interactions. Tuning the structure of HBPs permits to control the strength of the interaction between gene and carrier by modulating the charge density at its surface, adjusting its molecular weight, and preparing different molecular structures [152]. Besides, by controlling the functionality of HBPs multimolecular structures able to release its large cargo under a stimulus such as pH promoting demicellization have been prepared [134].

Individual HBPs can be assimilated to unimolecular micelles formed from solely one HBP molecule. Due to their covalent nature with interconnected structures similar to nanogels, these individual HBPs have an excellent stability in diluted environments such as *in vitro* and *in vivo* conditions as compared to micelles formed from the self-assembly of molecules, which can undergo demicellization at a concentration below its critical micelle concentration [153] and are more prone to sustained drug release. Popeney *et al.* have developed hydrophilic hyperbranched polyglycerol grafted on a hydrophobic hyperbranched polyethylene [154]. The chain walking copolymerization of ethylene and a siloxy-functionalized comonomer followed by the removal of the protecting groups produce a hyperbranched polyethylene core terminated with hydroxyl groups used for the ring-opening polymerization of glycidol. This polymer under diluted conditions has been used to encapsulate hydrophobic fluorescent dyes such as Nile red. This core-shell hyperbranched copolymer permits the uptake of the dye into A549 cancer cells by endocytosis, while hyperbranched polyglycerol grafted on an aliphatic linear hydrocarbon shows poor cellular uptake. Donskyi *et al.* have prepared hyperbranched polyglycerol grafted on fullerene [155]. These nanostructures self-assemble with a decrease in their size by increasing the number of polyglycerol branches, *i.e.* multimolecular nanostructures of 19 nm with two branches per fullerene and unimolecular nanostructures of 8 nm for fullerene bearing five polyglycerol branches, as the higher number of branches on fullerene reduces their self-assembly. The loading of a hydrophobic dye decreases with the number of branches on fullerene as the interaction of the drug with the fullerene core is decreased. For unimolecular nanostructures the release profile of the dye depends solely on the interactions between the dye and the carrier, while its release is faster for multimolecular nanostructures where the dye is encapsulated in the aggregates.

Due to their high density in functional groups, HBPs provides access to high drug payload by conjugation of the drug to the terminal functionalities of HBPs [156,157]. Kolhe *et al.* have conjugated ibuprofen as drug and fluorescein isothiocyanate (FITC) on the hydroxyl terminal groups present on hyperbranched polyglycerols using *N*,*N*'-dicyclohexylcarbodiimide (DCC) as coupling agent [156]. These conjugates have a high payload in ibuprofen (70%), enter A549 cells rapidly and are mainly distributed in the cytosol. The drug is released after cleavage of the ester bond by lysosomal enzymes present in the cell. Interestingly, the drug can also be one of the constituting units of HBPs. Liu *et al.* have synthesized HBPs with alternated hydrophobic diselenide and hydrophilic phosphate groups. While the phosphate groups act

as branching units [158], selenium compounds [159,160] have been reported as anticancer agents affording HBP as a self-delivery anticancer agent.

The conjugation of poly(ethylene glycol) (PEG) directly to the drug or its carrier has been proposed to improve their shelf-life, solubility and circulation half-life, thus favoring their accumulation at the tumor sites through the EPR effect [161]. Various types of HBPs, including hyperbranched polyether [162–164], polyester [165], and poly(amido amine) (PAA) [166], have been modified with PEG affording star-like HBPs. Xu *et al.* have reported the modification of hyperbranched polyglycerols [167] and hyperbranched poly(ethylene imine)s [168] with tri-PEGylated benzaldehydes forming an imine group labile under acidic conditions. These tri-PEGylated HBPs leads to a higher encapsulation of dyes as compared to unmodified HBPs and even mono-PEGylated HBPs. Similarly, the higher the degree of functionalization of HBPs with tri-PEGylated benzaldehydes, the higher the encapsulation of the dye. The release of dyes and drugs can be triggered under acidic pH with shorter half-life for a pH of 5 as compared to physiological pH (7.4). Other neutral hydrophilic polymers have been also conjugated to HBPs. Kurniasih *et al.* have developed core-shell nanostructures based on hyperbranched polyglycerol functionalized at the periphery with PEG and core with hydrophobic biphenyl species [169]. Pyrene has been encapsulated in the core of HBPs forming unimolecular nanostructures (10-11 nm), while Nile red being located in the outer shell of HBPs and prone to self-assemble has induced the formation of aggregates of HBPs (100-200 nm). No release of pyrene and Nile red at pH 7.4 has been observed. However, at pH 5 pyrene has not been released within two weeks, while the complete release of Nile red has been observed after one week with a half-life of 38 h and decrease of the hydrodynamic diameter from 200 to 10 nm indicating the release of the dye by disassembly of the HBPs. Poly(*N*-isopropylacrylamide) (PNIPAM) undergoes a reversible phase transition at its lower critical solution temperature (32 °C) that has been exploited in the field of drug delivery [170]. While Luo *et al.* have synthesized unimolecular core-shell micelles based on hyperbranched polyglycerols with a shell based on PNIPAM that collapses on heating and expands on cooling [171], Picco *et al.* have reported the synthesis of hyperbranched polyesters with a PNIPAM shell forming unimolecular nanostructures (20 nm) below the phase transition temperature that self-assemble into multimolecular nanostructures (220 nm) above this temperature [127]. Zhao *et al.* have prepared a PEGylated thermo-responsive HBPs consisting in a PAA core modified with PEG and PNIPAM [172]. This HBP promotes the fast release of indomethacin

used as model drug (90% of drug release in 12 h) at 30 °C, while at 37 °C a more sustained drug release (less than 30% in 12 h) is obtained.

1.4. Functionalization of hyperbranched polymers for active targeting in drug delivery

Although passive targeting is an effective strategy for targeted drug delivery, it has several limitations such as the inefficient diffusion of the nanocarrier into tumor cells due to its low interaction the cell surface [173], but also the extent of vascularization and porosity of the tumor depending on its type and status [114,174]. The development of strategies to promote active targeting (Figure 1.4) aims at increasing the cellular uptake of the nanocarriers for efficient delivery of its cargo and enhancing cell specificity. Active targeting in drug delivery systems considers the insertion of targeting moieties directly attached at the surface of the nanocarriers. These targeting moieties interact specifically with receptors expressed on cancer or angiogenic endothelial cells enhancing the binding and internalization of nanocarriers. Active targeting moieties are particularly beneficial for cancer therapy due to the reduced delivery of potentially toxic drugs to healthy tissue. A wide variety of targeting moieties have been considered including aptamers that can be either peptides [175–178] or oligonucleotides [179–181], and folic acid [182–184] that have been conjugated on HBPs.

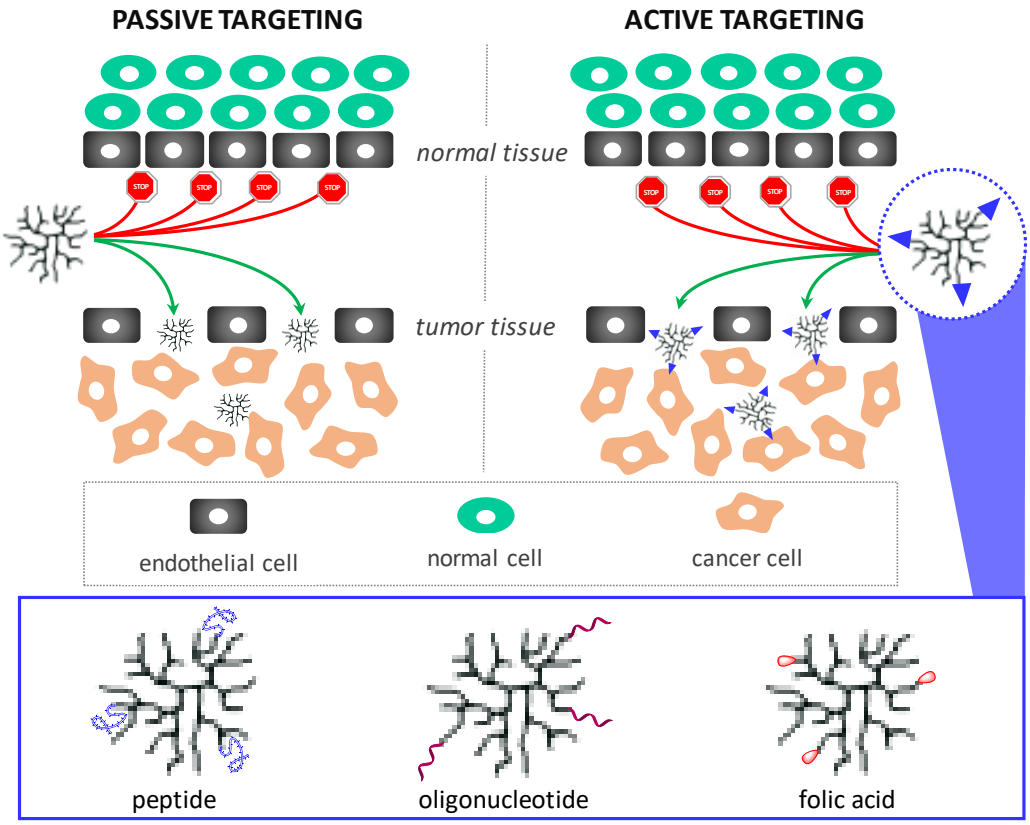

Figure 1.4. Passive and active targeting in HBP-based drug delivery

1.4.1. Peptides as active targeting groups

Peptides are good candidates as active targeting moieties for drug delivery systems due to their high avidity towards cell receptors and low immunogenicity, but also peptides are easy to synthesize and conjugate onto nanocarriers [185,186]. Peptides have been grafted onto the surface of different nanostructures such as gold [187], quantum dots [188], iron oxide [189], and silica nanoparticles [190], but also liposomes [191], carbon nanotubes [192], and micelles based on dendrimers [193], linear [194], brush [195], star [196], and hyperbranched [197] polymers.

Tumor targeting peptides (TTPs), usually shorter than cell penetrating peptides (three to ten residues), interact more specifically with receptors overexpressed by tumor cells [198–200]. TTPs are designed to bind to cell surface receptors, intracellular receptors, and the extracellular matrix. As an example, the most extensively studied ones are $\alpha_v\beta_x$ integrins targeting cell surface receptors [201]. Integrins are cell adhesion receptors [202] present on the cytoplasmic side of the lipid bilayer promoting the assembly of cytoskeletal polymers and signaling complexes, but also on the extracellular side of the lipid bilayer binding to the extracellular matrix or counter-receptors on adjacent cells. Various ligands have been identified to bind to integrins. The most common minimal peptide sequence used to target $\alpha_v\beta_3$ integrin overexpressed at the surface of endothelial tumor cells is Arg-Gly-Asp (RGD) that can be found as linear and cyclic (*e.g.* cyclic RGDdYK where dY stands for the D-isomer of tyrosine, and cyclic CRGDKGPDC known as iRGD) derivatives [203].

Peptide-conjugates are prepared through two main strategies: i) polymerization using peptide-containing macroinitiators or macromonomers and ii) post-polymerization modification with peptides. The use of either macromonomers or macroinitiators bearing a peptide sequence permits to introduce the peptide sequence during the polymerization. The synthesis of macromonomers and macroinitiators bearing a peptide sequence has been described in the literature through different routes including coupling reactions in solution and on resin end-capping of the peptide sequence with a polymerizable or initiating group. Peptide-functionalized macroinitiators have been designed to prepare linear and star polymers bearing a peptide at the extremity of the polymer chain [204]. Different approaches and polymerization techniques have been explored including NMP [205], ATRP [206] and RAFT [207] from a peptide grafted on the resin, peptide-bearing initiator or chain transfer agent used under ATRP [208] and RAFT [209–211] polymerization conditions, ring-opening

polymerization of *N*-carboxyanhydrides from peptide-PEG macroinitiator [212]. The use of peptide-containing macromonomers afford polymers bearing peptides on the side chains of the polymer backbone. Depending on the polymerization technique used, the functional groups on the peptide may have to be protected during the polymerization. Various polymerization techniques such as ATRP [213,214], RAFT [215–217], and ring-opening metathesis polymerization [218–220] have been used to (co)polymerize peptide-containing macromonomers.

Post-polymerization modification of polymers is a well-known strategy to prepare functional polymers through the introduction of further functionalities on polymers [221,222]. The functional groups present on the polymer should be able to react chemoselectively with those of the molecules to be introduced. Various routes have been exploited to further functionalize polymers either by presenting chemoselective functional groups at one extremity of the polymer or on the side chains of the repeat units constituting the polymer chains. Activated esters [223] such as *N*-hydroxysuccinimide (NHS) and pentafluorophenyl (PFP) esters readily reacts with primary amines to form stable amide linkages. Thiols have been widely used to functionalize polymers through either disulfide exchange, Michael addition or radical mechanism reacting with disulfide bridges, epoxides, isocyanates, maleimides, vinyl groups (including (meth)acrylates), and alkynes [224]. Alkynes are involved in different coupling reactions such as CuAAC [225], strain-promoted 1,3-cycloaddition reactions of cycloalkynes and azides [226], and copper-catalyzed Glaser coupling reactions of terminal alkynes [227]. Other routes for post-polymerization modification include ring-opening reaction of azlactones [228], atom transfer radical addition [229,230], nitroxide radical coupling [231], and Diels-Alder reactions [232]. Various synthetic routes have been considered for the conjugation of TTPs, but alos other targeting ligands, on HBPs by post-polymerization modification as depicted in Figure 1.5.

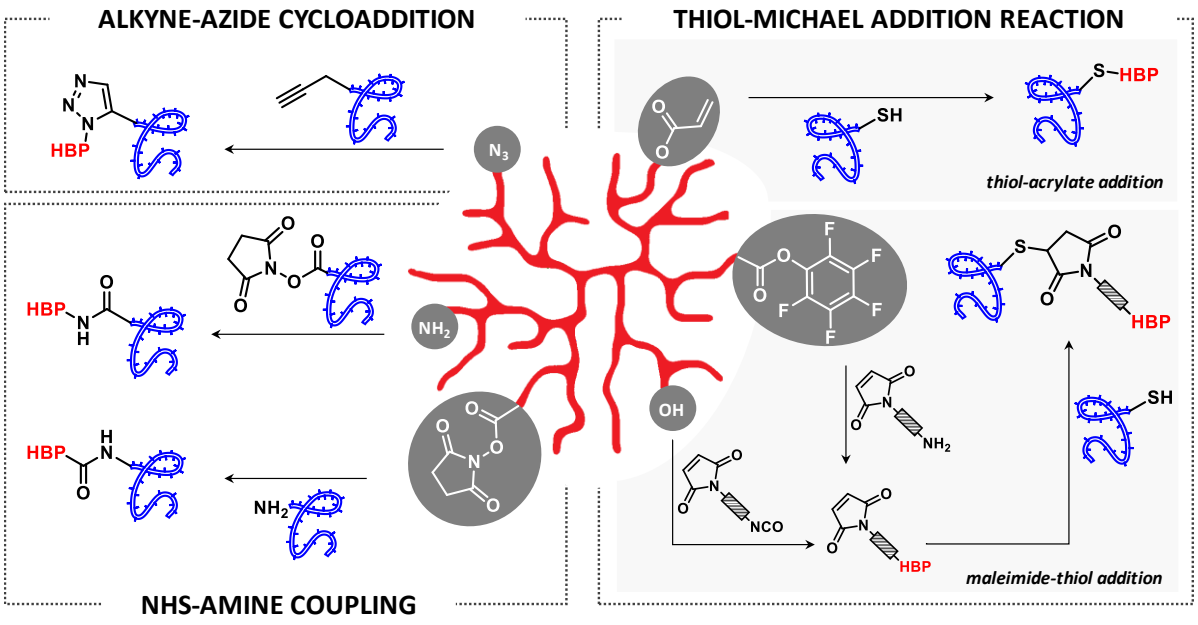

Figure 1.5. Synthetic routes used for the post-polymerization functionalization of HBPs with peptides.

1.4.2. Other ligands used as active targeting groups

Short strands of oligonucleotides (*i.e.* single-stranded DNA and RNA constituted of 15 to 40 bases) can specifically recognize a specific target molecule and have advantages such as their low molecular weight as compared to antibodies, simple modification, and remarkable affinity, but also high stability, non-immunogenicity and nontoxicity *in vivo* [233,234]. Oligonucleotides have gained attention as targeting moieties grafted on the surface of various nanostructures in recent years [235–238], including HBPs for targeted drug delivery.

Small molecules have been also considered as targeting groups. Among them, vitamin B9 also known as folate when naturally occurring or folic acid in its synthetic form (Figure 1.6) is the most investigated targeting ligand for tumor cells as folate receptors are highly overexpressed in epithelial, ovarian, cervical, breast, lung, kidney, colorectal, and brain tumors [239]. Folic acid has been conjugated to polymers including HBPs due to their stability over a broad range of temperatures and pH values, non-immunogenicity, facile functionalization, inexpensiveness, and small size [239–241].

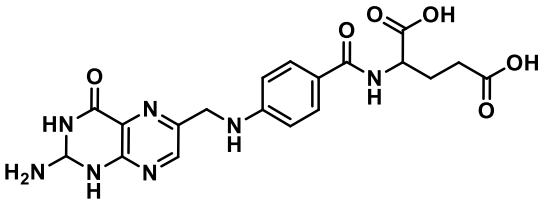

Figure 1.6. Structure of folic acid.

Other ligands, less extensively studied but that are worth to be mentioned, are *glutamate urea* that bind selectively to prostate-specific membrane antigen, that is overexpressed 10-fold higher in prostate cancer cells than in healthy prostate tissues, [242] [243–245] *alendronate* which is an amino bisphosphonate (Figure 1.7) used to treat different bone diseases including osteoporosis and bone metastasis, but is also employed as bone-targeting ligand due to its high affinity for hydroxyapatite mineral composing human and animal bones [246], [247] *monosaccharides* such as mannose and galactose (Figure 1.7) are able to bind to carbohydrate-binding proteins known as lectins that are overexpressed in cancer cells, [248][249][250] *transferrin* an iron-binding glycoprotein promoting its transport into cells through transferrin receptors [251] [252] that is overexpressed in cancer cells, and *hyaluronic acid* an anionic biopolymer which has several excellent properties such as biocompatible, biodegradable, non-toxic, and non-immunogenic [253] and interact with CD44, ICAM-1, and RHAMM receptors, which are overexpressed in many cancer cells, in particular in tumor-initiating cells [254] [255].

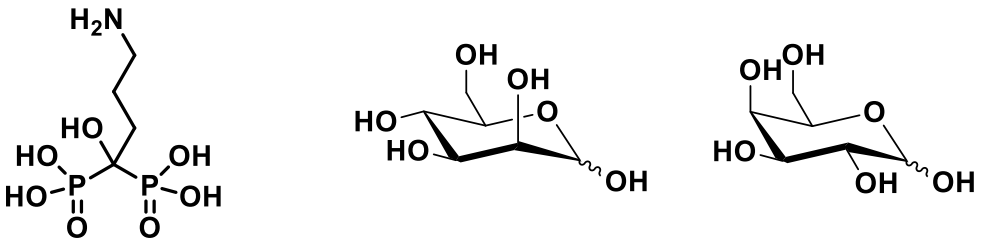

Figure 1.7. Structure of alendronate, mannose and galactose.

1.5. Conclusion

HBPs are highly branched three-dimensional macromolecules possessing unique properties such as low intrinsic viscosity, low glass transition temperature, presence of internal cavities, and a large number of functional groups at the periphery due to their globular and dendritic structures. These properties are attractive for applications in a large variety of fields such as coatings, modifier additives, light-emitting materials, and drug delivery systems. While HBPs are less regular than dendrimers, their syntheses are easier and can be achieved in a one-pot polymerization process. Various synthesis strategies have been developed to prepare HBPs including AB_x, "A_2 + B_n", self-condensing vinyl and self-condensing ring-opening polymerizations, click chemistry and multicomponent reactions.

In the field of drug delivery systems, HBPs have been used as carriers of drugs ranging from small molecules (*e.g.* DOX and CPT) to large nucleic acids (*e.g.* DNA and siRNA). Passive and active targeting can enhance the accumulation of the drug at the tumor sites, which can be achieved by modification of HBPs at their periphery using different synthetic routes (*e.g.* amide bond formation using carbodiimides, CuAAC, thiol-ene reactions). For passive targeting, functional groups promoting more prolonged circulation in the bloodstream, and thus higher accumulation at the tumor sites, such as PEG, have been covalently attached to HBPs. Active targeting of tumor sites has been first investigated by conjugating folic acid and extended to specific ligands, including peptides and oligonucleotides, on HBPs to target specific receptors overexpressed on cancer cells. The conjugation of such ligands has been proven to be an efficient approach to enhance the accumulation of the drug at the tumor sites. Antibodies have been successfully explored for targeted bioimaging [243,256] and could be of interest for targeted drug delivery.

The conjugation of targeting ligands are mostly achieved through post-polymerization modification. This strategy is efficient, but shows some limitations especially in the control of the number of ligands covalently attached at the periphery of HBPs. The copolymerization of inimers or transmers with a monomer bearing a targeting ligand by SCVP, especially under RAFT polymerization conditions, has more rarely been explored [244], but seems an interesting approach to better control the insertion of ligands in terms of number of ligands but also their localization on HBPs.

The field is evolving towards the development of HBPs for theranostics providing a dual role as drug carrier for targeted drug delivery and imaging probe (*i.e.* optical or magnetic resonance imaging) for diagnostic purposes. Regarding magnetic resonance imaging, different approaches have been reported: i) incorporation of a comonomer containing fluoride in the HBP by copolymerization [270, 276-277], ii) conjugation to HBPs of chelating ligands able to complex with copper [249] or gadolinium [251], and iii) grafting of HBP on Fe_3O_4 magnetic nanoparticles by either growth of the HBP from the surface of the nanoparticle [180,182] or coupling reaction between HBPs and nanoparticles by thiol-ene reaction [257]. Furthermore, fluorophores such as BODIPY [258] and cyanide dyes [276-277] have been conjugated to HBPs for optical imaging using conventional conjugation approaches affording HBPs decorated with targeting ligands and fluorophores for theranostics. More recently, luminescent nanoparticles have been investigated as imaging probes. For example,

hyperbranched polyglycerol has been prepared from the surface of red fluorescent silicon nanoparticles and modified with cyclic RGDfK to target $\alpha_v\beta_3$ integrins and afford optical imaging [157]. The recent advances in nanomaterials for optical imaging [259] pave the way to the development of novel nanoobjects for theranostics combining the potential of HBPs due to their high number of functional groups at their periphery to introduce various functionalities such as targeting ligands, and luminescent nanoparticles (*e.g.* gold nanoparticles, silicon nanoparticles, quantum dots and upconversion nanoparticles) due to their higher photostability, tunable emission wavelength and brightness as compared to organic dyes.

2. Upconversion nanoparticles for bioimaging

2.1. Upconversion luminescence

In most cases, the conventional luminescent materials used for bioimaging are based on the Stokes law principle in the spectral range of ultraviolet (UV) or blue-green lights [260]. In Stokes luminescence, a molecule absorbs a photon of shorter wavelength (higher energy) compare to the emitted photon. In other words, the emitted photon has lower energy than the adsorbed one [261]. For instance, fluorescent dyes [262] and fluorescent proteins [263] are fluorescent probes based on the Stokes luminescence. The application of this type of fluorescent probes is limited by broad emission spectra and low photochemical stability [264]. Nanotechnology allowed the design and elaboration of several nanomaterials for bioimaging including quantum dots (QDs), silicon dots, and carbon dots (CDs) [265]. These types of fluorescent probes have some advantages compared to organic fluorescent probes. For example, QDs nanoparticles have a narrow emission bandwidth and a high photostability, not to mention that the bandwidth can be tuned by adjusting QDs size [264]. However, toxicity of quantum dots is an issue because of the heavy metals (e.g. cadmium) involved in their composition [266].

Generally speaking, these above-mentioned Stokes luminescent materials suffer from some drawbacks. For example, when they are excited with high energy light in biological samples,

their fluorescence is accompanied will autofluorescence due to the emission of biological molecules such as collagen and melanin, thus increasing background interference during bioimaging, which results in low signal-to-noise ratio (SNR) [267]. Besides, short wavelengths (e.g. UV) for excitation of Stokes luminescent materials have low penetration depth in biological tissues as well as high phototoxicity which leads to tissue and cell damage [260,268].

Another class of fluorescent probes is anti-Stokes shift luminescent materials which recently have been developed for bio-applications as a new generation of fluorescent probes [269]. Anti-Stokes shift luminescent materials include hot-band absorption, Lanthanide-based upconversion and TTA-based upconversion [269]. In these materials, anti-stock emissions or upconversion (UC) process emits more energetically photons with lower wavelength than excitation photons [261]**.** In fact, upconversion luminescence is defined as a successive conversion of two or more lower-energy photons of near-infrared (NIR) to one output photon with more energy in the range of UV, visible or NIR radiation [270–273]. Figure 1.8 represents an example of three types of anti-Stokes shift luminescent materials for bioimaging.

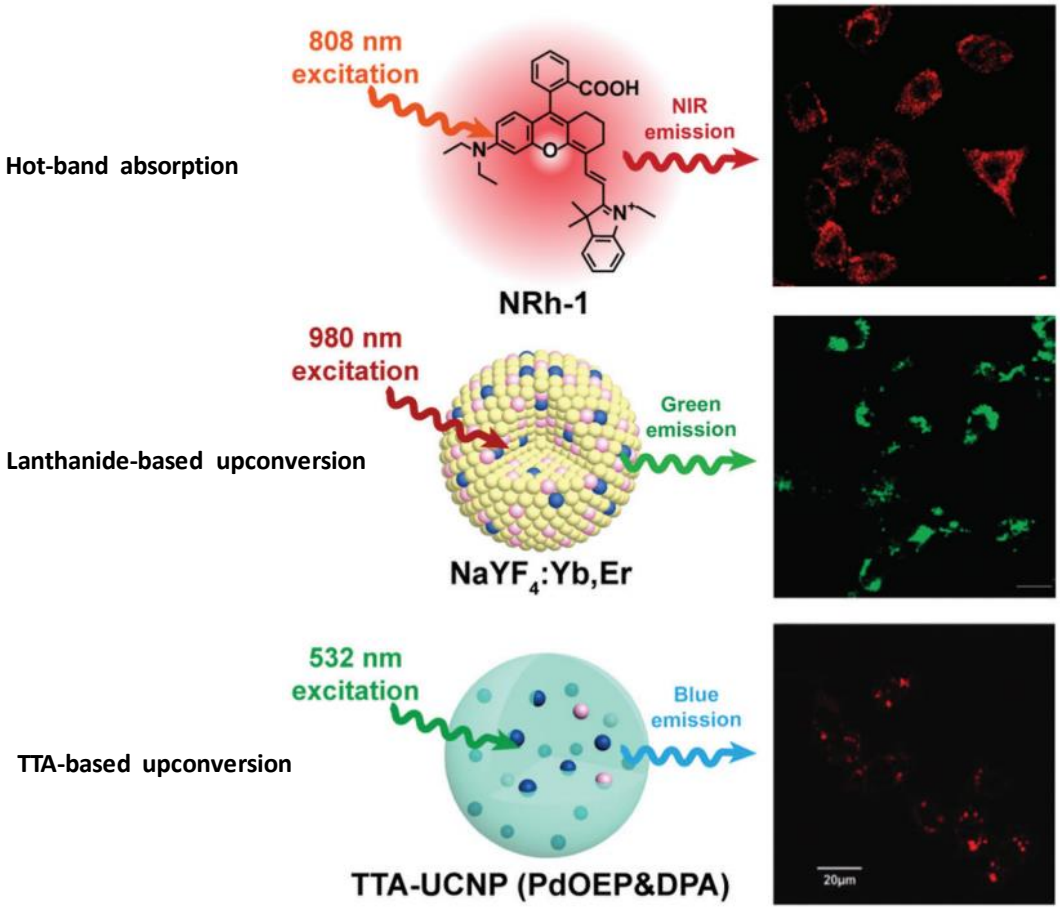

Figure 1.8. Three classes of anti-Stokes luminescent materials for cell imaging. Reproduced from Ref [269].

2.1.1. Upconversion Mechanisms

The mechanisms of upconversion luminescence are mainly based on three broad classes: i) Excited state absorption (ESA), ii) Photon avalanche (PA) effect, iii) Addition of photon by transfer of energy (APTE) effect or energy transfer UC (ETU).

2.1.1.1. Excited state absorption (ESA)

In exited state adsorption (ESA), successive absorption of two photons by a single ion leads to multistep, ladder-like excitation. At the first step, ground state absorption (GSA) occurs in which one lower-energy photon absorption results in a transition from the ground state (E_0) to a metastable state (E_1). In the second step, this excited electron absorbs a second pump photon and transfers from the intermediate level E_1 to a higher excited state (E_2). Finally, this excited electron returns to ground state E_0 through a radiative relaxation in which emitted photon has higher energy compared to both absorbed photons in transitions E_0 to E_1 and E_1 to E_2 [274]. Excited state absorption (ESA) mechanism is shown schematically in Figure 1.9.

2.1.1.2. Photon avalanche (PA) effect

Photon avalanche (PA) mechanism consists of three nonlinear phenomena and deals with four-energy level systems consisting in the ground state (E_0), intermediate states (E_1 and E_2), and upper excited state (E). At the first step, an electron or ion absorbs the excitation radiation and it is excited from the ground state to the intermediate states with a little energy higher than E_2 through a non-resonant absorption transition. It then returns to E_2 state via a cross-relaxation. The transfer of energy takes place between the E_2 state electron and the E_0 state, which leads to the formation of two electrons in the E_1 state. One of these electrons is excited to E state, as a result of absorption of excitation radiation. It then forms the third E_1 electrons by interaction with E_0 state electrons and second energy transfer. The absorption transition from E_1 to E occurs due to resonant excitation radiation. This process repeats over and over and causes an exponential increase in the population of electrons in the E state. Radiative relaxation of such high number of photons from E state to E_0 state leads to a strong emission [274]. Photon avalanche mechanism is shown schematically in Figure 1.9.

2.1.1.3. Energy transfer upconversion (ETU)

Energy transfer upconversion, which is also known as 'addition de photon par transfert d'énergies' (APTE), is the result of successive energy transfers between a neighboring pair of ions. One of these ions is called sensitizer (S), which is excited and acts as a donor of energy. While the other one acts as an acceptor of energy to whom the energy is transferred, it is called activator (A). The adequate concentration of these two ions is necessary for energy migration between them. The sensitizer concentration is usually in the range of 10 to 50 times more than the activator. Generally, there are three kinds of energy transfer namely: radiative (I), nonradiative (II), and phonon-assisted (III) [275].

I) Radiative energy transfer: this type of energy transfer happens as a result of the emission of a photon by the sensitizer and, subsequently, absorption of this emitted photon by the activator.

II) Non-radiative energy transfer: it is described as an interaction between two ions in which their energy gaps between their ground states and excited states are almost equal. If the ion interaction between them is sufficient, the excitation can transfer from one ion to another.

III) phonon-assisted energy transfer: a phonon is defined as a collective excitation in a periodic and elastic arrangement of atoms or molecules in condensed materials [276]. When two ions have different energy separations, there is an energy mismatch between sensitizer and activator atoms. Therefore, the presence of phonon assistance can be a way to make the energy transfer process feasible [274]. Energy transfer upconversion (ETU) mechanism is shown schematically in Figure 1.9.

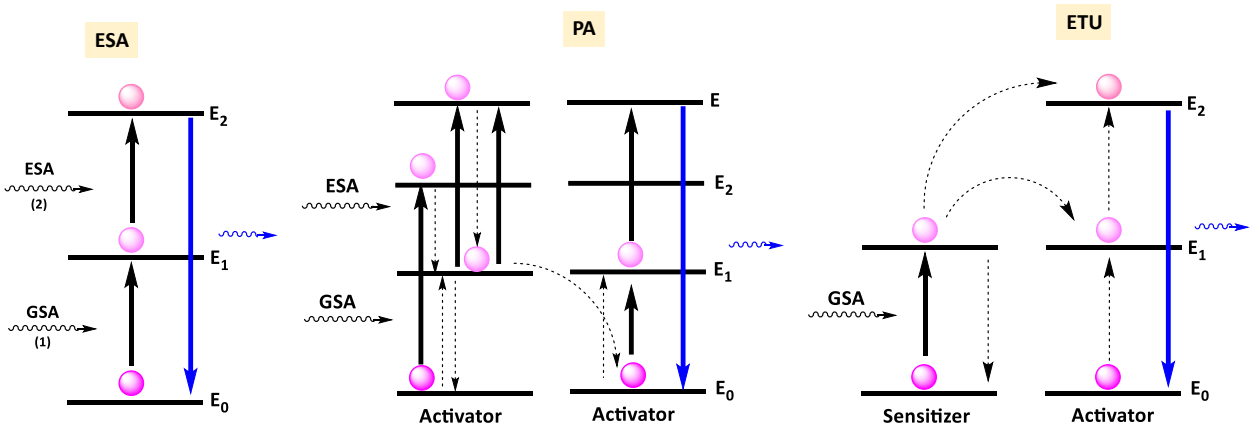

Figure 1.9. Schematic illustration of upconversion processes including excited-state absorption (ESA), photon avalanche (PA), and energy transfer upconversion (ETU). The black, blue, and dashed lines represent photon excitation, emission, and energy transfer processes respectively. Figure adapted from Ref [277,278].

Among the three anti-Stokes luminescent materials, Lanthanide-based upconversion have several advantages compared to other anti-Stokes shift luminescent materials such as slow metabolism rate, excellent photostability, long luminescence lifetime (ms), large anti-Stokes shift (more than 100 nm), narrow full width at half-maximum (FWHM) of emission peak (about 12 nm) [269]. Therefore, Lanthanide-based upconversion materials are promising fluorescent probes for biomedical applications.

2.2. Lanthanide-doped upconversion nanoparticles (UCNPs)

UCNPs are a group of crystalline inorganic guest–host lattice doped with metal ions which dimension is usually less than 100 nm. Generally, upconversion nanoparticles are excited with two or more long-wavelength photons in the range of near-infrared (NIR) light (980 nm or 808 nm) [279]. They then emit higher energy anti-Stokes luminescence with shorter

wavelength in the range of deep-ultraviolet (UV) to the near-infrared (NIR) [280,281]. Such low-energy NIR excitation results in several advantages such as low auto-fluorescence, high penetration depth, and low photo-damage. Furthermore, the wavelength for excitation of UCNPs is marched with optical transmission window of tissue which is in the range of 700 to 1000 nm (See Figure 1.10d). Therefore, these features make them an ideal and attractive nanomaterial for biomedical applications. Consequently, all of mentioned outstanding physicochemical characteristics besides the low toxicity and high chemical stability, make lanthanide-doped upconversion nanoparticles promising fluorescent probes [282]. Figure 1.10 shows several examples of UCNPs benefits for bioimaging that were reported in the literature [268,283–286].

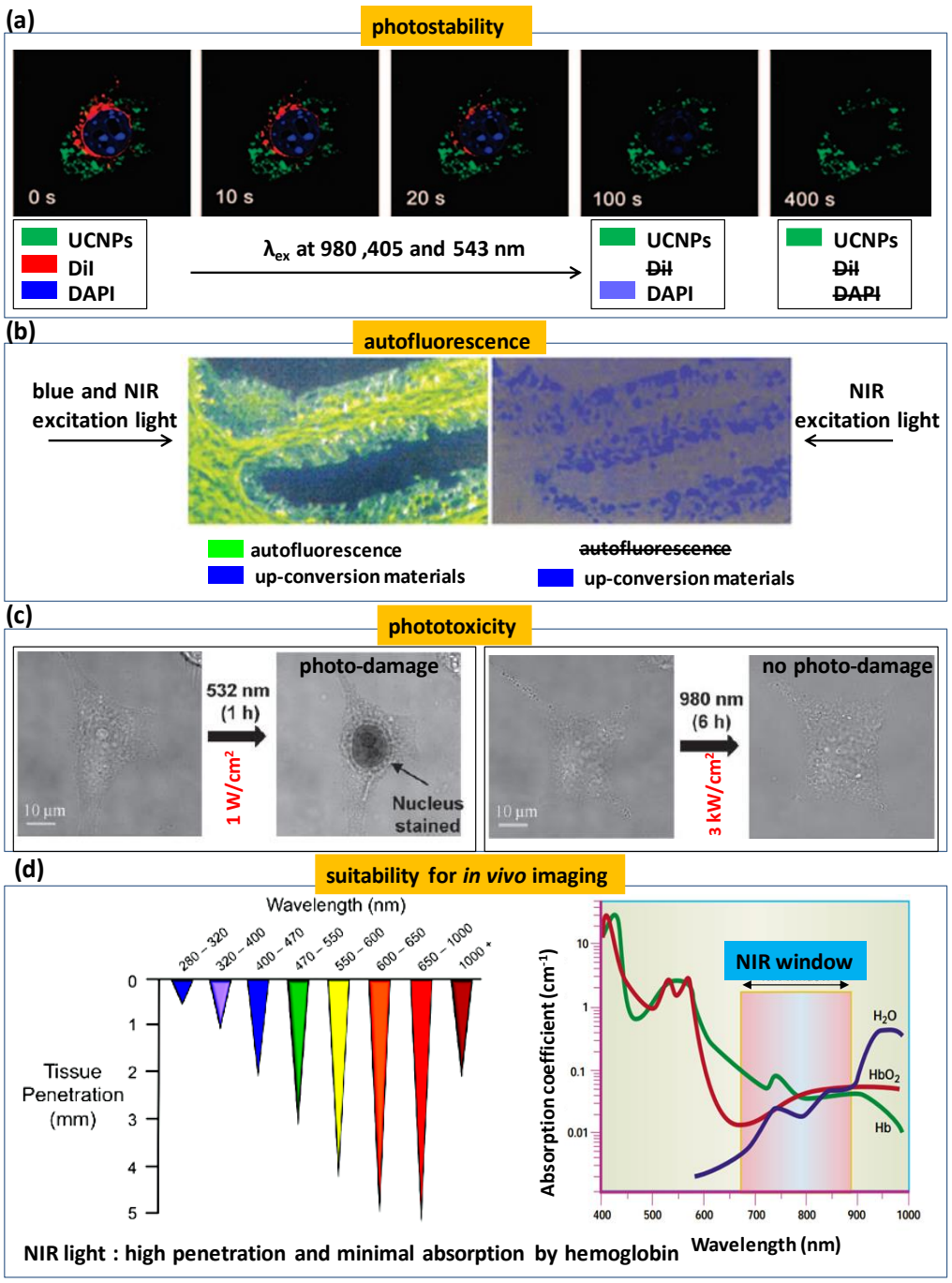

Figure 1.10. (a) Comparison of photobleaching in anti-Stokes and Stokes shift luminescent (UCNPs and two dyes respectively), reproduced from Ref [283]; (b) absence and presence of autofluorescence regarding excitation light, reproduced from Ref [284]; (c) phototoxicity of excitation light, reproduced from Ref [268]; (d) penetration depth of light for different wavelengths in skin tissue, reproduced from Ref. [285] (left), the optimal NIR window suitable for in vivo imaging because of minimal light absorption by hemoglobin (right),reproduced from Ref [286].

2.2.1. Composition of UCNPs

2.2.1.1. Host lattice

UCNPs are composed of three main components: a host lattice, a sensitizer and an activator (Figure 1.11). Host lattice is an inorganic crystalline matrix, doped with metal ions as active luminescent centers. The physicochemical properties of this host lattice directly influence the efficiency of resulting UC luminescence. In fact, an ideal host material should meet several criteria: 1) the transparency to the wavelength range in which UC luminescence occurs (e.g. UV-Vis light), 2) close ionic radius to the dopant ions to minimize lattice mismatch which results in crystal defect; 3) having strong crystal field to assist 4f-4f transition of lanthanide ion group dopants 4) bearing low phonon energy which reduces the non-radiative decay, and increases the UC luminance efficiency, 5) high chemical and thermal stability in order to keep original crystal structures [260,287,288].

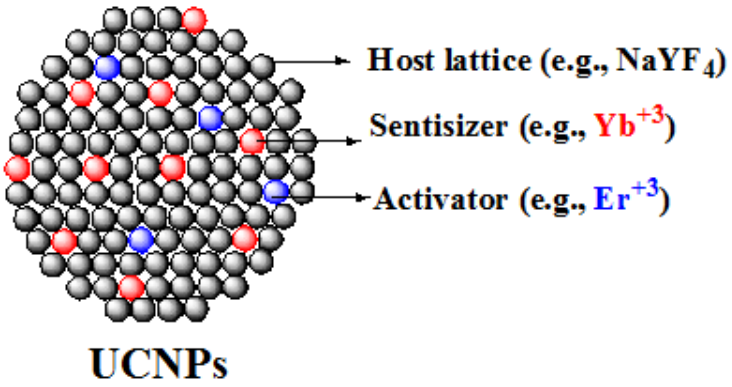

Figure 1.11. Schematic showing the composition of UCNPs (Yb^{3+} and Er^{3+} dopant ions in the $NaYF_4$ host).

There are different classifications of host material including oxides (e.g. Gd_2O_3, Y_2O_3, La_2O_3, Lu_2O_3, etc.), fluorides (e.g. $NaYF_4$, $NaYbF_4$, $NaGdF_4$, LaF_3, GdF_3, $BaYF_5$, $NaLuF_4$ etc.), vanadates (e.g. YVO_4), oxy-fluorides or chlorides (e.g. GdOCl), oxysulfide (e.g. Y_2O_2S) and halides such as chlorides, bromides, and iodides (e.g. $LaCl_3$) [289–294]. Table 1.1 presents various host lattices and their corresponding phonon energies. In this regard, some host lattices such as oxides have good chemical stability. On the other hand, relatively high phonon energy is a big limitation for them. Other compositions like halides have low phonon energy; however their low chemical stability is a big issue for these materials [295]. Among different host lattices, $NaYF_4$ is one of the most favorite compositions for producing efficient UC, thanks to its low phonon energy and high chemical stability [260,296,297].

Table 1.1. Various host lattices and their corresponding phonon energies [294,295]

Host lattice	Phonon energy (cm^{-1})	Host lattice	Phonon energy (cm^{-1})
Y_2O_3	550	$LaCl_3$	240
ZrO_2	500	GdOCl	500
$NaYF_4$	350	Y_2O_2S	520
YVO_4	890	$LaPO_4$	1050

2.2.1.2. Sensitizer and activator

In order to achieve a photon upconversion, the selection of suitable dopant is critical. There are many different dopants which are dispersed as a guest in an appropriate host lattice, including transition-metal ions (Ti^{2+}, Ni^{2+}, Mo^{3+}, Re^{4+}, or Os^{4+}) and lanthanide ions [298,299]. However, lanthanide ions show the highest upconversion efficiencies [300], high resistance to photo-blinking, large Stokes shifts, fixed energy level and long lifetime [301,302]. In fact, such unique properties are due to the electronic configuration of lanthanide ions (i.e. $1s^2 2s^2 2p^6 3s^2 3p^6 3d^{10} 4s^2 4p^6 4d^{10} 4f^n 5s^2 5p^6$, $0<n<14$).

The most stable and predominant state of Ln metals is trivalent Ln^{3+} ions. In this configuration, since the energy levels of $5s^2$ and $5p^6$ are lower than 4f orbital, it will be filled after them. Consequently, 4f electrons are completely shielded by $5s^2$ and $5p^6$ orbitals. This leads to weak electron-phonon coupling and weak interaction of 4f electrons with the surrounding field or chemical bonds. As a result, the energy level of trivalent lanthanide ion dopants slightly changes with varying the host lattice material. In addition, the shielding effect causes a sharp and narrow 4f-4f transition in Ln^{3+} ions [279,287].

Trivalent lanthanide ions can act either as activator or sensitizer. In fact, the sensitizer is a donor of energy. After being exited by an incident photon, it will transfer its extra energy (non-radiative) to the activator as an acceptor of energy. Then, it will emit radiation with more energy. To do so, sensitizer should have two main properties i) large absorption cross-sections and ii) matching energy levels with activator [288]. Between trivalent lanthanide ions, Yb^{+3} is

the best sensitizer due to high absorption cross-sections (at 980 nm, 9.11×10^{-21} cm^{-2}) and possess a quite simple energy level diagram with only one excited energy state ($^2F_{5/2}$). In addition, the energy gap of Yb^{+3} is similar to the energy level of most common activators, which make it an ideal sensitizer (See Figure 1.12). The concentration of Yb^{+3} in host lattice was generally optimized around 17-30 mol % concentrations above 30 % lead to prominent non-radiative cross-relaxations [288,303].

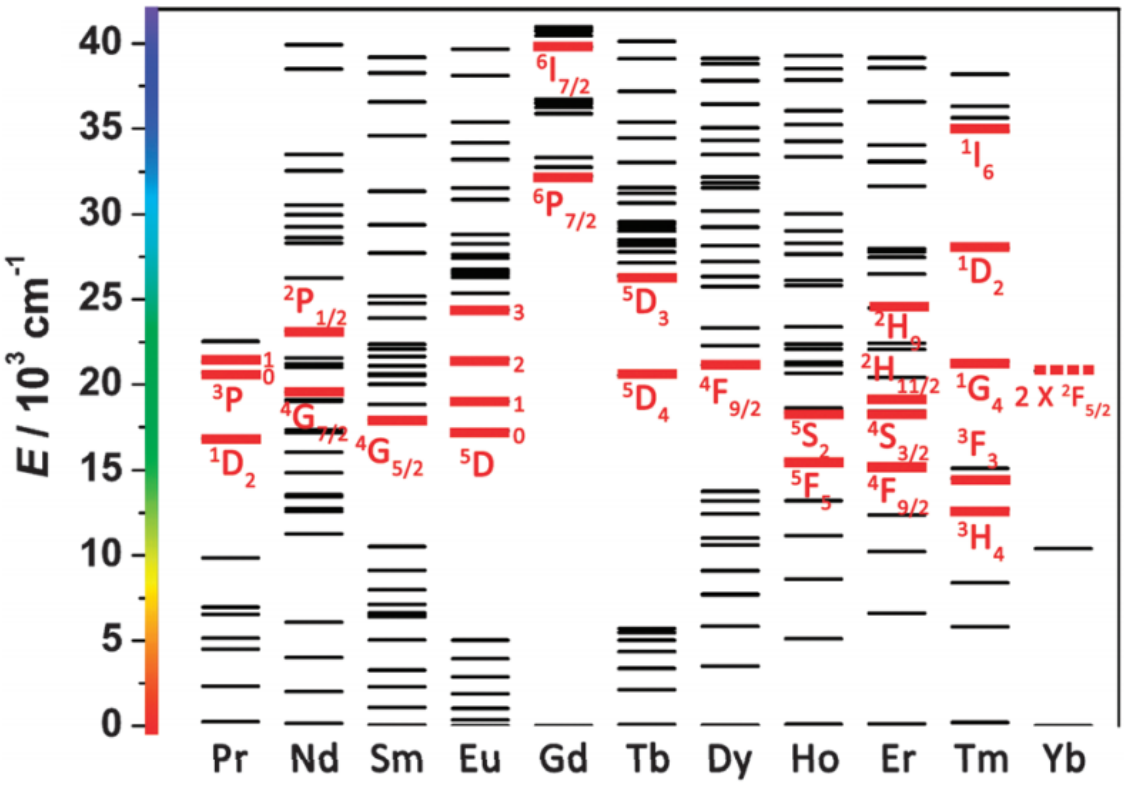

Figure 1.12. Partial energy level diagrams of trivalent lanthanide ions. Corresponding typical UC emissive excited levels are highlighted with red bold lines, reproduced from Ref [288].

On the other hand, activators should have close energy levels to assist ladder-like energy transfer as shown in Figure 1.12. In this regard, Erbium (Er^{3+}), Thulium (Tm^{3+}) and Holmium (Ho^{3+}) ions are the most proper activators for upconversion luminescence emission under 980 nm, which is the most used wavelength for their excitation. Those activators possess multilevel energy which matches well with the energy level of Yb^{+3} as sensitizer for effective resonant energy transfer (see Figure 1.12). In addition, a suitable activator should have long life metastable excited states. In this condition, the excitation of the electron is more likely to be induced by another incident photon or energy transfer from a nearby ion [299]. To avoid

quenching or non-radiative relaxation the optimization of activator concentration is so important that typically is less than 3 mol % [304]. Figure 1.13 presents one example of energy transfer processes between Yb^{+3} as sensitizer and Er^{3+} as activator. In this system, Yb^{+3} is excited from ground state to excitation state ($^2F_{7/2} \rightarrow {}^2F_{5/2}$) by 980 nm laser irradiation. Then, energy transfer occurs from Yb^{+3} to different energy levels of Er^{3+}. Due to long-lived metastable excited states in Er^{3+}, sequence energy transfer for reaching to high energy level happens. As a result of energy transfer, upconversion emission arises with relaxation. In the case of Er^{3+}, four main upconversion emissions exist that includes two strong emissions at 650 nm ($^4F_{9/2} \rightarrow {}^4I_{15/2}$) and 520 nm ($^4S_{3/2} \rightarrow {}^4I_{15/2}$) as well as relatively weak emission at 540 ($^2H_{11/2} \rightarrow {}^4I_{15/2}$) and 410 ($^2H_{9/2} \rightarrow {}^4I_{15/2}$). The figure 1b shows the UC luminescence spectrum of NaY:Yb, Er UCNPs.

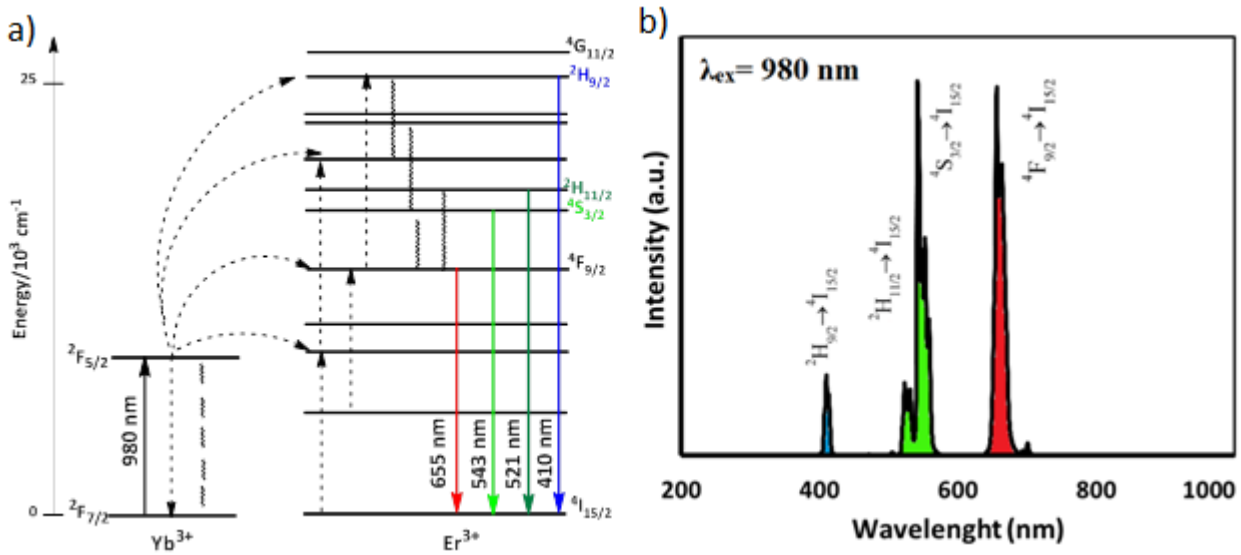

Figure 1.13. Energy level diagram of possible emitting levels in UCNPs doped Yb^{+3} and Er^{3+} (a). adapted from Ref [305], upconversion luminescence spectrum of $NaYF_4$:Yb (20%), Er (2%) UCNPs (b).

2.2.1.3. Crystal structure of $NaREF_4$

UCNPs with $NaREF_4$ formulation have two types of crystalline structure including cubic (α-phase) and hexagonal (β-phase). As shown in Figure 1.14, the cation distributions in two unit cell structures differ from each other totally (e.g. $NaYF_4$:RE) [306]. Indeed, distributions of Na^+ or RE^{3+} are more symmetric in crystal unit of cubic phase compared to hexagonal phase

[307–309]. As a result, the strength of crystals field and the probability for f-f transitions are different for cubic and hexagonal phase. For instance, β-$NaYF_4$ nanocrystal has a lower symmetric local crystal field compared to α-$NaYF_4$ and thus increased the probability of f-f level electronic transitions and subsequently leads to greater upconversion efficiency [310,311]. In this regard, upconversion efficiency of β-$NaGdF_4$ is generally ten times more than α-$NaGdF_4$ [312]. Therefore, synthesis of UCNPs with hexagonal β-phase for achieving proper upconversion quantum efficiency is crucial. The main challenge for attaining single β-phase is the formation of cubic α-phase nanocrystals earlier than hexagonal β-phase nanocrystals during synthesis of $NaREF_4$ UCNPs. Indeed, cubic phase nanocrystals with lower energy formation can nucleate earlier but are thermodynamically less stable than hexagonal β-phase nanocrystals (see Figure 1.14). In this regard, the free-energy barrier for the conversion from cubic to hexagonal is very high. Hence, in order to overcome an energy barrier for phase transition, heat treatment at high temperature is an important step. As a result, the formation of a pure and monodisperse hexagonal β-phase of UCNPs and the control of their size and shape is a real challenge. Therefore, up to now, many investigations have been reported on phase transition for the control of nanocrystals' size, shape, and fluorescence intensity. The main reported strategies involve: introducing trivalent lanthanide dopant ions with larger radius such as Gd^{+3} [309] and doping with alkali ions (Li^+ or K^+ ions) [313], applying mixture of surfactants such as oleic acid, oleylamine and tributylphosphine [314–316], change of chemicals ratio (oleic acid, octadecene, NaOH and NHF_4) [317–320], replacement of sodium oleate instead of oleic acid [321], change the addition way of NH_4F and NaOH [322], reaction time and temperature [323,324].

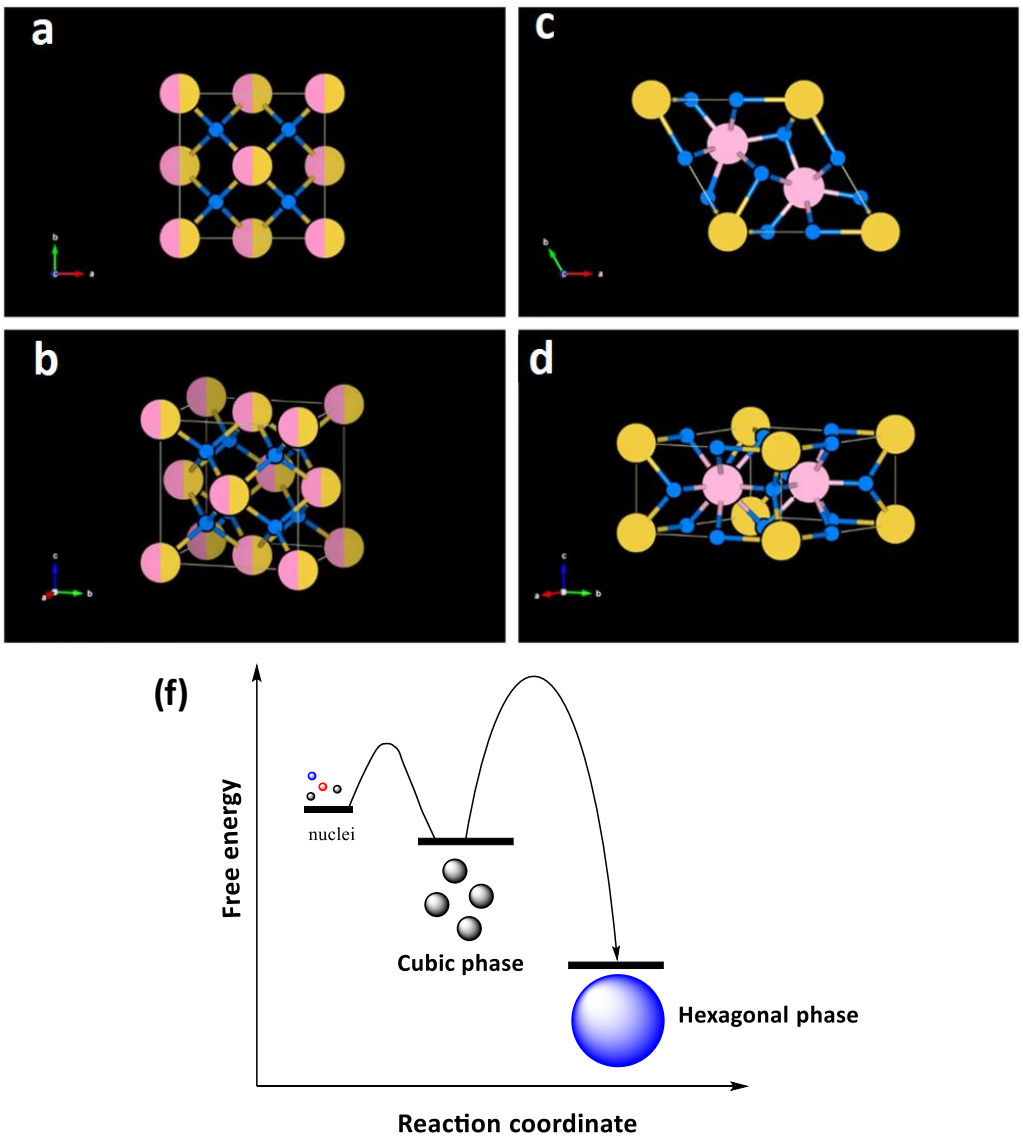

Figure 1.14. Cubic lattice unit cell structure (a, b) and hexagonal lattice unit cell (c, d) of $NaYF_4$ UCNPs. Na^+ ions are yellow; Y^{3+} and RE^{3+} dopant ions are pink; F^- ions are smaller and blue, reproduced from Ref [306]. Free energy diagram for the formation of cubic and hexagonal crystal phases of $NaYF_4$;RE UCNPs (f), adapted from Ref [311].

2.2.2. Synthesis of UCNPs

Various methods for the synthesis of lanthanide-doped UCNPs have been reported, such as thermal decomposition, hydrothermal/solvothermal, co-precipitation, microwave-assisted synthesis, ionic liquid-based synthesis, and microemulsion methods [260,275,325,326]. In this chapter, we will focus on three methods that are used more frequently which include thermal decomposition method, hydrothermal/solvothermal method and co-precipitation method.

2.2.2.1. Thermal decomposition method

Thermal decomposition method, also known as thermolysis strategy, is based on the decomposition of an organometallic compound as a precursor at high temperature (e.g. 250-330 °C) in the presence of a high boiling point organic solvent as a non-coordinating solvent, as well as a surfactant as a coordinating ligand. In most cases, metallic trifluoroacetate salts are used as precursor in anhydrous and free-oxygen environment, while 1-octadecene (ODE) is employed as a high boiling point organic solvent in which the decomposition reaction occurs [325]. However, paraffin was also reported as a solvent for the synthesis of $NaYF_4$: Yb, Er (Tm) UCNPs [327]. In this context, the common surfactant is either oleic acid (OA), oleylamin (OM), or trioctylphosphine oxide (TOPO). Generally, the role of these surfactants are the prevention of UCNPs from aggregation using their long hydrocarbon chains; furthermore they can coordinate metallic elements (e.g. Ln^{+3}) via their functional capping groups such as carboxylic group in the case of OA [270]. On the other hand, surfactants on surface of NPs via a selective absorption effect can control the growth of nanocrystals. Therefore, resultant UCNPs have a hydrophobic surface due to the presence of hydrophobic OA, OM, and TOPO. It is noteworthy that TOPO is used as a solvent and surfactant for synthesis $NaYF_4$: Yb, Er/Tm/Ho UCNPs at different temperatures [328].

Rapid decomposition of metallic trifluoroacetate as a RE^{3+} ion and fluorine source at high temperature leads to the formation of high number of nucleations which then results in producing monodisperse UCNPs (2-100 nm) [325]. In this approach the size, shapes, and phase of UCNPs can be controlled by temperature and time of reaction and ratio of Na^+/RE^{3+} and F^-/RE^{3+} [329,330]. It is worth mentioning that the preparation of core-shell UCNPs with this approach is achievable readily [331]. Although the thermal decomposition method allows synthesizing various types of high-quality UCNPs (with narrow size distribution, good crystallinity, and desirable optical properties), it has some disadvantages. These drawbacks include fast nucleation which can lead to the synthesize of UCNPs with high surface defects and consequently decrease the upconversion luminescent efficiency. On the other hand, for achieving a nanocrystal with high quality, anhydrous and free-oxygen reaction environment would be essential in this approach. Additionally, the production of toxic byproducts of fluorinated and oxyfluorinated carbon species limits the practicality of thermal decomposition method (Figure 1.15) [270,332].

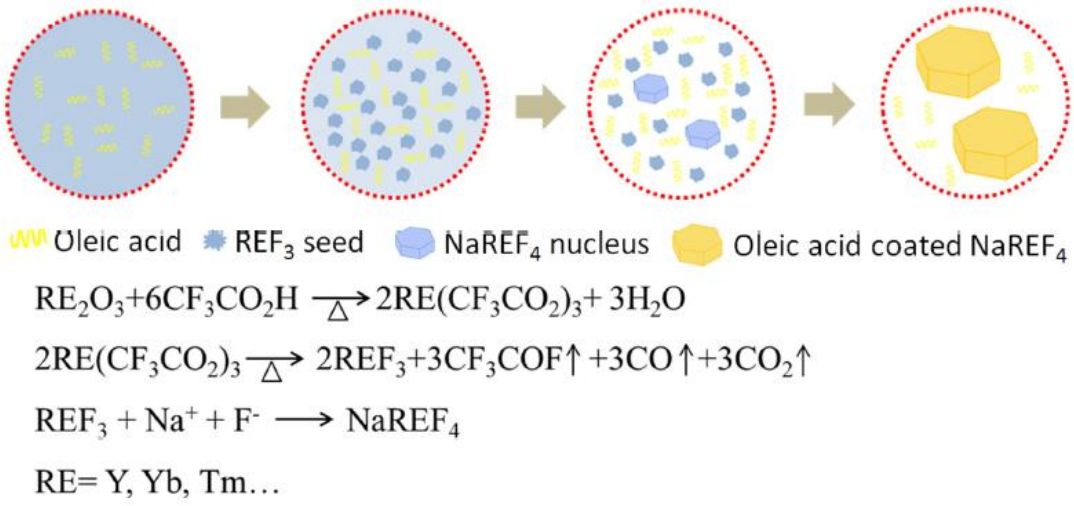

Figure 1.15. Schematic representation of thermal decomposition for the synthesis of NaY_4:Yb,Tm particle and possible reaction in this approach [332].

2.2.2.2. Hydrothermal/solvothermal method

Hydrothermal/solvothermal approach for the synthesis of UCNPs relies on mixing proper reaction precursors, solvents and surfactants under high pressure and temperature which is usually above the critical point of the solvent [270]. The reaction is carried out in a specific reaction vessel called Teflon-lined autoclave. Typically, polyethylenimine (PEI) [333], ethylenediaminetetraacetic acid (EDTA) [334], cetyltrimethylammonium bromide (CTAB) [335] and oleic acid (OA)[336] can be employed as surfactant or chelating agent which regulate the crystalline phase, size, morphology, and surface functional groups of UCNPs. In this approach, the growth of UCNPs can be controlled theoretically by tuning reaction temperature, reaction time and surfactants. The size of resultant UCNPs by this method is from µm to nm range with various shapes. For example, EDTA is able to reduce the size of $NaYF_4$: Yb, Er nanocrystals as a perfect chelating agent, and on the other hand, the morphology of UCNPs is affected by tuning the amount of CTAB as a surfactant (e.g. spherical NPs to nanorods) [335]. Surface properties of UCNPs depend on the type of surfactant and can be hydrophobic or hydrophilic. For instance, using PEI as a polymeric surfactant for preparation of water-soluble and biocompatible $NaYF_4$: Yb, Er/T, a one-pot synthesis was reported by Wang *et al.* [337]. The advantage of this strategy is the mild reaction condition,

for instance, reaction temperature is relatively low compared to thermal decomposition method, e.g. 100-220 °C [338–340]. Furthermore, water, ethanol, and ethylene glycol are the main solvents considered in this method which are low-cost compounds and thus would be an excellent fit for large-scale production [325]. However a challenge related to this approach is the difficulty of tuning the conditions in batch-type sealed reactors, which leads to low batch-to-batch reproducibility [260]. Figure 1.16 represents an example of UCNPs synthesis with solvothermal approach.

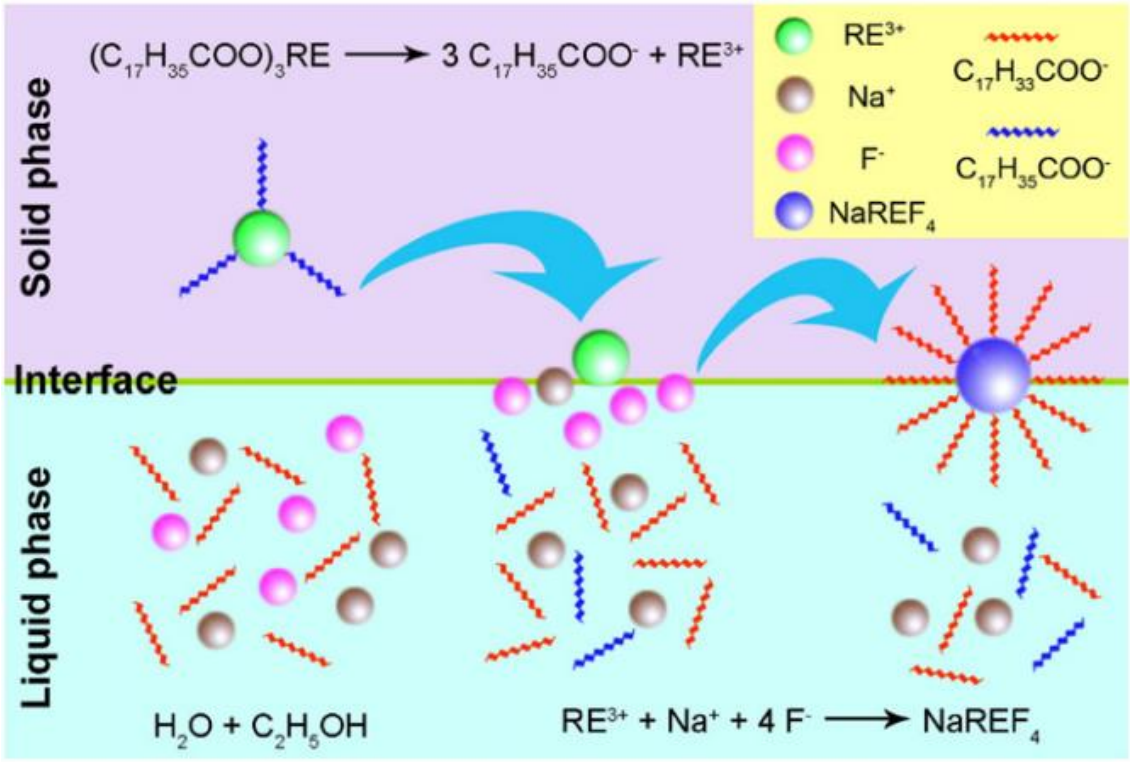

Figure 1.16. Mechanism for the formation of $NaREF_4$ nanoparticles via solvothermal method, reproduced from Ref [341].

2.2.2.3. Co-precipitation method

The preparation of UCNPs can be performed in aqueous or organic solutions in this approach [326]. Generally, this method has two steps which include precipitation at low temperature followed by a heat treatment at high temperature in order to improve the crystallinity of the products. Precipitation in aqueous solution for example in one of the earliest work reported and was achieved by a rapid mixing of two aqueous solutions comprising NaF and mixture of lanthanide salts and EDTA [342]. The sizes of as-synthesized nanoparticles were tunable to

certain extent, e.g. form 37 to 166 nm, simply by changing the molar ratio of ETDA to total lanthanides. After the heat treatment at high temperature under inert atmosphere (e.g. 400 and 600 °C/N_2 for 5h), the fluorescence emission was enhanced by up to 40-fold, which can be attributed to the phase transition from cubic to hexagonal. Although the preparation of UCNPs by precipitation in aqueous solution is very convenient, this approach has some drawbacks among which a low control on the nanoparticles' size of and structure [325].

Synthesis of a high-quality hexagonal $NaYF_4$ using the co-precipitation method in organic solvent was developed by Z. Li and Y. Zhang [343]. Generally, an oleate complex of lanthanide salts (acetate or chloride) is usually formed at 120 to 160° C in high boiling point solvent such as ODE under an inert atmosphere. A source of sodium and fluoride (NaOH and NH_4OH in methanol) is used for the primary nucleation with very low crystallinity at room temperature. The reaction is followed by a heat treatment at high temperature (e.g. 290 to 320° C) under inert atmosphere (see Figure 1.17). Such annealing is required to enhance the upconversion fluorescent intensity as a result of phase transfer from cubic to hexagonal phase and sharpening the crystal structure [344]. The temperature of the heat treatment step is critical to the phase transition in this method. For example, preparation of hexagonal phase UCNPs at high temperature is more favorable, and on the other hand lower temperatures tend to lead cubic phase nanoparticles [345]. Moreover, In this method, the use of oleic acid or oleyl amine as the coordinating ligand leads to the formation of a hexagonal crystal lattice or a cubic crystal lattice, respectively [346]. The size of resulting nanocrystals can be controlled by tuning the ratio of reactants, as well as temperature and time of heat treatment [343]. The use of mild reaction conditions, low costs compounds and equipment, simple protocols, and short reaction times make the co-precipitation method as one of the most convenient and promising strategies for synthesis of lanthanide-doped UCNPs [347]. However, it has a the disadvantage of heterogeneous heat transfer when relying on traditional stirred tank reactors [260,348].

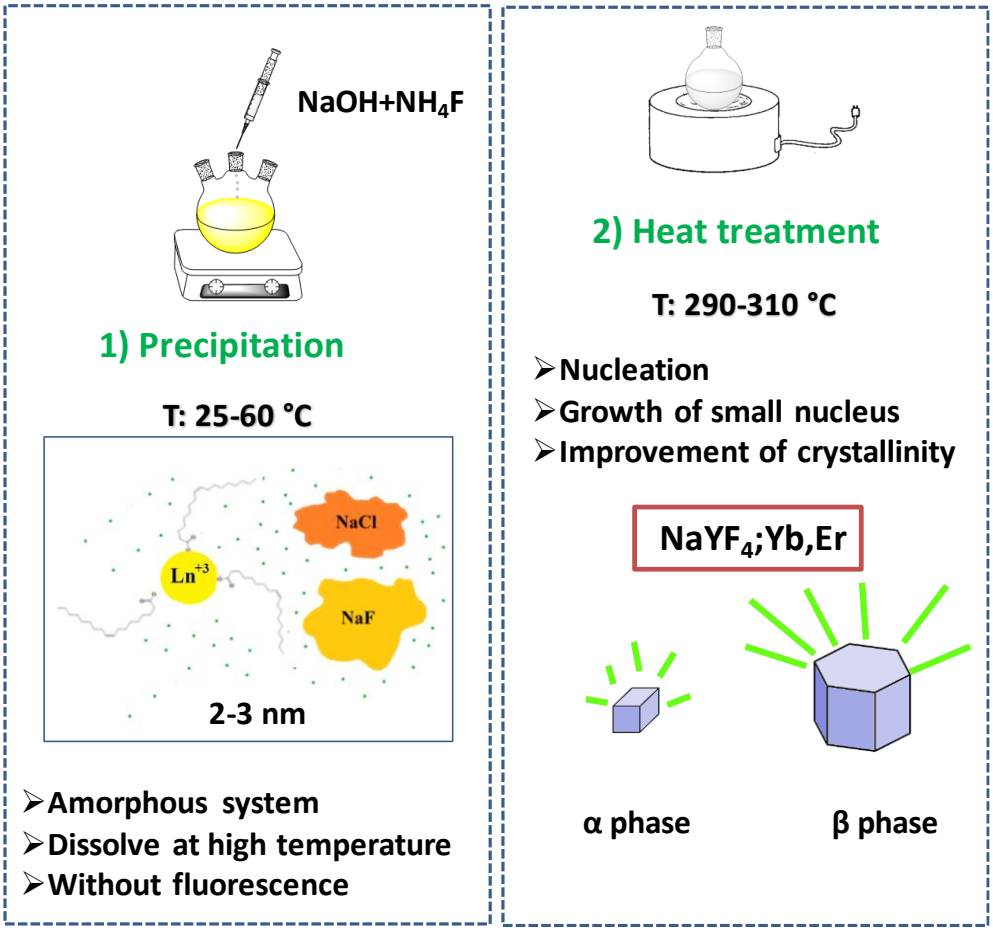

Figure 1.17. Schematic representation of the co-precipitation method for synthesis of $NaREF_4$ in an organic solvent.

2.2.3. Surface Modification of UCNPs

As mentioned above UCNPs have broad applications in different fields [349,350]. Therefore, the surface modification these types of nanomaterials for achieving a desired outcome are common is essential. These nanoparticles can be promising sensing probes for biomedical application [294,351–355] but will require to be modified with a proper material in order to be well-dispersed in aqueous media or biological buffers. In this section, different methods for surface functionalizations of UCNPs have been reviewed briefly.

Generally speaking, resultant UCNPs by popular methods such as thermal decomposition and co-precipitation method are stabilized by oleic acid (OA), oleylamine (MO) and trioctylphosphine oxide (TOPO) [275]. These NPs have a surface with hydrophobic nature, which thus needs to be properly modified for use in biological application. Generally,

modification of UCNPs is categorized in different approaches, including ligand exchange, ligand oxidation, ligand removal, ligand attraction, layer-by-layer assembly and surface silanization. Furthermore, in this chapter, recent methods for grafting polymer in surface of UCNPs will be reported briefly

2.2.3.1. Ligand exchange method

Ligand exchange methodology is one of the most common methods reported in the literature. After preparation of UCNPs, their surface is covered by a capping agent that prevents the aggregation of the nanoparticles. In ligand exchange, capping agent is exchanged with other ligands that have a higher affinity to bind to the surface of UCNPs compared to the capping agent. New hydrophilic ligands after replacement can change the nature of UCNPs surface. To date, different varieties of molecules have been used to modify UCNPs with hydrophilic groups such as citrate [356], PEG diacid [357], hexanedioic acid [358,359], polyethyleneimine (PEI) [360,361], 2-aminoethyl dihydrogen phosphate [362], PEG-phosphate [363], polyacrylic acid (PAA) and its derivatives [345,362,364–366], poly(aminoamine) (PAMAM) [367], 6-aminohexanoic acid [368] and polyallylamine (PAAm) [362].

2.2.3.2 Ligand oxidation method

Li and coworkers have reported pioneer work on surface modification of UCNPs via ligand oxidation [369]. In this method unsaturated carbon-carbon double bond of capping ligand (e.g. OA) is cleaved to hydrophilic functional group –COOH by Lemieux-von Rudloff reagent which includes sodium, periodate potassium or permanganate [370]; as a result, the nature of surface will be changed from hydrophobic (OA) to hydrophilic (azelaic acids). Furthermore, in order to oxidize OA into azelaic acid ligands and/or azelaic aldehyde, Yan and coworkers have used ozone as a clean and readily available strong oxidant [371]. The advantage of this method is its simplicity, which makes a straightforward route for creating carboxylic groups for bioconjugation of the surface of UCNPs [369]. However, this method has some drawbacks such as long reaction time with low yields, remaining side product (e.g. MnO_2) [364] and as well as low availability of ligands that contain unsaturated carbon-carbon double bonds.

2.2.3.3. Ligand removal

This method for modification of UCNPs capped with OA was first reported by Xu and coworkers [341]. The ligand on the surface of nanoparticles in the presence of excess amount

of solvent such as ethanol under vigorous sonication will be removed; thereby UCNPs with hydrophilic surface can be dispersed in aqueous solutions readily. Another method for removing ligand is acid treatment (e.g. HCl, at pH 4) that was reported by Capobianco and co-workers [371]. In acidic conditions, OA is protonated and dissociates from surface of UCNPs, and naked nanoparticles with positive charges can be dispersed very well in water. Indeed, the presence of abundant lanthanide ion on surface of UCNPs can provide strong coordination for the conjugation of biocompatible molecules with different functionalities. For instance, heparin was coordinated on surface of ligand-free $NaGdF_4$:Yb^{+3}, Er^{+3} for targeted bioimaging [372].

2.2.3.4. Ligand attraction

Ligand attraction occurs based on hydrophobic-hydrophobic and Van de Waals interaction between two molecules on the surface of UCNPs. Indeed, an amphiphilic block copolymer from hydrophobic part is absorbed by capping ligands on the NPs surface based on a hydrophobic interaction, and the hydrophilic outer block of the polymer allows aqueous dispersion. A martge variety of polymers and surfactants have been used to decorate UCNPs including sodium dodecyl sulphate (SDS), polyethylene glycol tertoctylphenylether (C8PhE10), cetyltrimethylammonium bromide (CTAB) [373], phospholipids [374], TWEEN [375], various amphiphilic co-polymers such as polyethylene glycol-block-polycaprolactone (PEG-b-PCL), poly(ethylene glycol)-block-poly(lactic-coglycolic acid) (PEG-b-PLGA), poly((ethylene glycol)-block-lactic acid) (PEG-b-PLA) [376], poly(L-lysine) (PLL) [377] and octylamine-polyacrylic acid-polyethylene glycol (OLA-PAA-PEG) [378].

2.2.3.5. Layer-by-layer assembly

This method is based on electrostatic interaction between two polymers with an opposite charge on surface which generates water-dispersed UCNPs. For instance, negatively-charged polymer like polystyrene sulfonate (PSS) and polycations such as poly(allylamine hydrochloride) are alternately deposited on surface by repeated incubation and washing [379,380]. Dextran sulphate sodium (DSS), PEI [381] poly(allylamine hydrochloride) (PAH) and poly(styrene sulfonate), poly(acrylic acid) (PAA) and PAH [382] have thus been used. In this simple method it is possible to control the hydrodynamic size, shapes and surface charge of the obtained UCNPs precisely [380]. However, time-consuming post-treatment is the main disadvantage of this method.

2.2.3.6. Surface silanization

One of the most promising methods for modification of nanomaterials for different applications is the surface silanization due to well-established surface chemistry [383]. In this method, a layer of silica is coated on the surface of inorganic particles with both hydrophobic and hydrophilic surfaces. The present silica layer around UCNPs has several advantages such as increasing bio-compatibility and stability in biological media and present minimal influence on fluorescence properties of UCNPs [384]. Furthermore, silica shell can provide abundant terminal hydroxyl (–OH) groups on surface for further modification with various functional groups such as amine [385], carboxylic [386] or thiol [387] for further bio-applications.

Two methods have been investigated for modification of UCNPs by silanization: 1) reverse microemulsion method that is suitable for modification of hydrophobic UCNPs [388,389] and 2) Stöber method which is used for silica coating of hydrophilic UCNPs. In reverse microemulsion method, typically the IGEPAL CO-520 is used as a surfactant, cyclohexane as a non-polar solvent, tetraethoxysilane (TEOS) and the ammonia or sodium hydroxide are added as a catalyst to hydrolyze TEOS in which silica precursors are condensed to form a Si-O-Si layer on the surface of UCNPs. The thickness of the silica layer can be accurately controlled by adjusting amount of TEOS, surfactant and reaction time [351,390]. The Stöber method is mainly performed in polar solvent such as ethanol and water conversely to the reverse microemulsion method [391,392]. In this latter method, the layer of silica is tunable thanks to the control of pH and amount of reactants, for example LaF_3:Yb^{+3}: Er^{+3} was coated with a silica shell thickness less than 15 nm [391] or $NaYF_4$ UCNPs was modified with a very thin layer of silica around 1-3 nm [392].

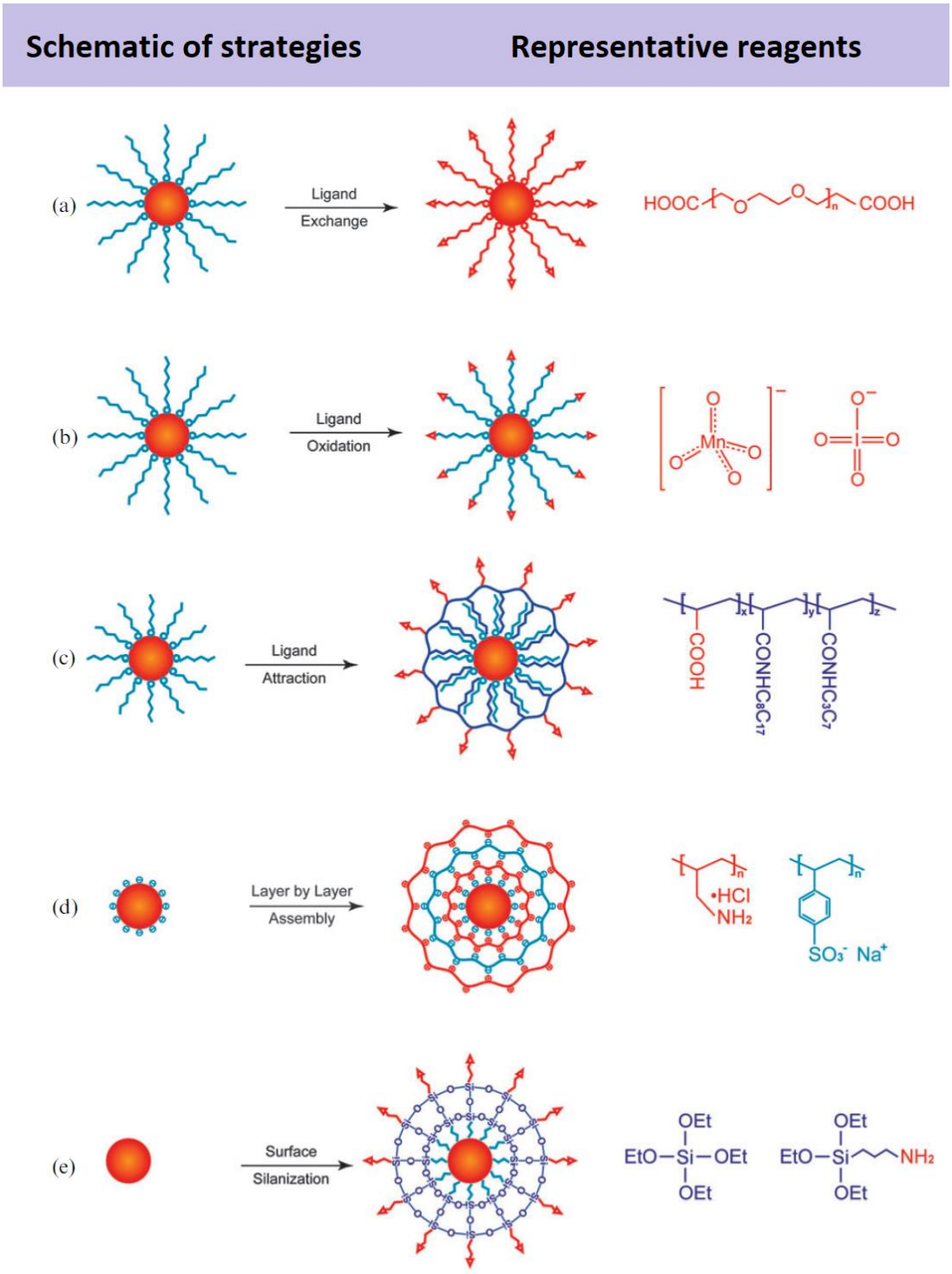

Figure 1.18. General method strategies for surface modification of UCNPs (direct method), reproduced from Ref. [304].

2.2.3.7. Grafting polymers on the surface of UCNPs

Polymer coating on the surface of UCNPs by above mentioned method such as ligand attraction and layer by layer assembly is based on a reversible physiosorption phenomenon. However, the latter is thermally and mechanically unstable. One the other hand, chemisorption or chemical bonding is another approach for modification of nanomaterials that is irreversible and involves covalent attachment of polymers on the surface.

Generally speaking, grafting of polymer on the surface of nanomaterials is classified into two categories i) “grafting-to” and ii) “grafting-from”.

In the “grafting-to” method, a polymer with an active end-functional group is reacted with a chemically activated substrate [393]. However, with this method, preparation of high grafting densities on the surface is a challenge due to steric hindrance of the first fraction of chains on the surface, which limits the diffusion of subsequent chains to reactive sites [394,395].

The “grafting-from” strategy is a bottom-up approach in which a small initiator molecule with low steric hindrance is covalently attached to a surface and then polymer chains are grown from the initiator on surface as shown in Figure 1.19.

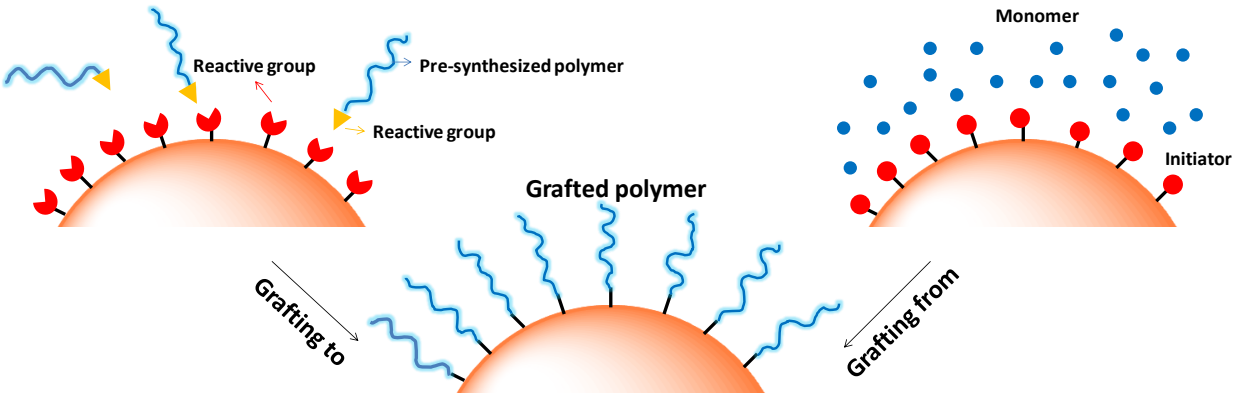

Figure 1.19. Schematic representation of two strategies for grafting polymers on the surface of NPs: “grafting-from” and “grafting-to” approaches.

2.2.3.7.1 "Grafting to" approach

The literature review shows that a few works have been reported about the modification of UCNPs with polymer via chemical bonding compared to other techniques such as ligand attraction, i.e., amphiphilic polymer coating.

In recent work Shaohua Liu and co-workers have modified $NaYF_4$:Yb/Er with poly (acrylic acid) (PAA) for oral drug delivery via the "grafting to" method [396]. In this work, the PAA chains were covalently grafted onto the mesoporous external surface of $NaYF_4$:Yb/Er@$mSiO_2$ by the reaction of carboxylic acid group in PAA and amino groups on surface of nanoparticles in the presence of N-(3-dimethylaminopropyl)-N-ethylcarbodiimide hydrochloride (EDC) as a coupling agent. Grafted PAA has been used as a reversible gatekeeper to control the release of the drug from mesoporous silica shell dependent on pH (Figure 1.20). In another work, chitosan was grafted on surface of UCNPs that was reacted with the carboxyl groups located on the surface of dimercaptosuccinic acid (DMSA)-modified $NaYF_4$: Yb/Er UCNPs [330].

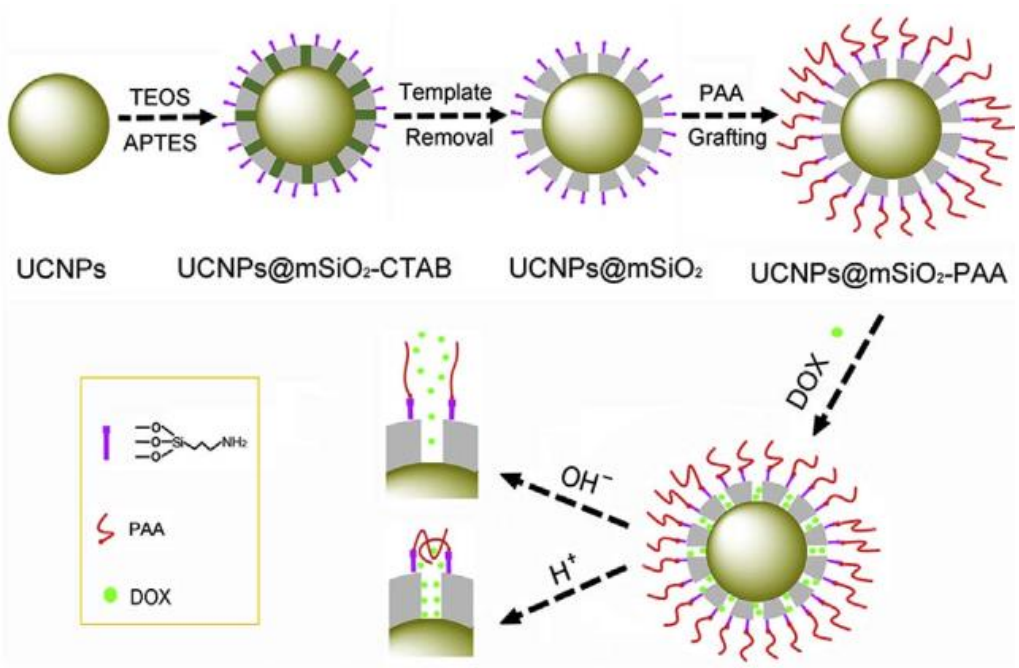

Figure 1.20. Schematic illustration of the preparation procedure of UCNPs@mSiO2-PAA nanocomposite and subsequent controlled release of DOX, reproduced from Ref. [396].

2.2.3.7.2 "Grafting from" approach

Generally, up to now, modification of UCNPs grafted polymer has been reported via several methods including 1) conventional radical polymerization, 2) surface-initiated RAFT polymerization (SI-RAFT), 3) surface-initiated ATRP polymerization and 4) surface-initiated ring opening polymerization.

2.2.3.7.2.1. Conventional radical polymerization

In this method UCNPs are modified with a layer of silica with the above-mentioned method. The following silica layer is then treated with the coupling agent methacryloxypropyltrimethoxysilane (MPS), which has vinyl groups and can react with the monomer or pre-polymer in solution by radical polymerization. For example, poly[(Nisopropylacrylamide)-co-(methacrylic acid)] (P(NIPAM-co-MAA)) [397], poly (methacrylic acid) (PMAA) [398–400] was coated on the surface of UCNPs using this method. It should be noted that using vinyl group in this method is suitable for preparation of polymeric hydrogels on surface of UCNPs in the presence of divinylbenzene (DVB) or Ethylene glycol dimethyl acrylate (EGDMA) for different application such as molecularly imprinted technology and drug delivery. The general scheme of this method is shown in Figure 1.21.

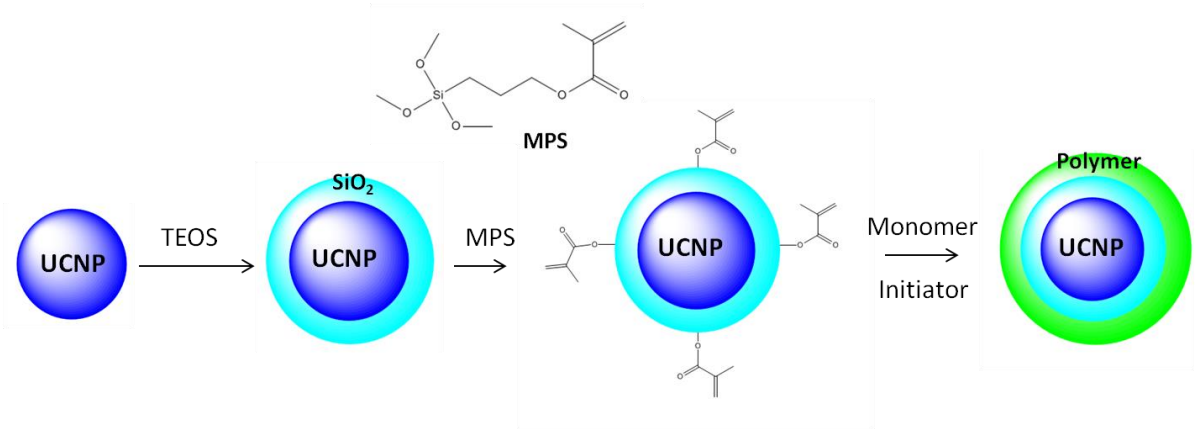

Figure 1.21. Schematic illustration of the general procedure for modification of UCNPs by conventional radical polymerization.

2.2.3.7.2.2. Surface-initiated ring-opening polymerization

Generally, in this method, ring-opening polymerization is initiated from amine or hydroxyl groups on substrate [401]. Grafting various biocompatible polymer such as poly (ε-

caprolactone) (PCL), polylactide, poly(glutamate) and poly(N-propionylethyleneimine) (PPEI) on different surfaces with this method was reported [402]. In this context, modification of UCNPs with linear and hyperbranched polymer via surface-initiated cationic ring-opening polymerization was reported by Li Zhou and coworkers [403,404]. In those studies, UCNPs with hydroxyl groups were prepared by solvothermal reaction in which ricinoleic acid was used instead of oleic acid as a capping agent. As a result, hydrophobic UCNPs with hydroxyl groups were synthesized. UCNP-OH was selected as initiator for anionic ring opening polymerization of ε-caprolactone and glycidol in the presence of $Sn(Oct)_2$ as a catalyst for the preparation of linear poly (ε-caprolactone) and multihydroxy hyperbranched polyglycerol (HPG) respectively [405]. A high-density layer of hyperbranched polyglycidol was coated on the surface of $NaYF_4$:Yb/Er UCNPs.

2.2.3.7.2.3. Surface-Initiated Atom Transfer Radical Polymerization (SI-ATRP)

One of the most efficient, robust, and well-controlled techniques for the preparation of different types of polymer is Atom Transfer Radical Polymerization (ATRP), that was reported by Matyjaszewski in 1995 [406]. Generally, ATRP reaction system includes solvent, a transition metal in lower oxidation state such as Cu^{I}, various N-containing ligands in order to stabilize transition metal and initiator with a halogen atom such as Br and Cl. Transition metal catalyst (Cu^{I} X/L) can appear in two different oxidation stages, as such it can generate reversibly propagating radicals ($P_n^{\bullet}$) by activating the alkyl halide initiators/dormant species (P_n–X). This electron transfer leads to the oxidation of the transition metal to the higher oxidation state as a deactivator ((Cu^{II} X/L)). General scheme for ATRP mechanism is depicted in Figure 1.22.

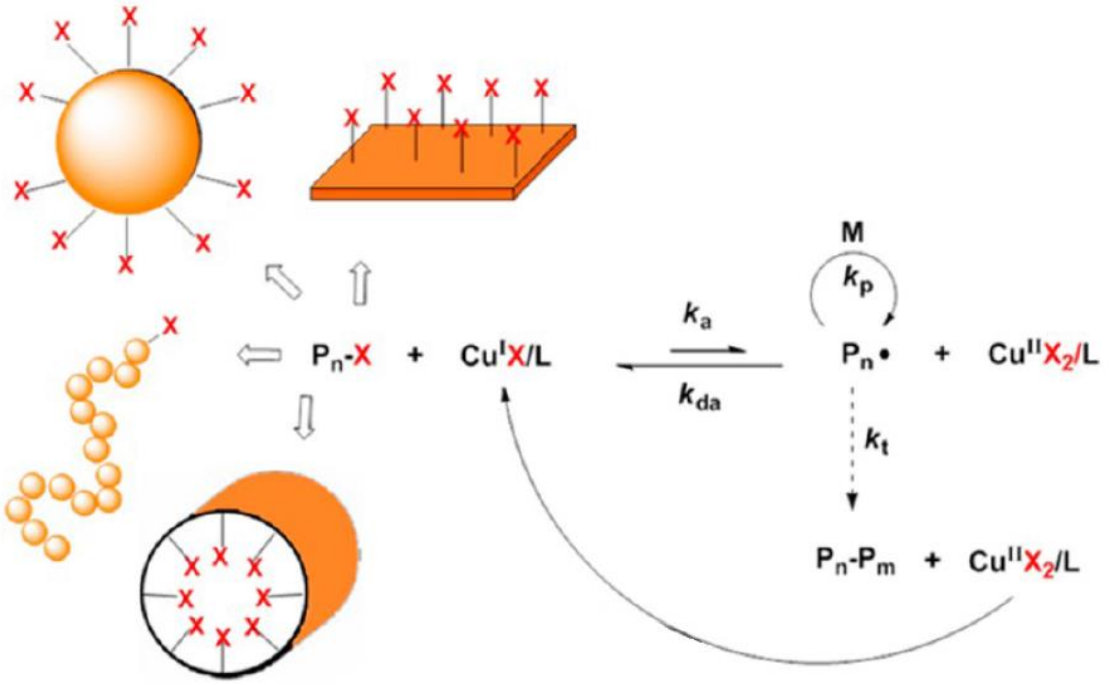

Figure 1.22. General scheme for ATRP mechanism, reproduced from Ref. [407]

A few studies have been reported to modify UCNPs by SI-ATRP [408–410]. For instance, very recently an ultraviolet (UV)-sensitive amphiphilic diblock copolymer based on poly(4,5-dimethoxy-2-nitrobenzyl methacrylate) (PNB), and poly(methoxy oligoethylene glycol monomethacrylate) ((POEG)) has been synthesized on the surface $NaYF_4$:Yb/Tm@$NaYF_4$ [410]. The main role of UCNPs in this formulation was emission of UV light under 980 nm laser exposure in which hydrophobic UV-sensitive in PNB block (o-nitrobenzyl groups) was cleaved to carboxylic acid groups. As a result, polymer on surface has been more water-soluble which leads to trigger drug release. In another work, poly(ethylene glycol) as a hydrophilic polymer with well-defined and various thicknesses on the surface of $NaYF_4$:Yb/Er UCNPs has been prepared via SI-ATRP [409]. However, the main limitation of SI-ATRP polymerization for UCNPs modification for biomedical applications is the presence of toxic metal catalysts such as copper.

2.2.3.7.2.4. Surface-initiated RAFT polymerization

The reversible addition-fragmentation (chain) transfer (RAFT) has been first introduced by CSIRO in 1998 [411]. This technique of polymerization is promising due to its facile, simple operating mode and compatible with a wide range of vinyl monomers [412,413]. This technique of controlled radical polymerization is so attractive for the preparation of polymers

with different architectures (linear, star, brash, hyperbranched polymer) for biological and medical applications due to free toxic metal catalysts [414]. Furthermore, this technique is appropriate for preparation of high molecular weight polymers [415]. The main difference between conventional radical polymerization and RAFT polymerization relies in the use of a chain-transfer agent based on thiolcarbonylthiol derivative compounds. As shown in Figure 1.23, RAFT agents include R and Z groups. Z group acts as a stabilizing group that has two roles including stabilizing intermediate free radical and activation of carbonylthiol for radical addition. On the other hand, R-group is able to leave as a free radical and re-initiate polymerization easily.

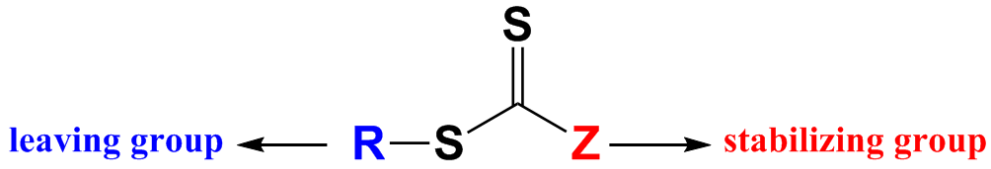

Figure 1.23. Typical RAFT agent structures

The first step of RAFT polymerization, like conventional radical polymerization is the decomposition of initiator for generating free radicals. After addition of monomer, the radical species react with chain transfer agent, which forms dormant species. The equilibrium happens between active and dormant species (steps III and V, Figure 1.24). Indeed, chain propagation occurs by reaction of monomer after the fragmentation of the free radical followed by a reversible addition. In order to control all chains with the same degree of polymerization, the rate of addition and fragmentation equilibrium should be higher than chain propagation. The mechanism of RAFT polymerization is depicted in Figure 1.24.

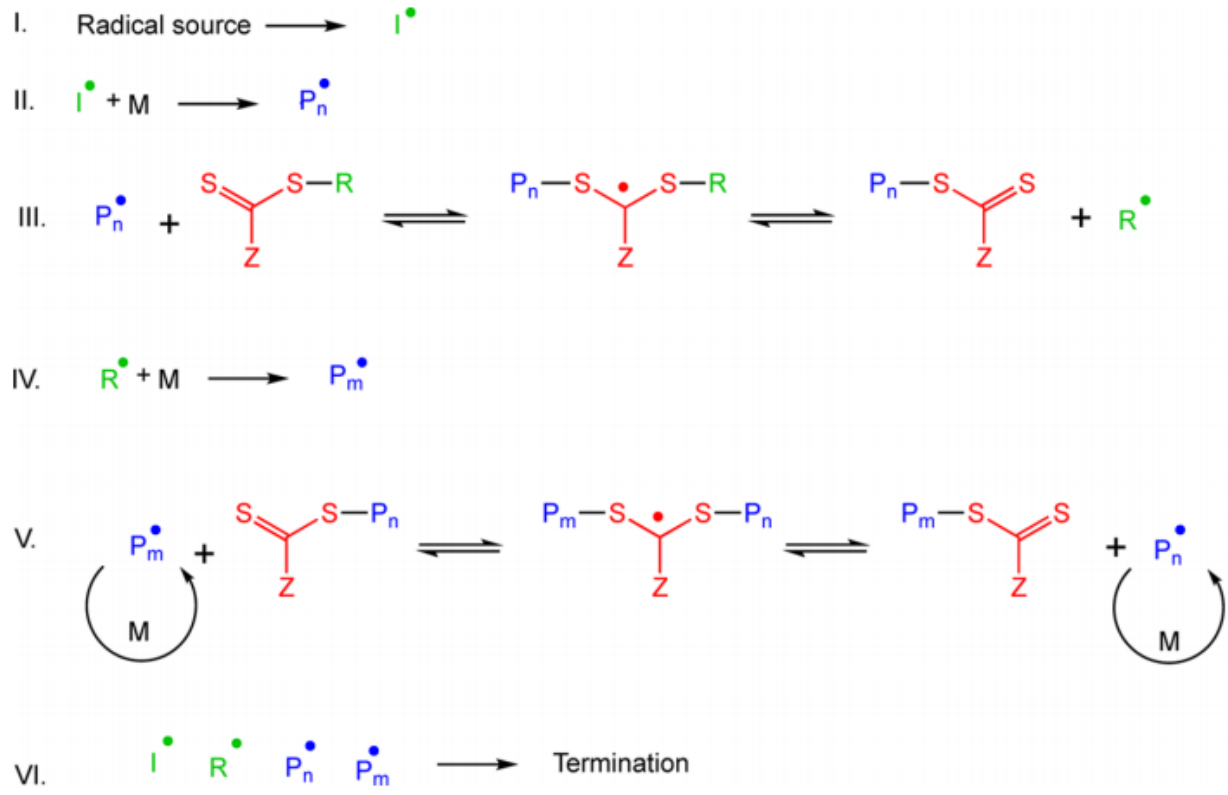

Figure 1.24. Mechanism of reversible addition-fragmentation chain transfer (RAFT) polymerization, reproduced from Ref.[412]

A large number of existing studies in the broader literature have modified various types of nanoparticles with polymer via surface-initiated RAFT (SI-RAFT) polymerization [416]. In SI-RAFT polymerization, chain transfer agent (CTA) is anchored on the surface of the nanoparticles with leads to different controlled grafting densities. As shown in Figure 1.23, RAFT agent including R and Z group that for S-RAFT polymerization is possible to anchor CTA on surface either by Z group or R group (Figure 1.25). These two approaches of anchoring have some advantages and disadvantages, but generally, the literature review shows that most studies have used R group approach due to availability of carboxylic acid residue on the R-group, which is easy to anchor on the surface of the nanoparticles. In addition, in R-group approach dormant species is on outmost surface layer of nanoparticle therefore steric hindrance for diffusion of monomer for chain propagation is low. As a result, R-group approach allows to prepare high molecular weight and grafted polymers on the surface of nanoparticles. In Z-group approach, polymeric radical chain from surface after fragmentation is released in solution and will diffuse back to the surface by reversible deactivation. This method is difficult for polymers with high molecular weights to diffuse back to surface

because of huge steric hindrance. As a result, grafting density of polymers by Z-group approach compared to R- group approach is lower on surface of nanoparticles. The mechanism of SI-RAFT polymerization on the surface of NPs with R and Z-group approaches is presented in Figure 1.25.

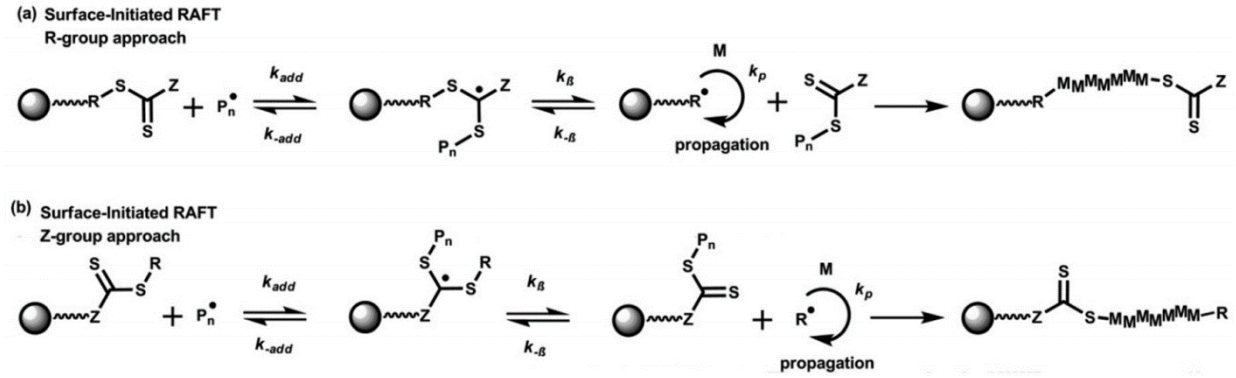

Figure 1.25. General mechanisms of surface-initiated RAFT polymerization with R-group approach (a) and Z-group approach (b), gray spheres represent nanoparticles, M denotes the monomers. k_{add} and $k_{-\beta}$ are the rate constants for the addition reaction of CTA (or macro-CTA) with the propagating radicals, whereas k_{-add} and k_{β} are the fragmentation rate constants for the intermediate radicals. Reproduced from Ref.[414]

There are plenty of reports on SI-RAFT polymerization to synthesize different polymers on the surface of polymeric substrates, Fe_2O_3 NPs, silica NPs, indium tin oxide, nanoclays carbon nanotubes, hydroxyapatite nanocrystals [416]. However, quite few articles have been published about the surface modification of UCNPs using SI-RAFT polymerization [417–419].

For instance, Cyrille Boyer and co-workers have modified UCNPs with Poly(oligo(ethylene glycol) methyl ether methacrylate) (POEGMA) via photoenergy/electron transfer RAFT (PET-RAFT) polymerization. In this work, RAFT agent has been anchored on $NaYF_4$:Yb/Tm UCNPs and propagation polymer chains on surface was investigated in presence of visible light (λ_{max} = 635 nm). The thickness and grafting density of the polymer layer was tunable easily by switching the visible light on and off. The same research group in another study has modified UCNPs with polymer for the delivery of nitric oxide (NO). In this study, $NaYF_4$:Yb/Tm UCNPs were coated with different polymers such as poly (glycidyl methacrylate (GMA), poly(oligo(ethylene glycol) methyl ether methacrylate) (POEGMA) or hydroxyethyl methacrylate (HEMA) via surface-initiated photo-RAFT polymerization in the absence of catalysts or initiators [417]. Interestingly, Zhongxi Xie *et al.* have used UCNPs as a source of

UV for photoinduced RAFT polymerization [418]. In this early study, the surface of $NaYF_4$:Yb/Tm@$NaYbF_4$:Gd@$NaNdF_4$:Yb@$NaYF_4$ was modified with the RAFT agent and UCNPs were excited with NIR (808 nm). As a result, emitting UV from UCNPs triggered the RAFT polymerization on surface without adding any photocatalyst. A layer of block copolymer (6.5 nm) based on poly(acrylic acid) (PAA) and poly(oligo(ethylene oxide)methacrylate has been successfully prepared on the surface of UCNPs.

3. Overall conclusion

In this chapter, the synthesis and use of hyperbranched polymers (HBPs) for the delivery of a drug, the synthesis of lanthanide-doped upconversion nanoparticles (UCNPs) and the different strategies to modify their surface with a polymer layer have been reviewed.

For several years great efforts have been devoted to the preparation of hyperbranched polymers in solution by radical control polymerization (CRP). However, only a few works have reported the growth of hyperbranched polymers from the surface of nanoparticles using CRP (e.g. ATRP). Although RAFT polymerization is a promising method for the synthesis of polymers for biomedical applications, the preparation of hyperbranched polymers at the surface of nanoparticles has not been yet reported .

Regarding the bibliography section on UCNPs, it was highlighted that for the synthesis of UCNPs, the mechanism by which α-nanocrystals are transformed into β-nanocrystals is still not yet fully elucidated as is the effect of the reactor geometry on the control of the β-nanocrystals shape and size. Indeed previous reported studies have been more focused on tuning the ratio of chemicals and addition of different doping agents to control their size and shape.

Thus, in the following chapters, we will address these key points by running i) an extensive investigation on the production of lanthanide-doped UCNPs in flask and microtubular reactors of different heat transfer features (Chapter 2), ii) an investigation of the growth of hyperbranched polymer from the surface of these UCNPs by surface-initiated RAFT polymerization (Chapter 3), iii) a study on the potential of HBPs grafted on UCNPs for the delivery of 5-fluorouracil (5-FU) as a model drug for cancer therapy implementing redox and enzymatic triggering features in the design of the HBPs (Chapter 4).

CHAPTER 2 : Controlled synthesis of $NaYF_4$:Yb,Er upconverting nanocrystals: a focus on heat treatment

1. Introduction

Through the last decade, lanthanide-doped upconversion nanoparticles (UCNPs) have been widely investigated for their potential application in many areas, such as therapeutics, multimodal bioimaging, solar cells, sensors, high-density optical storage and three-dimensional flat-panel displays [350,354,420–422].

Numerous investigations have been reported on rare-earth (RE) doped fluorides UCNPs especially $NaYF_4$ nanocrystals because of their excellent properties such as low phonon energy (< 400 cm^{-1}), excellent chemical stability, and a superior refractive index (1.430-1.470) [423,424]. Several methods of producing this type of nanocrystals have been adopted, which includes co-precipitation, thermal decomposition, hydrothermal synthesis, sol-gel synthesis, combustion synthesis, and flame synthesis. [423].

Generally speaking, the synthesis of $NaREF_4$ nanocrystals by co-precipitation method comprises two steps that include precipitation step at low temperature and heat treatment process at high temperature (typically around 300 °C)[343]. Control of heat treatment step for tuning the properties of final nanocrystals, such as the phase of nanocrystals, size, crystal morphology, and size distribution is so critical. Indeed, the evolution of size, morphology, and phase transition will occur during this step.

These nanocrystals have two major types of crystalline structures, including cubic α-phase and hexagonal β-phase, the latter exhibits enhanced fluorescence intensity [425]. However, cubic α-phase with lower forming energy is the first to be produced during the synthesis. Then, as a thermodynamic product, it is converted into β-phase following a heat treatment at high temperature. Therefore, up to now, many investigations have been reported on phase transition for the control of nanocrystals' size, shape and fluorescence intensity. For example, introducing trivalent lanthanide dopant ions with larger radius such as Gd^{+3} [309] and doping of alkali ions (Li^+ or K^+ ions) [313], applying mixture of surfactants such as oleic acid, oleylamine and tributylphosphine [314–316], change of chemicals ratio (oleic acid, octadecene, NaOH and NHF_4) [317–320], replacement of sodium oleate instead of oleic acid [321], change of addition way of NH_4F and NaOH [322], reaction time and temperature [323,324]. Also, significant effort has been invested in the perception of growth and phase transition mechanism [426–433]. For instance, Suter *et al.* have investigated the growth of nanocrystals from cubic α-phase to hexagonal β-phase by real-time monitoring using NIR-to-

visible upconversion emission [431]. They have defined four stages related to the evolution of $NaYF_4$ nanocrystals phase in which the longest period in heat treatment time is between the initial formation of the small cubic α-phase nanocrystals and the start of the phase transition that was called relative stasis phase. Also, May *et al.* have studied the mechanism of crystals growth by means of a mathematical model [433], while very recently Radunz *et al.* have investigated the evolution of size and optical properties of $NaYF_4$ nanocrystals with different techniques such as SAXS, TEM, XRD and ICP-OES [427].

However, to the best of our knowledge, despite significant effort invested in controlling the phase, shape, and growth of nanocrystals, nobody has studied the effect of vessels with different heat transfer rates on growth of $NaLnF_4$ nanocrystals via co-precipitation. In this study, the significance of using an appropriate reactor for growth of $NaYF_4$:Yb,Er nanocrystals during the heat treatment step has been investigated. On the other hand, in addition to studying the growth of $NaYF_4$:Yb,Er nanocrystals, new reactors have been considered that benefit from scale-up capability. Therefore, in this report, we set out to design a system for the heat treatment step based on stainless steel microtubes that can be used at different lengths with capacities ranging from several milliliters to a few hundred milliliters. In addition to the advantage of scale-up, these tubes as a closed system, allow eliminating some of the parameters that have a tangible effect on the final product. For instance, some of these parameters are argon gas flow, stirring rate, the volume of the mixture for reaction. [434]. Sometimes the simultaneous control of all these parameters is difficult and the growth of nanocrystals may present some discrepancies from batch to batch. Therefore, the use of microtubes can put aside these parameters, which results in repeatability of the growth process of nanocrystals.

2. Results and discussion

2.1. Comparison of nanocrystals growth and phase transition between a microtube and a round-bottom flask

One of the most common conditions for the synthesis of $NaYF_4$:Ln^{+3} nanocrystals by co-precipitation method is the use of the formulation with 1.0 mmol of rare-earth chloride, 4.0 mmol NH_4F, 2.5 mmol NaOH, 6 mL of oleic acid and 15 mL of octadecene and a heat treatment is carried out at 300 to 310 °C [343]. In this context, the reactors influence on the growth of

crystals and phase control has been investigated through the heating process step for this formulation. Generally, we have used two heating systems, which include the flask system (round-bottom flask) as a typical and the most common heating system and microtubes with various internal diameters (879, 1753 and 4083 µm).

First, we have started with 4083 µm microtube at 300 °C with different heat treatment times. Figure 2.1a illustrates the comparison of growth nanocrystals in the microtube and round bottom flask. In the latter system, the β nucleation was observed only after 30 min of heat treatment (Figure 2.1b) and was completed after 120 min since TEM micrograph revealed bigger nanocrystals with a lattice fringe of 0.52 nm which is attributed to the β-phase (Figure 2.1c). Experiments conducted in the microtube showed that the nucleation process of the β-phase has been associated with a long delay in comparison with the flask system. For instance, the results of XRD (Figure A.2.1) and TEM revealed that only cubic α-phase nanocrystals were present for 120 min heating since the lattice fringe was equal to 0.31 nm (Figure 2.1d). However, when the heat treatment time was increased to 180 min, β nucleation had clearly occurred since bigger particles coexisted with smaller α-phase nanocrystals (Figure 2.1e). Upon extended time (up to 330 min), no α-phase nanocrystals was still observed (Figure 2.1f) and the growth phase (α→ β) was completed. Influence of temperature and type of reactor on the time range of phase transition will be discussed in section 2.2.

Regarding shape and size of resultant β-$NaYF_4$:Yb,Er nanocrystals, rod-like particle was the final shape of β-phase nanocrystals from microtube with a mean length size of 47.6 ± 12.3 nm and a width of 21.6 ± 2.4 nm (Figure 2.1f) while β-$NaYF_4$:Yb,Er nanocrystals from the flask system were more spherical with an average size around 30 ± 0.7 nm (Figure 2.1c). This difference in shape will be discussed in section 2.3.

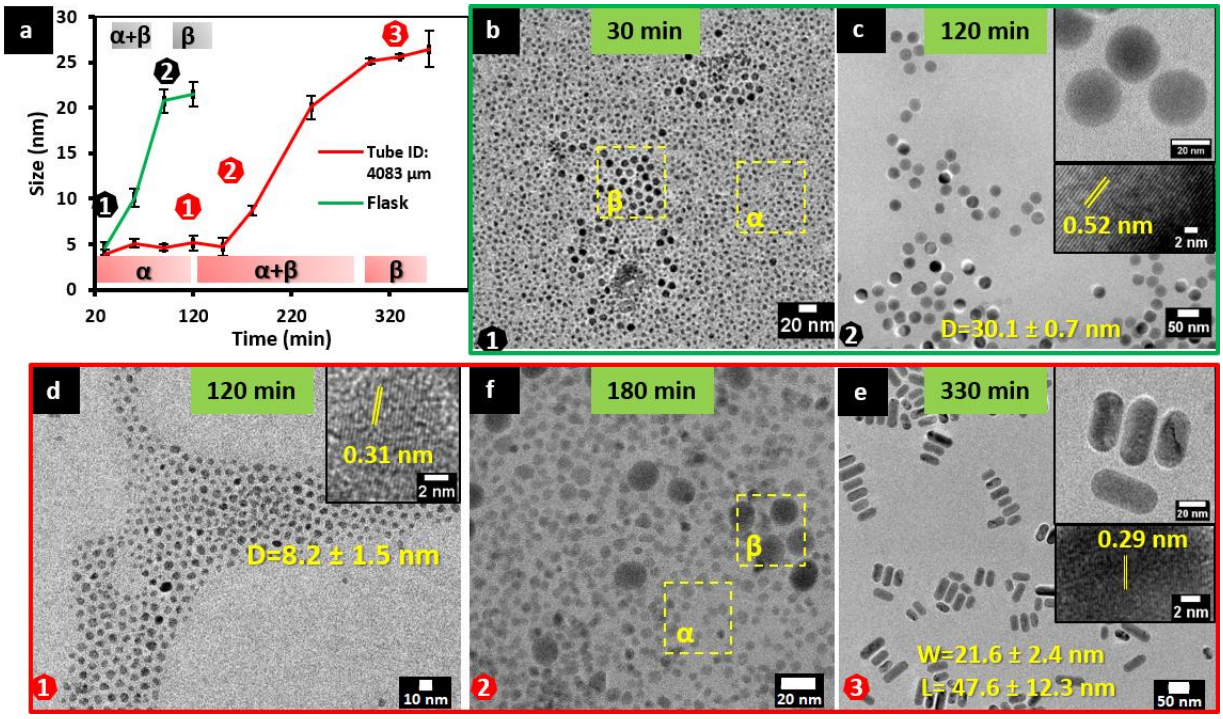

Figure 2.1. Evolution of the nanocrystals' size, as returned by DLS measurements, with respect to the heat treatment time for a round bottom flask and a 4083 µm microtube (a). TEM images of nanocrystals synthesized at 300 °C: mixture of cubic and hexagonal phase (flask system, 30 min) (b), hexagonal β-phase nanocrystals (flask system, 120 min) (c), cubic phase (microtube system, 120 min) (d), mixture of cubic and hexagonal β-phase (microtube system, 180 min) (e), hexagonal β-phase (microtube system, 330 min) (f).

2.2. Influence of temperature and type of reactor on the time range of β-phase transition

The above experiments conducted in the microtube system showed that the dissolution process of the cubic α-phase nanocrystals (α→ β) was carried out with a slow rate, notwithstanding the high heat transfer and subsequent temperature homogeneity of microtube compared to flask system (see section 2.2.4).

The primary implication of the previous results is that the low rate of dissolution of cubic α-phase nanocrystals in microtube leads to a low concentration of monomers for β-phase nucleation (i.e. below supersaturation for crystallization). In fact, ultrasmall β-phase nuclei are thermodynamically less stable than α-phase nuclei [435]. Therefore, at a low concentration of monomers, β-phase nuclei after being formed do not have the opportunity to reach the critical radius corresponding to the minimum size allowing them surviving in solution without being redissolved and thus evolve back to the α-phase [436,437]. On the other hand, if the concentration of monomers is high enough in the system (i.e. supersaturation), the β-phase nuclei can reach the critical size above which they can survive

[311,317]. In conclusion, it seems that the type of reactor has a strong effect on the range of heat treatment times over which the phase transition occurs. Therefore, to confirm this assumption new experiments with in another microtube having a smaller diameter were performed.

2.2.1. Comparison of nanocrystals growth in large and small ID microtubes (4083 and 879 µm)

In this next step, we used a microtube with an internal diameter of 879 µm, which is about 4.5-fold smaller than the previous microtube (ID = 4083 µm). The morphologies of the resultant $NaYF_4$:Yb,Er nanocrystals at various heat treatment times were observed with TEM (Figure 2.2). The results showed that β-phase nucleation occurred for 60 min of heating and resulted in a mixture of α-phase nanocrystals having an average size of 5.7 ± 1.2 nm and β-phase nanocrystals with a narrow size distribution (9.4 ± 0.6 nm) as shown in Figure 2.2b. The extension of heating led to an increase in the size of β-phase nanocrystals with a very broad size distribution as well as a change in their morphologies to rod-like shapes (Figure 2.2c). The resultant β-$NaYF_4$:Yb,Er nanocrystals for 150 min heating (Figure 2.2e) included a mixture of spherical and rod-like β-phase nanocrystals shapes with sizes around 10-18 nm and 20 to 40 nm (length) respectively. One also could observe some impurities constituted by the presence of residual α-phase nanocrystals.

As a conclusion, two major differences were revealed between 879 µm and 4083 µm microtubes in their β-phase nucleation times range and nanocrystals size distribution. In this regard, in 879 µm microtube the first β-phase nanocrystals were observed for 60 min heating while for 4083 µm microtube it was around 180 min heating. On the other hand, the obtained β-phase nanocrystals from 879 µm microtube had a poor size distribution compared to the other bigger size microtube. It seems that, the consumption of cubic α-phase nanocrystals, β-phase nucleation, and growth of β-phase nanocrystals overlap strongly in the smaller microtube. Indeed for this system, β-$NaYF_4$:Yb,Er nanocrystals ranging from 10 nm (as a primary β nanocrystal with spherical shape) coexisted with 40 nm rod-like nanocrystals after 150 min heating (Figure 2.2e). At this stage, one can question about the effect of temperature and the possibility of getting narrow size distribution of β-phase nanocrystals in the smaller microtube.

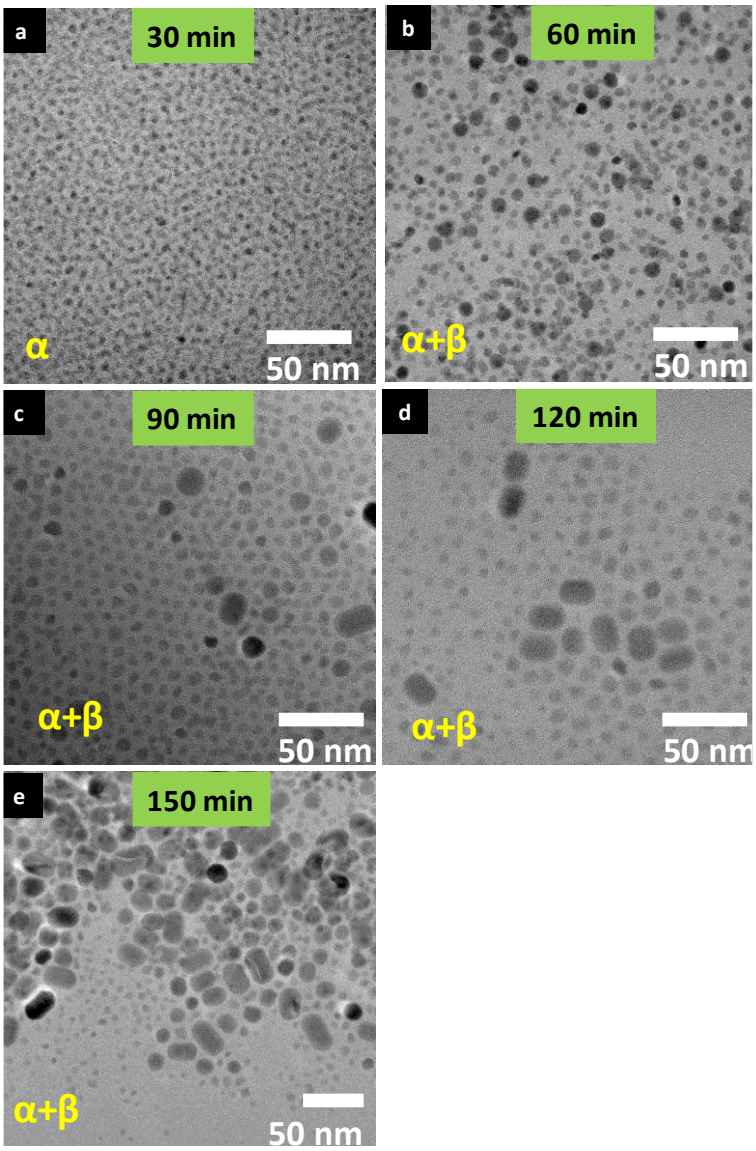

Figure 2.2. TEM images of $NaYF_4$:Yb,Er nanocrystals obtained in a 879 µm microtube at 300 °C and different heat treatment times.

2.2.2. Comparison of nanocrystals growth between a smaller ID microtube (879 µm) and flask systems at constant temperature 310 °C and various heat treatment times

In order to investigate the effect of the temperature on the formation of $NaYF_4$:Yb,Er nanocrystals, experiments at 310 °C were performed in the same smaller microtube (879 µm). The nanocrystals obtained after 30 min of heating had a cubic α-phase as reported by XRD analysis (Figure A.2.2) and the HRTEM image of a nanocrystal also indicated the lattice fringes (0.31 nm) of α-$NaYF_4$:Yb,Er nanocrystals (Figure 2.3a). These nanocrystals were spherical with size 5.9 ± 0.5 nm and highly monodisperse. By increasing the heat treatment time from 30 to

90 min, an increase in the particle size from ~ 4-6 to ~ 8-9 nm could be observed (Figure 2.3a-c). Furthermore, the morphology of the nanocrystals has been changed without altering the crystalline phase of the outcome α-$NaYF_4$:Yb,Er nanocrystals. For instance, a bimodal distribution of α-phase nanocrystals was observed for 60 min of heating since small and spherical nanocrystals coexisted with irregular shape nanocrystals with bigger sizes (Figure 2.3b). As clearly shown in Figure 2.3c, the majority of α-$NaYF_4$:Yb,Er nanocrystal had an irregular shape with a broad size distribution after 90 min. The XRD crystal structure studies indicated nanocrystals to be a single α-phase nanocrystal without the presence of any impurity (Figure A.2.2) and also the obvious lattice fringes with the spacing d values of ~0.31 nm corresponding to the (111) d-spacing of α-$NaYF_4$:Yb,Er in the HRTEM images confirmed that the individual particles were highly crystalline (Figure 2.3c).

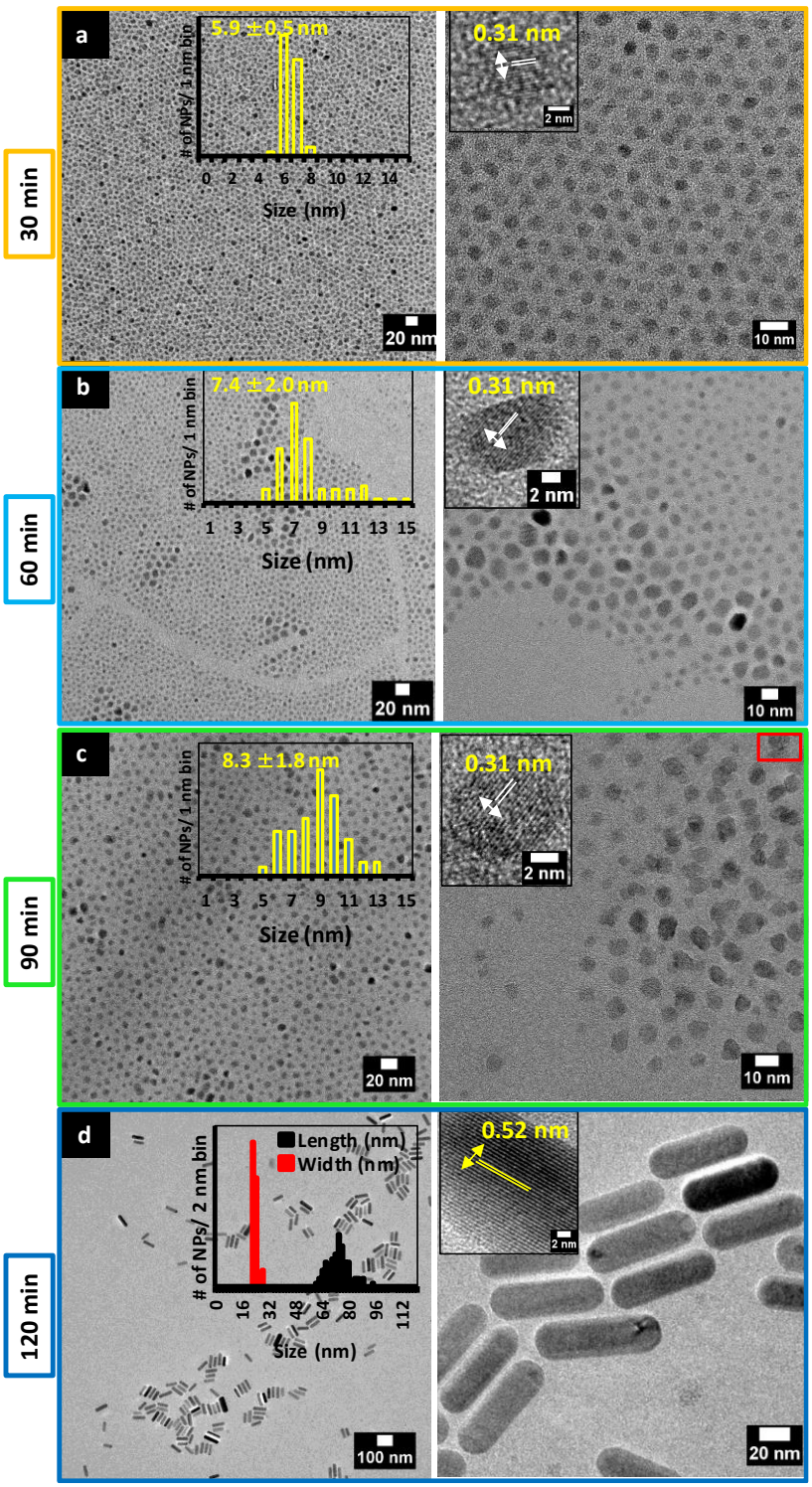

Figure 2.3. TEM images of $NaYF_4$:Yb,Er nanocrystals with two magnifications at different heat treatment time at 310 °C in 879 µm microtube. The red box for the micrograph at 90 min is reported in Figure 2.4.

The upconversion emission of resultant α-$NaYF_4$:Yb,Er nanocrystals for 30 and 90 min heating was measured under the same conditions and concentrations in cyclohexane as shown in

Figure A.2.3. The α-$NaYF_4$:Yb,Er nanocrystals for 90 min of heating show a twofold increase in intensity compared to the α-$NaYF_4$:Yb,Er nanocrystals obtained for 30 min of heating. It is thought that this increase may result from a reduction in defects induced by a rearrangement of atoms in the internal and surface structure of nanocrystals as well as growth in nanocrystal size during the heating process. Furthermore, the integral intensities of green (500-600 nm) and red (600-700 nm) emissions were investigated and showed a difference between two α-$NaYF_4$:Yb,Er nanocrystals (30 min: $R_{g/r}$=1.2 and 90 min: $R_{g/r}$=1.0). With a deeper investigation of the TEM micrograph from the irregular shape α-$NaYF_4$:Yb,Er nanocrystals obtained after 90 min of heating, one can observed oriented attachment (OA) between two nanocrystals before relaxing into a sphere shape in which the resulting size larger than the size of the two individual nanocrystals (Figure 2.4). This manner of crystals growth supports the assumption of an oriented attachment mechanism, i.e. coalescence process [438].

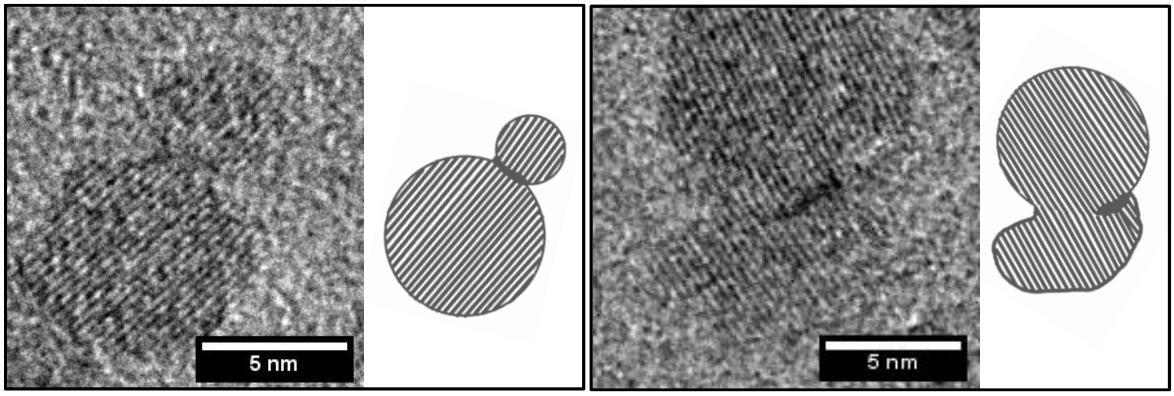

Figure 2.4. Two examples of sintering of α-$NaYF_4$:Yb,Er nanocrystals by coalescence mechanism in 879 µm microtube at 310 °C for 90 min heating.

Therefore, it seems that for phase transition (α→ β), the primary step could be the growth of small α-phase nanocrystals with coalescence process to the bigger irregular shape and anisotropic nanocrystals with a size around 8-9 nm. The surface energy reduction is a good driving force for the coalescence process because the surface area of the new formed nanocrystals is less than that of the sum of the surface areas of the primary nanocrystals. Overall these results are in accordance with findings reported by Leite and coworkers [439]. They have indeed shown that oriented attachment is an effective mechanism for the

formation of anisotropic nanocrystals under hydrothermal annealing. Interestingly, their results, such as the change in the morphology of primary nanocrystals from spherical to anisotropic and producing irregular-shaped nanocrystal by heat treatment, are compatible with our results.

According to the report of May and coworkers, the period of heat treatment before phase transition (>25 min) could be defined as a relative stasis of α-phase nanocrystals population that is however still unclear and under discussion [431]. Nevertheless, the current results provide now clear evidences that the α-phase nanocrystals may also grow by the coalescence process beside the Ostwald ripening phenomenon that was reported in the literature [427,431,433].

Surprisingly, despite the high temperature (310 °C) and homogeneous heat transfer of microtube (879 μm), one could not observe any hexagonal β-phase with HRTEM before 90 min heating. This main observation was related to the slow change in the shape and size of α-phase nanocrystals.

We have extended the heat treatment time above 90 min and observed a sharp phase transition for which all the α-phase nanocrystals were dissolved to the benefit of the β-phase nanocrystals growth. The sizes and morphologies of the obtained β-$NaYF_4$:Yb,Er were characterized by TEM. As shown in Figure 2.3d, resultant nanocrystals from microtube after 120 min heating appeared rod-like in shape and have a narrow size distribution and good uniformity. The average size of the resultant β-$NaYF_4$:Yb,Er nanocrystals, evaluated from more than 150 random nanocrystals, was 72.8 ± 6.5 nm in length and 22.2 ± 1.5 nm in width (Figure 2.3d). The HRTEM image displayed an interplanar spacing of 0.52 nm corresponding to the (1010) plane of β-$NaYF_4$:Yb,Er (Figure 2.3d). This single β-phase of nanocrystals was also confirmed by XRD analysis (Figure A.2.4). Meanwhile, Na and coworkers have prepared β-$NaYF_4$:Yb,Er nanorods (L= 60.1 nm and W= 21.5 nm) with the same components but with a higher ratio of oleic acid to solvent, i.e. 9.5 (in our case 0.4) and higher temperature at 320 °C (in our case 310 °C) in a flask system [440]. It is worth noticing that in order to check the repeatability of our system for nanorods synthesis, the experiments were duplicated with a 150 min heat heating. The resultant β-$NaYF_4$:Yb,Er had a size (L= 76.5 ± 7.2 nm and W= 22.1

± 1.4 nm) and shape such as those produced in the previous experiment, which indicates that the system has a good repeatability for the formation of nanorods (Figure 2.5).

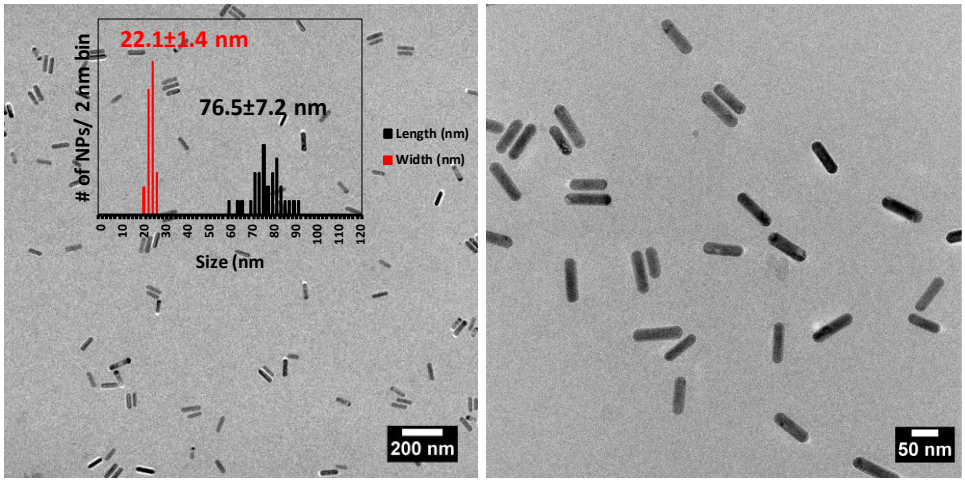

Figure 2.5. TEM images of β-$NaYF_4$:Yb,Er nanocrystals with two magnifications obtained in 879 µm microtube for 150 min heating at 310 °C.

As a summary, the growth of nanocrystals in 879 µm microtube at 310 °C includes two different stages i) growth of α-phase nanocrystals and consequently accumulation of irregular shape nanocrystals without presence of any β-phase nanocrystals; ii) fast phase transition (α→ β) which produces pure β-$NaYF_4$:Yb,Er nanorods.

About the first stage, it seems that irregular shape α-$NaYF_4$:Yb,Er nanocrystals could be the mature-form of the cubic α-phase. However, this type of nanocrystal could be less stable than primary cubic nanocrystals despite their bigger size. This instability issue may be due to different interaction of the oleic acid (capping agent) on the surface of the nanocrystals (i.e. strong coordination interaction or weak Van der Waals interaction) as explained by Chun-Hua Yan and co-workers for α-$NaYF_4$:Yb,Er nanocrystals with different shapes and sizes [428]. Indeed, if the adhesion energy or interaction on the surface is low, the odds of instability and dissolution of the nanocrystal will be high [428]. On the other hand, nanocrystals with irregular or anisotropic shapes have lower stability compared to spherical nanocrystals of the same volume due to their higher surface areas which renders them metastable [441]. Therefore, dissolution of this type of nanocrystals should be a source of monomers for the growth of β-phase nanocrystals. As one observed in microtube, the phase transition happened when the majority of the cubic α-phase changes to irregular shape with a critical

size around 12 nm. It seems that if the number of this type of nanocrystal in the system goes up, e.g. when heating time is increased, and then more monomers are produced by their dissolution. As a result, the concentration of monomers will reach a critical concentration for β nucleation in which phase transition will happen (Figure 2.6).

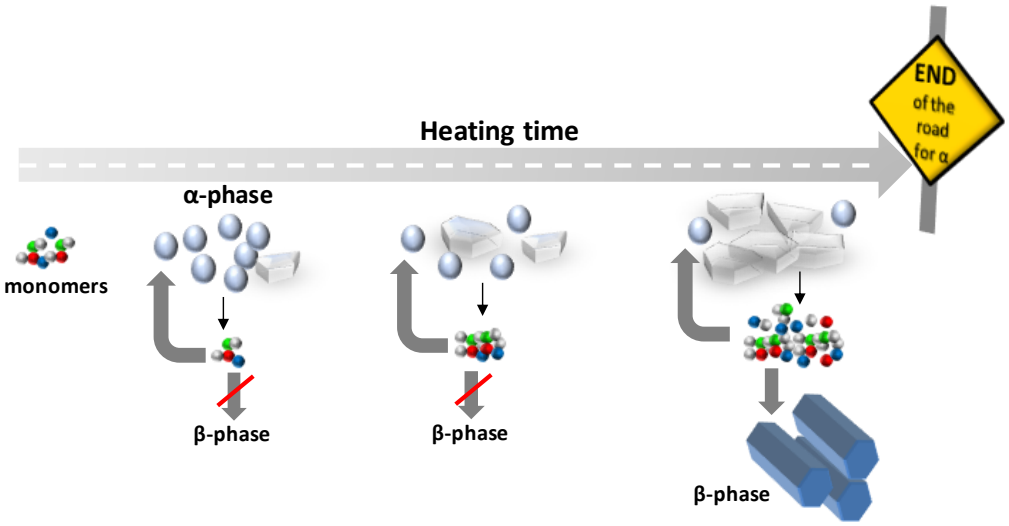

Figure 2.6. Schematic illustration of size, morphology and phase evolution of $NaYF_4$:Yb,Er nanocrystals when increasing the heat treatment time from 30 to 120 min at 310 °C in 879 µm microtube

2.2.3. Size and morphology of α-phase nanocrystals before full conversion in α-phase nanocrystals at different temperatures for the flask system

To get a deeper insight, we have studied the size and morphology of α-$NaYF_4$:Yb,Er nanocrystals before full conversion of the cubic α-phase into hexagonal β-phase for the flask system at 310 °C. First of all, in contrast to microtube, for 30 min of heating, a mixture of cubic and hexagonal phase was observed. The results of TEM showed that the size and morphology of α-$NaYF_4$:Yb,Er nanocrystals were the same as the ones produced with the microtube before phase transition regarding the size and the morphology (Figure 2.7a). After heating for an additional 30 min, the rest of these α-$NaYF_4$:Yb,Er nanocrystals were dissolved completely, and finally, the pure β-$NaYF_4$:Yb,Er nanocrystals phase was produced (Figure 2.7b). In addition, the formation of these irregular shape α-$NaYF_4$:Yb,Er nanocrystals at low temperature such as 290 °C in flask system was investigated. The size histogram corresponding to the TEM images for cubic α-phase is given in Figure 2.8; the mean particles' size was 9.1 ± 1.1 nm. As observed, both size and shape were similar to those of the α-

$NaYF_4$:Yb,Er nanocrystals observed at 310 °C and obtained either from the bottom flak or the microtube.

Overall, if one compares the time for nucleation and growth processes of β-phase in flask system and microtube at 310 °C, it can be concluded that in flask system the β nucleation happens faster. This issue may be interpreted by considering that a homogeneous heat transfer system (microtube) could impede the formation of irregular shape α-$NaYF_4$:Yb,Er nanocrystals by suppressing the coalescence process. Therefore, the accumulation of this type of nanocrystals as a source of monomers for β-phase transition could be delayed. Another or additional reason may be related to the high pressure inside the microtube which may lead to the decrease in diffusivity. Indeed the collision between two nanocrystals is another critical parameter for promoting the coalescence process [439,442]. It is also worthy to note that the microtube system was devoid of any physical source of mixing. To summarize, our experiments seem to indicate that a system with heterogeneous heat transfer facilitates phase transition (α→ β). For a better insight on this issue, we have considered another type of flask system.

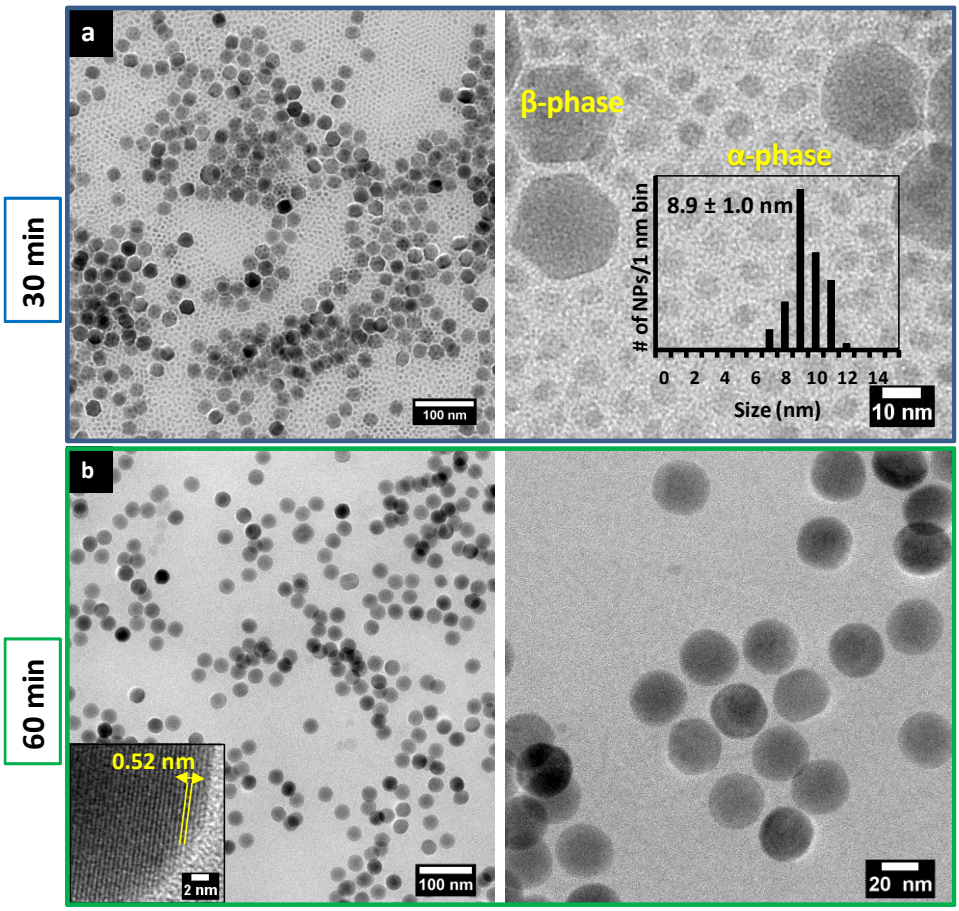

Figure 2.7. TEM image of obtained $NaYF_4$:Yb,Er nanocrystals in round bottom flask at 310 °C for different heat treatment 30 min (a) 60 min (b) of heating. Particle size histograms of α-$NaYF_4$:Yb,Er nanocrystals corresponding to the TEM images (a, right).

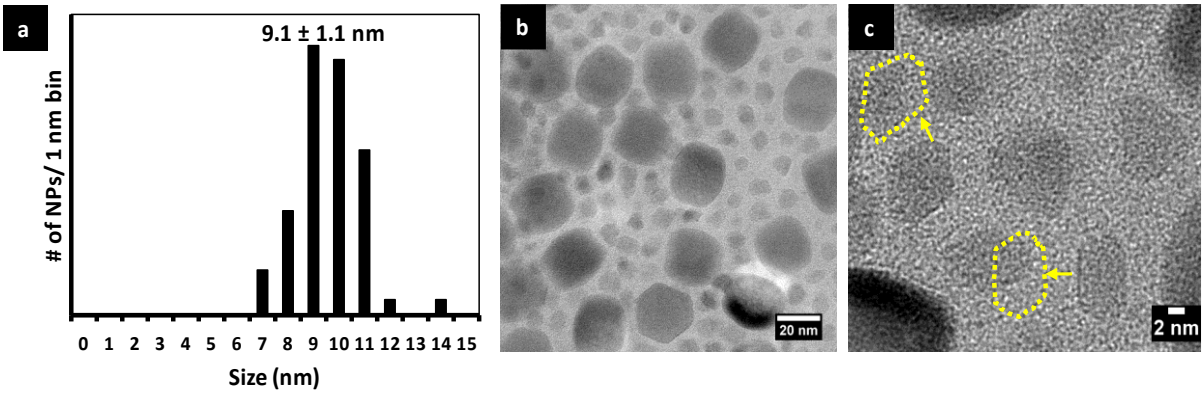

Figure 2.8. Particle size histograms of α-$NaYF_4$:Yb,Er nanocrystals corresponding to the TEM images (a) TEM images at low and high magnifications at 290 °C in flask system for 150 min heating (b, c).

2.2.4. Comparison of nanocrystals growth in different temperature gradient reactors

To get more evidence, we have designed experiments with two different stirred flask systems (Erlenmeyer and round bottom flasks) at 290 °C that present different heat transfers (Figure A.2.5). The Erlenmeyer flask presents the highest temperature gradient (~100 °C) between its its external wall (~190 °C) and the bulk of the liquid at 290°C (set temperature); while the round bottom flask exhibits a temperature gradient 3 times lower (30 °C) between its external wall (320 °C) and its center (290 °C).

The phase transition of the cubic to hexagonal phase (α→ β) in the two above systems was studied with TEM at different heat treatment times. We found that consumption of α-$NaYF_4$:Yb,Er nanocrystals and phase transition in Erlenmeyer flask took approximately 120 min to fulfill a pure β-phase entirely; on the contrary, this time for the round bottom flask was about 180 min of heating. As shown in Figure 2.9a and b, after 150 min of heating in the round bottom flask a mixture of α and β-phases was observed while for the Erlenmeyer flask all of cubic α-phase disappeared and only β-$NaYF_4$:Yb,Er could be observed (see XRD analyses in Figure 2.9c). The particle size of hexagonal β-phase after full conversion of cubic α-phase in the Erlenmeyer flask was about 27.6 ± 0.5 nm and in the round bottom flask 26.6 ± 0.6 nm. According to a tangible difference in the consumption rate of the cubic α-phase (120 min compared to 180 min heating for Erlenmeyer flask and round bottom flask, respectively), it seems that high temperature gradients could facilitate the phase transition which confirms our previous assumption.

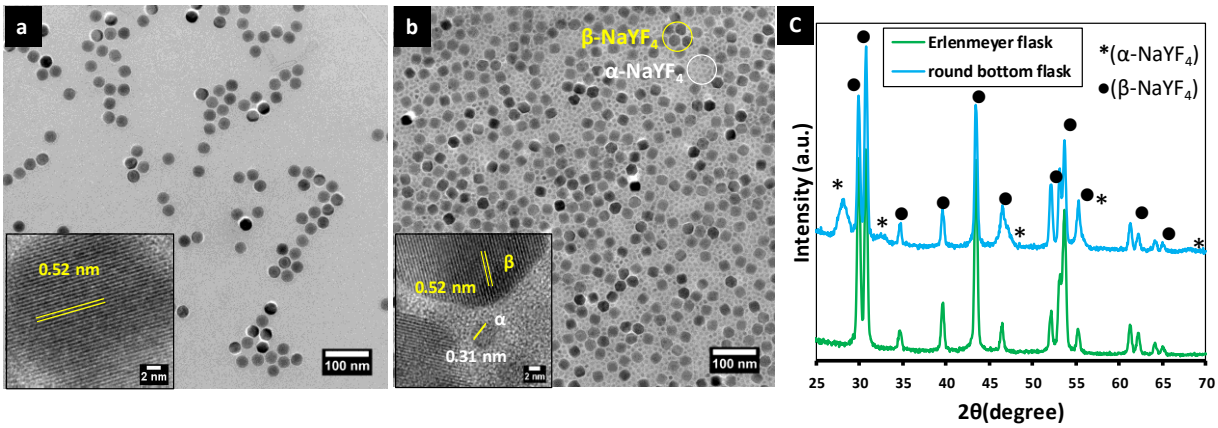

Figure 2.9.TEM images of $NaYF_4$ nanocrystals obtained with the Erlenmeyer flask (a), the round bottom flask (b) and XRD analyses (c) after 150 min heating at 290 °C**.**

In addition, we have observed that the phase transition did not happen in the 879 µm microtube at 290 °C after 150 minutes (TEM in Figure A.2.6), a system considered with a small temperature gradient owing to the high surface to volume ratio. Therefore, it can be concluded that the temperature gradient could be an important parameter that affects the phase transition.

As reported by Yin and Alivisatos [441], nanocrystals growth depends upon the capability of the surfactant for on and off-exchange at the crystals' surface while preventing from aggregation. This exchange of surfactant is strongly affected by the temperature and is fastly occurring for higher temperatures. Since the temperature gradient for the Erlenmeyer flask is significantly higher than for the round bottom one, the α-phase nanocrystals near its inner wall undergo a higher temperature. As a result, aggregation and dissolution of α-phase nanocrystals could be most likely occurring due to the fast exchange of surfactant.

2.3. Influence of temperature, heating time and type of reactor on the shape of β-phase nanocrystals

2.3.1. Nanocrystals produced in microtubes with different IDs and temperatures

In a new set of experiments, the synthesis of β-$NaYF_4$:Yb,Er nanocrystals was carried out at different temperatures from 300 to 315 °C and with microtubes of different internal diameters (4083 and 1753 µm). The results illustrate that the characteristics of the obtained nanorods depend on the internal diameter of microtube and temperature of the heat treatment. TEM images and size distribution histograms of β-$NaYF_4$:Yb,Er nanocrystals are shown in Figure 2.10.

As shown in Figure 2.10a and b, the average length of the as-synthesized β-$NaYF_4$:Yb,Er nanocrystals in a 4083 µm microtube at 305 °C was higher than that obtained with a 1753 µm microtube. Also, the nanocrystals formed with 4083 µm microtube had a narrow size distribution compared to the other microtube. However, the widths of nanocrystals had roughly the same value. At 310 °C the size (length and width) and size distribution of β-$NaYF_4$:Yb,Er nanocrystals were significantly different for both microtubes (Figure 2.10c and d). The nanorods prepared at 315 °C with the two microtubes had the same length (ca. 39 nm), however, the width of nanocrystals from 4083 µm microtube was 22.3 ± 1.5 nm which is slightly higher than the width of those obtained with the 1753 µm microtube, ca. 20.4 ± 2.3

nm (Figure 2.10e and f). In addition, the nanocrystals from 4083 µm microtube had uniform shape and narrow size distribution.

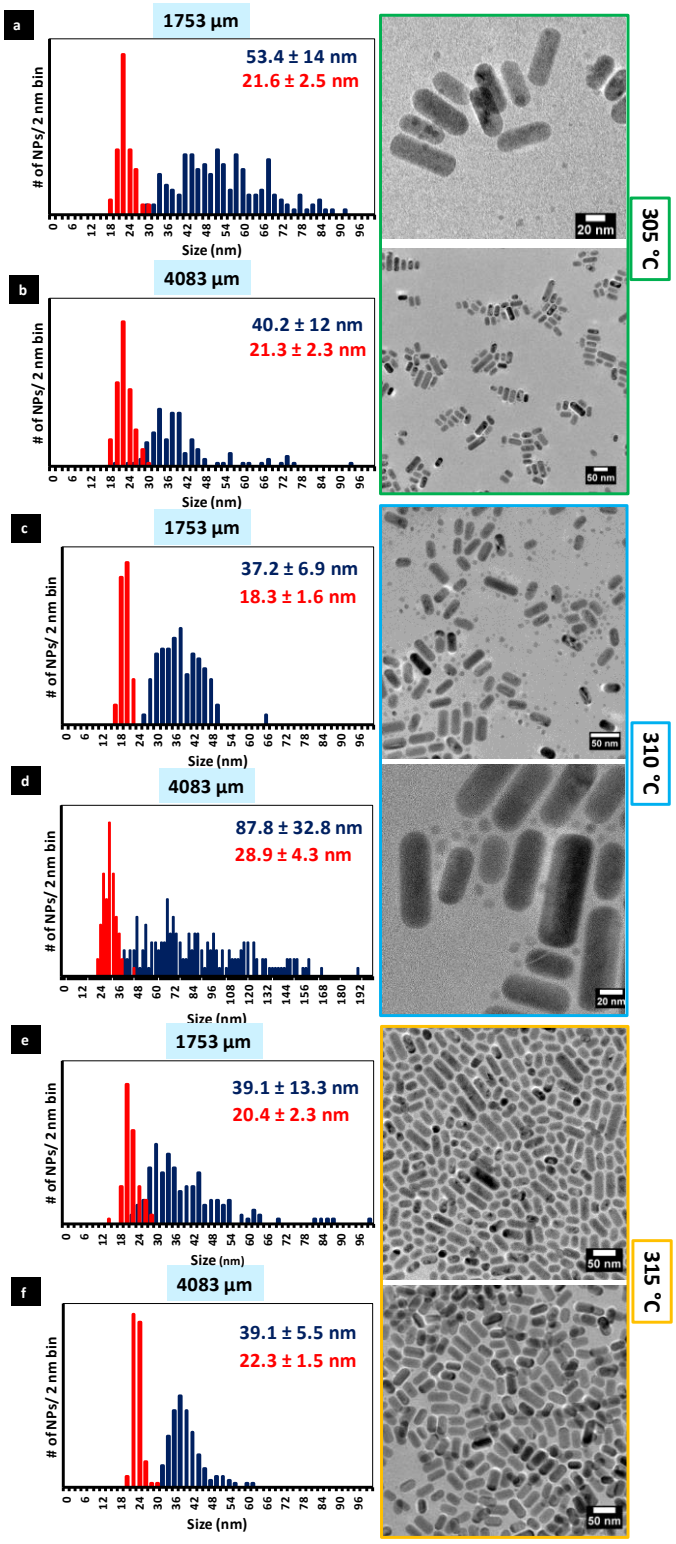

Figure 2.10. TEM images and size distribution histograms of β-$NaYF_4$:Yb,Er nanocrystals obtained in 1753 µm and 4083 µm microtubes at different temperatures. Blue and red colors represent length and width of nanorods respectively.

All information about the lengths and widths of the as-synthesized nanorods is summarized in Figure 2.11. Overall, the results obtained with the two microtubes showed that i) β-$NaYF_4$:Yb,Er nanocrystals had an epitaxial growth along [001] direction (longitudinal), ii) their longitudinal size was influenced by the diameter of the microtube and the temperature. On the other hand, the transversal growth of nanocrystals was the same whatever the temperature and the diameter of the microtube are. Consequently, the width of the nanorods remained at the same value of ca. 20-22 nm. The length of nanocrystals produced with 1753 µm microtube was quite similar to that obtained with the larger diameter (4083µm) except at 310 °C.

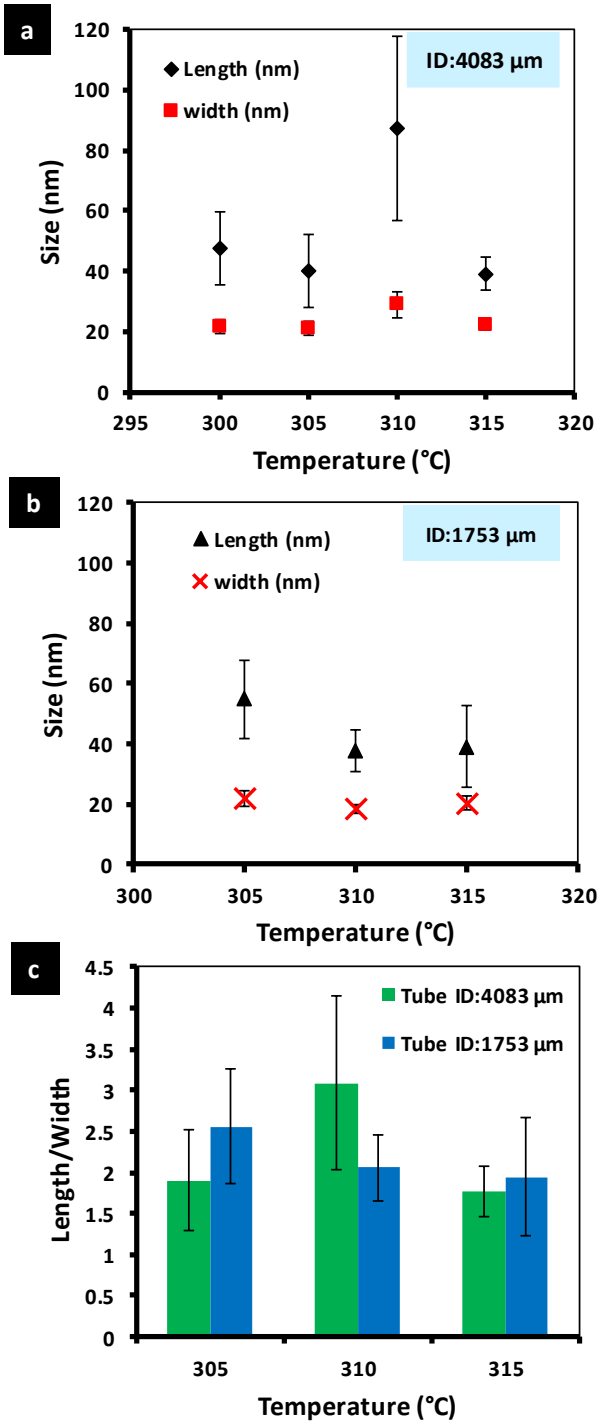

Figure 2.11. Length and width evolution of β-$NaYF_4$:Yb,Er nanorods with changing reaction temperature and internal diameter of microtube: 4083 µm (a), 1753 µm (b). The aspect ratio of nanorods in the two microtubes at different temperatures (c).

2.3.2. Step by step study of the anisotropic growth of β-phase nanocrystals

By comparing the growth processes of nanocrystals for different reaction times but constant temperature (310°C) and microtube (4083 µm), it was observed that for all samples the

nanocrystals have an epitaxial growth in the longitudinal direction at an almost constant width (Figure 2.12a). The size of the β-phase nanocrystals increased by a symmetric epitaxial growth once a spherical nanocrystal of 18 nm was formed after a setpoint of 90 min heating. Then the β-phase nanocrystals evolved from a spherical shape to nanorods by increasing their length. Moreover, the temperature seems to affect this setpoint. For example, the longitudinal epitaxial growth of the β-phase nanocrystals for the same microtube heated at 300 °C started after about 180 min of heating (Figure A.2.7) while at 315 °C it was after 60 min (Figure A.2.8). Step by step, the average size of nanocrystal increased until cubic α-phase being completely consumed. Based on results, it seems that the re-nucleation of β-phase has been stopped and β-phase nanocrystals have an asymmetric epitaxial growth in a longitudinal direction. As a matter of fact, when nucleation and growth of crystals are separated, nanocrystals with an anisotropic shape such as nanorod is observed in the system [443]. On the other hand, resultant β-$NaYF_4$:Yb,Er nanocrystals from flask had a spherical shape after full consumption of the cubic α-phase (Figure 2.12b). Before the full conversion of cubic α-phase, β-phase nanocrystals have a hexagonal shape that evolved into a spherical shape presumably due to symmetric epitaxial growth.

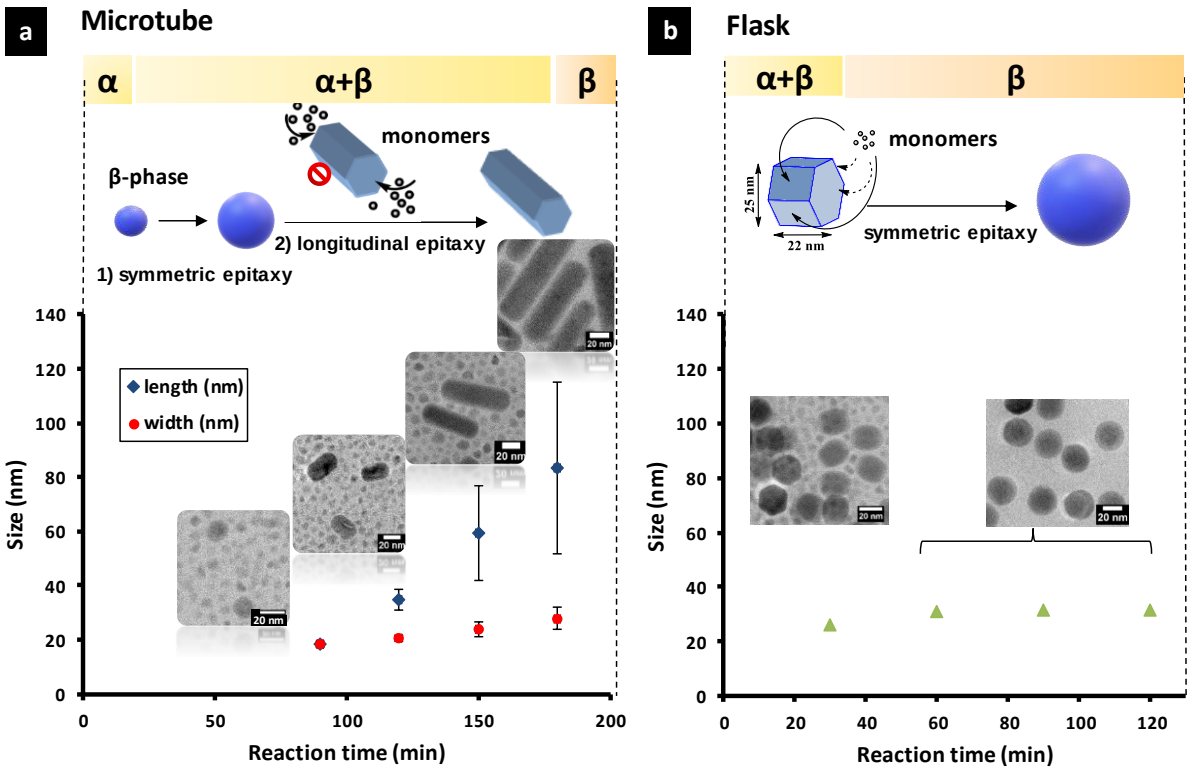

Figure 2.12. Longitudinal epitaxial growth of β nanocrystals in 4083 µm microtube (a) and symmetric epitaxial growth of β nanocrystals in flask (b) for different heat treatment times at 310 °C. Insets are the corresponding β-$NaYF_4$:Yb,Er nanocrystals TEM images.

2.3.3. Summary of nanocrystal phase evolution at different temperatures, heating times and reactors

In order to precisely determine the influence of the temperature, heat treatment time and type of heating system on nanocrystals phase, three graphs were designed. The complete phase transition point and some details related to the type of phase for different conditions are thus reported in Figure 2.13. This information related to the size evolution, phase, and shapes of nanocrystals was extracted from TEM images. Conclusions can be drawn as follows: the microtubes of 4083 and 1753 µm ID almost have the same phase transition pattern that is quite similar to the flask system. The main difference is that the phase transition in these microtubes is much slower than the flask system (e.g. it required more reaction time to proceed). The nanocrystals produced in a 879 µm microtube at 290 °C are only cubic α-phase while at 300 °C a mixture of α and β-phase is observed. Interestingly a sharp phase transition was observed in the 879 µm microtube at 310 °C, which was not observed for other conditions.

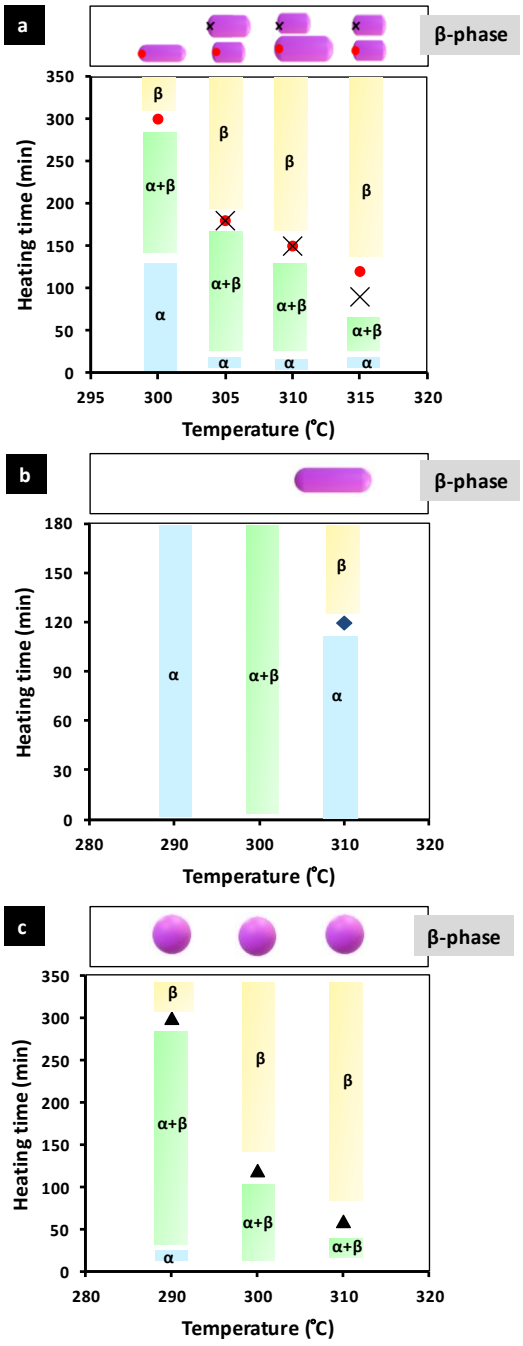

Figure 2.13. Summary information about phase evolution of $NaYF_4$:Yb,Er nanocrystals as a function of temperature and heating time for 4083 µm (circle) and 1753 µm (cross) microtubes (a), 879 µm microtube (b) and round bottom flask system (c). Circle, cross, diamond and triangle represent the point at which the single phase β-$NaYF_4$:Yb,Er nanocrystals are formed.

2.4. Overall summary

As a conclusion of this part, experimental results reveal that the nucleation, growth, and evolution of shape and size of α-$NaYF_4$:Yb,Er nanocrystals seem to follow a cycle that is shown in Figure 2.14a. This cycle has three parts in which after early nucleation of the cubic α-phase,

the size of nanocrystals is about 4-6 nm with more spherical shape (NPs cubic 1). These nanocrystals grow with the coalescence process beside Ostwald ripening and undergo a rearrangement of atoms followed by the formation of irregular shape α-$NaYF_4$:Yb,Er nanocrystals (increase surface area) with a size around 8-9 nm (NPs cubic 2). Then some nanocrystals dissolve into monomers under the instabilities as mentioned earlier. These monomers with a low concentration (below critical concentration for β-nucleation) will start the cycle again. However, if the number of these NPs cubic 2 increase, the concentration of monomers will increase also. Note that the number of irregular shapes α-$NaYF_4$:Yb,Er nanocrystals with critical size can be influenced by the heating system employed as emphasized above. In the flasks compared to the microtube, formation of irregular shape α-$NaYF_4$:Yb,Er nanocrystals as a metastable form of cubic α-phase could be more likely to occur by the coalescence process due to higher temperature gradients, normal pressure and effective collision. As a result, the number of this type of cubic nanocrystals in the flasks can be increase and subsequently after their dissolution the concentration of monomers will also increased till reaching the critical concentration required for the formation of the β-phase. From that point, the shape of the final β-nanocrystals will depend upon the system used for the post-heat treatment. Indeed, our results confirmed that rod-like crystals are observed with the microtube while spherical ones are produced with the flasks. One reason for this might be the rate of dissolution of the α-phase nanocrystals. In fact, for the flasks, it is expected to be faster compared to the microtube according to our results. This situation leads to the production of a large among of monomers that will induce the growth of the β-nanocrystals into a spherical shape. However, for the microtube, the dissolution is slower. Thus the resulting low concentration of monomers will induce the growth of the β-nanocrystals into an anisotropic shape (rod-like in our case) as discussed by Yin and Alivisatos [441] and Wang *et al.* [444].

In an attempt to summarize the above discussion, a free energy diagram for the formation of cubic α-phase and hexagonal β-phase is presented in Figure 2.14b. The growth of NPs cubic 1 by coalescence and Ostwald ripening then rearrangement to less stable anisotropic shape α-phase nanocrystals can reduce the phase transfer energy barrier, hence favoring the formation of the hexagonal β-phase. Indeed the rod-like nanocrystals, as anisotropic

nanocrystals with a surface to the volume being greater than that of the spherical nanocrystals, will be thermodynamically less stable [441].

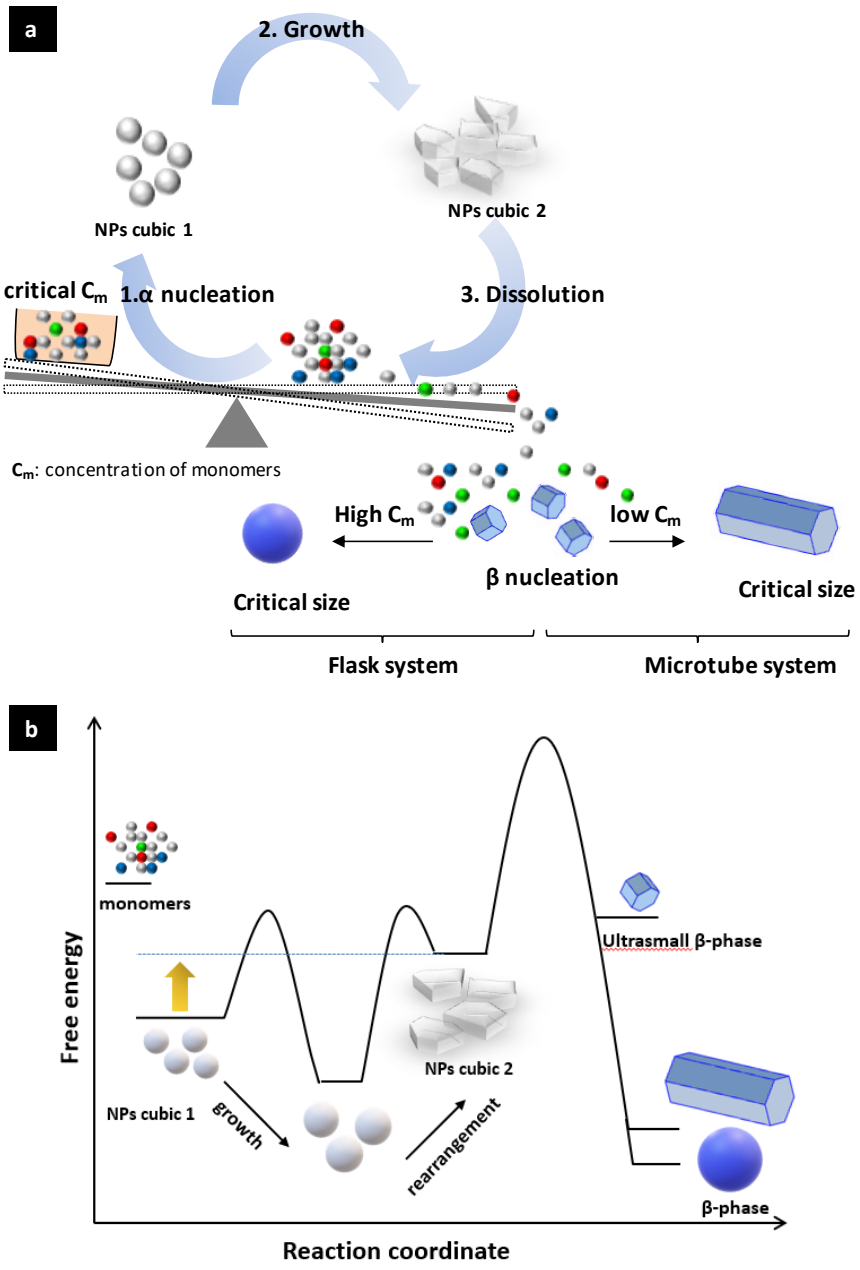

Figure 2.14. Schematic illustration of the size and morphology evolution of α-$NaYF_4$ nanocrystals and supply of monomers with different concentrations in flask and microtube systems (a); free energy diagram as a function of the reaction coordinate for the formation of cubic α-phase (NPs cubic 1 and 2) and hexagonal β-phases of nanorods and spherical nanocrystals (b).

2.5. Upconversion luminescence of β-$NaYF_4$:Yb,Er nanocrystals

Luminescence properties of β-$NaYF_4$:Yb,Er were investigated under 980 nm diode laser excitation as shown in Figure 2.15b. The strong emission peak at 650 nm related to the electronic transition from the $^4F_{9/2}$ level to the $^4I_{15/2}$ level of the Er^{3+} ions and the green emission peaks at 520 nm and 540 nm were characteristic of upconversion luminescence expected from the Er^{3+} ions electronic transitions $^2H_{11/2}$ and $^4S_{3/2}$ levels to the $^4I_{15/2}$ state respectively. Furthermore, emission peak at 410 nm is attributed to the electronic transitions from the $^2H_{9/2}$ levels to $^4I_{15/2}$ state. All of β-$NaYF_4$:Yb,Er revealed an intense green light with 40 mg/ml in cyclohexane under 980 nm laser excitation with power density 200 mW (the photos not shown).

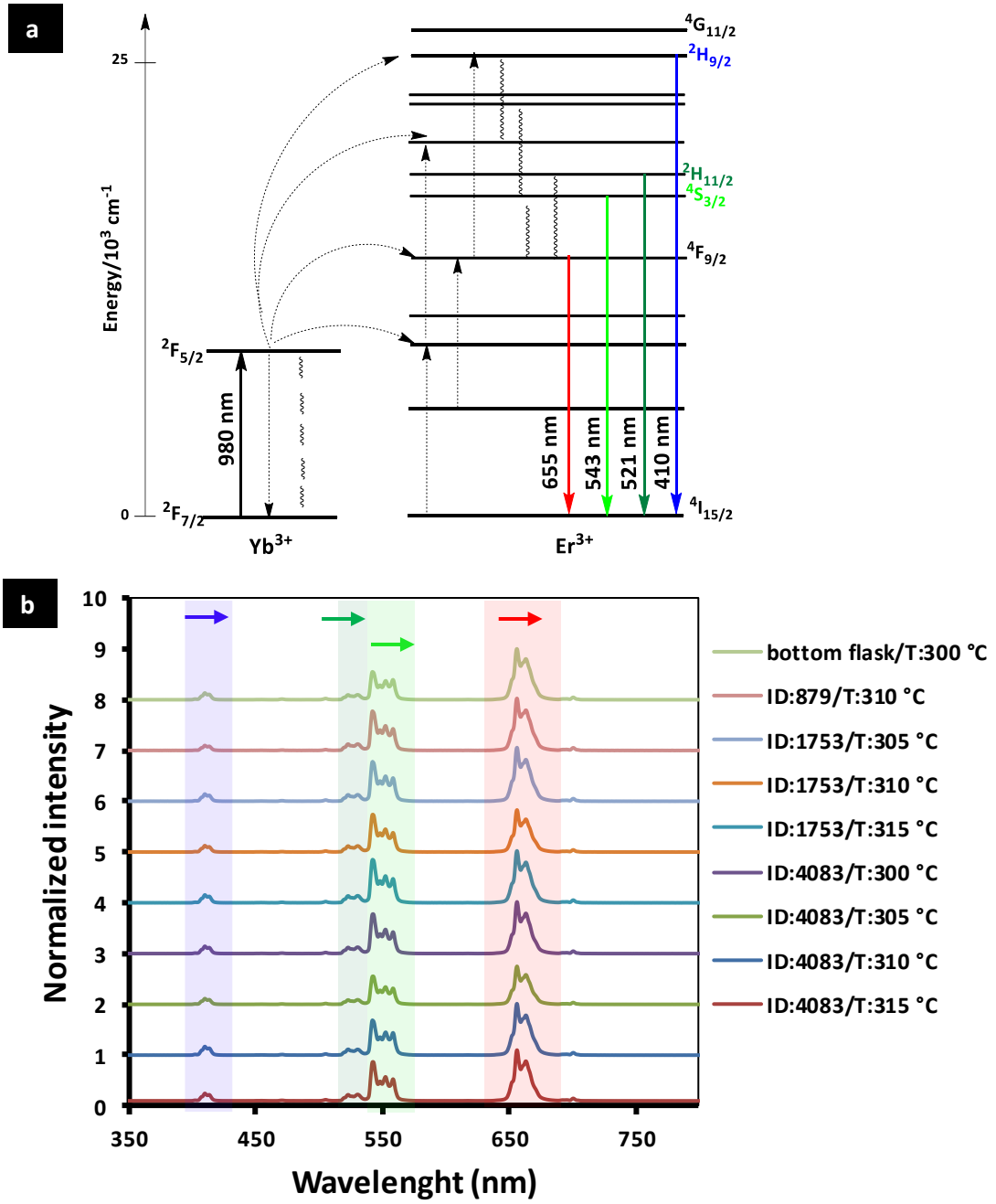

Figure 2.15. Proposed energy-transfer mechanisms in the $NaYF_4$:Yb,Er nanocrystal (dashed arrows represent energy transfer and the solid arrows represent photon excitation and emission processes) (a). Normalized upconversion luminescence spectra of prepared β-$NaYF_4$:Yb,Er nanocrystals at various conditions under the excitation of 980 nm NIR light (b).

3. Conclusion

The size, crystalline phase and shape of $NaYF_4$:Yb,Er nanocrystals, synthesized by the co-precipitation method followed by a heat treatment at high temperature (above 300 °C),

proved to be highly dependent on the type of reactor used for the heat treatment. Thus, at a given temperature, the phase transition between the α-cubic and β-hexagonal phases was much faster for reactors characterized by high temperature gradients, like in an Erlenmeyer flask, than for low temperature gradients reactors as the round-bottom flask or microtubes. Given the slow growth of β-$NaYF_4$:Yb,Er nanocrystals in microtubes, we could detect two populations of nanocrystals with cubic α-phase before phase transition. We thus observed for the very first time that α-$NaYF_4$:Yb,Er nanocrystals passed through an anisotropic metastable intermediate by a coalescence mechanism, similar to the so-called oriented attachment, before to rearrange and dissolve to give rise to the β-$NaYF_4$:Yb,Er nanocrystals by Ostwald ripening phenomenon. Delay in phase transition for the microtubes could also be attributed to the building pressure inside, low collision possibility of nanocrystals and homogeneous heating which hindered the coalescence. We also found that in the microtubular reactors the β-$NaYF_4$:Yb,Er nanocrystals grow in an anisotropic hexagonal shape (nanorods) conversely to the flask system for which only spherical nanocrystals were produced. The length of the nanorods could be changed with the heating temperature and diameter of microtube while the width remained pretty much constant. In perspective, microtubes could be considered for β-$NaYF_4$:Yb,Er nanocrystals production scale-up and used to investigate the phase transition of other formulations.

CHAPTER 3: Investigating the growth of hyperbranched polymers by self-condensing vinyl RAFT copolymerization from the surface of upconversion nanoparticles

1. Introduction

Hybrid materials are attractive to respond to the increasing demand for novel materials with well-defined properties. The preparation of hybrid materials based on polymers and inorganic nanoparticles has been investigated notably by encapsulation of inorganic nanoparticles in polymer particles and attachment of polymers at the surface of inorganic nanoparticles [445]. In the latter case, the two main methods are the "grafting to" consisting in the reaction between orthogonal functional groups present on the polymer and at the surface of the nanoparticles and "grafting from" involving the polymerization of monomers from the surface of the nanoparticles. A wide range of inorganic nanoparticles [446] have been used to grow polymers from their surface using different polymerization techniques such as cationic [447,448], anionic [449,450], and radical [451–453] polymerizations. These hybrid materials provide access to the compatibilisation of inorganic particles in polymer matrices [454], and enhancement of the nanoparticles stealthiness for biomedical applications [455].

Self-condensing vinyl polymerization (SCVP) was first introduced by the group of Fréchet [86] consisting in using a vinyl (co)monomer possessing an initiating or chain transfer agent (inimer or transmer respectively) on its side chain to create branching points. The degree of branching (DB) can be tuned by changing the ratio between monomer and inimer/transmer. SCVP has been investigated through the three main controlled radical polymerization techniques [416,456], *i.e.* nitroxide-mediated polymerization, atom transfer radical polymerization (ATRP), and reversible addition-fragmentation chain transfer (RAFT) polymerization. The use of SCVP to grow hyperbranched polymers (HBPs) on nanoparticles has been mostly performed using ATRP from silica [80], and ZnO [457] nanoparticles [458]. Herein we report the growth of HBPs prepared by SCVP under RAFT conditions from the surface of UCNPs. To the best of our knowledge SCVP under RAFT conditions has not been attempted on nanoparticles. The surface of UCNPs was modified by silanization to introduce functional groups permitting to covalently attach the anchoring groups that will promote the polymerization. Various approaches have been reported in the literature to functionalize the surface to conduct surface-initiated RAFT polymerization including anchoring the initiator or chain transfer agent (Z-C(=S)S-R) through its R- or Z-group to the surface with a strong preference for the anchoring of the chain transfer agent through its R group [416] that was adopted here. SCVP was investigated varying the grafting density in chain transfer agent at

the surface of UCNPs and the ratio of transmer to monomer and comparing to the results to those for the preparation of linear polymers.

2. Results and discussion

2.1. Preparation of UCNPs with a well-defined density of RAFT chain transfer agents at their surface

Monodispersed spherical β-$NaYF_4$:Yb^{+3}, Er^{+3} nanocrystals (UCNP@OA) with a diameter of 27.8 ± 0.5 nm were prepared by co-precipitation method using oleic acid as capping agent according to the protocol described by Li *et al* [343]. and characterized by high-resolution transmission electron microscopy (HR-TEM, Figure 3.1), dynamic light scattering (DLS, Figure 3.2), X-ray diffraction (Figure 3.3) and luminescence measurements (Figure 3.4). HR-TEM (Figure 3.1) showed monodispersed spherical UCNPs with lattice fringes of 0.52 nm for single-crystalline of β-$NaYF_4$ nanocrystal. The crystalline structure was confirmed by X-ray diffraction showing diffraction peaks that can be assigned to lattice planes (110), (101), (200), (111), (201), (210), (002), (300), (211), (102), (112), (220) and (202) of β-$NaYF_4$ with a hexagonal phase without any impurity (*e.g.* cubic phase nanocrystals) in good agreement with the standard XRD pattern of β-$NaYF_4$ (JCPDS no. 16-0334) [343]. $NaYF_4$:Yb^{3+}, Er^{3+} UCNPs excited at 980 nm using a diode laser led to an intense green light and the spectrum revealed its expected characteristic peaks at 410, 526, 542 and 654 nm corresponding to $^4H_{9/2}$,$^4H_{11/2}$, $^4S_{3/2}$, and $^4F_{9/2}$ to $^4I_{15/2}$ transitions of Er^{3+} respectively.

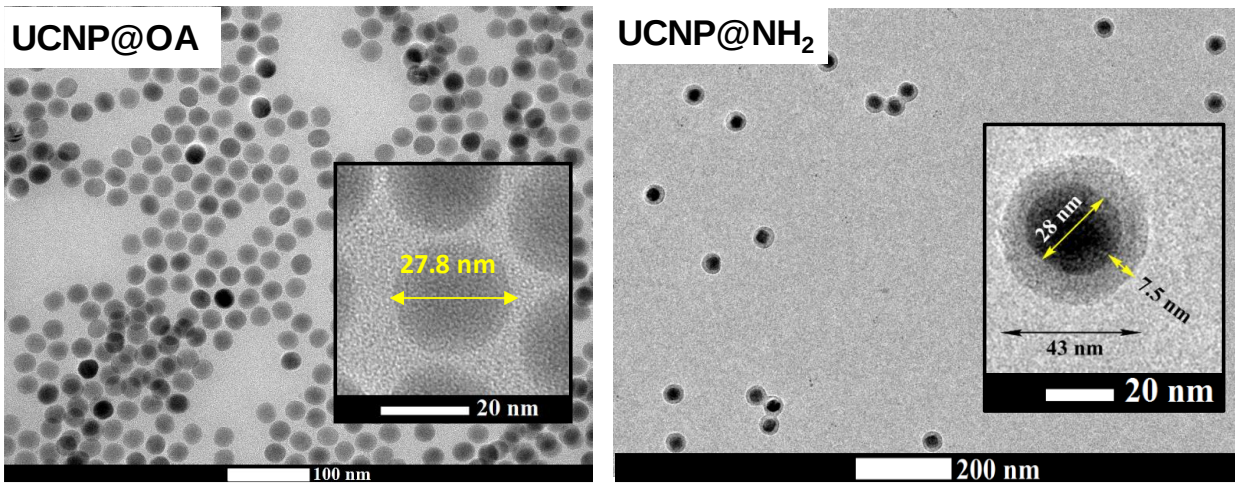

Figure 3.1. HR-TEM images of UCNP@OA and UCNP@NH_2 (zoom on a single nanoparticle in inset).

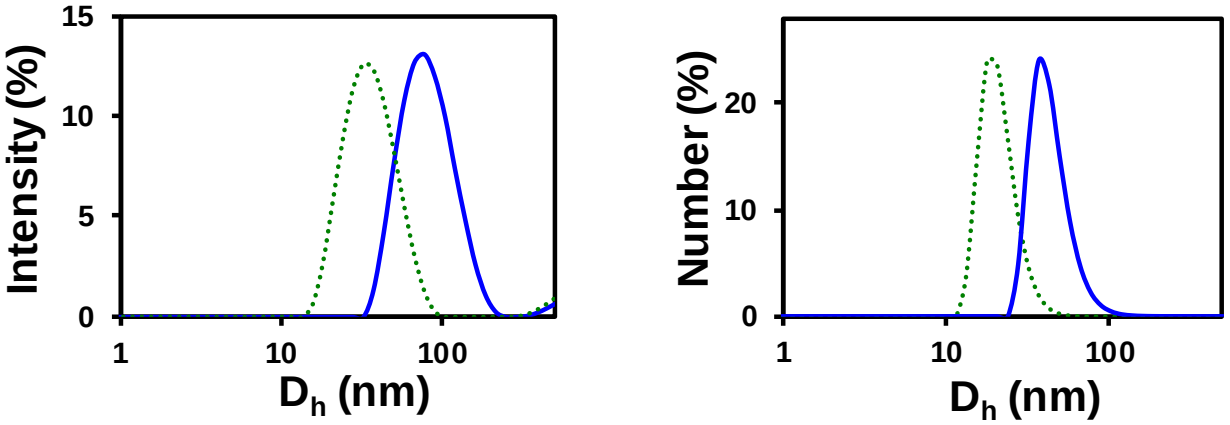

UCNPs	DLS in number		DLS in intensity	
	D_h (nm)	PDI	D_h (nm)	PDI
UCNP@OA	22	0.32	39	0.30
UCNP@NH_2	45	0.24	87	0.29

Figure 3.2. DLS measurements in intensity and number of UCNP@OA dispersed in cyclohexane (dashed green line) and UCNP@NH_2 dispersed in ethanol (full blue line).

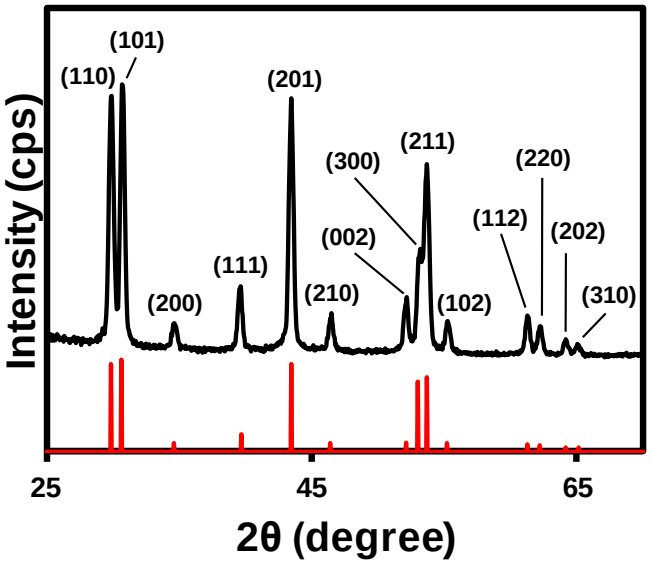

Figure 3.3. X-ray diffractogram of the synthesized UCNP@OA in black) and the standard pattern of β-$NaYF_4$ (JCPDS 06-0334) in red.

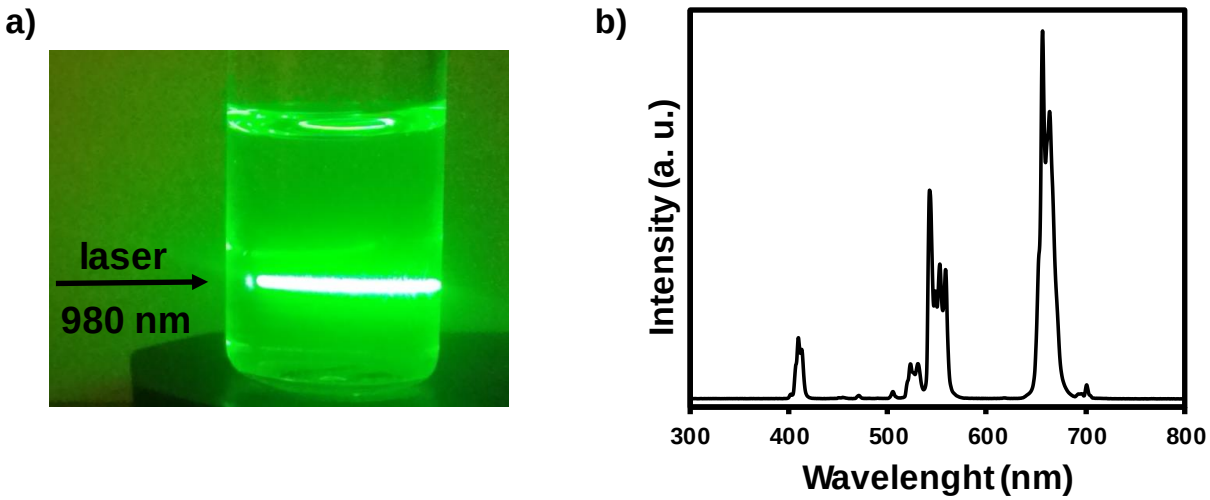

Figure 3.4. Upconversion emission of UCNP@OA solution in cyclohexane excited at 980 nm: (a) image and (b) spectrum.

The surface of UCNP@OA was modified to create a silica shell possessing amine groups at their surface (UCNP@NH_2) by reverse microemulsion technique [388] through the successive condensation of tetraethylorthosilicate and (3-aminopropyl)triethoxysilane (APTS). The formation of the silica shell was confirmed by HR-TEM showing a silica shell of 7.5 nm around the UCNPs (Figure 3.1), DLS showing monomodal peaks without aggregates with an increase in hydrodynamic diameter (D_h) from 22 to 45 nm (values in number, Figure 3.2), and Fourier-transform infrared (FT-IR, Figure 3.5a) spectroscopy exhibiting the characteristic stretching peak of -Si-O-Si- groups at 1062 cm^{-1}. The presence of amine groups on the nanoparticles was identified at 1650 cm^{-1} (NH in-plane stretching) and 3420 cm^{-1} (NH_2) on the FT-IR spectrum. Furthermore, the presence of primary amines was confirmed by the colorimetric Kaiser test [459] (Figure 3.5b): one droplet of UCNP@NH_2 suspension in ethanol showed an intense blue color. The surface area of UCNP@NH_2 was determined by establishing the nitrogen adsorption/desorption isotherms according to the Brunauer-Emmet-Teller theory (Figure 3.6) and resulted in a value of 45.44 ± 0.15 $m^2 \cdot g^{-1}$ (considering 30 mg of UCNP@NH_2, the surface area could be estimated to 1.4 m^2). These nanoparticles dispersible in water, ethanol, acetone, and DMF were prepared with different amounts of APTS (*i.e.* 38, 76, and 152 μmol of APTS for 80 mg of UCNP@OA) to vary the grafting density of amine groups present at the surface of UCNPs.

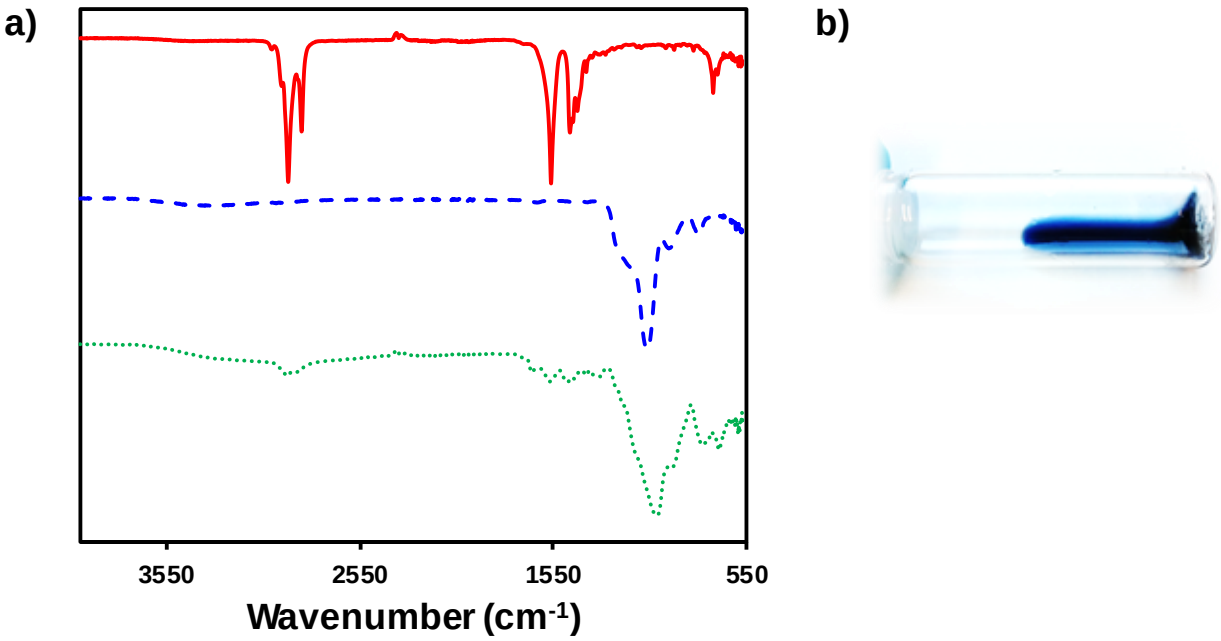

Figure 3.5. Identification of the amino groups at the surface of UCNPs: (a) IR spectra of UCNP@OA (solid red line), UCNP@SiO_2 (blue dashed line), and UCNP@NH_2 (green dotted line) and (b) Kaiser test of UCNP@NH_2.

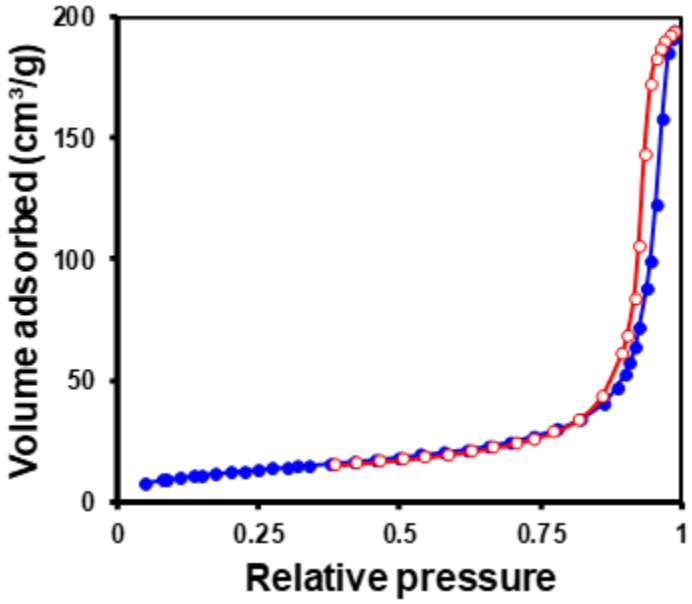

Figure 3.6. N_2 isotherms of adsorption (filled blue symbols) and desorption (open red symbols) for UCNP@NH_2 at standard temperature and pressure.

A carboxylic acid-terminated RAFT chain transfer agent suitable for the polymerization of methacrylates, 4-cyano-4-(thiobenzoylthio)pentanoic acid (CPABD), was coupled to the amine groups present at the surface of UCNPs using as coupling agent *N*,*N*,*N'*,*N'*-tetramethyl-*O*-(1H-benzotriazol-1-yl)uronium hexafluorophosphate in the presence of 1-hydroxybenzotriazole hydrate and diisopropylethylamine in DMF (Scheme 3.1). The color

of the UCNPs changed from white to red corresponding to the color of CPABD (Figure 3.7c). UCNP@CPABD were characterized by FT-IR spectroscopy (Figure 3.7a) showing the characteristic stretching absorption band of nitrile groups at 2160 cm^{-1} and UV-vis spectroscopy as a suspension in ethanol exhibiting the strong absorption of the thiocarbonyl group at 315 nm (Figure 3.7b) confirming the presence of CPABD at the surface of UCNPs [460]. The grafting density in CPABD attached to UCNPs was determined by TGA[419,461] (Figure 3.8) as 0.6, 1.4 and 3.1 CPABD per square nanometer of UCNPs ($UCNP@CPABD_{low}$, $UCNP@CPABD_{medium}$, $UCNP@CPABD_{high}$ respectively, Table 3.1).

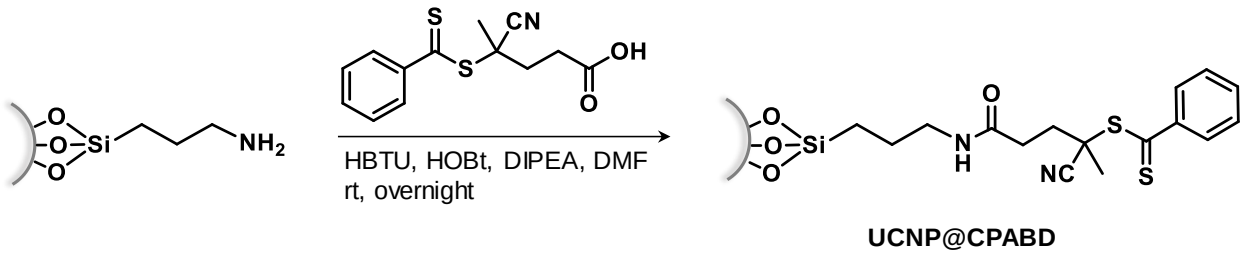

Scheme 3.1. Synthesis of UCNP@CPABD.

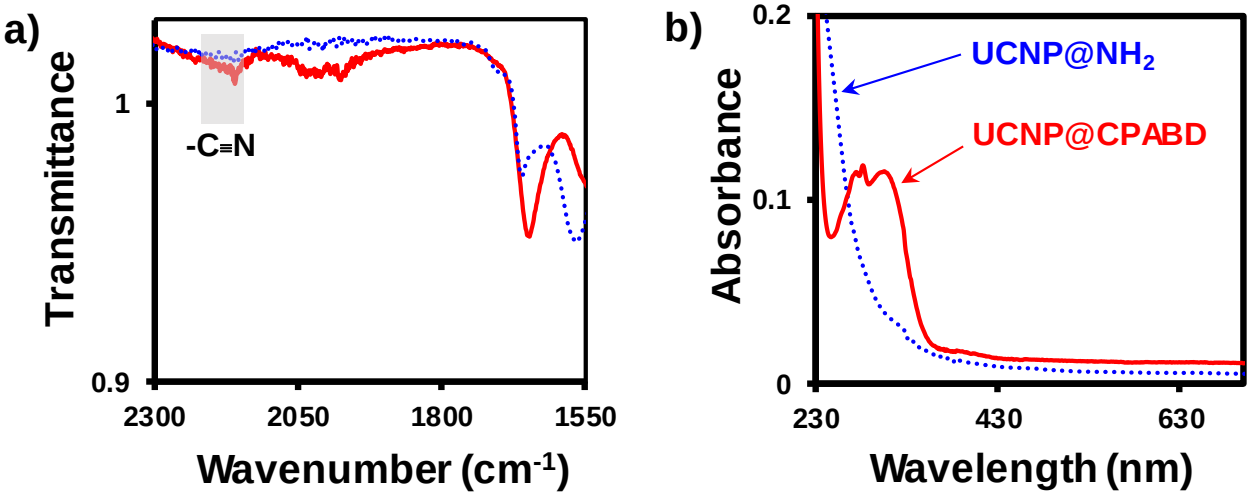

c)

Figure 3.7. Characterization of UCNP@CPABD by (a) FT-IR, and (b) UV-vis spectroscopies, along with the (c) observation of the color change of the UCNP powders (from left to right: UCNP@NH_2, UCNP@$CPABD_{low}$, UCNP@$CPABD_{medium}$, UCNP@$CPABD_{high}$).

Table 3.1. Quantification of CPABD grafting density on UCNPs by TGA

Samples	APTS (µL)	%wt	mmol of CPABD/g UCNP	Grafting density (CPABD/nm^2)
UCNP@CPABD$_{low}$	7.5	1.2	0.044	0.60
UCNP@CPABD$_{medium}$	15	2.6	0.094	1.41
UCNP@CPABD$_{high}$	30	6.8	0.240	3.13

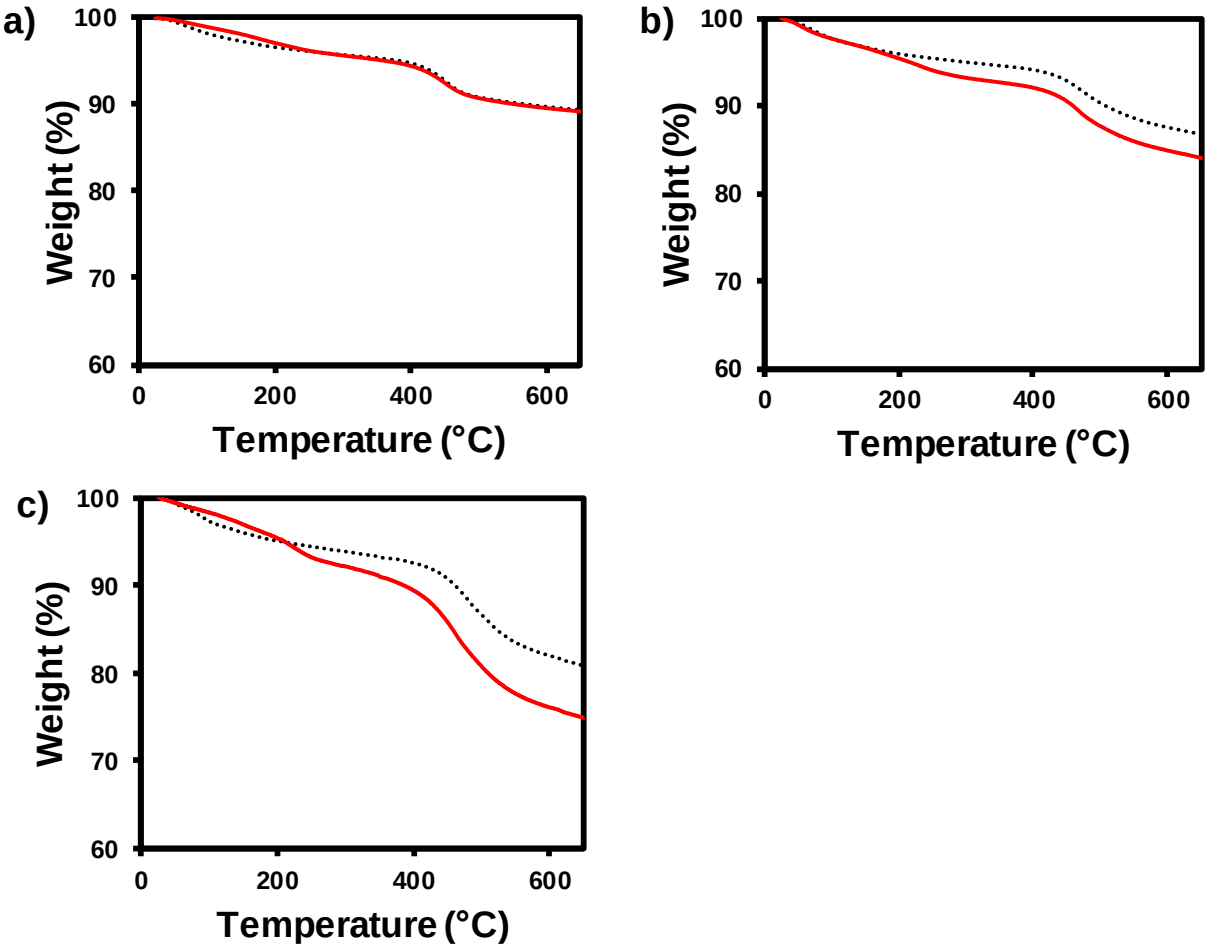

Figure 3.8. TGA thermograms of (a) UCNP@CPABD$_{low}$, (b) UCNP@CPABD$_{medium}$, and (c) UCNP@CPABD$_{high}$ (solid red line) compared to UCNP@NH_2 (black dotted line) prepared with 7.5, 15 and 30 µL of APTS respectively for 80 mg of UCNP@OA.

2.2. Polymerization of *N*-(2-hydroxypropyl) methacrylamide from the surface of UCNP@CPABD

Poly(*N*-(2-hydroxypropyl) methacrylamide) is commonly used to prepare drug conjugates [462,463], which led our choice to *N*-(2-hydroxypropyl methacrylamide) (HPMA) as monomer for this study. The nature of the solvent is detrimental especially since the polymerization was performed at the surface of UCNPs. Various reports highlight the effects of surface confinement and diffusion of monomers towards the propagating chains grafted on a surface emphasizing the importance of the solvent quality to perform a surface-initiated controlled radical polymerization [464,465]. Linear poly(*N*-(2-hydroxypropyl) methacrylamide) (polyHPMA) was first prepared from the surface of UCNP@CPABD investigating DMF, 1,4-dioxane, and MeOH as solvent for the polymerization (Scheme 3.2). The polymerization of HPMA from UCNP@CPABD was conducted in an oil bath thermostated at 65 °C fixing the concentration in nanoparticles to 10 $mg \cdot mL^{-1}$ and the monomer concentration to 0.57 M using a molar ratio between HMPA, CPABD and initiator (azobisisobutyronitrile, AIBN) of 200:1:0.2. HPMA conversion was determined by ^{1}H NMR spectroscopy by comparing the integrations of the vinylic proton at 5.7 ppm to the methyl protons of the polymer backbone at 0.5-1.1 ppm. The polymerization of HPMA seemed more suitable when conducted in 1,4-dioxane rather than in MeOH and DMF as HPMA conversion after 21 h of polymerization from UCNP@$CPABD_{high}$ reached 18% in 1,4-dioxane compared to 7% in DMF and MeOH, while TGA indicated a content in polyHPMA of 25 and 6 wt% using UCNP@$CPABD_{high}$ and UCNP@$CPABD_{low}$ respectively for the polymerization in 1,4-dioxane and almost no polymer formation on UCNPs for the polymerizations in DMF and MeOH (Figure 3.9).

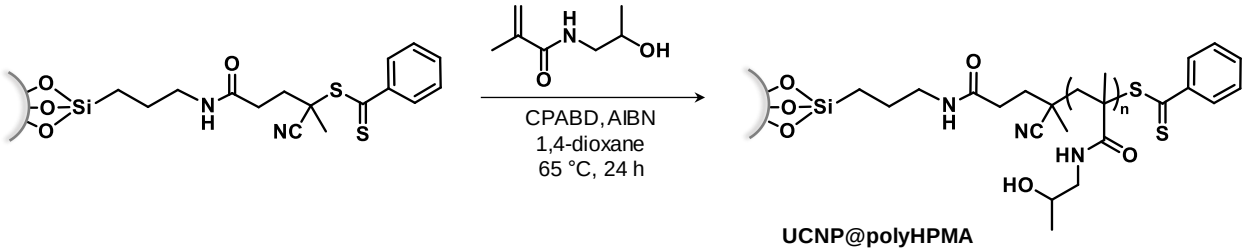

Scheme 3.2. Synthesis of linear polymer from the surface of UCNPs (UCNP@polyHMPA).

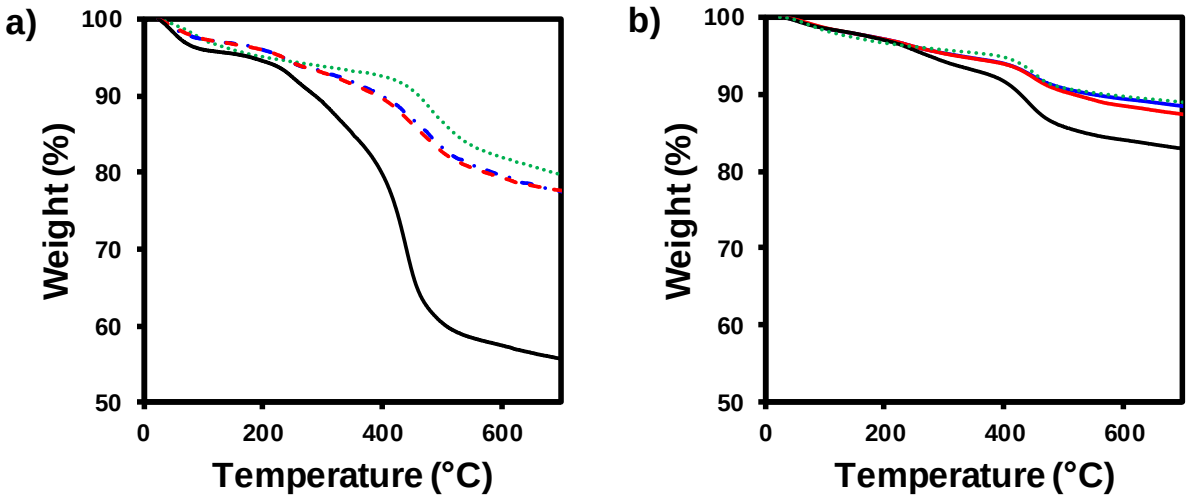

Figure 3.9. TGA thermograms of UCNP@polyHPMA for polymerizations conducted in MeOH (blue dashed line), DMF (red dashed line) and 1,4-dioxane (black solid line) using (a) UCNP@CPABD$_{high}$ and (b) UCNP@CPABD$_{low}$ relative to UCNP@CPABD (green dotted line).

2.3. Self-condensing vinyl copolymerization from the surface of UCNP@CPABD

HBPs grafted on UCNPs were prepared by self-condensing vinyl copolymerization of HPMA with a methacrylate-based transmer bearing CPABD, 2-(methacryloyloxy)ethyl-4-cyano-4-((phenylcarbonothioyl)thio)pentanoate[466] (MA-CPABD) inducing the formation of branching points (Scheme 3.3). The polymerization was conducted in 1,4-dioxane in an oil bath thermostated at 65 °C for 24 h using UCNP@CPABD$_{high}$ (10 mg·mL^{-1}), HPMA (0.56 mM) and a molar ratio between HMPA, MA-CPABD and AIBN of 200:1:0.2. The consumption of MA-CPABD to form the HBP was observed by the decrease in the pink color of the polymerization solution (Figure 3.10a, photo in insert) and reached a monomer conversion of 18% determined gravimetrically (compared to 21% for the preparation of polyHPMA under the same conditions). After cleavage of the polymer from the surface of UCNPs by treatment with HF, its number-average molecular weight was determined by size-exclusion chromatography (SEC) as 220 kg·mol^{-1} with a dispersity (Đ) of 6.75 as compared to 1794 kg·mol^{-1} and 3.15 respectively for polyHMPA. As the same ratio of UCNP@CPABD$_{high}$ and HPMA were used in both cases, it would have been expected that similar molecular weights would have been observed. However, the HBP had a lower molecular weight and higher dispersity, which could be attributed to the mechanism of RAFT polymerization from a surface and the increased steric hindrance due to the synthesis of HBP on a surface.

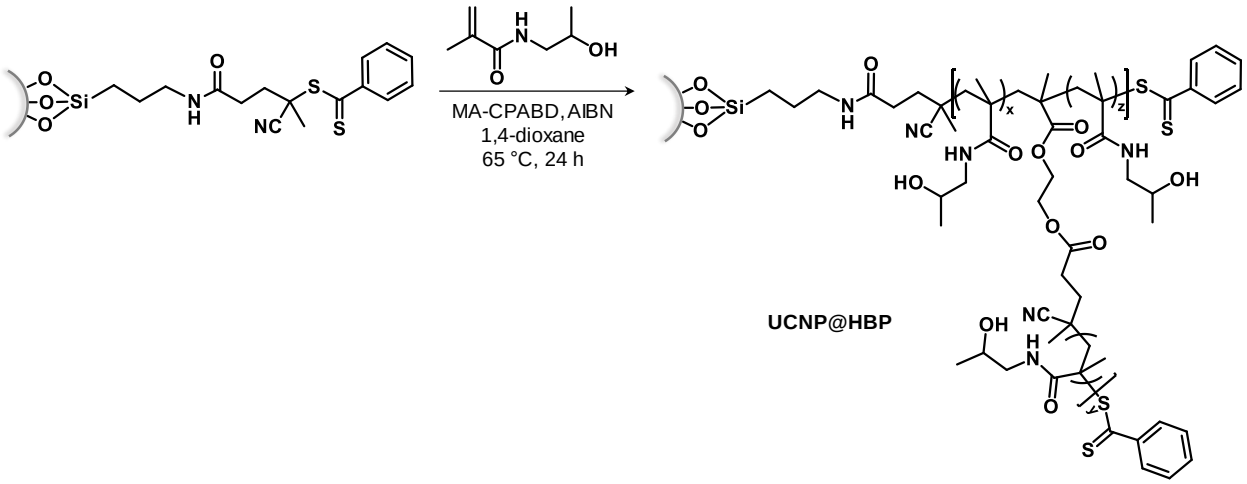

Scheme 3.3. Synthesis of hyperbranched polymers from the surface of UCNPs (UNCP@HBP).

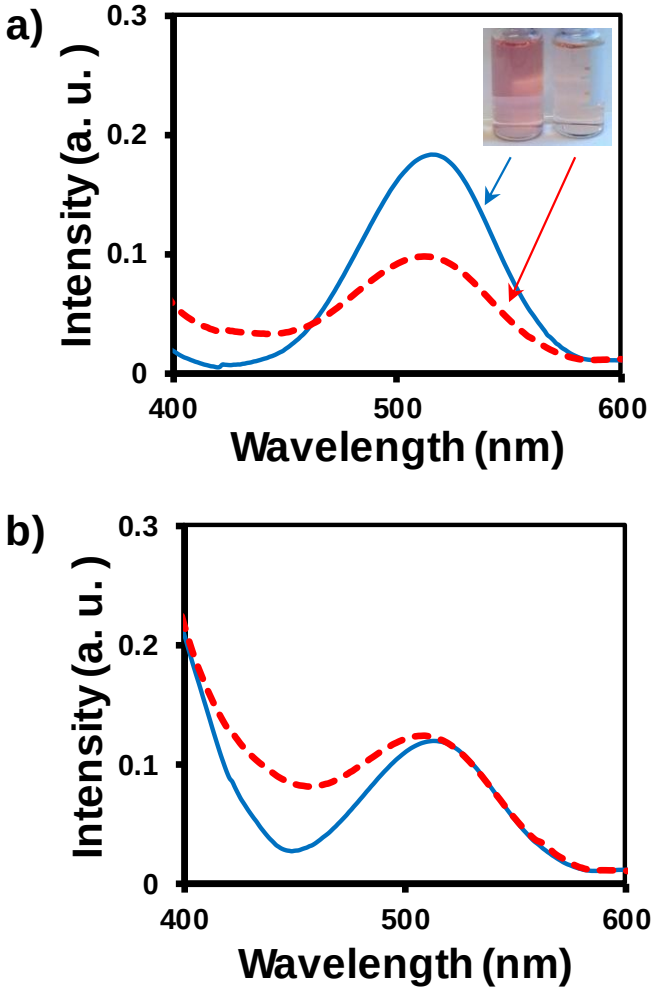

Figure 3.10. UV-spectra of decanted solution after 24 h of polymerization (red dashed line) and control solution (blue solid line) using UCNP@CPABD$_{high}$ (10 mg·mL^{-1}) for the preparation of (a) HBP with HPMA:MA-CPABD:AIBN = 200:1:0.2 (in insert a photo of the control solution and the polymerization solution after 24 h) and (b) linear polymer with HPMA:CPABD:AIBN = 200:1:0.2.

If the polymerization was living, all the terminal points of the HBP should possess a CPABD group and the number of CPABD groups should be correlated to the number of branching points (*i.e.* for n CPABD terminal groups, the HBP would have (n-1) branching points). Due to i) the steric hindrance induced by the presence of polymer chains on UCNPs hindering the access to all CPABD, ii) the necessity of the monomer to diffuse towards the active centers present at the surface of UCNPs, and iii) the transfer of CPABD between active and dormant chains that are in close proximity, the number of branching points may be underestimated by considering the amount of CPABD. However, it is not possible to determine directly the number of branching points. The determination of the amount of CPABD incorporated in the HBP grafted on UCNPs (UCNP@HBP) was first attempted by ^{1}H NMR spectroscopy on the cleaved HBPs. However, the characteristic peaks of the branching points and the terminal CPABD groups were difficult to identify due to their low content on the HBP and the potential hydrolysis of the thioester groups during the cleavage of the HBPs from the surface of UCNPs with HF. Thiocarbonyl end groups show $\pi \rightarrow \pi^*$ and $n \rightarrow \pi^*$ absorption bands in the UV and visible range respectively (300 and 515 nm for CPABD).[467] As the direct quantification of CPABD groups present on UCNP@HBP by UV-vis spectroscopy could not be achieved due to the scattering interference of UCNP@polymer, the number of CPABD groups in the supernatant after 24 h of polymerization was determined using this technique and compared to a control solution consisting in the same initial concentration of CPABD in MeOH (*i.e.* 3 mM). The intensity of the absorption at 515 nm decreased (Figure 3.10) associated to the consumption of MA-CPABD corresponding to 140 µmol of MA-CPABD incorporated on the grafted HBP per gram of UCNPs and thus the formation of branching points on the polymer. To confirm our observation, the same experiment was conducted for the synthesis of a linear polymer on UCNPs indicating a constant concentration in CPABD and confirming also the stability of the RAFT chain transfer under the polymerization conditions used. The number of micromoles of CPABD on UCNP@HBP per gram of UCNP (m), the number of branching points per polymer chains assuming a constant branching length,[468] the degree of branching (DB), and the grafting density (number of polymer chains per nm^2 of UCNP, σ) were estimated using Equations 1, 2, 3 and 4 [36,469] respectively as 140, 122, 0.17, and 0.014 chain per nm^2 using UCNP@CPABD$_{high}$.

$$m = \frac{\left[n_0 - n_s\left(n_{control} \times \frac{A2}{A1}\right)\right]}{m_{UCNP}}$$

Equation 1

where m is the molality of CPABD for UCNP@HBP (*i.e.* number of moles of CPABD on UCNP@HBP per gram of UCNP), n_0 and n_s the number of moles of MA-CPABD in solution at t = 0 and 24 h respectively, $n_{control}$ the number of moles of CPABD in the control experiment, A_1 and A_2 the absorbance of MA-CPABD for the control solution and supernatant after polymerization respectively, and m_{UCNP} the mass of UCNP used.

$$\text{branching point per chain} = \frac{M_n}{\frac{n_1}{n_2} \times M}$$

Equation 2

where M_n is the number-average molecular weight of the polymer grafted on UCNPs determined by SEC, n_1 the number of moles of HPMA per gram of UCNPs calculated from TGA, n_2 the number of moles of MA-CPABD per gram of UCNPs calculated from UV-Vis spectroscopy and M the molecular weight of HPMA as repeating unit (143.1 g·mol^{-1}).

$$\mathbf{DB} = \frac{\mathbf{2D}}{\mathbf{2D+L}}$$

Equation 3

where D is the total number of branching units derived from MA-CPABD, and L the total number of linear repeat units derived from HPMA consumption. The factor of 2 in Equation 3 is related to the fact that each branching unit induces the formation of two active centers and thus two branches [470,471]. The value for D was determined by UV-vis spectroscopy considering the absorbance at 515 nm corresponding to the thiocarbonyl group of MA-CPABD (based on its number of moles per gram of UCNPs), while L was calculated from TGA measurement (based on its number of moles of HPMA per gram of UCNPs).

$$\sigma = \frac{(w/M_{n,UCNP}) \times N_a}{m_{UCNP} \times S_{UCNP}}$$

Equation 4

where w is the weight loss determined by TGA measurement, $M_{n,UCNP}$ the number-average molecular weight of the polymer grafted on UCNP determined by SEC analysis, N_a the Avogadro number, m_{UCNP} the weight of UCNP and S_{UCNP} the specific surface area of UCNP calculated by BET analysis.

DLS characterization of UCNP@HBP indicated a D_h of 141 nm (PDI = 0.087) corresponding to a polymer corona of 27 nm considering the D_h of UCNP@NH_2 of 87 nm. UCNP@polyHPMA

exhibited a larger polymer corona of 82 nm (D_h = 251 nm, PDI = 0.258, Figure 3.11) that could be associated to the higher molecular weight observed for this system as compared to the hyperbranched one. TGA revealed a lower content in polymer when preparing HBP from the surface of UCNPs as compared to the linear ones (Figure 3.12) with an estimation of 1.4 and 3.4 mmol of HPMA units per gram of UCNPs for the HBP and linear polymer respectively.

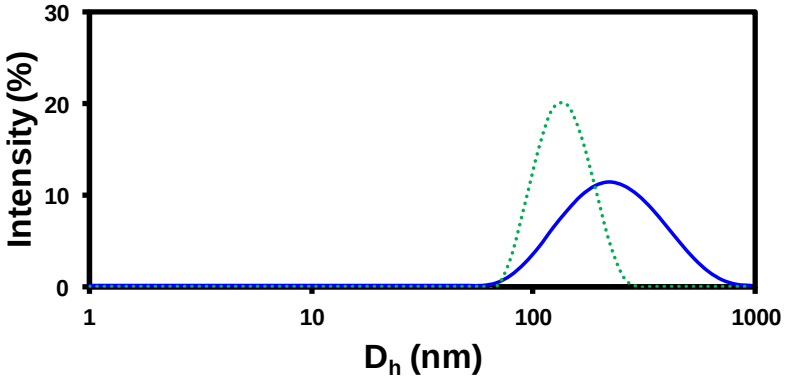

Figure 3.11. DLS in intensity of UCNP@polyHMPA (blue solid line) and UCNP@HBP (green dotted line) obtained from UCNP@CPABD$_{high}$.

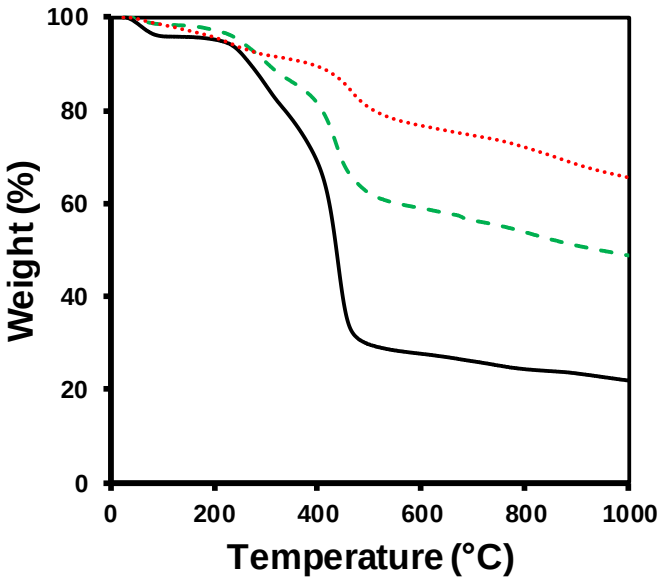

UCNPs	Char (wt%)	Polymer content in nanohybrid (wt%)
UCNP@CPABD	75	0
UCNP@polyHPMA	22	53
UCNP@HBP	49	26

Figure 3.12. TGA of UCNP@CPABD (red dotted line), UCNP@polyHPMA (black solid line), and UCNP@HBP (green dashed line). The polymers were prepared from UCNP@CPABD$_{high}$ using 3 mM of CPABD and MA-CPABD for the linear and hyperbranched polymers respectively.

2.4. Effect of the grafting density in CPABD on UCNPs

The results from SEC and TGA measurements both suggested that the growth of HBPs from UCNPs under these conditions were hindered as compared to linear polymers. The migration of chain transfer agents when performing surface-initiated RAFT polymerization to obtain linear polymers has been reported leading to chain-breaking reactions such as termination and transfer reactions [472–474]. Furthermore, the synthesis of hyperbranched structures induces steric hindrance that can affect the proper propagation of the polymer chains and thus enhance the propensity of chain-breaking reactions especially as the concentration in CPABD at the surface of UCNPs is locally high. The grafting density in CPABD on UCNPs was therefore investigated considering the self-condensing vinyl copolymerization from UCNP@CPABD$_{medium}$ and UCNP@CPABD$_{low}$ in the presence of 3 mM of MA-CPABD. According to UV-vis spectroscopy, the number of branching points incorporated on the HBP grafted on UCNPs was 140, 90 and 34 µmol per gram of UCNP@HBP for HBP prepared from UCNP@CPABD$_{high}$, UCNP@CPABD$_{medium}$ and UCNP@CPABD$_{low}$ respectively. TGA of UCNP@HBP (Figure 3.13) indicated that the weight percentage of polymer grafted on UCNP from UCNP@CPABD$_{medium}$ was two times higher than for the nanohybrids obtained from UCNP@CPABD$_{high}$ indicating a higher consumption of HMPA and thus a lower DB (*i.e.* 0.14 and 0.05 for the HBP obtained from UCNP@CPABD$_{high}$ and UCNP@CPABD$_{medium}$ respectively). The chain-breaking reactions seemed less pronounced with the decrease of the grafting density in CPABD affording a higher conversion of HMPA. The number of branching points per HBP chains was determined as 410 and 6 for UCNP@CPABD$_{medium}$ and UCNP@CPABD$_{low}$ respectively as compared to 122 for UCNP@CPABD$_{high}$. The calculation of σ revealed that UCNP@CPABD$_{high}$ and UCNP@CPABD$_{medium}$ had very low grafting densities estimated as 0.014 and 0.003 chain per nm^2 respectively, while the one of UCNP@CPABD$_{low}$ was higher (0.06 chain per nm^2). These results suggested that transfer reactions for UCNP@CPABD$_{high}$ and UCNP@CPABD$_{medium}$ were more pronounced at the surface of UCNPs leading to a higher proportion of dead chains [473].

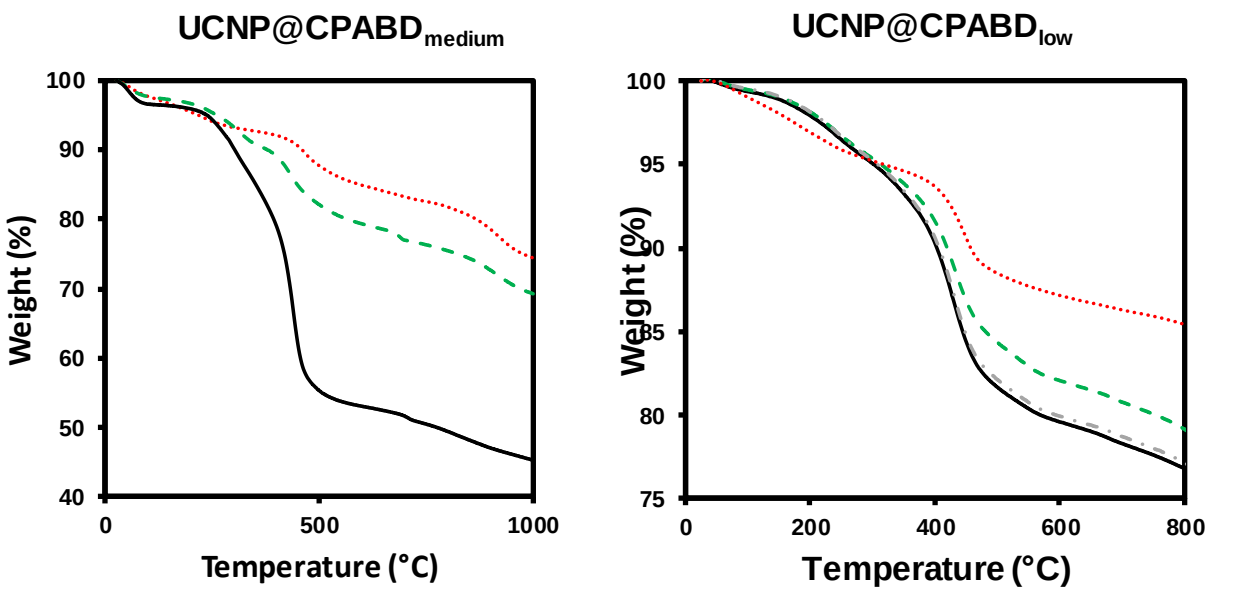

UCNPs	Char (wt%)	Polymer content (wt%)
UCNP@CPABD	74	0
UCNP@HBP (3 mM MA-CPABD)	45	31
UCNP@HBP (6 mM MA-CPABD)	69	6

UCNPs	Char (wt%)	Polymer content (wt%)
UCNP@CPABD	85	0
UCNP@polyHPMA (3 mM CPABD)	77	7.3
UCNP@HBP (3 mM MA-CPABD)	77	7.8
UCNP@HBP (6 mM MA-CPABD)	79	5.4

Figure 3.13. TGA thermograms of UCNP@CPABD (red dotted line), UCNP@polyHMPA using 3 mM CPABD (dashdotted gray line), UCNP@HBP using 3 mM of MA-CPABD (black solid line), and UCNP@HBP using 6 mM of MA-CPABD (green dashed line) from UCNP@CPABD$_{medium}$ and UCNP@CPABD$_{low}$.

As initiation takes place in solution in our system, the propagating chains can either consume HMPA and MA-CPABD in solution leading to HBP formed in solution or go through a chain transfer reaction with the CPABD present at the surface of UCNPs creating an active center to grow a HBP at the surface of UCNPs. The HBP formed in solution is expected to be less affected by chain breaking reactions as the concentration in active centers will be lower as compared to the HBP immobilized on UCNPs. To better understand the polymerization behavior, the polymer grafted on UCNPs and formed in solution during the polymerization were both characterized by SEC. The polymer formed in solution had a lower number-average molecular weight as compared to the polymer formed at the surface of UCNPs (Figure 3.14), *i.e.* 16 and 13 kg·mol^{-1} (Đ = 8.39 and 12.86 respectively), for polymers obtained from UCNP@CPABD$_{medium}$ and UCNP@CPABD$_{high}$ in solution compared to 2341 and 220 kg·mol^{-1} (Đ = 2.68 and 6.75 respectively) for polymers grafted on UCNPs. The molecular weights of the

polymers formed in solution were lower than the calculated ones with relatively low dispersity, which could be attributed to cyclization reactions as previously reported in the literature [475,476]. However, the polymers formed at the surface of UCNPs had a higher molecular weight and a broader molecular weight distribution that could be attributed to the high concentration in radicals per polymer chain leading to irreversible termination reaction notably between neighboring propagating chains. The higher the grafting density in CPABD on UCNPs was, the more pronounced this phenomenon would be observed. Further lowering of the grafting density in CPABD, *i.e.* using UCNP@CPABD$_{low}$, afforded polymers grafted on UCNPs with a lower molecular weight (M_n = 19 kg·mol^{-1}) and narrower molecular weight distribution (Đ = 1.65), closer to the characteristics of the polymer obtained in solution. It indicated a lower contribution of the chain-breaking reactions associated to the surface-initiated self-condensing vinyl RAFT copolymerization, for which CPABD were anchored at the surface of UCNPs inducing a high localized concentration in RAFT chain transfer agents. In solution, this phenomenon is less pronounced due to the homogeneous and lower localized concentration in RAFT chain transfer agent [477].

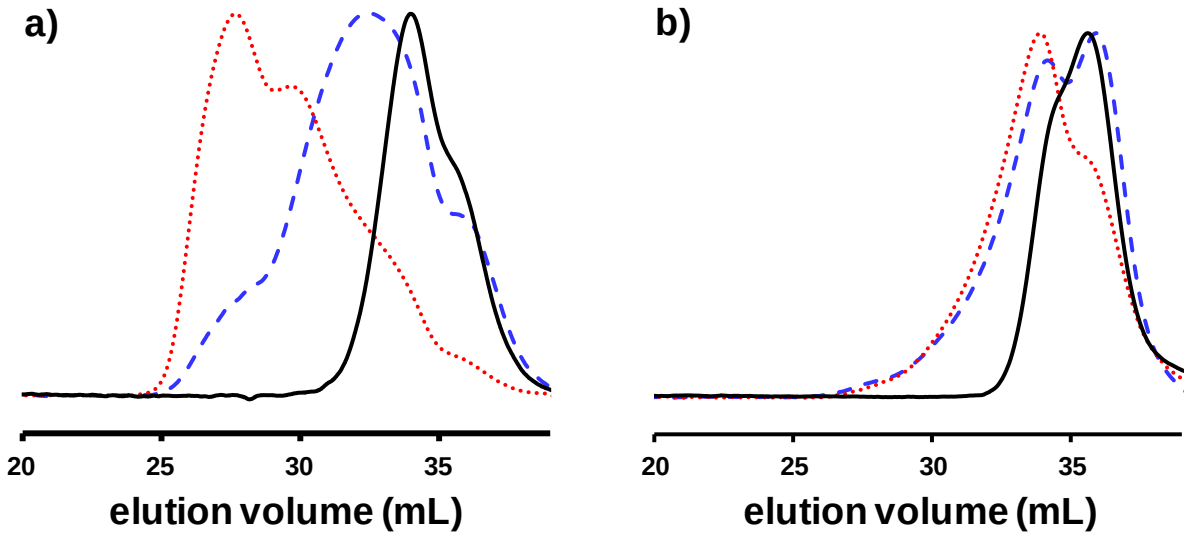

Figure 3.14. SEC traces for HBPs (a) grafted on UCNPs and (b) formed in solution prepared using 3 mM of MA-CPABD from UCNP@CPABD$_{low}$ (black solid line), UCNP@CPABD$_{medium}$ (red dotted line), and UCNP@CPABD$_{high}$ (blue dashed line).

2.5. Effect of the concentration in MA-CPABD transmer

Considering UCNP@CPABD$_{low}$, the concentration of MA-CPABD used during the polymerization was increased to 6 mM to determine its effect on the HBP formed at the surface of UCNPs. According to UV spectroscopy, the number of MA-CPABD incorporated as

branching points increased from 34 to 67 µmol per gram of UCNP for 3 and 6 mM of MA-CPABD used for the polymerization. TGA measurement permitted to determine the content of HPMA as 0.52 mmol per gram of UCNP, which was similar to the value obtained for the HBP prepared with 3 mM of MA-CPABD (*i.e*. 0.678 mmol). Thus, DB increased from 0.08 to 0.19 when doubling the amount of MA-CPABD used. SEC measurement indicated a decrease of the number-average molecular weight with the increase of the concentration in MA-CPABD, *i.e.* 19 kg·mol^{-1} in the case of 3 mM of MA-CPABD compared to 11 kg·mol^{-1} (Figure 3.15) when using 6 mM of MA-CPABD, with a decrease of the dispersity from 1.65 to 1.55. Under the same polymerization conditions (3 mM of CPABD), polyHPMA had a lower number-average molecular weight (9 kg·mol^{-1}) and narrower molecular weight distribution (Đ = 1.46).

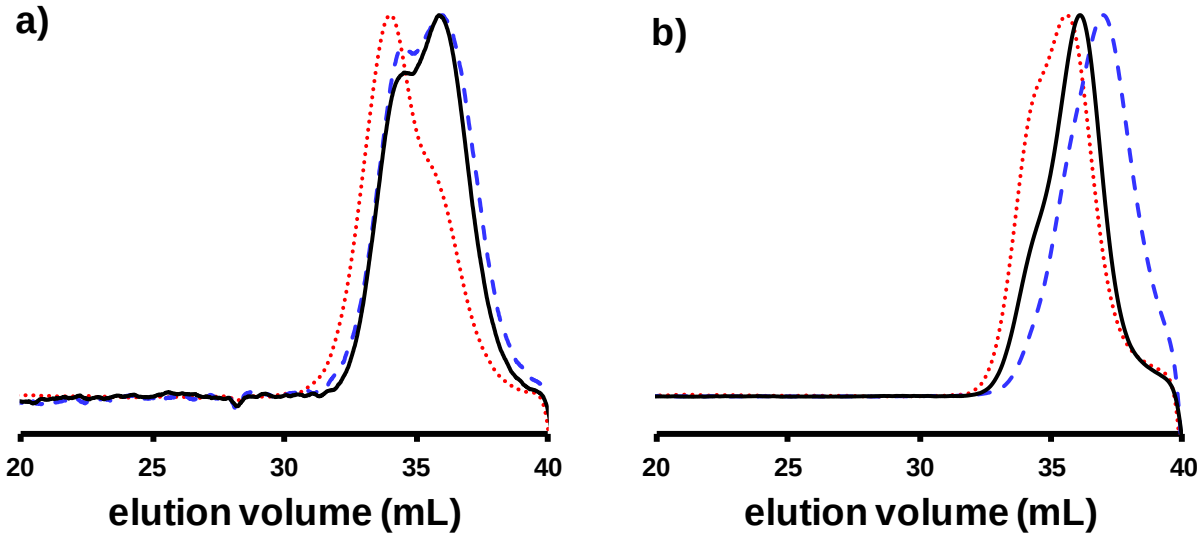

Figure 3.15. SEC traces for polymers (a) grafted on UCNPs and (b) formed in solution prepared from UCNP@CPABD$_{low}$. HBPs were synthesized using 3 mM (red dotted line) and (b) 6 mM (blue dashed line) of MA-CPABD, while the preparation of linear polymers was conducted with 3 mM of CPABD (black solid line).

The number of branches per polymer chain was calculated as 6 and 9 for 3 mM and 6 mM of MA-CPABD respectively. The grafting density of polymer was determined as 0.06 chain per nm^2 for 3 mM of MA-CPABD, which was similar to the one using 6 mM of MA-CPABD (*i.e*. 0.07 chain per nm^2). However, when preparing linear polymer from UCNPs under the same conditions, the number of polymer chains was 0.11 chain per nm^2, which was twice as compared to the HBP. The three-dimensional structure of HBPs affected strongly the propagation of the polymer chains from the surface of UCNPs inducing steric hindrance and enhancing the probability of chain-breaking reactions. These phenomena illustrated in Figure

3.16 would not only decrease the grafting density, but also increase the dispersity of the polymer formed [465,478] (Đ = 1.46 and 1.65 for polyHPMA and HBP, respectively).

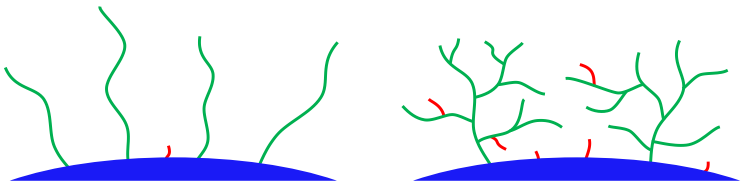

Steric hindrance	low	high
Probability of chain-breaking reactions	low	high
Grafting density (chain per nm^2)	0.11	0.06

Figure 3.16. Growing linear vs hyperbranched polymers from UCNP@$CPABD_{low}$ and the influence of steric hindrance and chain-breaking reactions on their chain propagation.

Increasing the grafting density of CPABD on UCNPs using 6 mM of MA-CPABD led to a reduction of the amount of polymer formed at the surface of UCNPs as compared to the HBPs formed using 3 mM of MA-CPABD (*i.e.* 0.5 and 16.8 wt% of polymer formed with 3 and 6 mM of MA-CPABD for UCNP@$CPABD_{high}$, and 6.3 and 24.3 wt% for UCNP@$CPABD_{medium}$ respectively) that was attributed to the enhancement of chain-breaking reactions due to the increased grafting density in CPABD [477,479,480] on UCNPs and the higher amount of terminal active centers. In summary, the ratio between the molecular weight of the HBP formed on UCNPs and in solution significantly increased with the increase in grafting density of CPABD on UCNPs (Figure 3.17a). The effect of the concentration of MA-CPABD (Figure 3.17b) had a less pronounced influence on the difference in molecular weight between the HBP formed on UCNPs and in solution, while for polyHMPA ([MA-CPABD] = 0 mM) this difference was minimal. This phenomenon could be attributed to the higher probability of coupling reactions between propagating chains for HBPs as compared to linear polymers due to their higher number of terminal active centers.

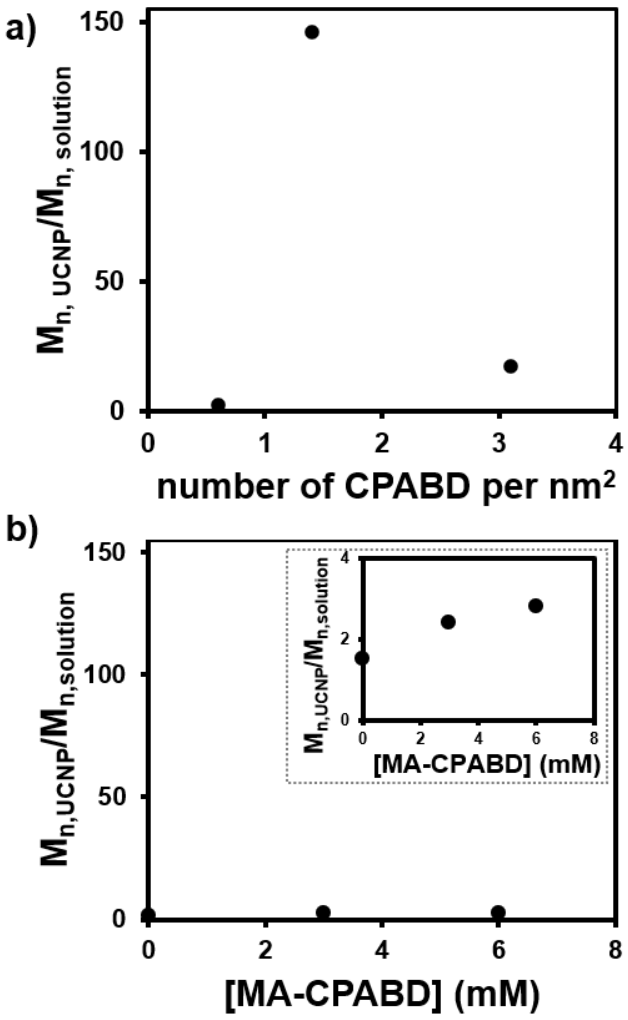

Figure 3.17. Comparison of the differences in molecular weight between HBPs grafted on UCNPs and formed in solution for different (a) grafting density in CPABD on UCNPs using 3 mM of MA-CPABD and (b) concentration in MA-CPABD using UCNPs with a grafting density of 0.6 CPABD/nm^2 (in inset zoom on a reduced scale).

To further investigate these coupling reactions, the grafting density in polymer chains per surface area of UCNPs was determined after 6 and 24 h of polymerization. The grafting density of the HBP was estimated as 0.35 chain per nm^2 after 6 h (M_n = 2.6 kg·mol^{-1}, Đ = 1.16) and 0.10 chain per nm^2 after 24 h (M_n = 13.4 kg·mol^{-1}, Đ = 2.72). This decrease in grafting density suggested the high propensity of chain-breaking reactions. Tsujii *et al*. proposed for the growth of linear polymers by RAFT polymerization from a flat surface that the decrease of the grafting density could be attributed to the high rate of termination reaction at the early stage of the polymerization [473]. However for the synthesis of HBP, this phenomenon could be worsened due to steric hindrance. Furthermore, hopping and rolling mechanisms for surface-initiated RAFT polymerization and the coupling between hyperbranched propagating chains

(*e.g*. between HBP formed in solution and those growing at the surface of UCNPs) could also contribute to this phenomenon.[472]

2.6. Luminescence properties of UCNP@HBP

The luminescence properties of UCNP@HBP dispersed in water (2 mg·mL^{-1}) were investigated using a diode laser exciting at 980 nm (Figure 3.18). The expected characteristic peak maxima of UCNPs doped with Er^{3+} were observed at 409 nm ($^4H_{9/2}\rightarrow{}^4I_{15/2}$), 542 nm ($^4H_{11/2}\rightarrow{}^4I_{15/2}$), 552 nm ($^4S_{3/2}\rightarrow{}^4I_{15/2}$), and 654 nm ($^4F_{9/2}\rightarrow{}^4I_{15/2}$) and UCNP@HBP had a strong emission as judged by an intense green light of its dispersion in water and as powder indicated that the modification of the surface of UCNPs did not extinguish their luminescent characteristics.

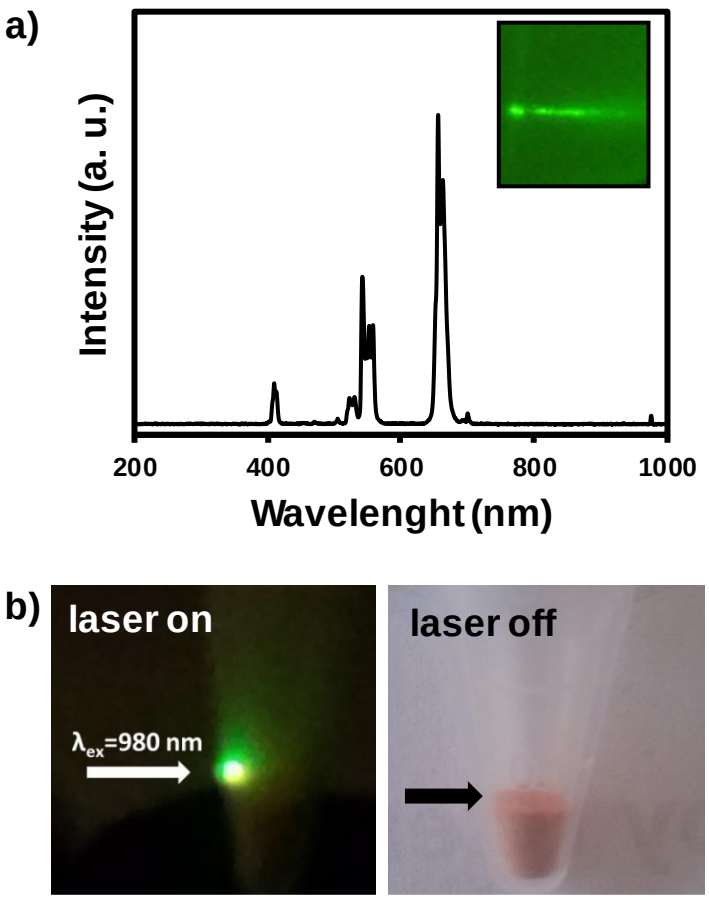

Figure 3.18. Upconversion emission of UCNP@HBP excited at 980 nm: (a) spectrum of a dispersion of UCNP@HBP in water (2 mg·mL^{-1}) and (b) digital images of the powder of UCNP@HBP upon exposure (left) or not (right) to the laser lamp.

3. Conclusion

Surface-initiated self-condensing vinyl RAFT copolymerization of HMPA from the surface of UCNPs was proposed. UCNPs were first functionalized with CPABD to promote RAFT polymerization from their surface. Polymerization of HPMA was first conducted to identify the suitable polymerization conditions before attempting the synthesis of HBPs by copolymerization with MA-CPABD. The preparation of HBPs from UCNPs was challenging due to the increased number of active centers on HBPs and the surface-initiated RAFT polymerization leading to an increased propensity to chain-breaking reactions. Different phenomena have yielded to HBPs grafted on UCNPs of high molecular weight and dispersity including a) the concentration in propagating chains at the surface of UCNPs increased due to the formation of HBPs by SCVP, b) the close proximity of the propagating chains, and c) the fact that RAFT polymerization from a surface was more prone to migration of the active center through hopping and rolling mechanisms. These UCNP@HBP are of interest for theranostic as UCNPs hold great potential for biomedical imaging and photodynamic therapy, while the HBP corona could act as drug carrier that could be tuned through further modification to fulfill the needs for sustained, triggered or targeted drug delivery.

CHAPTER 4 : Hyperbranched Polymers Grafted on Upconversion Nanoparticles for the Delivery of 5-Fluorouracil

1. Introduction

Theranostics is a fascinating field in biomedicine combining the delivery of a therapeutic drug and diagnostics through bioimaging on a same carrier [481]. The development in nanotechnologies has influenced this field leading notably to the use of inorganic nanoparticles [482]. A wide range of nanoparticles have been investigated including iron oxide nanoparticles used for magnetic resonance imaging [483], but also dye-doped silica nanoparticles [484], quantum dots [485], and upconversion nanoparticles [486] as optical contrast agents. Their surface has been modified with various functionalities by adsorption or conjugation to introduce for example a nucleic acid as drug [487], targeting ligands such as peptides [488], and poly(ethylene glycol) to provide stealthiness to the nanoparticles [489]. In this work, the UCNP@polymer based on HPMA previously synthesized were tuned for theranostics. While UCNPs will act as luminescent probes for bioimaging, the polymer corona will act as drug carrier.

The model drug used in this work was 5-fluorouracil (5-FU), which is a well-known anticancer agent introduced in 1958 used for the treatment of a wide range of cancers (*e.g.* colorectal cancer, skin, breast, brain, liver, and cancers of the aerodigestive tract)[490] through several mechanisms of action including interference with mRNA translation and DNA synthesis [491]. Unfortunately, 5-FU drug has a short plasma half-life of 8-20 min, is metabolized enzymatically in the liver [491], and has a low selectivity towards cancer cells leading to its exposure to healthy cells.[490] Its clinical use is thus limited due to severe side effects such as gastrointestinal and bone marrow toxicity as well as liver diseases[492,493]. Recent developments have aimed of improveing the bioavailability of 5-FU [490] by its encapsulation in polymer particles (*e.g.* alginate [494], aliphatic polyester [495], and poly(alkylcyanoacrylate) [496]) or vesicles such as liposomes [497], the preparation of prodrugs [498] and its conjugation to polymers (*e.g.* hyaluronic acid [499] and polyaspartamide [500]).

The work described here covers various aspects of drug delivery systems from the encapsulation of 5-FU to its conjugation on the polymer considering various release mechanisms such as hydrolytic and stimuli-responsive release. The development of stimuli-responsive drug conjugates is an interesting approach to control the release of the drug at the targeted site. Relevant stimuli in cancer cells are the acidity of the tumor environment,

high concentration of reducing agent (*i.e.* glutathione), and overexpressed enzymes such as cathepsin B and esterase [501]. The formation of ester linkages by reaction with the hydroxyl group of HPMA repeat units considered as such linkages can be hydrolytically degraded in the presence of acids, bases, human serum albumin, and metal ions, but also esterases that are frequently expressed in cancer cells, *e.g.* carboxylesterase [502,503]. Other stimuli considered in this work are redox sensibility through the insertion of disulfide bridges degradable by glutathione [504] and enzymatic stimulus by introducing a peptide sequence (GLFG) sensitive to cathepsin B [505]. These stimuli responsive linkages were introduced either on the side chains between the drug and polymer backbone or at the branching points through the use of the relevant transmer.

2. Results and discussion

2.1. Passive loading of 5-FU in UCNP@polyHPMA and UCNP@HBP

UCNP@polyHPMA and UCNP@HBP (DB = 0.17) obtained from UCNP@CPABD$_{high}$ having respectively 44 and 42 wt% of polymer grafted on UCNPs were used to investigate the drug loading, encapsulation efficiency, and drug release. The nanohybrids (3.3 mg/mL) were passively loaded by incubating them in water at room temperature for 24 h varying the amount of 5-FU from 0.7 to 3.3 mg/mL corresponding to a feed in drug of 16 to 50 wt% relative to the nanohybrids. The drug loading was determined by UV spectroscopy (Figure 4.1) using a calibration curve of 5-FU in water established with the characteristic absorbance of 5-FU at 265 nm (Figure A.4.15). For UCNP@polyHMPA, the drug loading increased from 0.5 to 1.4 wt% when increasing the feed in drug, while for UCNP@HBP the drug loading increased from 0.7 to 2.9 wt% respectively. These results indicated a low drug loading for these systems that could be detrimental for a use as drug delivery system, but a higher encapsulation efficiency of HBPs to load 5-FU as compared to polyHMPA attributed to the formation of internal cavities in the HBP structure promoting a better retention of the drug [506] [507].

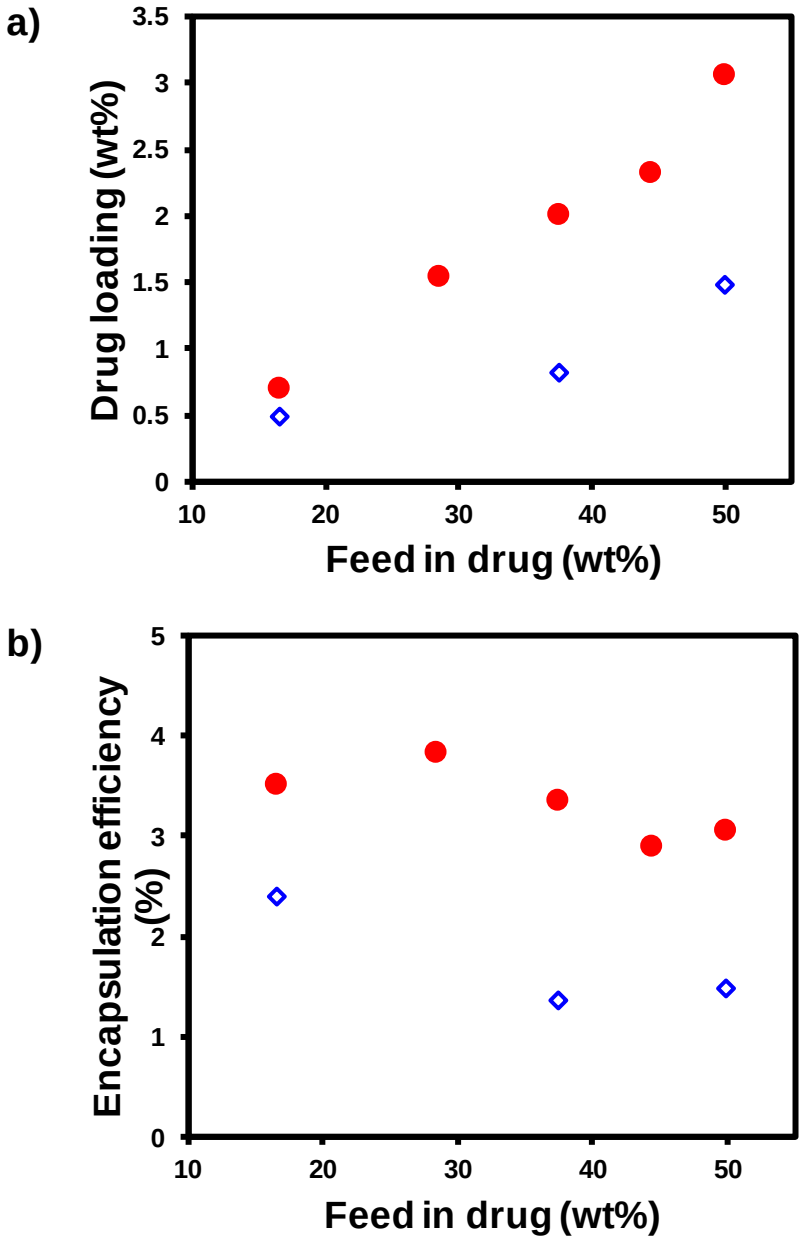

Figure 4.1. Passive loading of 5-FU in UCNP@polyHPMA (open blue diamonds) and UCNP@HBP (filled red circles): evolution of the (a) drug loading and (b) encapsulation efficiency as a function of the feed in drug.

The cumulative amount of drug released (Figure 4.2) was monitored for drug-loaded UCNP@HBP by placing it in a phosphate buffer solution (PBS) at pH 7.4 and 37 °C withdrawing aliquots in triplicate at predetermined times. The results indicated that after 8 h, more than 70 % of 5-FU loaded in UCNP@HBP was released under these conditions. This burst release was related to the hydrophilicity of 5-FU and polyHPMA. PolyHPMA did not act as a barrier against the diffusion of this drug of small size. After 24 h, almost all the drug (78 %) was

released. This nanocarrier was not suitable to be used for drug delivery as the drug would be released while the carrier would be circulating in the blood stream before reaching the targeted site.

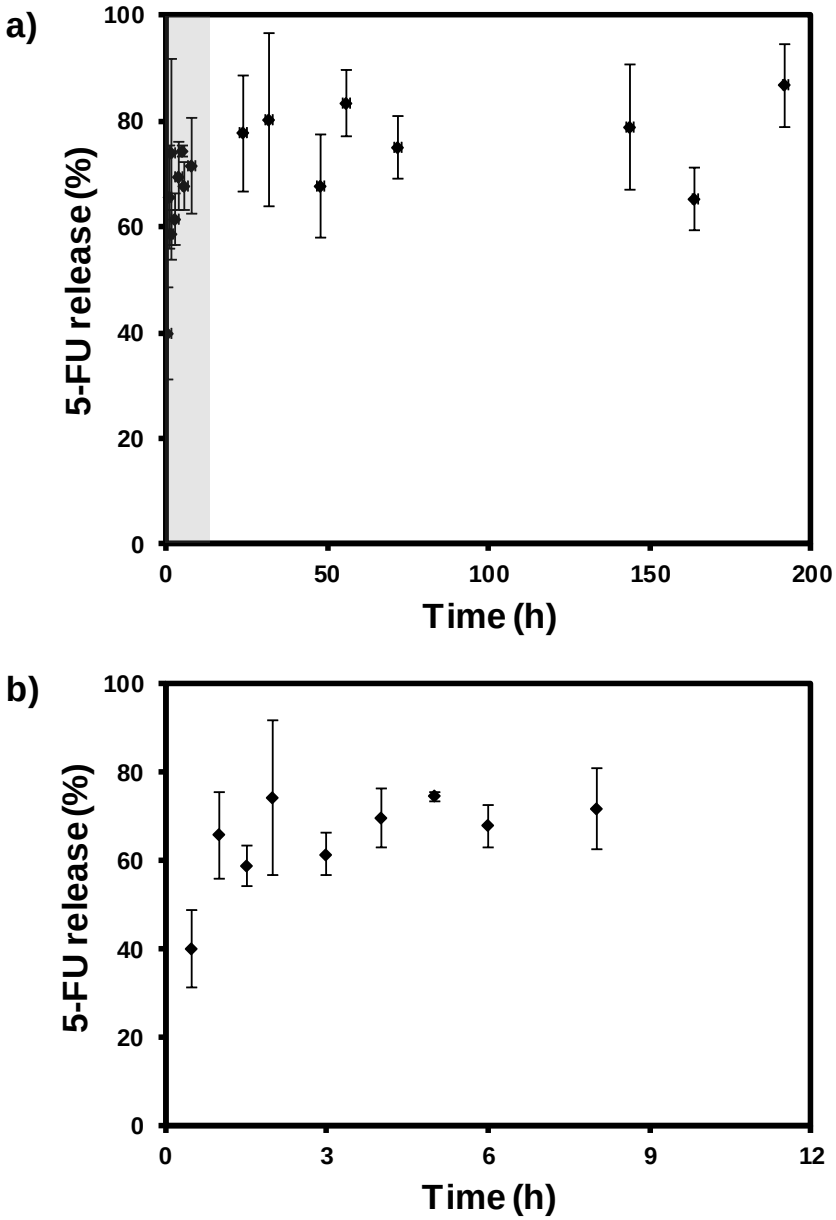

Figure 4.2. Drug release profile of 5-FU-loaded UCNP@HBP under physiological simulated conditions (PBS, 37 °C, pH 7.4) for experiments conducted in triplicate: (a) study over 8 days and (b) zoom on the first 12 h of the study highlighted in gray in (a).

2.2. Conjugation of 5-FU on UCNP@HBP through ester linkages

To improve the encapsulation stability in the blood stream and increase the drug loading, drug conjugation was considered, in which the drug is covalently bound to the nanocarrier and its release occurs thanks to a labile bond. Due to the number of hydroxyl groups on

polyHPMA [508], the drug conjugation with drugs was considered through reaction of these groups with a carboxylic acid present on the drug to promote the formation of an ester linkage[503] that is degradable by hydrolysis in physiological conditions in the presence of esterase or hydrolytic enzymes, but also catalyzed with acids or bases [503].

As 5-FU does not have a carboxylic group, it was modified with chloroacetic acid under basic conditions according to a previous report [509] (Scheme 4.1) to obtain 5-fluorouracil-1-acetic acid (5-FU-COOH). 5-FU-COOH was conjugated to the polymer backbone of UCNP@HBP by esterification reaction using HBTU as coupling agent (Scheme 4.2). 5-FU-conjugated UCNP@HBP was characterized by FT-IR spectroscopy (Figure 4.3). The spectrum of 5-FU-conjugated UCNP@HBP was similar to the one of UCNP@HBP with additional peaks notably at 1243 and 1699 cm^{-1} attributed to the C-F stretching bands and the C=O group of pyrimidine ring of 5-FU respectively, confirming the conjugation of 5-FU onto UCNP@HBP.

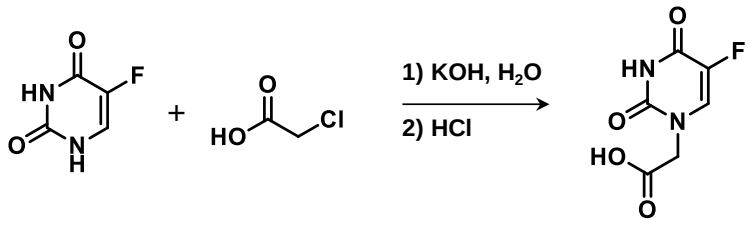

Scheme 4.1. Synthesis of 5-FU-COOH.

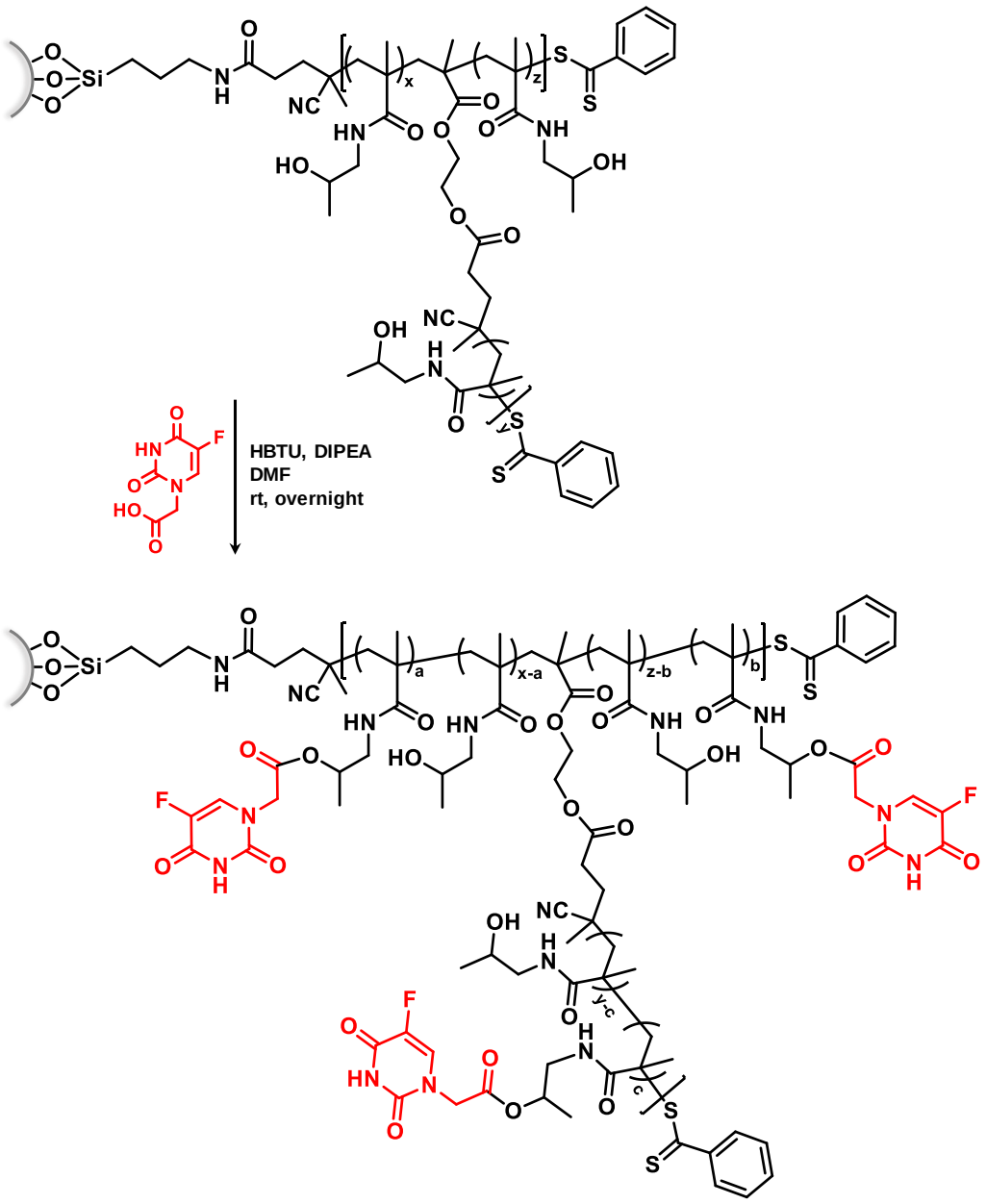

Scheme 4.2. Conjugation of 5-FU-COOH on UCNP@HBP.

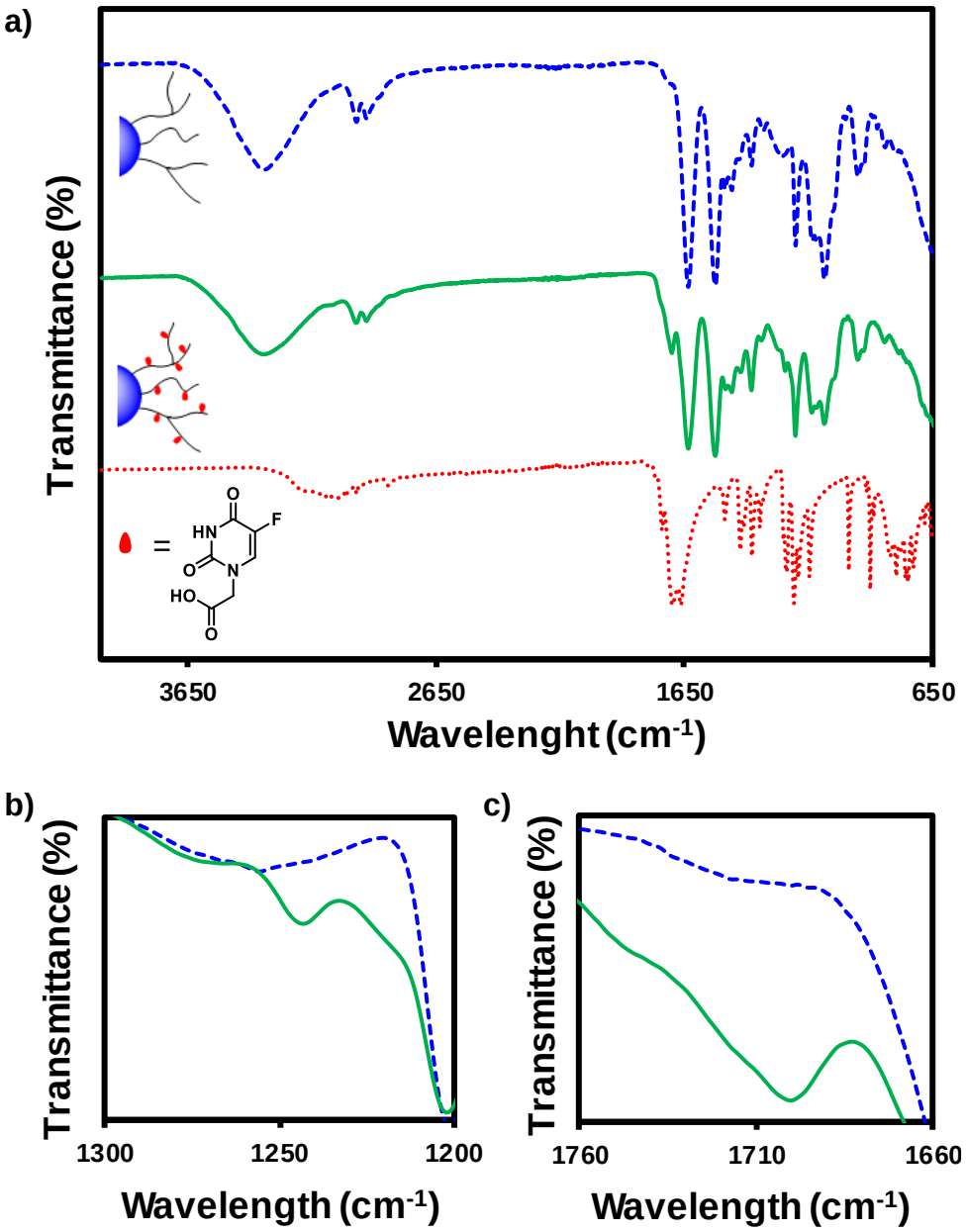

Figure 4.3. Characterization of UCNP@HBP (dashed blue line), 5-FU-conjugated UCNP@HBP (solid green line), and 5-FU-COOH (red dotted line): (a) full spectra and zoom on the range of wavelengths of (b) 1200-1300 and (c) 1660-1760 cm^{-1}.

The zeta potential of 5-FU-conjugated-UCNP@HBP (Figure 4.4) was −14.7 mV, while UCNP@HBP revealed a lower negative surface charge measured as −0.05 mV. It seems that the conjugation of 5-FU to HBPs increased the surface charge of UCNPs, which could be attributed to the presence of non-covalently conjugated 5-FU leading to a negative charge.

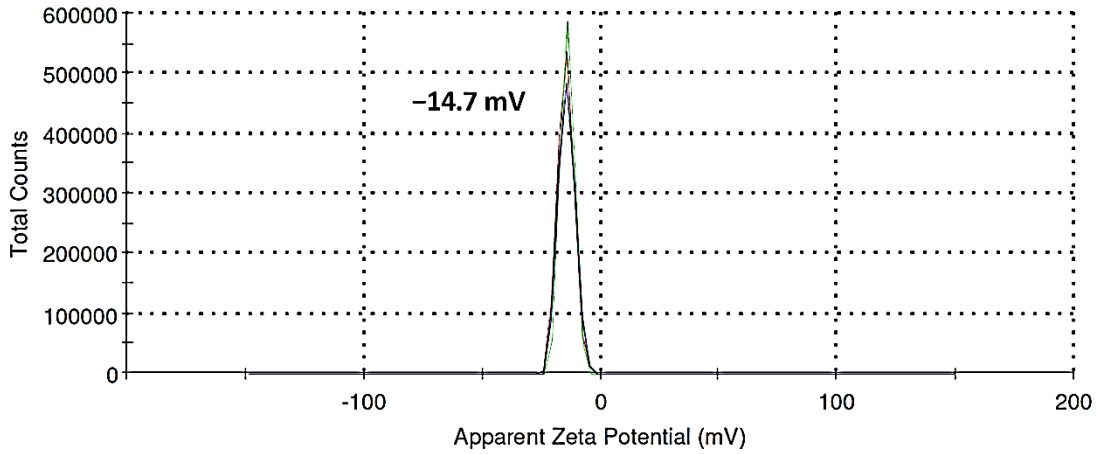

Figure 4.4. Zeta potential of analysis of UCNP@HBP and 5-FU-conjugated UCNP@HBP

5-FU loading in 5-FU-conjugated UCNP@HBP was determined via hydrolysis of the ester bonds between drug and polymer under basic conditions. The recovered 5-FU was quantified by UV spectroscopy at 265 nm using the 5-FU calibration curve as 12 w% (Figure A.4.16). In comparison to passive loading, the drug loading through conjugation was four times higher for the same feed in drug (i.e. 3 vs 12 wt%). The drug release was then carried out in PBS at 37 °C at pH 7.4 (Figure 4.5). When comparing it to the system involving passive loading of 5-FU, the initial burst release was only 11 wt% of 5-FU with the first 6h (compared to 68 wt% for passive loading) followed by a sustained release of the drug reaching 60 wt% after (456 h) 19 days. The influence of the pH was investigated conducting the same experiment at pH 3.2 to mimic gastric environment [510]. The cumulative drug release profile indicated an initial burst release of 10 wt% followed by a plateau. These results suggested a better hydrolysis of ester bonds between the drug and polymer backbone at neutral pH as compared to acidic conditions which has been previously reported [511,512].

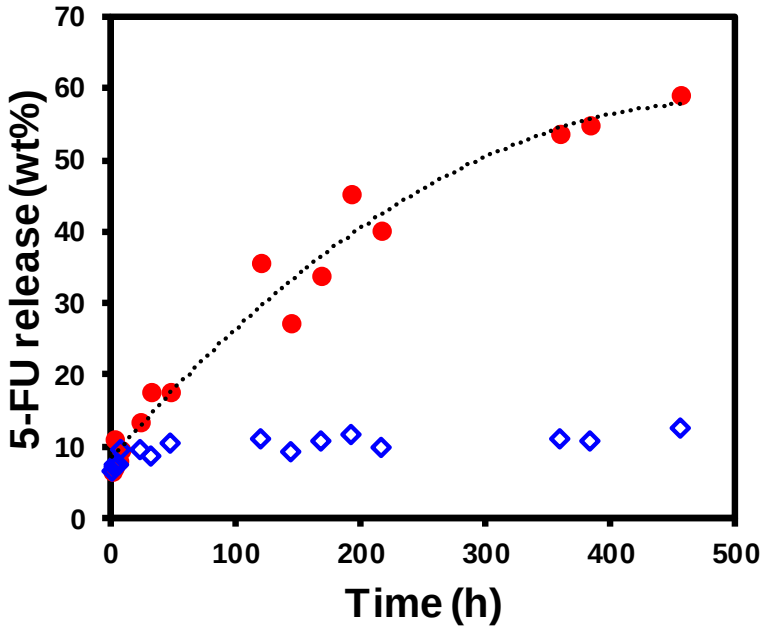

Figure 4.5. Drug release profiles of 5-FU from 5-FU conjugated UCNP@HBP under simulated conditions (PBS, 37 °C) at pH 7.4 (filled red circles) and 3.2 (open blue diamond).

2.3. 5-FU-conjugated on UCNP@HBP with stimuli-sensitive branching points

The degradation of ester bonds can also be triggered by esterases which are overexpressed in cancer cells [513,514]. However, due to the hyperbranched structure of the polymer and the large size of esterases such as carboxylesterases (61-65 kDa),[515] the access of the esterase to the ester groups may be sterically hindered reducing its ability to promote the drug release (Figure 4.6). To overcome this difficulty, the introduction of degradable branching points was considered to break down the polymer and thus provide access of the esterase to the ester linkages present between the drug and the polymer. However, these degradable branching points should be stable while the polymer-drug conjugate is circulating in the bloodstream and should be able to degrade solely when at the targeted site. Redox- and enzyme-sensitive branching points through the use of the corresponding transmers (Figure 4.7) were thus considered for the design of the nanocarrier due to the high concentration in reducing agents and cathepsin B respectively in cancer cells.

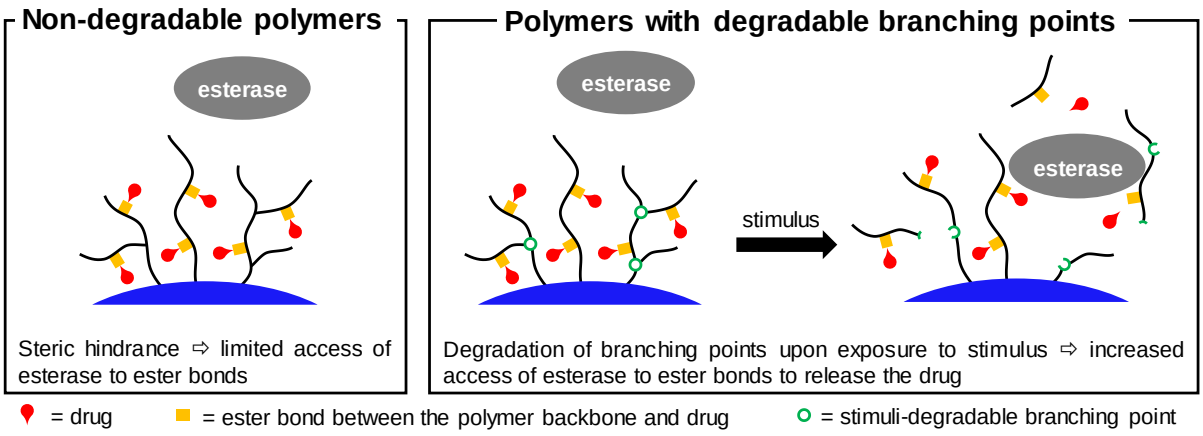

Figure 4.6. Enzymatic activity of esterases on non-degradable polymers and polymers with stimuli-degradable branching points grafted on UCNPs.

redox-sensitive transmer (MA-SS-CPABD)

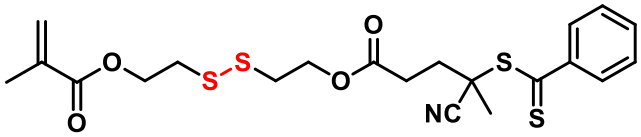

cathepsin B-sensitive transmer (MA-GFLG-CPABD)

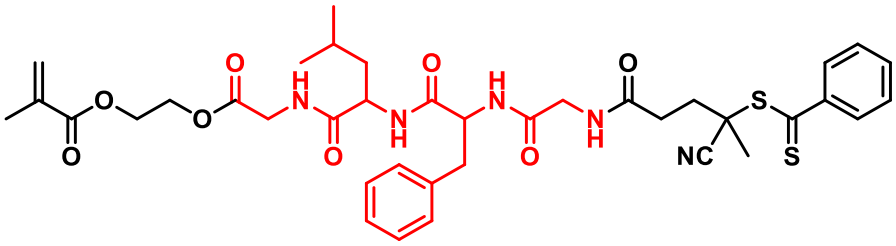

Figure 4.7. Structure of redox- and cathepsin B-transmers.

2.3.1. Redox-sensitive linkages

Disulfide bonds are stable in biological conditions, but cleave in the presence of a reducing agent. Glutathione is one of the most important reducing agents highly overexpressed in cancer cells [516]. Its concentration is about 2-10 mM in the cytosol as compared to less than 10 µM in extracellular fluids [517]. We proposed in this work to introduce a disulfide bridge on the transmer (MA-SS-CPABD, Figure 4.8) that was prepared in two steps according to the protocol reported by Tao *et al.* (*i.e.* synthesis of 2-((2-hydroxyethyl)disulfanyl)ethyl 4-cyano-4-(phenylcarbonothioylthio)pentanoate by reaction between CPABD and 2-hydroxyethyl disulfide, followed by an esterification reaction with methacrylic acid) [518]. The polymerization from UCNP@CPABD$_{high}$ (10 mg/mL) was conducted at 65 °C using MA-SS-

CPABD as transmer in the molar ratio of [HPMA]:[MA-SS-CPABD]:[AIBN] of 200:1:0.2. TGA of redox-sensitive UCNP@HBP (UCNP@HBP$_{redox}$) indicated a content of 31 wt% of polymers (Figure 4.8), while UV spectroscopy afforded the determination of the amount of MA-SS-CPABD incorporated on the polymer as 0.121 mmol per gram of UCNP corresponding to a DB of 0.17.

The degradation of the polymer was studied in PBS at pH 7.4 at 37 °C using dithiothreitol (DTT) as reducing agent, which has a similar activity as glutathione (Scheme 4.3). TGA analysis was used to measure the amount of polymer remaining at the surface of UCNPs after adding the reducing agent (Figure 4.8). The HBP with redox sensitive linkages showed a weight loss of 25 and 5 wt% in the absence and presence of DTT respectively. The weight loss in the presence of DTT was similar to UCNP@CPABD suggesting the full degradation of the polymer under these conditions. Furthermore, DLS indicated a D_h of 248 and 149 nm (based on intensity) before and after adding DTT confirming the polymer degradation (Figure 4.9).

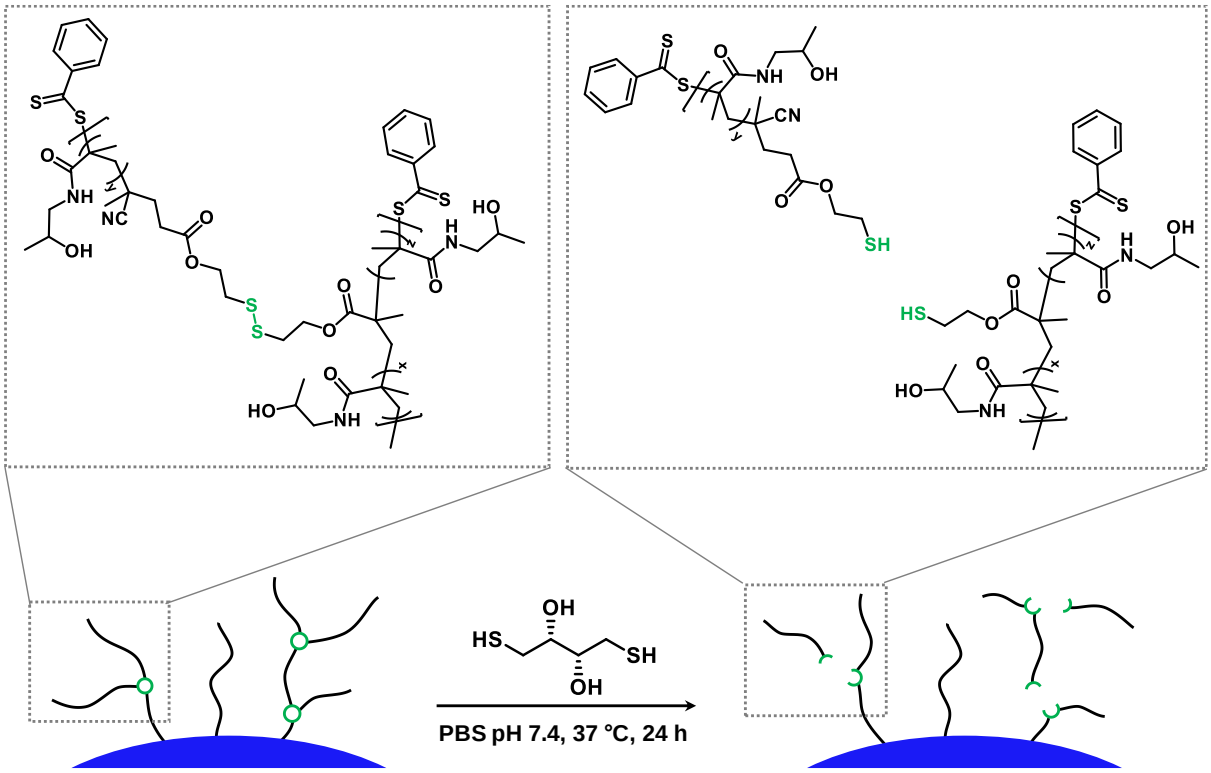

Scheme 4.3. Degradation of redox-sensitive branching points of UCNP@HBP$_{redox}$ in the presence of DDT.

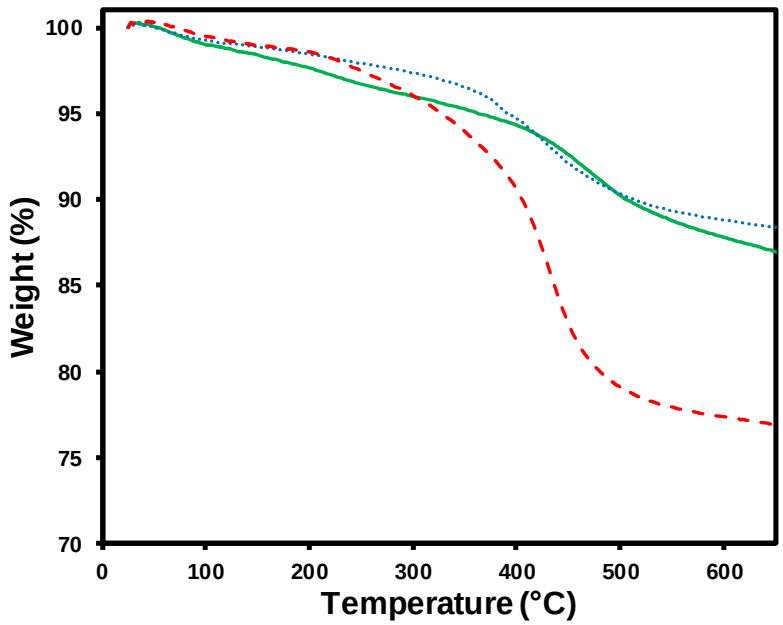

Figure 4.8. TGA of UCNP@CPABD (green solid line), UCNP@HBP$_{redox}$ as control in water (red dashed line) and after addition of 10 mM of DTT (blue dotted line).

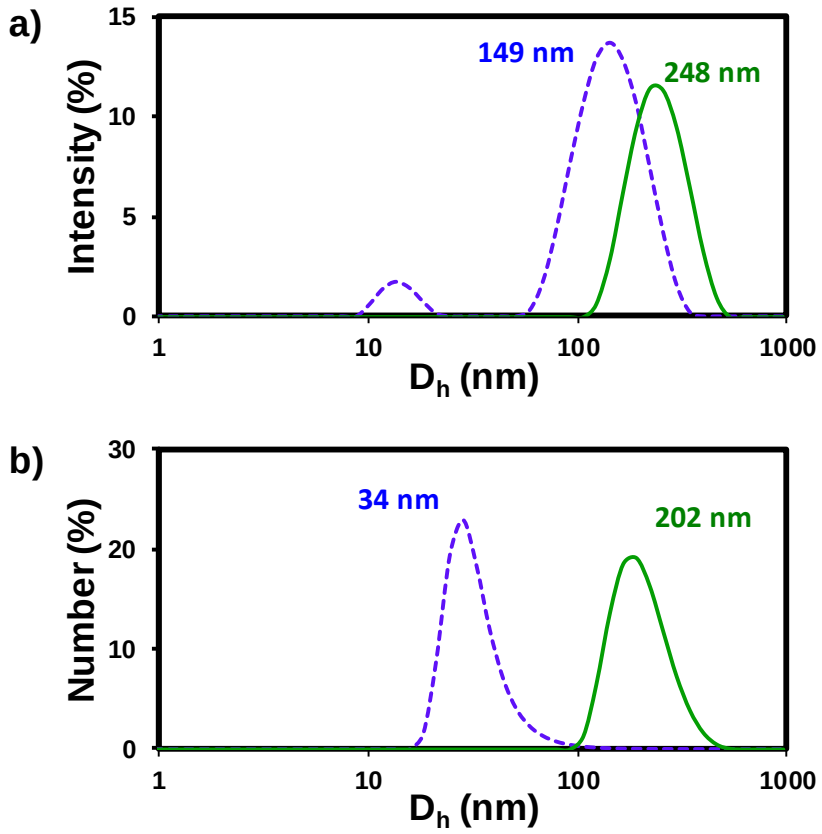

Figure 4.9. DLS measurements of UCNP@HBP$_{redox}$ before (solid green line) and after (dashed blue line) addition of 10 mM of DTT in a) intensity and b) number.

To investigate the rate of degradation of HBP_{redox} in the presence of DTT, the polymer was labeled with Rhodamine B linked to the polymer through a GLFG peptide sequence. Rhodamine B-GFLG was synthesized by solid-phase peptide synthesis followed by on resin end-capping of the peptide sequence with Rhodamine B (Scheme 4.4). The peptide sequence was synthesized by solid-phase peptide synthesis from a 2-chlorotrityl chloride resin adding iteratively each amino acid using HBTU as coupling agent. The peptide sequence was then end-capped on the resin with Rhodamine B by esterification reaction using *N*,*N*'-diisopropylcarbodiimide (DIC) as coupling agent [519]. The coupling between Rhodamine B and peptide on resin was not completed, therefore with capping unreacted amine on resin, cleaving step was done. Rhodamine B-GFLG was conjugated on UCNP@HBP_{redox} by esterification reaction using HBTU as coupling agent. The amount of Rhodamine B was determined by UV spectroscopy as 0.3 µmol per gram of UCNPs using a calibration curve of Rhodamine B in water (Figure A.4.17). Upon addition of DTT, the degradation of HBP_{redox} occurred readily and was monitored by UV-vis spectroscopy at 552 nm for the supernatant (Figure 4.10). The results indicated a fast degradation of the polymer observed by the presence of fragments of Rhodamine B-labeled polymer in solution up to 60% in the first 30 min following the addition of DTT reaching a plateau around 73% after 120 min.

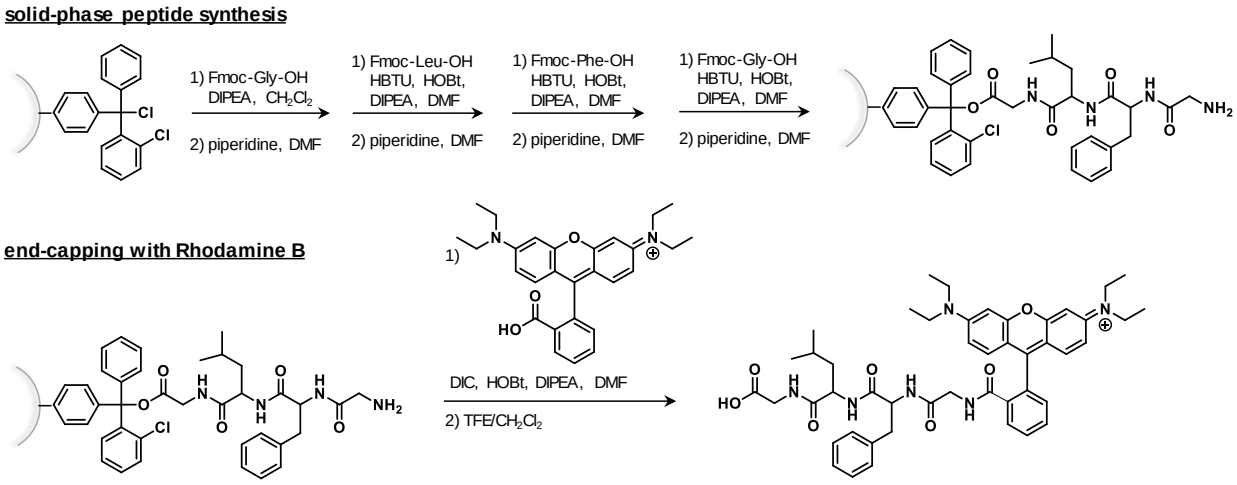

Scheme 4.4. Synthesis of Rhodamine B-GFLG.

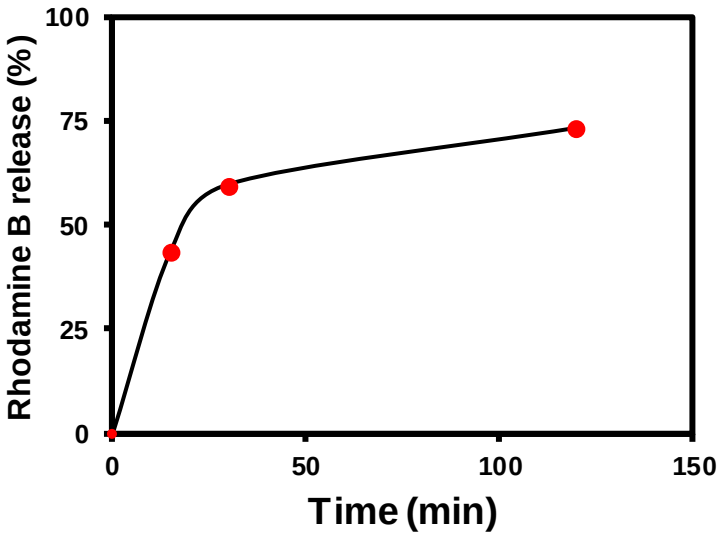

Figure 4.10. Rhodamine B release profile from Rhodamine B-labelled UCNP@HBP$_{redox}$ in PBS at pH 7.4 at 37 °C in the presence of DTT.

2.3.2. Enzyme-sensitive linkages

In order to prepare an enzyme-responsive HBP, a transmer based on an enzyme-sensitive peptide sequence was synthesized. The peptide sequence chosen was Gly-Phe-Leu-Gly (GFLG) as it was identified to be cleavable in the presence of cathepsin B, which is an enzyme highly upregulated in cancer cells [520]. The targeted transmer (MA-GLFG-CPABD, Scheme 4.5) was constituted of the GFLG peptide sequence with CPABD at its *N*-terminus and a methacrylate group at its *C*-terminus. The peptide sequence was synthesized similarly by solid-phase peptide synthesis and then end-capped on the resin with CPABD by amidation reaction (Scheme 4.5). GLFG-CPABD was cleaved from the resin using a solution of 2,2,2-trifluoroethanol (TFE) in dichloromethane and was then coupled to 2-hydroxy methacrylate by esterification reaction using HBTU as coupling agent. The structure of the enzyme-sensitive transmer (MA-GLFG-CPABD) was confirmed by ^{1}H and ^{13}C NMR spectroscopies and mass spectroscopy (Figure 4.11).

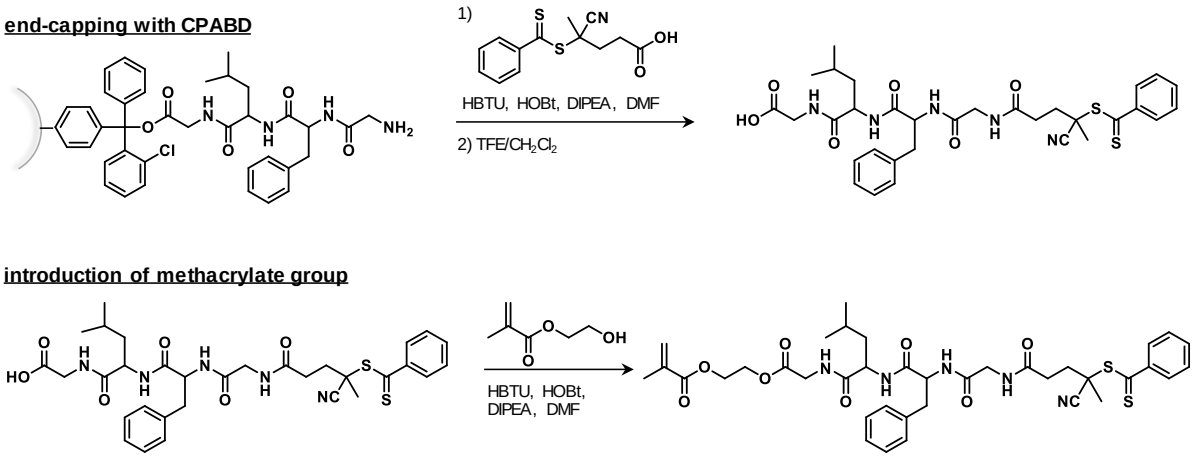

Scheme 4.5. Synthesis of MA-GLFG-CPABD

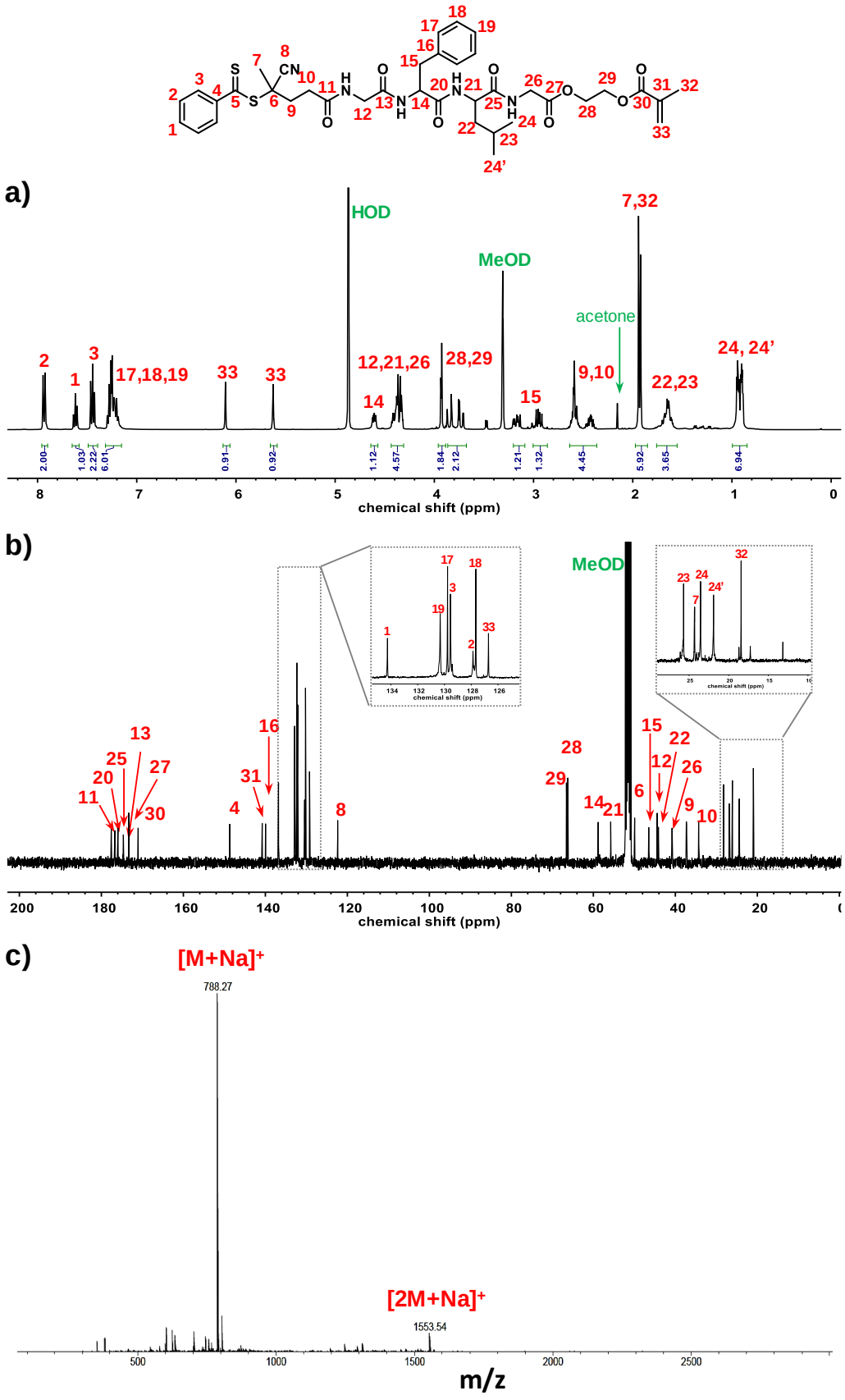

Figure 4.11. Characterization of MA-GLFG-CPABD: (a) ^{1}H and (b) ^{13}C NMR spectra in MeOD and (c) mass spectrometry.

The polymerization from UCNP@CPABD$_{high}$ (10 mg/mL) was conducted using MA-GFLG-CPABD as transmer using similar conditions as those used to prepare UCNP@HBP$_{redox}$, *i.e.* 65 °C using a molar ratio [HPMA]:[MA-SS-CPABD]:[AIBN] of 200:1:0.2, affording enzyme-sensitive UCNP@HBP (UCNP@HBP$_{enzyme}$). Mean size of the prepared UCNP@HBP$_{enzyme}$ was measured about 120 nm without any aggregated particle (Figure 4.12). TGA of UCNP@HBP$_{enzyme}$ indicated a percentage of polymer grafted on UCNPs of 25 wt% (Figure 4.13) corresponding to 0.735 mmol of HPMA repeat units per gram of UCNPs. The amount of MA-GFLG-CPABD involved in RAFT polymerization at the surface was measured by UV spectroscopy as 0.087 mmol/g$_{NPs}$, and DB was estimated around 0.19.

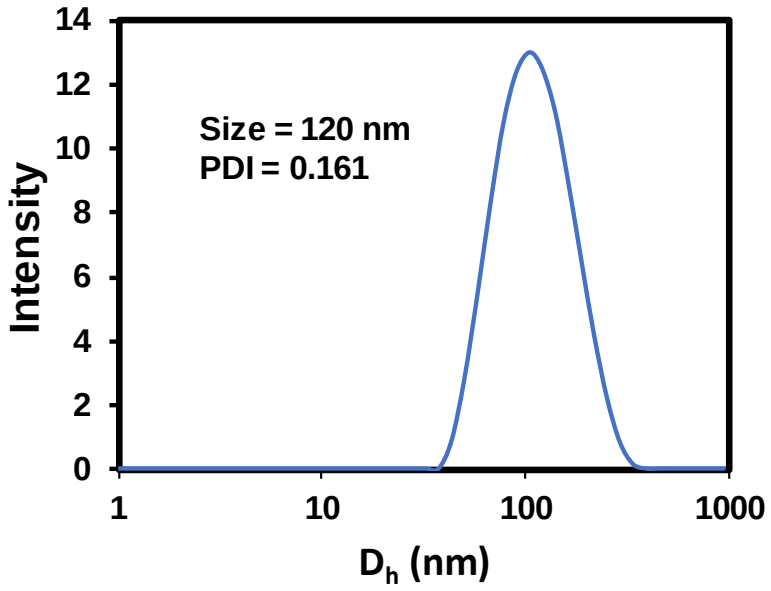

Figure. 4.12. DLS measurement of UCNP@HBP$_{enzyme}$ in PBS.

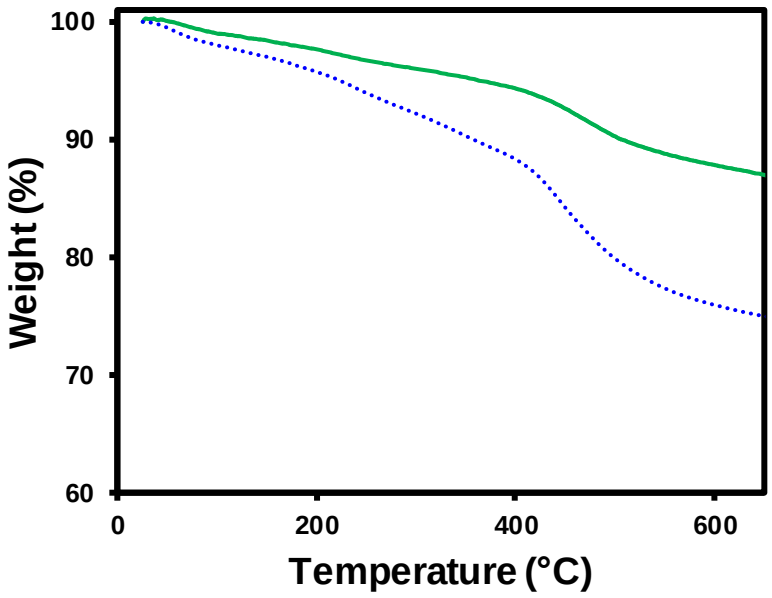

Figure 4.13. TGA thermogram of UCNP@CPABD (green solid line) and UCNP@HBP$_{enzyme}$ (blue dotted line).

3. Conclusion

In summary, we have studied the potential UCNP@HBP as nanocarrier for the delivery of 5-FU. Drug loading via passive loading for UCNP@HBP and UCNPs@polyHPMA revealed a higher capacity of drug loading for UCNP@HBP (*e.g.* 1.4% and 2.9% drug loading for UCNPs@polyHPMA and UCNP@HBP, respectively). Drug release from UCNP@HBP passively loaded with 5-FU was fast reaching 78% of drug released after 24 h. To enhance drug loading and encapsulation stability of 5-FU, drug conjugation was considered through ester bonds, which are susceptible to hydrolysis to release the drug under physiological conditions in cancer cells due to their high concentration in esterases. By conjugating 5-FU to UCNP@HBP, the drug content increased by four folds as compared to passive loading and more sustained release of 5-FU was observed.

To promote a higher accessibility of esterases to the ester bond between the polymer and drug, redox-degradable groups were introduced on UCNP@HBP at their branching points. The degradation of UCNP@HBP$_{redox}$ was studied by TGA and DLS in the presence of DTT as reducing agent. The amount of polymer on surface of UCNPs and hydrodynamic size decreased clearly confirming the degradation of HBPs grafted at the surface of UCNPs. The insertion of enzyme-sensitive branching point based on a specific peptide sequence, *i.e.* GLFG,

prepared by solid-phase peptide synthesis was also considered to obtain enzyme degradable nanohybrids, UCNP@HBP_{enzyme}. Future work will include the degradation study of UCNP@HBP_{enzyme} in the presence of Papain enzyme having the same activity as Cathepsine B in cancer cells. To validate the potential of this work, the investigation of the cytotoxicity of these nanohybrids will be necessary along with their study in cell culture.

EXPERIMENTAL SECTION

1. Materials

Yttrium(III) chloride hexahydrate (99.99%), ytterbium(III) chloride hexahydrate (99.99%), erbium(III) chloride hexahydrate (99.99%), oleic acid (OA, technical grade, 90%), 1-octadecene (technical grade, 90%), sodium hydroxide (anhydrous, ACS reagent, ≥97%), ammonium fluoride (ACS reagent, ≥98.0%, IGEPAL® CO-520, tetraethylorthosilicate (TEOS, 98%), (3-aminopropyl)triethoxysilane (APTES, 98%), 1-hydroxybenzotriazole hydrate (HOBt, ≥97%), 2,2'-azobis(isobutyronitrile) (AIBN, 98%), *N*,*N*'-dicyclohexylcarbodiimide (DCC, 99%), 4-(dimethylamino)pyridine (DMAP, 99%), 4-cyano-4-(thiobenzoylthio)pentanoic acid (CPABD, >98%), ammonium hydroxide (28%), Fmoc-L-Leu-OH (>97%), piperidine (99%), methacrylic acid (99%), N,N'-Diisopropylcarbodiimide (DIC, 99%) silica gel (high-purity grade, pore size 60 Å, 230-400 mesh), phosphate buffered saline tablets (PBS), *N*,*N*-dimethylformamide anhydrous, (DMF, 99.8%), anhydrous methanol (MeOH, 99.8 %), anhydrous dichloromethane (DCM, ≥99.8%), and *N*,*N*-dimethylformamide (DMF, >99%) were purchased from Sigma-Aldrich. *N*,*N*,*N'*,*N'*-Tetramethyl-*O*-(1H-benzotriazol-1-yl)uronium hexafluorophosphate (HBTU, 99%), 2-chlorotrityl chloride resin (1.6 mmol/g, 100-200 mesh), Fmoc-Phe-OH (>99%) and Fmoc-Gly-OH (>98%) were purchased from Iris Biotech. 2-Hydroxyethyl methacrylate (HEMA, 98%) and 5-fluorouracil (5-FU, 98%) were purchased from ABCR. *N*-Ethyldiisopropylamine (DIPEA, 99%), 1,4-dioxane (≥99.5%), 1-amino-2-propanol (94%), methacryloyl chloride (97%) and 2,2,2-trifluoroethanol (TFE, 99+%) were purchased from Alfa Aesar. Rhodamine B (95%) was purchased from Merck. Hydrofluoric acid (HF, 40% in H_2O) was purchased from Ridel de Haen. Ethanol (absolute, 99.99%), cyclohexane (99.8%), and acetone (99.8%), Diethyl ether (99%) were purchased from Carlo Erba. Dialysis tubing (regenerated cellulose, MWCO of 1 kDa, SpectrumLab) was purchased from Roth. All chemicals were used as received, except if noted otherwise. AIBN was recrystallized twice from ethanol. *N*-(2-Hydroxypropyl) methacrylamide [521] (HPMA), 2-(methacryloyloxy)ethyl 4-cyano-4-(phenylcarbonothioylthio)pentanoate [466] (MA-CPABD), 5-fluorouracil-1-acetic acid [509] (5-FU-COOH) and the redox-sensitive transmer [518] (MA-SS-CPABD) were synthesized as reported in the literature. All the syntheses on solid support were performed in solid phase extraction (SPE) tubes (12 and 25 mL polypropylene SPE tubes with polyethylene frits, 20 µm porosity purchased from SUPELCO®) and shaken using a modified IKA KS 130 basic shaker.

2. Characterization techniques

UV-vis spectroscopy was carried out using a Perkin Elmer Lambda 25 spectrophotometer.

Dynamic light scattering (DLS) experiments were performed on a Malvern Zetasizer Nano ZS at 633 nm (He-Ne laser beam) with a scattering angle fixed at 173° at 25 °C. Before measurement, the solutions were filtered through a 0.45 μm syringe filter.

High resolution transmission electron microscopy (HR-TEM) images were obtained on a JEOL 2100F electron microscope with an accelerating voltage of 200kV. TEM samples were prepared by placing few drops of nanoparticle suspension onto a carbon-coated grid and air-drying under ambient conditions. The size distributions of the samples based on TEM images for more than 100 particles were investigated by the open-source ImageJ software (Version 1.51n, Wayne Rasband, National Institutes of Health, USA).

Fourier transform infrared (FTIR) spectra were recorded on a Bruker Vertex 70 spectrometer using the attenuated total reflectance (ATR) technique between 500 and 4000 cm^{-1}.

^{1}H and ^{13}C NMR spectra were recorded in $CDCl_3$, DMSO-d_6, MeOD, or D_2O on a 400 MHz Bruker Avance III HD spectrometers equipped with a BBO type probe at 25 °C.

Size-exclusion chromatography (SEC) was performed on DIONEX Ultimate 3000 system equipped with a guard column and four Shodex OH-pak columns (7.5 x 300 mm, 803HQ, 804HQ, 806HQ, 807HQ), a Wyatt OPTILAB rEX differential refractometer, and a Wyatt DAWN HELEOS II light scattering detector and was operated at 30 °C using 60/40 water/acetonitrile with 0.1 M $NaNO_3$ as eluent at a flow rate of 0.5 $mL \cdot min^{-1}$.

Luminescence spectra of UCNPs were obtained using an inverted microscope (Olympus IX71) equipped with a high numerical aperture objective (Olympus, UApo N 100x/1.49 Oil) excited at 980 nm using a continuous-wave laser coupled to a single-mode fiber with a maximum output of 350 mW (Qphotonics, QFBGLD-980-350) [522]. (ILLKIRCH)

X-ray powder diffraction (XRD) measurements were performed on a Rigaku SmartLab diffractometer with Cu $K\alpha_1$ radiation (45 kV, 200 mA, λ=0.15406 nm) for the characterization of crystallinity and phase of nanocrystals. (IPCMS)

Nitrogen adsorption/desorption isotherms according to the Brunauer–Emmett–Teller (BET) theory were recorded on a Micromeritics TriStar 3000 V6.07A analyzer. The samples were degassed at 150 °C for 3 h in the degassing port of the adsorption apparatus. (ECPM)

3. Experimental protocols for Chapter 2

3.1. Synthesis of $NaYF_4$:Yb^3,Er^{3+} nanocrystals

$NaYF_4$:20% Yb^{3+},2% Er^{3+} nanocrystal was synthesized according to a previously reported procedure with some modification [343]. In a typical recipe: 1 mmol of $RECl_3$ (Y:Yb:Er = 78%: 0.2%:0.02%) was added into a mixture solution of oleic acid (6 mL) and 1-octadecene (15 mL) in a round bottom flask with vigorous stirring and heated at 150 °C to form a homogeneous solution which was further cooled down to 30 °C under argon atmosphere. Then, a mixture of NaOH (0.1 g, 2.5 mmol) and NH_4F (0.1448 g, 4 mmol) in 5 mL of methanol was added to the above solution and stirred for 30 min at 30 °C. Afterward, the mixture was heated from 80 to 110 °C for the removal of methanol. Then, the mixture was heated to a given temperature (290, 300, 305, 310, 315 °C) for 30, 60, 90, 120 or180 min under an argon atmosphere for the formation of nanocrystals. For the microtube setup, the primary nuclei solution was transferred to a microtube with different internal diameters (ID) (4083, 1753 and 876 μm) under argon atmosphere and placed into a thermoregulated oven at different fixed temperatures (290, 300, 305, 310 and 315 °C) and maintained at these temperatures for different times (30 to 330 min) and then cooled down to room temperature. The products were precipitated by the addition of acetone, collected by centrifugation, and finally redispersed into cyclohexane.

4. Experimental protocols for Chapter 3

4.1. Synthesis of $NaYF_4$; Yb 20%; Er 2% upconversion nanoparticles with amine groups at their surface (UCNP@NH_2)

$NaYF_4$:20% Yb^{3+}, 2% Er^{3+} nanocrystals having a diameter of 25-30 nm were prepared by the co-precipitation method according to a previously reported procedure [343] with some modifications. Briefly, 1 mmol of lanthanide chloride (Y:Yb:Er = 78:20:2) were dissolved into a solution of oleic acid (6 mL) in 1-octadecene (15 mL) under vigorous stirring and heated to 150 °C to obtain a homogeneous solution that was then cooled to 30 °C under argon. A mixture of NaOH (0.10 g, 2.5 mmol) and NH_4F (0.14 g, 4.0 mmol) dissolved in 5 mL of MeOH was then added and stirred for 30 min at 30 °C. The mixture was then heated at 110 °C for 50 min to remove MeOH, then at 290 °C for 180 min under argon. The solution was cooled to

room temperature and 25 mL of acetone was added. The precipitate was centrifugated, isolated and redispersed in 20 mL of cyclohexane. The concentration of the dispersion of $NaYF_4$:20% Yb^{3+}, 2% Er^{3+} nanocrystals capped with oleate ligands (UCNP@OA) in cyclohexane was around 40 mg·mL^{-1}.

UCNP@OA were modified with silanol (Si-OH) in the presence of TEOS under basic conditions by reverse microemulsion method [388,523] followed by the introduction of primary amine groups by treating with APTS [388]. Briefly, 1.5 g of IGEPAL® CO-520 (3.33 mmol) was charged in a 50 mL centrifuge tube followed by 21 mL of cyclohexane and 4 mL of UCNP@OA dispersion (20 mg·mL^{-1} in cyclohexane) were added into the tube. After 1 min of sonication, the mixture was poured to a 100 mL flask under vigorous stirring (750 rpm). 0.165 mL of ammonium hydroxide (28%) was added slowly and stirred for 30 min. 50 µL of TEOS (0.22 mmol) were added to the reaction mixture that was stirred for 24 h. 30 µL of APTS (152 µmol) was then added and stirred for 24 h. 50 mL of a mixture of acetone and ethanol (50:50) was added to the reaction tube. The mixture was centrifuged at 6500g for 30 min at room temperature and the supernatant was discarded. The UCNPs were washed several times with redispersion by vortex and sonication in ethanol and finally with acetone. The nanoparticles were dried under vacuum yielding 140 mg of amine-functionalized UCNPs. UCNP@NH_2 with a lower amount of amine groups were prepared similarly by adding 7.5 or 15 µL of APTS (38 and 76 µmol respectively) yielding to 121 and 129 mg of UCNP@$NH_{2,low}$ and UCNP@$NH_{2,medium}$ respectively.

4.2. Synthesis of CPABD-functionalized UCNPs (UCNP@CPABD)

120 mg of UCNP@$NH_{2,high}$ were dispersed in 5 mL of DMF. A solution of HBTU (154 mg, 0.4 mmol), HOBt (55 mg, 0.4 mmol), CPABD (113 mg, 0.4 mmol) and DIPEA (142 µL, 0.8 mmol) in 2 mL of DMF was added to the dispersion of UCNP@NH_2 under argon. The reaction mixture was stirred vigorously overnight at room temperature. The UCNPs were then collected by centrifugation and washed five times with DMF and three times with acetone by redispersion in the solvent followed by sonication for 10 s. UCNP@CPABD with a high CPABD grafting density (UCNP@$CPABD_{high}$) was finally dried under vacuum at room temperature for 48 h affording 115 mg of UCNP@$CPABD_{high}$ (95% yield). The preparation of UCNP@CPABD with a medium (UCNP@$CPABD_{medium}$) and low (UCNP@$CPABD_{low}$) CPABD grafting density were carried out according to the same protocols using 77 mg of HBTU (0.2 mmol), 22.5 mg of HOBt

(0.2 mmol), 57 mg of CPABD (0.2 mmol) and 71 µL of DIPEA (0.4 mmol) for UCNP@CPABD$_{medium}$ and 39 mg of HBTU (0.1 mmol), 12 mg of HOBt (0.1 mmol), 29 mg of CPABD (0.1 mmol) and 40 µL of DIPEA (0.2 mmol) for UCNP@CPABD$_{low}$.

4.3. Preparation of polyHPMA from UCNP@CPABD by surface-initiated RAFT polymerization from UCNPs (UCNP@polyHPMA)

In a 5 mL round bottom flask, 30 mg of UCNP@CPABD, 250 mg of HPMA (1.7 mmol), 2.52 mg of CPABD (9 µmol, 3 mM), and 3 mL of solvent (1,4-dioxane, DMF or MeOH) were added and dispersed under ultrasonication for 6 min (three times 2 min in a cold water bath). 0.33 mg of AIBN (2 µmol) dissolved in 50 µL of the solvent used for the polymerization was added to the reaction flask. The reaction mixture was degassed by bubbling argon into the solution for 30 min. The reaction mixture was stirred in an oil bath thermostated at 65 °C. For kinetic studies, aliquots were withdrawn at predetermined intervals during the polymerization to determine the monomer conversion of the polymer formed in solution. HPMA conversion was determined by ^{1}H NMR spectroscopy by comparing the integration of the vinyl protons at 5.7 ppm of HPMA to the integration of the methyl protons at 0.5-1.1 ppm of the backbone of polyHPMA. After 24 h of reaction, the reaction mixture was then quenched by placing the reaction flask in an ice bath. UCNP@polyHMPA were isolated by centrifugation. The supernatant was collected and precipitated in Et_2O to isolate the polymer formed in solution. UCNP@CPABD were further purified by performing cycles of centrifugation and redispersion in MeOH (five times) and acetone (twice) to remove any ungrafted polymer. The polymers formed in solution and at the surface of UCNPs (UCNP@polyHMPA) were dried under vacuum at room temperature for 48 h.

4.4. Preparation of HBP from UCNP@CPABD by surface-initiated RAFT copolymerization (UCNP@HBP)

30 mg of UCNP@CPABD, 250 mg of HPMA (1.7 mmol), 3.52 mg of MA-CPABD (90 µmol), and 3 mL of 1,4-dioxane were placed in a 5 mL bottom flask and dispersed under ultrasonication for 6 min (2 min × 3) in a water bath at 10 °C. 0.33 mg of AIBN (2 µmol) dissolved in 50 µL of 1,4-dioxane was added the reaction mixture. The reaction mixture was degassed by bubbling argon into the solution for 30 min. The reaction mixture was stirred in an oil bath

thermostated at 65 °C. For kinetic studies, aliquots were withdrawn at predetermined intervals during the polymerization to determine the monomer conversion of the polymer formed in solution. After 24 h of reaction, the reaction mixture was then quenched by placing the reaction flask in an ice bath. UCNP@HBP were isolated by centrifugation, MeOH was added to redisperse the nanoparticles and centrifuged again. The supernatant was collected after each washing step. The degree of branching (DB), monomer conversion and molecular weight of the polymer formed in solution were determined by UV-vis spectroscopy, ^{1}H NMR spectroscopy, and SEC measurement respectively. UCNP@HBP were further purified by performing cycles of centrifugation and redispersion three times in successively 1,4-dioxane, MeOH, and acetone to remove any ungrafted polymer. The polymers formed in solution (HBP_{sol}) and at the surface of UCNPs (UCNP@HBP) were dried under vacuum at room temperature for 48 h. The UCNPs were dried under vacuum at room temperature for 48 h.

4.5. Cleavage of the polymers from the surface of UCNPs

30 mg of UCNP@polymer dispersed in 2.5 mL of deionized water were sonicated for 2 min before adding 0.5 mL of 40 % HF (Caution: HF is highly corrosive). The solution was shaken for 4 h and then neutralized by adding very slowly a saturated solution of $NaHCO_3$. The mixture was dialyzed against water for 2 days and then centrifuged to collect the supernatant that was lyophilized.

4.6. Monitoring of CPABD concentration by UV-vis spectroscopy

For accurate comparison, a stock solution of CPABD was prepared using one part for the polymerization and another part as control. After polymerization, the supernatant was collected from the washing steps and concentrated by rotary evaporation. The pink residue was dissolved in 5 mL of MeOH and the solutions were characterized by UV-vis spectroscopy.

5. Experimental protocols for Chapter 4

5.1. 5-FU loading

5.1.1. Passive loading

Loading. 5-FU (1 to 5 mg) was dissolved in 0.5 mL of water, while 5 mg of UCNP@HBP or UCNP@polyHPMA was dispersed in 1 mL of water and sonicated for 30 s. The drug solution

and suspension of UCNP@polymer were mixed, sonicated for 30 s and shacked at room temperature for 24 h as depicted in Figure E1. The mixture was centrifuged at 6,500 g for 10 min at room temperature and the supernatant was discarded. The loaded UCNP@polymer were washed by redispersion in 1 mL of water followed by vortexing, centrifuged discarding the supernatant, and dried under vacuum.

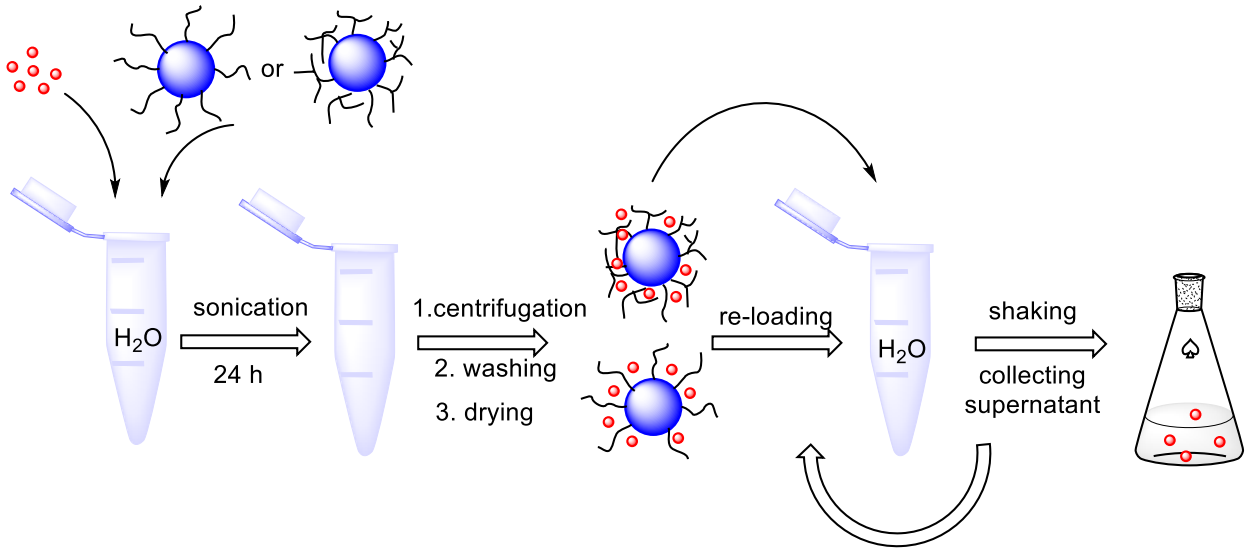

Figure E.1. Passive loading of 5-FU in UCNP@polyHPMA and UCNP@HBP.

Quantification. 2.5 mg of loaded UCNPs was dispersed in 2 mL of distilled water that was shaken for 3 h. The supernatant was collected after centrifugation and the UCNPs were redispersed in fresh distilled water. These steps were repeated to collect the supernatant 6, 24 and 48 h from the beginning of the experiment. The supernatants were combined and the volume was adjusted to 25 mL. The absorbance value of 5-FU was determined at 265 nm by UV spectroscopy. The amount of drug was determined from the calibration curve of 5-FU in water (Figure 4.1).

5.1.2. Conjugation on UCNP@HBP

Loading. 10 mg of UCNP@HBP was sonicated for 2 min (2×1 min) in 2 mL of anhydrous DMF. 10 mg of 5-FU-COOH (0.054 mol) and 41 mg of HBTU (0.108 mmol) were dissolved in 1 mL of DMF that were placed in an ice bath for 10 min. 0.04 mL of DIPEA (0.216 mmol) was added to the solution of 5-FU-COOH. After 10 min, the solution of UCNP@HBP were added dropwise. The mixture was allowed to stir overnight at room temperature. The solution was centrifuged and the particles were collected. Cycles of centrifugation and redispersion in DMF and water

were repeated at least five times to ensure that no free drug remained at the surface of UCNPs. The product was freeze-dried.

Quantification. To determine the amount of 5-FU conjugated on the polymer, the drug was cleaved using KOH and quantified by UV spectroscopy. Briefly, 2 mg of 5-FU-conjugated UCNP@HBP were dispersed in 2 mL of 50/50 water/THF and sonicated for 1 min. 95 mg of KOH were added to the solution that was stirred in an oil bath at 50 °C overnight. The mixture was centrifuged and the supernatant was collected. Cycles of centrifugation and redispersion in water were repeated three times. All the supernatants were collected and concentrated by rotary evaporation. The resulting solution was neutralized with diluted HCl. The solution was added in a 25 mL volumetric flask that was filled with water used for characterization by UV-Vis spectroscopy at 275 nm. The concentration in drug was calculated based on the calibration curve (Figure 4.5). Drug loading and encapsulation efficiency were calculated from Equations 1 and 2 respectively.

$$\text{Drug loading (wt\%)} = \frac{\text{drug weight in nanocarrier}}{\text{weight of nanocarrier}} \times 100$$

Equation 1

$$\text{Encapsulation efficiency (\%)} = \frac{\text{drug weight in nanocarrier}}{\text{weight of the feeding drugs}} \times 100$$

Equation 2

5.2. 5-FU release

Drug release studies were carried out in PBS buffer (pH 7.4) at 37 °C. 2 mg of samples were dispersed into 2 mL of PBS buffer. The solution was dialyzed against 50 mL of PBS buffer at 37 °C under a gentle agitation. 2 mL of the release medium was withdrawn at predetermined times and replaced with an equal volume of fresh medium to keep the total volume constant. Using UV–Vis spectroscopy at 265 nm, the drug release percentage was calculated with respect to the initial drug content using the 5-FU standard calibration curve (Figure 4.1) using Equation 3.

$$\text{drug release (\%)} = \frac{\mathrm{M_t}}{\mathrm{M_0}} \times 100$$

Equation 2

where M_0 and M_t represent the amount of loaded and released drug at time t, respectively.

5.3. Preparation of cathepsin B-sensitive transmer (MA-GLFG-CPABD)

The synthesis involved first solid-phase peptide synthesis to obtain GLFG-CPABD followed by its coupling to HEMA in solution.

5.3.1. Synthesis of GLFG-CPABD

1 g of 2-chlorotrityl chloride resin (1.6 mmol) was swollen in 10 mL of DCM in a 25 mL SPE tube and washed 3 times with DCM. 0.38 g of Fmoc-Gly-OH (1.28 mmol, 0.8 eq) was added to the tube. The vessel was degassed by performing three vacuum/argon cycles. 8 mL of anhydrous DCM was added and agitated for 10 min under argon. 0.9 mL of DIPEA (5.12 mmol, 3.2 eq) was added and the mixture was agitated for 90 min under argon. The solution was filtered and the resin was washed six times with DMF. 10 mL of a solution of DCM, MeOH, and DIPEA (8:1.5:0.5) was added to tube and agitated for 10 min (twice). The solution was filtered and the resin was washed six times with DMF and DCM. The resin was dried under vacuum at room temperature for 48 h. The grafting density in glycine on the resin was determined by gravimetric analysis as 1.1 mmol/g. Fmoc protecting groups were removed by agitation for 5 min with 10 mL of 25 v% piperidine in DMF. After filtration and washing the resin, a fresh solution was added and agitated for 30 min followed by washing with DMF and DCM.

The other amino acids were added iteratively using the following protocol. Fmoc-amino acid-OH (2.2 mmol,2 eq), HBTU (0.83 g, 2.2 mmol) and HOBt (0.30 g, 2.2 mmol) were weighted in a vial and dissolved in 8 mL of anhydrous DMF. 1.5 mL of DIPEA (8.8 mmol) were added to the solution that was poured into the SPE tube containing the resin. The mixture was agitated for 90 min. After filtration and washing the resin, the deprotection step was conducted with 25 v% piperidine in DMF and the resin was washed with DMF and DCM.

The peptide sequence was then end-capped with CPABD using a similar protocol using replacing Fmoc-amino acid-OH by CPABD (205 mg, 0.7 mmol). The resin was transferred to a glass vessel. A solution of 20 v% TFE in DCM was added to cleave GLFG-CPABD from the resin and agitated for 1 h. The solution was extracted from resin by filtration. The cleaving steps were performed three times. The solution was concentrated by rotary evaporation and the product was isolated by precipitation in diethyl ether. The product was dried under vacuum for 48 h at room temperature (2/3 of resin: 430 mg, 90%).

^{1}H NMR (400 MHz, CD_3OD, 3.31) δ 7.90-7.93 (m, 2H), 7.58-7.60 (m, 1H), 7.42-7.44 (m, 2H), 7.41-7.19 (m, 5H), 4.58-4.62 (m, 1H), 4.41-4.43 (m, 1H), 3.72-3.87 (m, 4H), 3.13-3.15 (m, 1H), 2.93-2.96 (m, 1H), 2.54-2.64 (m, 2H), 2.37-2.51 (m, 1H), 1.93 (s, 2H), 1.55-1.72 (m, 3H), 0.87-0.94 (m, 6H). ^{13}C NMR (101 MHz, CD_3OD, 49.00) δ 173.49, 172.74, 172.02, 171.22, 170.61, 144.75, 136.83, 132.88, 128.97, 128.40, 128.19, 126.50, 126.30, 118.48, 54.83, 51.79, 46.02, 42.50, 40.45, 40.28, 37.02, 33.38, 30.42, 24.34, 22.96, 22.18, 20.55.

5.3.2. Synthesis of MA-GLFG-CPABD

400 mg of GLFG-CPABD (0.61 mmol, 1 eq), 150 µL of HEMA (1.22 mmol, 2 eq) and 0.46 mg of HBTU (1.22 mmol, 2 eq) were dissolved in 3 mL of DMF in a 5 mL bottom flask, which was then put in ice bath for 10 min. 426 µL of DIPEA (2.44 mmol, 4 eq) was added to the mixture. After 20 min, the ice bath was removed and the mixture was kept to stir for 16 h at room temperature. The mixture was precipitated in cold water. The precipitate was collected by centrifugation and dried under vacuum for 24 h. The product was dissolved in MeOH and precipitated in cold diethyl ether twice. The compound was passed through a C18 column (Discovery® DSC-18 SPE Tube) using a mixture of 30/70 water/acetonitrile and the main fraction was isolated and concentrated by rotary evaporation The product was redissolved in MeOH and precipitated in cold diethyl ether. The product was collected by centrifugation and dried under vacuum at room temperature for 48h yielding a pink powder (390 mg, 83%).
^{1}H NMR (400 MHz, CD_3OD, 3.31) δ 7.87-7.98 (m, 2H), 7.55-7.65 (m, 1H), 7.38-7.47 (m, 2H), 7.11-7.31 (m, 5H), 6.10 (s, 1H), 5.62 (s, 1H), 4.55-4.72 (m, 1H), 4.29-4.54 (m, 1H?), 3.92 (s, 2H), 3.68-3.89 (m, 4H), 2.88-3.29 (m, 2H), 2.35-2.65 (m, 4H), 1.94 (s, 3H), 1.92 (s, 3H), 1.52-1.76 (m, 2H), 1.24-1.40 (m, 2H), 0.69-1.01 (m, 6H). ^{13}C NMR (NMR (101 MHz, CD_3OD, 49.00) δ 174.98, 174.14, 173.35, 172.06, 170.80, 168.52, 146.16, 138.22, 137.43, 134.22, 130.32, 129.76, 129.56, 127.88, 127.66, 126.65, 119.86, 64.04, 63.68, 56.24, 53.23, 47.45, 43.97, 41.94, 41.65, 38.30, 34.81, 31.82, 25.73, 24.33, 23.51, 21.93, 18.39. ESI-MS (m/z) $[M+H]^+$ calculated from C38H47N5O8S2Na 788.28, found 788.27.

5.4. Preparation of stimuli-responsive HBP from UCNP@CPABD$_{high}$ by surface-initiated RAFT copolymerization (UCNP@HBP$_{redox}$ and UCNP@HBP$_{enzyme}$)

30 mg of UCNP@CPABD$_{high}$, 250 mg of HPMA (1.7 mmol), and 3 mL of 1,4-dioxane (3.0 mL) with either 3.52 mg of MA-SS-CPABD (90 µmol) or 6.9 mg of MA-GFLG-CPABD (90 µmol) were

added to a 5 mL round bottom flask and dispersed under ultrasonication for 6 min (2 min × 3) in a cold water bath. 0.33 mg of AIBN (2 µmol) dissolved in 50 µL of 1,4-dioxane was added to the reaction mixture that was purged by bubbling argon for 30 min. Polymerization was carried out in a preheated oil bath thermostated at 65 °C for 24 h. The reaction was stopped by placing the vessel in an ice-water bath. The UCNPs were separated by centrifugation. Cycles of centrifugation and redispersion of UCNPs in successively 1,4-dioxane, MeOH and acetone (three times for each solvent) were performed to remove any ungrafted polymer from the nanohybrids.

5.5. Degradation study of redox-responsive HBP grafted on UCNPs in the presence of DTT

20 mg of UCNP@HBP_{redox} were dispersed in 4 mL of PBS (ph = 7.4) by ultrasonication. The solution was divided into two parts (solutions A and B). 2 mL of 20 mM of DTT in PBS was added to solution A, while 2 mL of PBS (pH = 7.4) was added to solution B (control). The solutions were shaken at 37 °C for 24 h. The nanoparticles were separated by centrifugation and washed several times with distilled water. The nanoparticles were dispersed in water by sonication and one droplet was taken for DLS measurement. Finally, the nanoparticles were separated and dried under vacuum for 48 h.

5.6. Synthesis of Rhodamine B-GFLG

GLFG sequence was synthesized by solid-phase peptide synthesis as in Section 5.3.1. The end-capping was performed on 0.2 g of resin bearing the GLFG sequence (0.4 mmol) with 0.38 g of Rhodamine B (0.8 mmol, 2eq) in the presence of 0.12 mL of DIC (0.8 mmol, 2eq) and 0.1 g of HOBt (0.8 mmol, 2eq) in 6 mL of a mixture of DMF and DCM (50:50). The solution was agitated for 16 h at room temperature under argon. The resin was washed six times with DMF and six times with DCM. To remove all unreacted Rhodamine B, the resin was agitated with 30 mL of a mixture of DCM and DMF (50:50) overnight. Rhodamine B-GFLG was isolated after cleavage from the resin as described in Section 5.3.2 using 20% TFE in DCM as a pink solid.

5.7. Conjugation of Rhodamine B-GFLG on UCNP@HBP_{redox}

25 mg of UCNP@HBP_{redox} dispersed in 3 mL of DMF was sonicated for 2 min (1 min × 2). 10 mg of Rhodamine B-GFLG (0.012 mmol) and 9.1 mg of HBTU (0.024 mmol) were dissolved in 0.5 mL of DMF and placed in an ice bath for 10 min. 20 µL of DIPEA (0.049 mmol) was added

followed by the suspension of UCNP@HBP dropwise. The solution was stirred overnight at room temperature and then centrifuged to collect the nanoparticles. Cycles of centrifugation and redispersion in DMF, water, and MeOH were repeated at least five times to ensure the full removal of unreacted Rhodamine B-GFLG. The pink product was dried under vacuum at room temperature for 48 h.

5.8. Degradation rate of the polymer in the presence of DTT

10 mg of redox-sensitive of Rhodamine B-labeled UCNP@HBP_{redox} was dispersed in 1 mL of water. 1 mL of 20 mM DTT in water was added. The solution was agitated on a shaker at 37 °C for 15 min and centrifuged to collect the supernatant. The nanoparticle was redispersed in water and a fresh solution of DTT was added. The procedure was repeated to collect the supernatant at 30 min, 2 h and 3 days of incubation.

CONCLUSION AND PERSPECTIVES

The objective of this work was to develop a platform for theranostics based on hyperbranched polymers (HBPs) acting as drug carrier and upconversion nanoparticles (UCNPs) as bioimaging probe. The first part of this work focused on the synthesis of UCNPs and more specifically on the effect of the type of reactor (i.e. flask and microtube) used for the phase transition between α- and β-phase nanocrystals. Based on experimental evidences, we summarized the fate of α-phase nanocrystals namely nucleation, growth by coalescence and Oswald ripening, rearrangement to irregular shape nanocrystals, dissolution and phase transition as a function of the heat treatment temperature and type of reactor. To the best of our knowledge, for the first time was observed that α-$NaYF_4$:Yb,Er nanocrystals passed through an anisotropic metastable intermediate by a coalescence mechanism, similar to the so-called oriented attachment, before to rearrange and dissolve to give rise to the β-$NaYF_4$:Yb,Er nanocrystals by Ostwald ripening phenomenon. The resultant β-$NaYF_4$:Yb,Er nanocrystals with rod-like shape showed a longitudinal epitaxy growth unlike the flask system which promoted a symmetric epitaxy growth The diameter of microtube plays a critical role in the shape evolution of the final products from spheres to nanorods due to different dissolution rates of α-$NaYF_4$:Yb,Er nanocrystals. By tuning the temperature and diameter of microtube, different nanorods in size were prepared. To conclude, microtube could be a promising reactor in order to scale up the production of nanorods UCNPs.

From this original work, several perspectives could be considered, such as:

1. Investigation of the effect of solvent ratio and capping agent
2. Promotion of an internal mixing in the microtube (e.g. by intense vibration) in order to understand the effect of collision of nanocrystals in phase transition and comparison with static condition
3. Investigation of different compositions of UCNPs with addition of some doping agent, e.g. Gd^{+3} and Li^{+}
4. Preparation of core-shell UCNP nanorods using microtube (i.e. producing anisotropic shell)
5. Investigation of luminescence properties of the β-$NaYF_4$:Yb,Er nanorods produced with different microtube IDs
6. Investigation of continuous-flow synthesis of β-$NaYF_4$:Yb,Er nanocrystals using the microtube system

7. Investigation of an oscillated heating system in continuous- flow process in order to better understand the effect of temperature gradient during phase transition.

Having in hands tools to tune the shape, size and phase of UCNPs, and aiming at growing hyperbranched polymers at their surface, a silica shell bearing amine groups was prepared using reported protocols in the literature. The presence of amine groups was used to attach a RAFT chain transfer agent to promote the growth of a biocompatible polymer based on *N*-(2-hydroxypropyl) methacrylamide (HMPA) from their surface. Hyperbranched polymers were prepared by self-condensing vinyl copolymerization with 2-methacryloyloxy)ethyl-4-cyano-4-((phenylcarbonothioyl)thio)pentanoate as transmer. By tuning the grafting density in chain transfer agent at the surface of UCNPs and the concentration in transmer, HBPs with different molecular weights and degrees of branching were prepared. Results revealed that the polymerization from the surface of UCNPs with a high grafting density in RAFT agent led to chain-chain coupling reaction leading to HBPs with high molecular weights and molecular weight distributions. However, the use of a low grafting density in RAFT agent afforded the preparation of HBPs with an acceptable degree of branching and narrow molecular weight distribution. In summary, termination reactions were the main challenge of this work and affected the preparation of hyperbranched polymers from the surface of UCNPs. Therefore, it would be interesting to investigate the effect of the polymerization temperature and the concentration in nanoparticles on the hyperbranched polymer obtained. Furthermore, more advanced RAFT polymerization techniques such as photo-induced electron/energy transfer (PET)-RAFT, and microwave assisted-RAFT polymerization could be of interest to decrease the probability of termination reactions occurring at the surface.

The nanohybrids based on UCNPs and HBPs were evaluated as potential carriers for 5-fluorouracil (5-FU). 5-FU was passively loading in the polymer corona of the synthesized nanohybrids, but low loading and low encapsulation stability were observed. 5-FU was then conjugated through an ester bond, which led to improved drug loading and encapsulation stability. Aiming at triggered drug release, nanohybrids based on hyperbranched polymers with redox- and enzyme-degradable branching points were prepared for the first time to the best of my knowledge. The prepared redox-sensitive system showed a tangible degradation in the presence of dithiothreitol making it a promising nanocarrier due to the enhanced accessibility of esterase to the ester bonds between the drug and the polymer. From this platform, triggered and targeted drug delivery could be envisaged. For triggered drug release

in cancer cells, a stimuli-responsive linkage between the drug and polymer would be considered instead of ester bonds. For instance, redox-sensitive linkage between 5-FU and polymer would be a promising strategy to simultaneously trigger drug release and degradation of the polymer in cancer cells. For targeted drug delivery, targeting ligands would be conjugated to the abundant terminal groups of UCNP@HBP to achieve active targeting. More precisely, thiol groups could be introduced on UCNP@HBP by aminolysis of CPABD terminal groups and used to conjugate the tripeptide Arg-Gly-Asp (RGD) functionalized with an acrylate group via Michael addition reaction to UCNP@HBP. Finally, these nanohybrids could be good candidates for theranostic due to the high potential of hyperbranched polymers for drug delivery and UCNPs as promising luminescence probe for bioimaging.

APPENDIX : Supplementary material

1. Appendix for Chapter 2

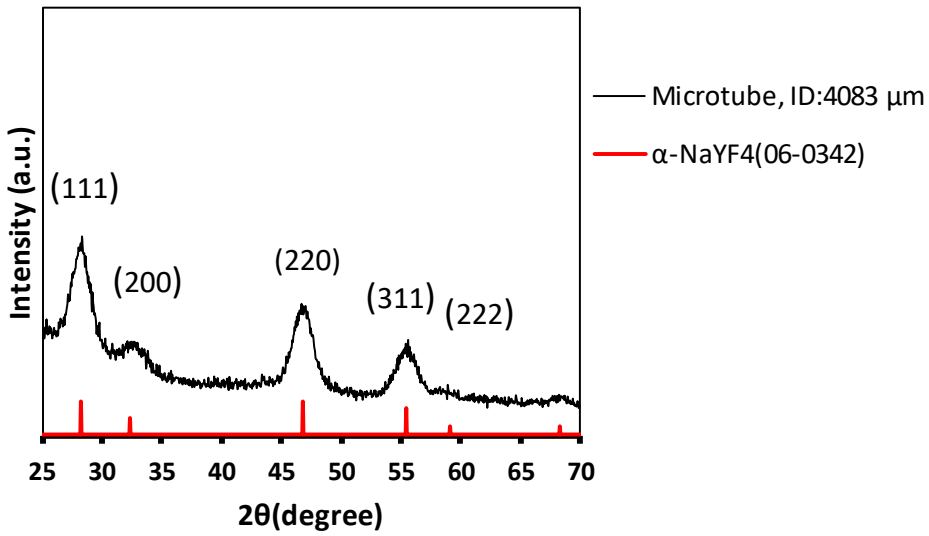

Figure A.2.1. XRD analyses of resultant nanocrystals at 300 °C in the 4083 µm microtube after 120 min heating.

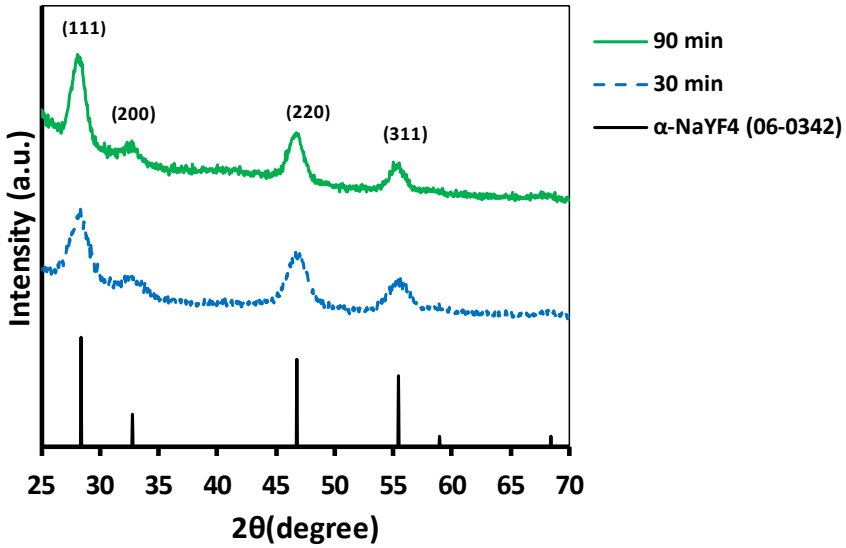

Figure A.2.2. XRD analyses of resultant nanocrystals at 310 °C in the 879 µm microtube for 30 and 90 min heating.

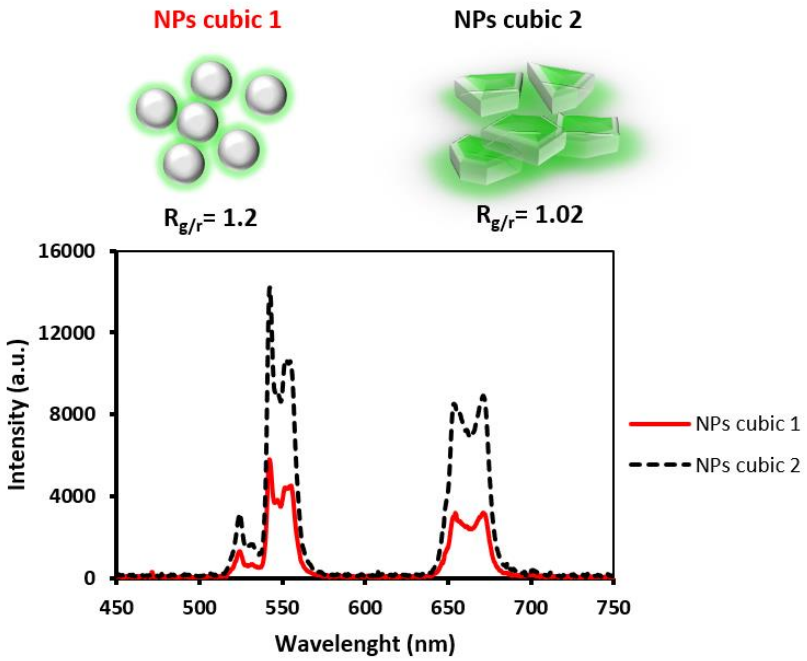

Figure A.2.3. Comparison of the luminescence intensity of α-$NaYF_4$:Yb,Er nanocrystals in 879 µm microtube at 310 °C after 30 min (red solid line) and 90 min (black dash line) of heating (λ_{ex} = 980 nm).

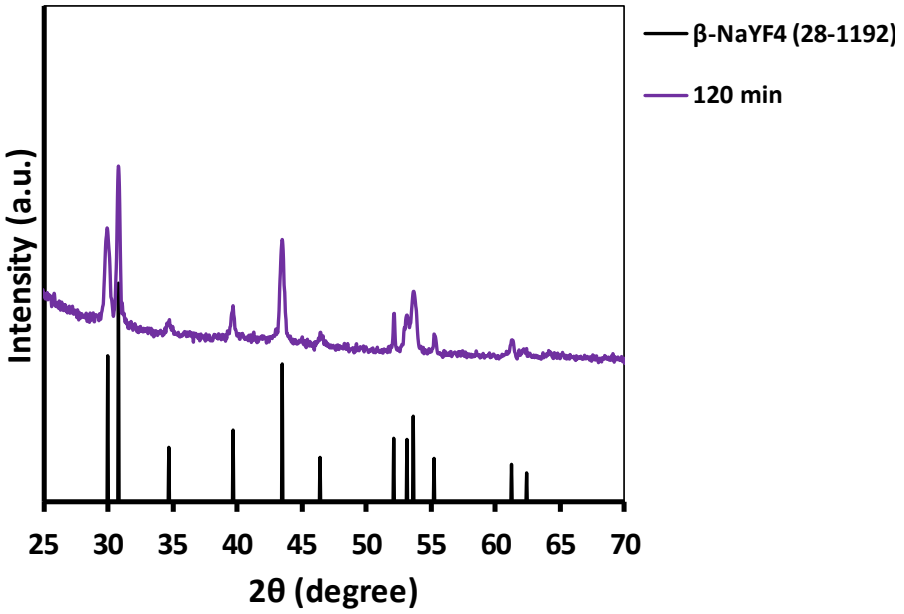

Figure A.2.4. XRD analysis of resultant nanocrystals at 310 °C in the 879 µm microtube for 120 min heating.

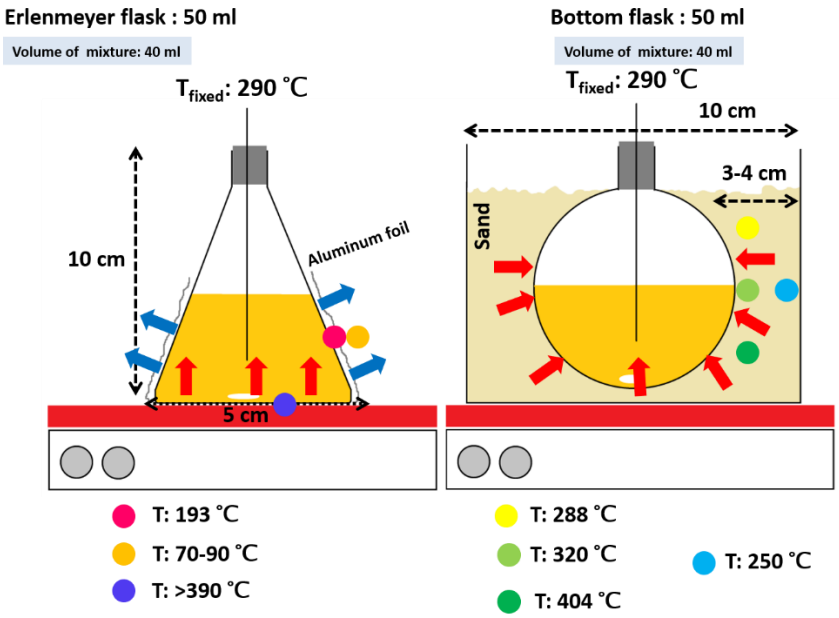

Figure A.2.5. Schematic illustration of the two setups used to investigate the effect of heat transfer in the synthesis of β-$NaYF_4$:Yb,Er nanocrystals at 290 °C: Erlenmeyer flask (left side) and round bottom flask (right side). The illustration shows as well the temperature as returned by a digital thermometer placed in different parts of the setups.

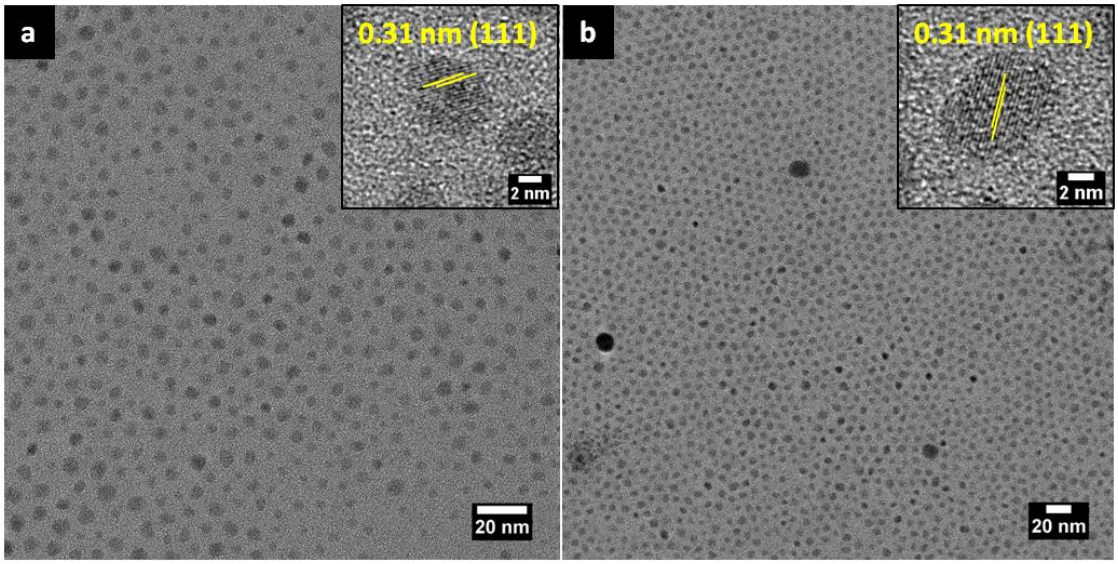

Figure A.2.6. TEM images of $NaYF_4$:Yb,Er nanocrystals obtained in 879 µm microtube after 60 min (a) and 150 min (b) heating at 290 °C.

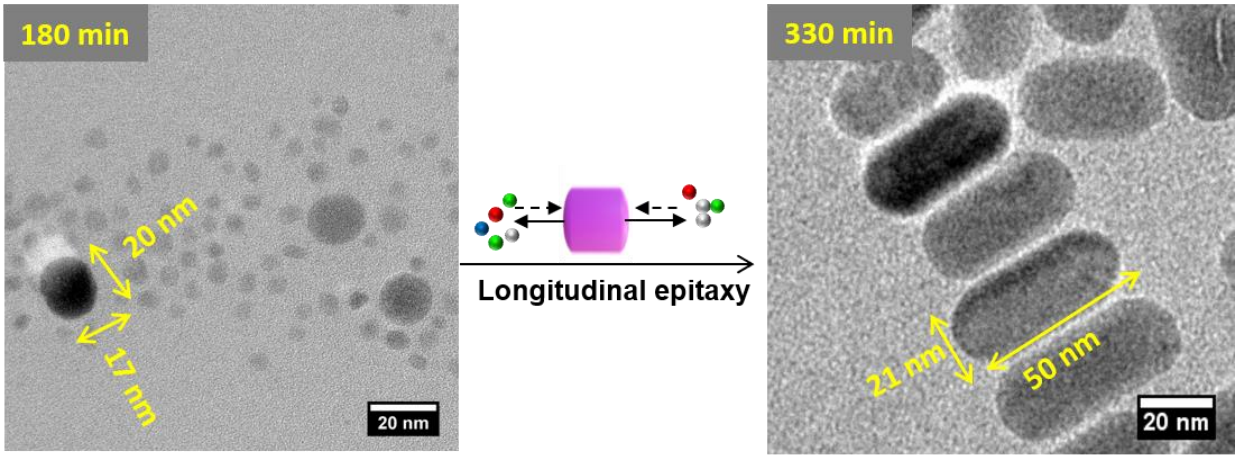

Figure A.2.7. Longitudinal epitaxial growth of β nanocrystals in 4083 µm microtube for different heat treatment times at 300 °C.

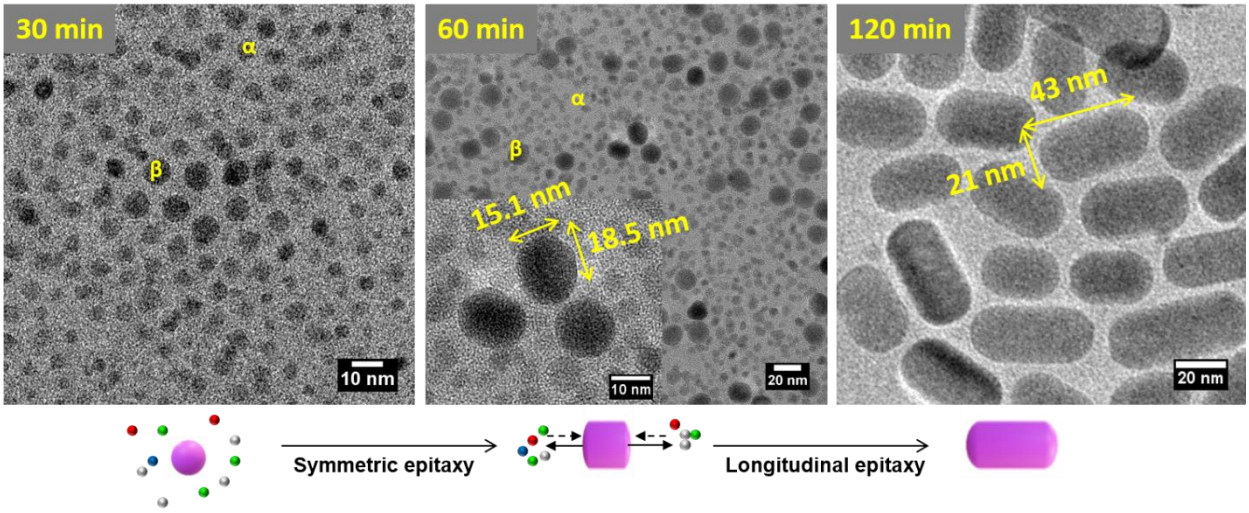

Figure A.2.8. Longitudinal epitaxial growth of β nanocrystals in 4083 µm microtube for different heat treatment times at 315 °C.

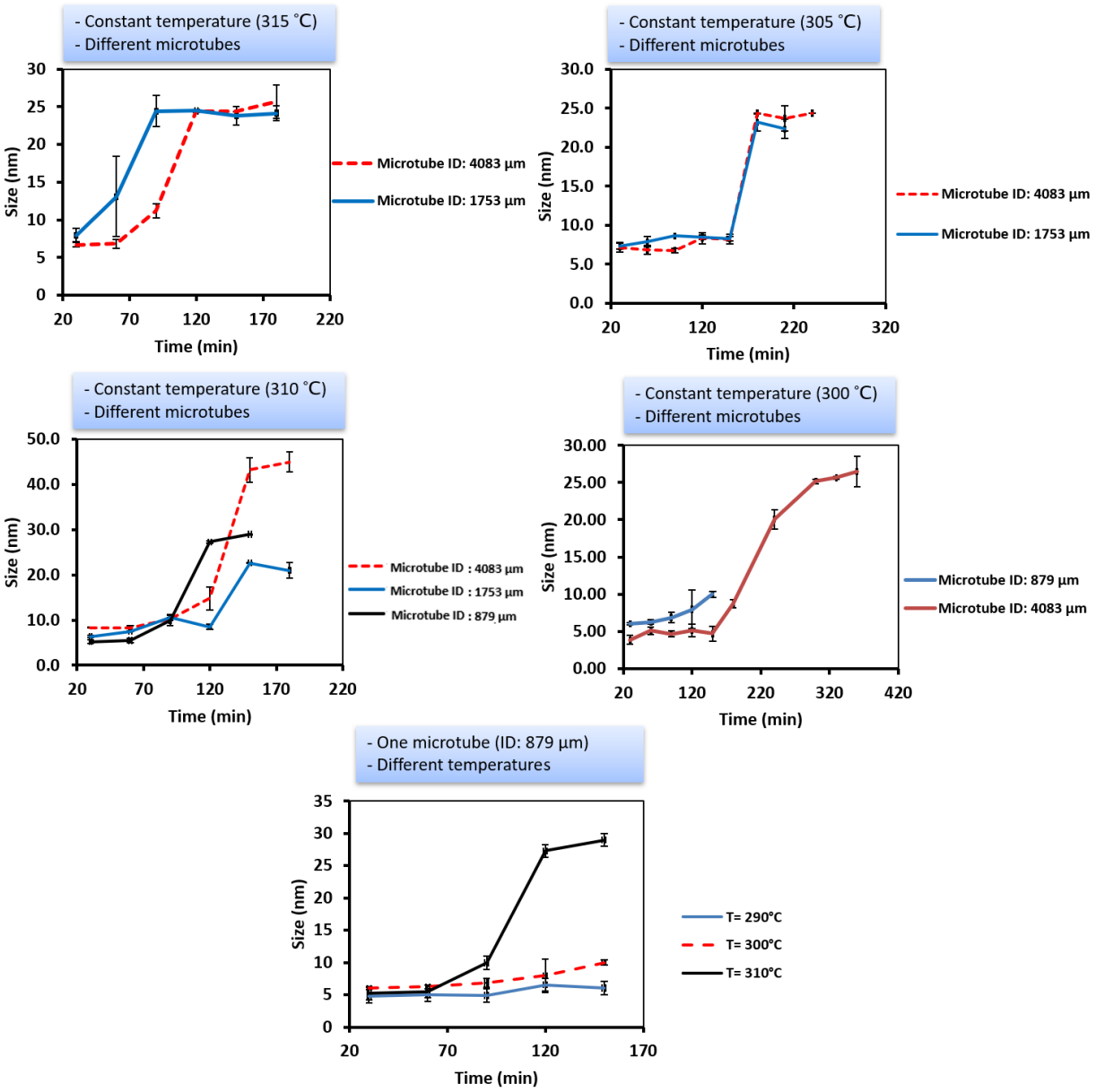

Figure A.2.9. Size evolution of obtained $NaYF_4$:Yb,Er nanocrystals for different microtubes and temperatures (from DLS measurements).

2. Appendix for Chapter 3

2.1. *N*-(2-Hydroxypropyl) methacrylamide (HPMA)

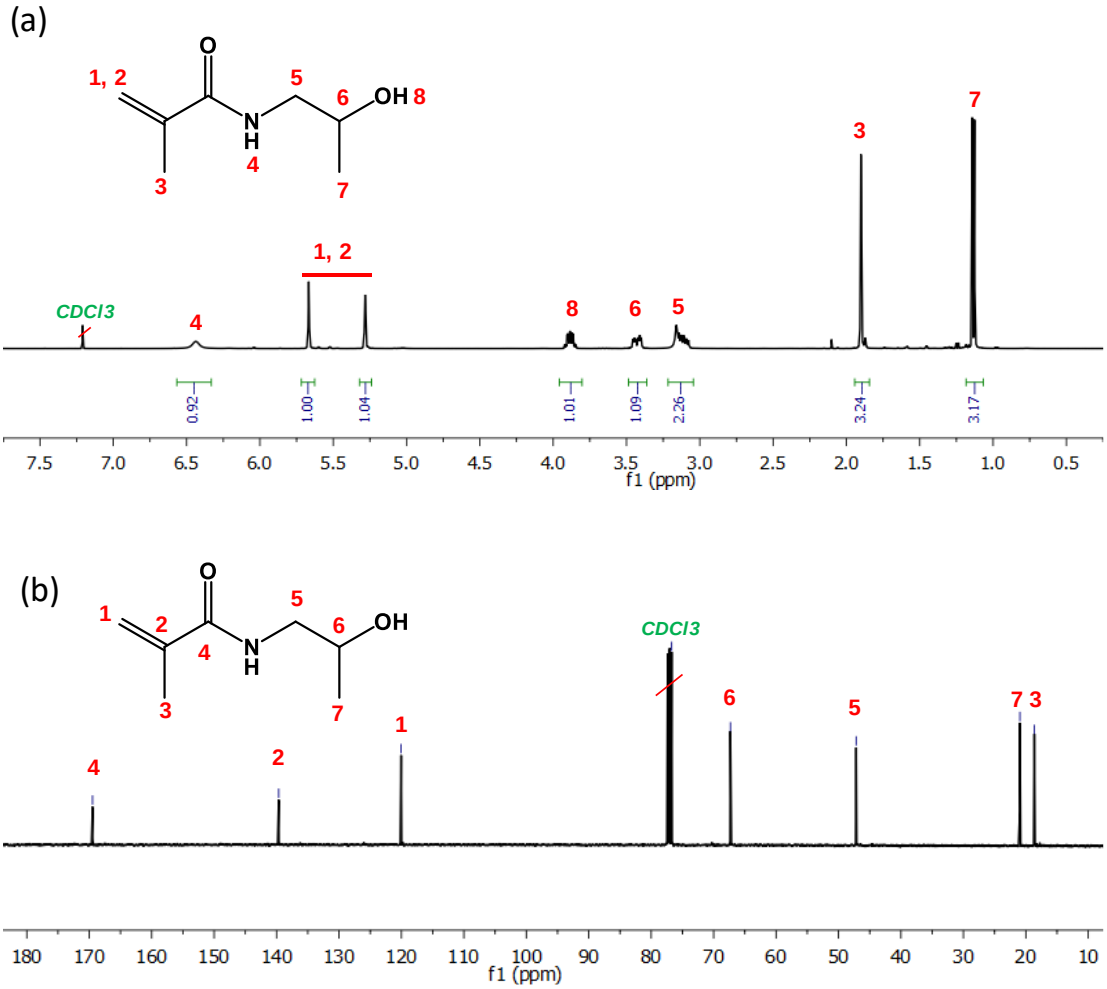

Figure A.3.10. ^{1}HNMR (a) and ^{13}CNMR (b) spectra of HPMA in $CDCl_3$

2.2. 2-(methacryloyloxy)ethyl 4-cyano-4-(phenylcarbonothioylthio)pentanoate (MA-CPABD)

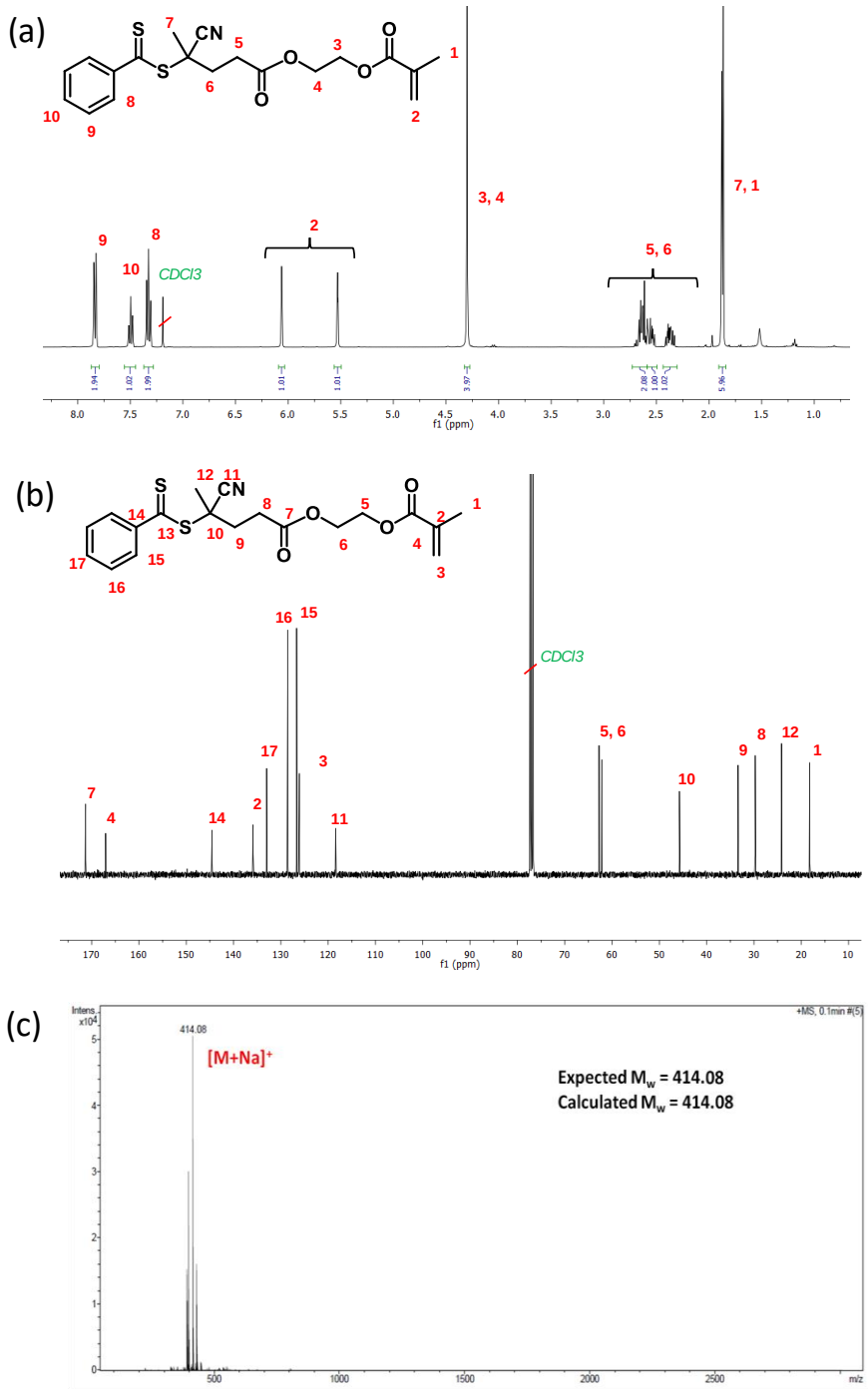

Figure A.3.11. ^{1}HNMR (a) and ^{13}CNMR (b) spectra in $CDCl_3$ and ESI-MS spectrum (c) of chain transfer monomer (CTM)

3. Appendix for Chapter 4

3.1. 5-FU-COOH

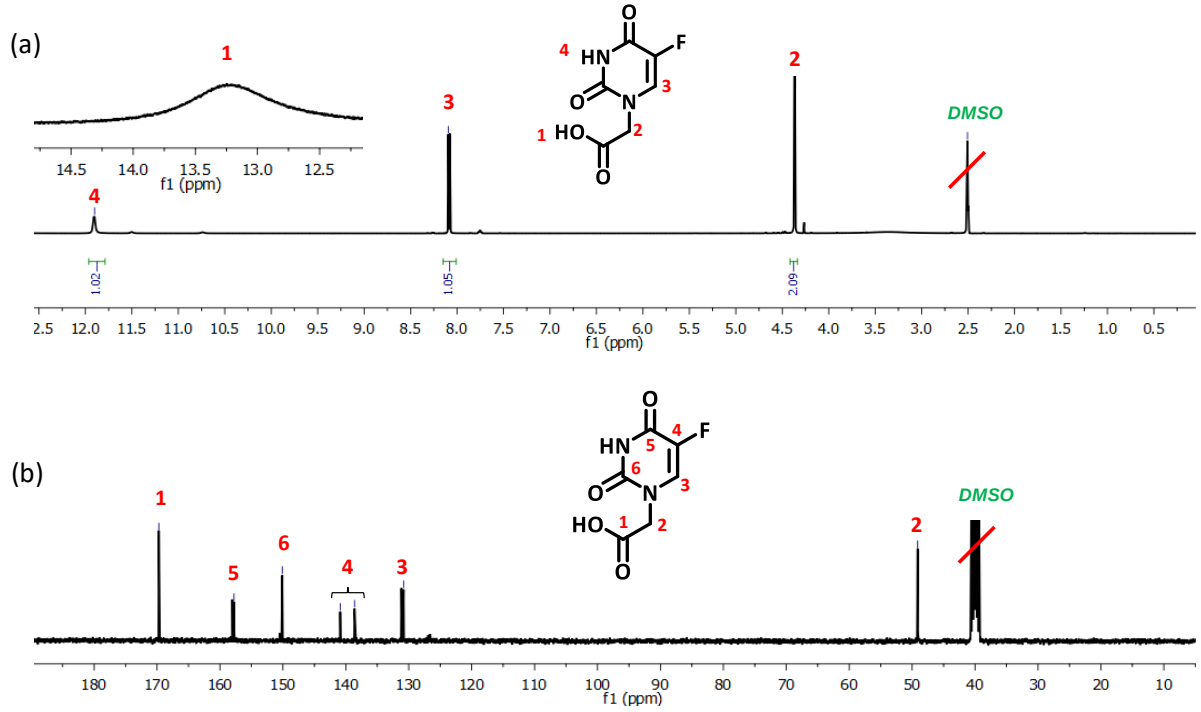

Figure A.4.12. ^{1}HNMR (a) and ^{13}CNMR (b) spectra of 5-FU-COOH in DMSO-d_6

3.2. redox-sensitive transmer (MA-SS-CPABD)

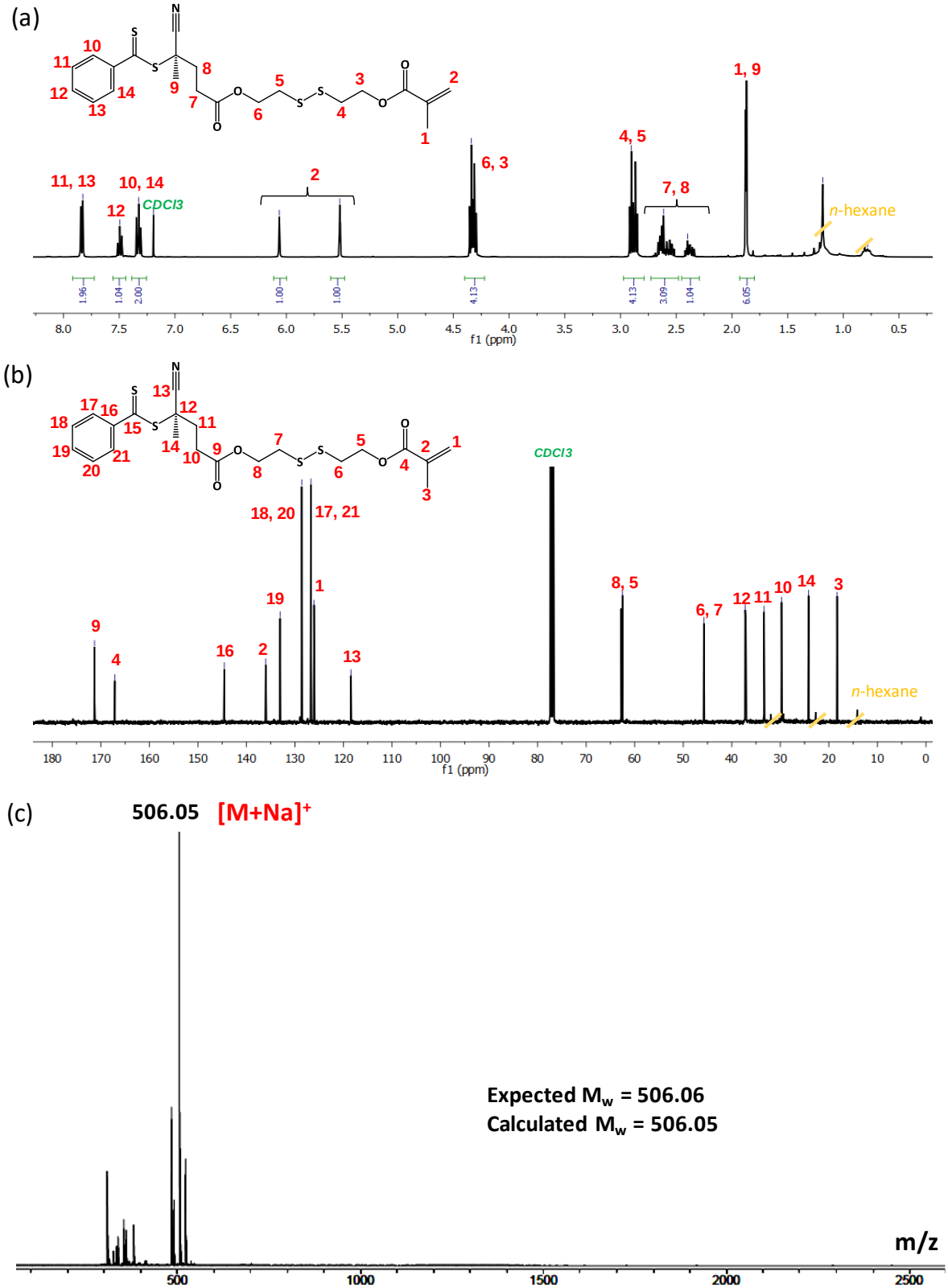

Figure A.4.13. ^{1}HNMR (a), ^{13}CNMR spectra (b) in $CDCl_3$ and ESI-MS (c) of MA-SS-CPABD

3.1. Rhodamine B-GFLG

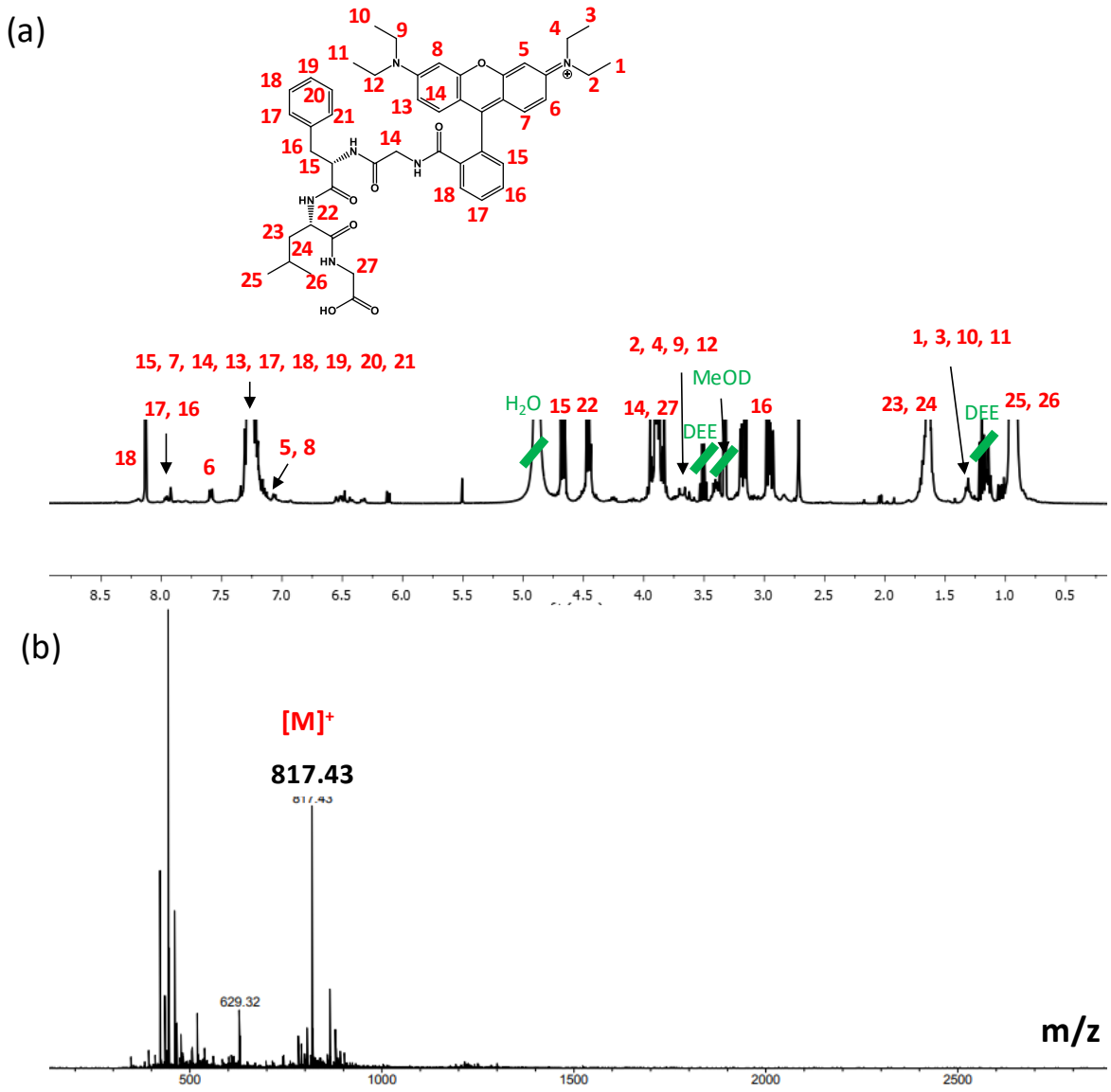

Figure A.4.14. [1]HNMR spectrum in MeOD (a) and ESI-MS spectrum (b) of Rhodamine B-GFLG

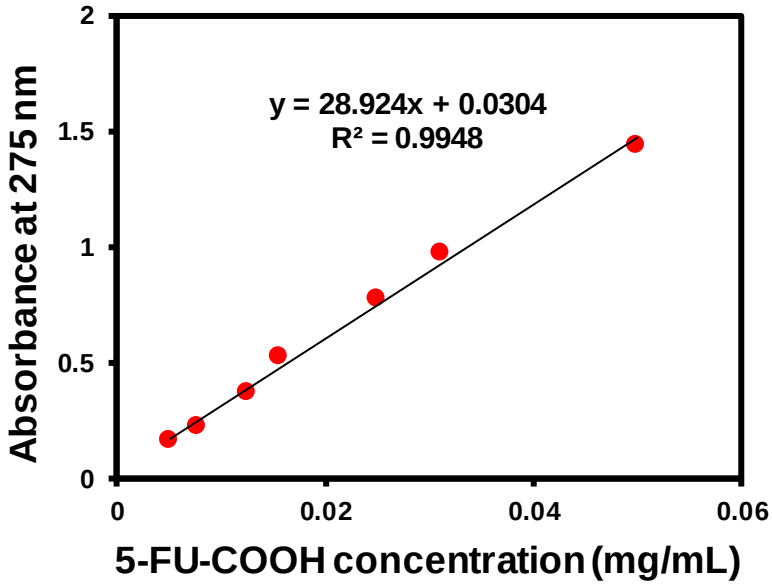

Figure A.4.15. Calibration curve of 5-FU-COOH in water by UV spectroscopy at 275 nm.

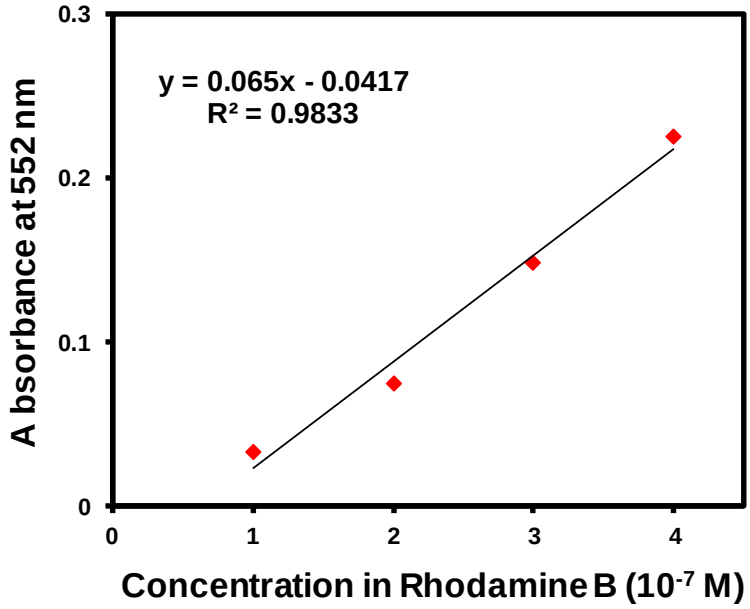

Figure A.4.16. Calibration curve of Rhodamine B in water at 552 nm.

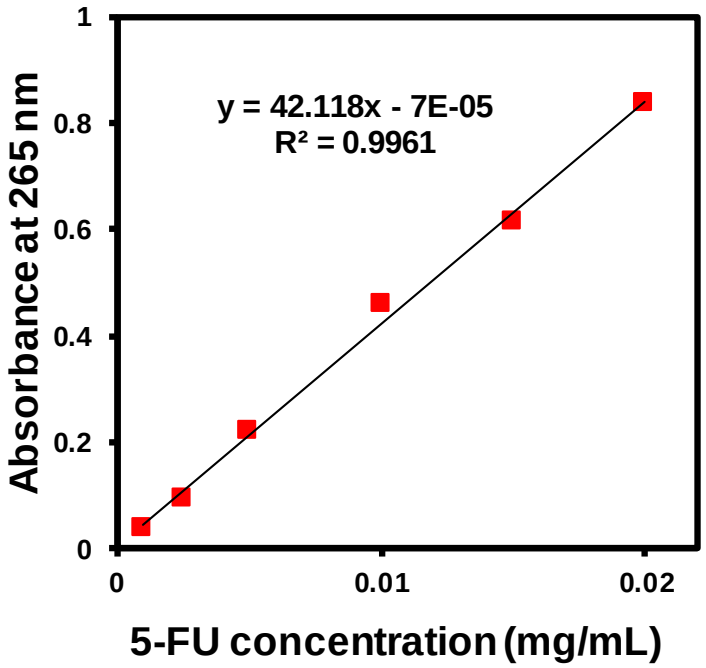

Figure A.4.17. Calibration curve of 5-FU in water by UV spectroscopy at 265 nm.

REFERENCES

[1] Baker JHE, McPhee KC, Moosvi F, Saatchi K, Häfeli UO, Minchinton AI, et al. Multi-modal magnetic resonance imaging and histology of vascular function in xenografts using macromolecular contrast agent hyperbranched polyglycerol (HPG-GdF). Contrast Media Mol Imaging 2016;11:77–88. doi:10.1002/cmmi.1661.

[2] Ding D, Wang G, Liu J, Li K, Pu K-Y, Hu Y, et al. Hyperbranched conjugated polyelectrolyte for dual-modality fluorescence and magnetic resonance cancer imaging. Small 2012;8:3523–30. doi:10.1002/smll.201201216.

[3] Rolfe BE, Blakey I, Squires O, Peng H, Boase NRB, Alexander C, et al. Multimodal polymer nanoparticles with combined 19F magnetic resonance and optical detection for tunable, targeted, multimodal imaging in vivo. J Am Chem Soc 2014;136:2413–9. doi:10.1021/ja410351h.

[4] Wang X, Shi Y, Graff RW, Cao X, Gao H. Synthesis of hyperbranched polymers with high molecular weight in the homopolymerization of polymerizable trithiocarbonate transfer agent without thermal initiator. Macromolecules 2016;49:6471–9. doi:10.1021/acs.macromol.6b00994.

[5] Luo K, Li C, Li L, She W, Wang G, Gu Z. Arginine functionalized peptide dendrimers as potential gene delivery vehicles. Biomaterials 2012;33:4917–27. doi:10.1016/J.BIOMATERIALS.2012.03.030.

[6] Zhang C, Pan D, Luo K, She W, Guo C, Yang Y, et al. Peptide dendrimer-doxorubicin conjugate-based nanoparticles as an enzyme-responsive drug delivery system for cancer therapy. Adv Healthcare Mater 2014;3:1299–308. doi:10.1002/adhm.201300601.

[7] Gao C, Yan D. Hyperbranched polymers: from synthesis to applications. Prog Polym Sci 2004;29:183–275. doi:10.1016/j.progpolymsci.2003.12.002.

[8] Peng Y-Y, Diaz-Dussan D, Kumar P, Narain R. Acid degradable cationic galactose-based hyperbranched polymers as nanotherapeutic vehicles for epidermal growth factor receptor (EGFR) knockdown in cervical carcinoma. Biomacromolecules 2018;19:4052–8. doi:10.1021/acs.biomac.8b01066.

[9] Zou L, Shi Y, Cao X, Gan W, Wang X, Graff RW, et al. Synthesis of acid-degradable hyperbranched polymers by chain-growth CuAAC polymerization of an AB_3 monomer. Polym Chem 2016;7:5512–7. doi:10.1039/C6PY01265E.

[10] Li F, Chen C, Yang X, He X, Zhao Z, Li J, et al. Acetal-linked hyperbranched polyphosphoester nanocarriers loaded with chlorin e6 for pH-activatable photodynamic therapy. ACS Appl Mater Interfaces 2018;10:21198–205. doi:10.1021/acsami.8b06758.

[11] Tonhauser C, Schüll C, Dingels C, Frey H. Branched acid-degradable, biocompatible polyether copolymers via anionic ring-opening polymerization using an epoxide inimer. ACS Macro Lett 2012;1:1094–7. doi:10.1021/mz300265z.

[12] Qi M, Li K, Zheng Y, Rasheed T, Zhou Y. Hyperbranched multiarm copolymers with a UCST phase transition: topological effect and the mechanism. Langmuir 2018;34:3058–67. doi:10.1021/acs.langmuir.7b04255.

[13] Kojima C, Yoshimura K, Harada A, Sakanishi Y, Kono K. Synthesis and characterization of hyperbranched poly(glycidol) modified with pH- and temperature-sensitive groups. Bioconjugate Chem 2009;20:1054–7. doi:10.1021/bc900016x.

[14] Sideratou Z, Agathokleous M, Theodossiou TA, Tsiourvas D. Functionalized hyperbranched polyethylenimines as thermosensitive drug delivery nanocarriers with controlled transition temperatures. Biomacromolecules 2018;19:315–28. doi:10.1021/acs.biomac.7b01325.

[15] Shi Y, Cao X, Zou L, Gan W, Gao H. Preparation of water-soluble hyperbranched polymers with tunable thermosensitivity using chain-growth CuAAC copolymerization. Polym Chem 2016;7:7500–5. doi:10.1039/C6PY01712F.

[16] Peng Y-Y, Diaz-Dussan D, Kumar P, Narain R. Tumor microenvironment-regulated redox responsive cationic galactose-based hyperbranched polymers for siRNA delivery. Bioconjugate Chem 2018;30:405–12. doi:10.1021/acs.bioconjchem.8b00785.

[17] Wang Y, Wei H, Zheng L, Wu Z, Zhang X, Zhang X. One-pot synthesis of dual-responsive hyperbranched polymeric prodrugs using an all-in-one chain transfer monomer. ACS Macro Lett 2018;7:1203–7. doi:10.1021/acsmacrolett.8b00603.

[18] Du G, Wang S, Yuan H, Wang J, Song Y, Liu T. Size-stable supramolecular hyperbranched polymer vesicles for redox-triggered double-drug release. Macromol Chem Phys 2018;220:1800467. doi:10.1002/macp.201800467.

[19] Chen C-J, Jin Q, Liu G-Y, Li D-D, Wang J-L, Ji J. Reversibly light-responsive micelles constructed via a simple modification of hyperbranched polymers with chromophores. Polymer 2012;53:3695–703. doi:10.1016/J.POLYMER.2012.06.024.

[20] Chen C, Liu G, Liu X, Pang S, Zhu C, Lv L, et al. Photo-responsive, biocompatible polymeric micelles self-assembled from hyperbranched polyphosphate-based polymers. Polym Chem 2011;2:1389–97. doi:10.1039/c1py00094b.

[21] Sun C, Ji S, Li F, Xu H. Diselenide-containing hyperbranched polymer with light-induced cytotoxicity. ACS Appl Mater Interfaces 2017;9:12924–9. doi:10.1021/acsami.7b02367.

[22] Dong R, Liu Y, Zhou Y, Yan D, Zhu X. Photo-reversible supramolecular hyperbranched polymer based on host–guest interactions. Polym Chem 2011;2:2771–4. doi:10.1039/c1py00426c.

[23] Wu W, Tang R, Li Q, Li Z. Functional hyperbranched polymers with advanced optical, electrical and magnetic properties. Chem Soc Rev 2015;44:3997–4022. doi:10.1039/C4CS00224E.

[24] Sun L, Li X, Wei X, Luo Q, Guan P, Wu M, et al. Stimuli-responsive biodegradable hyperbranched polymer-gadolinium conjugates as efficient and biocompatible nanoscale magnetic resonance imaging contrast agents. ACS Appl Mater Interfaces 2016;8:10499–512. doi:10.1021/acsami.6b00980.

[25] Yao M, Ma Y, Liu H, Khan MI, Shen S, Li S, et al. Enzyme degradable hyperbranched polyphosphoester micellar nanomedicines for NIR imaging-guided chemo-photothermal therapy of drug-resistant cancers. Biomacromolecules 2018;19:1130–41. doi:10.1021/acs.biomac.7b01793.

[26] Mallepally RR, Smirnova I, Arlt W, Seiler M, Klee-Laquai SK, Hills G. Enzymatic degradation of hyperbranched polyesters. J Appl Polym Sci 2009;112:1873–81. doi:10.1002/app.29524.

[27] Wang D, Jin Y, Zhu X, Yan D. Synthesis and applications of stimuli-responsive

hyperbranched polymers. Prog Polym Sci 2017;64:114–53. doi:10.1016/j.progpolymsci.2016.09.005.

[28] Liu J, Li K, Geng J, Zhou L, Chandrasekharan P, Yang C-T, et al. Single molecular hyperbranched nanoprobes for fluorescence and magnetic resonance dual modal imaging. Polym Chem 2013;4:1517–24. doi:10.1039/C2PY20837G.

[29] Xiong R, Cheng L, Tian Y, Tang W, Xu K, Yuan Y, et al. Hyperbranched polyethylenimine based polyamine-N-oxide-carboxylate chelates of gadolinium for high relaxivity MRI contrast agents. RSC Adv 2016;6:28063–8. doi:10.1039/C6RA03589B.

[30] Wang K, Peng H, Thurecht KJ, Puttick S, Whittaker AK. Segmented highly branched copolymers: rationally designed macromolecules for improved and tunable 19F MRI. Biomacromolecules 2015;16:2827–39. doi:10.1021/acs.biomac.5b00800.

[31] Wang K, Peng H, Thurecht KJ, Puttick S, Whittaker AK. Multifunctional hyperbranched polymers for CT/19F MRI bimodal molecular imaging. Polym Chem 2016;7:1059–69. doi:10.1039/c5py01707f.

[32] Hutchings L. Hyperbranched Polymers: synthesis, properties, and applications. vol. 51. Hoboken. N.J: John Wiley & Sons, Ltd; 2012. doi:10.1002/anie.201108985.

[33] Voit B. New developments in hyperbranched polymers. J Polym Sci Part A Polym Chem 2000;38:2505–25. doi:10.1002/1099-0518(20000715)38:14<2505::AID-POLA10>3.0.CO;2-8.

[34] Jikei M, Kakimoto M. Hyperbranched polymers: a promising new class of materials. Prog Polym Sci 2001;26:1233–85. doi:10.1016/S0079-6700(01)00018-1.

[35] Gao C, Yan D. Hyperbranched polymers: from synthesis to applications. Prog Polym Sci 2004;29:183–275. doi:10.1016/J.PROGPOLYMSCI.2003.12.002.

[36] Zheng Y, Li S, Weng Z, Gao C. Hyperbranched polymers: advances from synthesis to applications. Chem Soc Rev 2015;44:4091–130. doi:10.1039/C4CS00528G.

[37] Bhat SI, Ahmadi Y, Ahmad S. Recent advances in structural modifications of hyperbranched polymers and their applications. Ind Eng Chem Res 2018;57:10754–85. doi:10.1021/acs.iecr.8b01969.

[38] Voit BI, Lederer A. Hyperbranched and highly branched polymer architectures—synthetic strategies and major characterization aspects. Chem Rev 2009;109:5924–73. doi:10.1021/cr900068q.

[39] Kricheldorf HR, Fritsch D, Vakhtangishvili L, Schwarz G. Multicyclic poly(ether sulfone)s of phloroglucinol forming branched and cross-linked architectures. Macromolecules 2003;36:4337–44. doi:10.1021/ma021569i.

[40] Kricheldorf HR. Polycondensation of 'a − bn' or 'a2 + + bn' monomers - a comparison. Macromol Rapid Commun 2007;28:1839–70. doi:10.1002/marc.200700261.

[41] Kricheldorf HR. Hyperbranched cyclic and multicyclic polymers by "a $_2$ +b $_4$ " polycondensations. J Polym Sci Part A Polym Chem 2009;47:1971–87. doi:10.1002/pola.23232.

[42] Bai Y, Fan X, Yao H, Yang Z, Liu T, Zhang H, et al. Probing into the supramolecular driving force of an amphiphilic β-cyclodextrin dimer in various solvents: host–guest recognition or hydrophilic–hydrophobic interaction? J Phys Chem B 2015;119:11893–9. doi:10.1021/acs.jpcb.5b05317.

[43] Mou Q, Ma Y, Jin X, Yan D, Zhu X, Chen G, et al. Host–guest binding motifs based on hyperbranched polymers. Chem Commun 2016;52:11728–43. doi:10.1039/C6CC03643K.

[44] Tian W, Li X, Wang J. Supramolecular hyperbranched polymers. Chem Commun 2017;53:2531–42. doi:10.1039/C6CC09678F.

[45] Emrick T, Chang H-T, Fréchet JMJ. An A 2 + B 3 approach to hyperbranched aliphatic polyethers containing chain end epoxy substituents. Macromolecules 1999;32:6380–2. doi:10.1021/ma990687b.

[46] Fang J, Kita H, Okamoto K. Hyperbranched polyimides for gas separation applications. 1. Synthesis and characterization. Macromolecules 2000;33:4639–46. doi:10.1021/ma9921293.

[47] Hao J, Jikei M, Kakimoto M. Preparation of hyperbranched aromatic polyimides via A 2 + B 3 approach. Macromolecules 2002;35:5372–81. doi:10.1021/ma012113o.

[48] Pandey S, Mishra SP, Kolli B, Kanai T, Samui AB. Hyperbranched photo responsive and

liquid crystalline azo-siloxane polymers synthesized by click chemistry. J Polym Sci Part A Polym Chem 2012;50:2659–68. doi:10.1002/pola.26042.

[49] Ban Q, Chen H, Yan Y, Tian N, Kong J. Tunable intramolecular cyclization and glass transition temperature of hyperbranched polymers by regulating monomer reactivity. Eur Polym J 2017;96:474–83. doi:10.1016/J.EURPOLYMJ.2017.09.039.

[50] Chen H, Kong J. Hyperbranched polymers from $A_2 + B_3$ strategy: recent advances in description and control of fine topology. Polym Chem 2016;7:3643–63. doi:10.1039/C6PY00409A.

[51] Yan D, Gao C. Hyperbranched polymers made from A 2 and BB' 2 type monomers. 1. Polyaddition of 1-(2-aminoethyl)piperazine to divinyl sulfone. Macromolecules 2000;33:7693–9. doi:10.1021/ma000438j.

[52] Jin Han , Bo Zhao , Yanqin Gao AT and CG. Sequential click synthesis of hyperbranched polymersvia the A2 + CB2 approach. Polym Chem 2011;2:2175. doi:10.1039/C1PY00235J.

[53] Lin Y, Gao J-W, Liu H-W, Li Y-S. Synthesis and characterization of hyperbranched poly(ether amide)s with thermoresponsive property and unexpected strong blue photoluminescence. Macromolecules 2009;42:3237–46. doi:10.1021/ma802353f.

[54] Chen H, Kong J, Tian W, Fan X-D. Intramolecular cyclization in A 2 + B 3 polymers via step-wise polymerization resulting in a highly branched topology: quantitative determination of cycles by combined NMR and SEC analytics. Macromolecules 2012;45:6185–95. doi:10.1021/ma300686b.

[55] Unal S, Long TE. Highly branched poly(ether ester)s via cyclization-free melt condensation of A 2 oligomers and B 3 monomers. Macromolecules 2006;39:2788–93. doi:10.1021/ma0523724.

[56] Kakuchi R. Multicomponent reactions in polymer synthesis. Angew Chem Int Ed 2014;53:46–8. doi:10.1002/anie.201305538.

[57] Deng X-X, Cui Y, Du F-S, Li Z-C. Functional highly branched polymers from multicomponent polymerization (MCP) based on the ABC type Passerini reaction. Polym Chem 2014;5:3316–20. doi:10.1039/c3py01705b.

[58] Zhang Z, Tan Z-B, Hong C-Y, Wu D-C, You Y-Z. One-pot sequential multicomponent reaction and a multicomponent polymerization method for the synthesis of topologically different polymers. Polym Chem 2016;7:1468–74. doi:10.1039/C5PY01758K.

[59] O'Brien N, McKee A, Sherrington DC, Slark AT, Titterton A. Facile, versatile and cost effective route to branched vinyl polymers. Polymer 2000;41:6027–31. doi:10.1016/S0032-3861(00)00016-1.

[60] Isaure F, Cormack PAG, Sherrington DC. Facile synthesis of branched poly(methyl methacrylate)s. J Mater Chem 2003;13:2701–10. doi:10.1039/B303321J.

[61] Liu Y, Haley JC, Deng K, Lau W, Winnik MA. Synthesis of branched poly(butyl methacrylate) via semicontinuous emulsion polymerization. Macromolecules 2008;41:4220–5. doi:10.1021/ma800215m.

[62] Isaure F, Cormack PAG, Sherrington DC. Synthesis of branched poly(methyl methacrylate)s: effect of the branching comonomer structure. Macromolecules 2004;37:2096–105. doi:10.1021/ma030445i.

[63] Chisholm M, Hudson N, Kirtley N, Vilela F, Sherrington DC. Application of the "strathclyde route" to branched vinyl polymers in suspension polymerization: architectural, thermal, and rheological characterization of the derived branched products. Macromolecules 2009;42:7745–52. doi:10.1021/ma901081v.

[64] Baudry R, Sherrington DC. Synthesis of highly branched poly(methyl methacrylate)s using the "strathclyde methodology" in aqueous emulsion. Macromolecules 2006;39:1455–60. doi:10.1021/ma052187q.

[65] Bannister I, Billingham NC, Armes SP, Rannard SP, Findlay P. Development of branching in living radical copolymerization of vinyl and divinyl monomers. Macromolecules 2006;39:7483–92. doi:10.1021/ma061811b.

[66] Liu B, Kazlauciunas A, Guthrie JT, Perrier S. One-pot hyperbranched polymer synthesis mediated by reversible addition fragmentation chain transfer (RAFT) polymerization. Macromolecules 2005;38:2131–6. doi:10.1021/ma048035x.

[67] Smeets NMB. Amphiphilic hyperbranched polymers from the copolymerization of a vinyl and divinyl monomer: The potential of catalytic chain transfer polymerization.

Eur Polym J 2013;49:2528–44. doi:10.1016/J.EURPOLYMJ.2013.05.006.

[68] Smeets NMB, Freeman MW, McKenna TFL. Polymer architecture control in emulsion polymerization via catalytic chain transfer polymerization. Macromolecules 2011;44:6701–10. doi:10.1021/ma201393b.

[69] Guan Z. Control of polymer topology through transition-metal catalysis: synthesis of hyperbranched polymers by cobalt-mediated free radical polymerization. J Am Chem Soc 2002;124:5616–7. doi:10.1021/ja025609+.

[70] McEwan KA, Haddleton DM. Combining catalytic chain transfer polymerisation (CCTP) and thio-Michael addition: enabling the synthesis of peripherally functionalised branched polymers. Polym Chem 2011;2:1992–9. doi:10.1039/c1py00221j.

[71] Flory PJ. Principles of polymer chemistry. Ithaca (NY): Cornell University Press; 1953.

[72] Lach C, Müller P, Frey H, Mülhaupt R. Hyperbranched polycarbosilane macromonomers bearing oxazoline functionalities. Macromol Rapid Commun 1997;18:253–60. doi:10.1002/marc.1997.030180306.

[73] Gorodetskaya IA, Choi T-L, Grubbs RH. Hyperbranched macromolecules via olefin metathesis. J Am Chem Soc 2007;129:12672–3. doi:10.1021/ja0759040.

[74] Miravet JF, Fréchet JMJ. New hyperbranched poly(siloxysilanes): variation of the branching pattern and end-functionalization. Macromolecules 1998;31:3461–8. doi:10.1021/ma971778g.

[75] Ishida Y, Sun ACF, Jikei M, Kakimoto M. Synthesis of hyperbranched aromatic polyamides starting from dendrons as AB x monomers: effect of monomer multiplicity on the degree of branching. Macromolecules 2000;33:2832–8. doi:10.1021/ma992021n.

[76] Spindler R, Frechet JMJ. Synthesis and characterization of hyperbranched polyurethanes prepared from blocked isocyanate monomers by step-growth polymerization. Macromolecules 1993;26:4809–13. doi:10.1021/ma00070a013.

[77] Zhi L, Wu J, Li J, Stepputat M, Kolb U, Müllen K. Diels-alder reactions of tetraphenylcyclopentadienones in nanochannels: fabrication of nanotubes from hyperbranched polyphenylenes. Adv Mater 2005;17:1492–6.

doi:10.1002/adma.200500290.

[78] Flory PJ. Molecular size distribution in three dimensional polymers. VI. Branched polymers containing A—R—B f-1 type units. J Am Chem Soc 1952;74:2718–23. doi:10.1021/ja01131a008.

[79] Hanselmann R, Hölter D, Frey H. Hyperbranched polymers prepared via the core-dilution/slow addition technique: computer simulation of molecular weight distribution and degree of branching. Macromolecules 1998;31:3790–801. doi:10.1021/ma971197r.

[80] Bharathi P, Moore JS. Controlled synthesis of hyperbranched polymers by slow monomer addition to a core. Macromolecules 2000;33:3212–8. doi:10.1021/ma992027c.

[81] Bernal DP, Bedrossian L, Collins K, Fossum E. Effect of core reactivity on the molecular weight, polydispersity, and degree of branching of hyperbranched poly(arylene ether phosphine oxide)s. Macromolecules 2003;36:333–8. doi:10.1021/ma021510b.

[82] Ohta Y, Fujii S, Yokoyama A, Furuyama T, Uchiyama M, Yokozawa T. Synthesis of well-defined hyperbranched polyamides by condensation polymerization of AB 2 monomer through changed substituent effects. Angew Chem Int Ed 2009;48:5942–5. doi:10.1002/anie.200901714.

[83] Roy RK, Ramakrishnan S. Control of molecular weight and polydispersity of hyperbranched polymers using a reactive B 3 core: a single-step route to orthogonally functionalizable hyperbranched polymers. Macromolecules 2011;44:8398–406. doi:10.1021/ma201817a.

[84] Chen J-Y, Smet M, Zhang J-C, Shao W-K, Li X, Zhang K, et al. Fully branched hyperbranched polymers with a focal point: analogous to dendrimers. Polym Chem 2014;5:2401–10. doi:10.1039/c3py01401k.

[85] Zhu M, Hao N, Yang J, Li L. A comparative study of intrachain cyclization and solution properties of long-subchain hyperbranched polymers prepared *via* Y-type and V-type macromonomer approaches. Polym Chem 2018;9:2830–42. doi:10.1039/C8PY00362A.

[86] Fréchet JMJ, Henmi M, Gitsov I, Aoshima S, Leduc MR, Bernard RG. Self-condensing

vinyl polymerization: an approach to dendritic materials. Science 1995;269:1080–3. doi:10.1126/science.269.5227.1080.

[87] Baskaran D. Synthesis of hyperbranched polymers by anionic self-condensing vinyl polymerization. Macromol Chem Phys 2001;202:1569–75. doi:10.1002/1521-3935(20010601)202:9<1569::AID-MACP1569>3.0.CO;2-Z.

[88] Simon PFW, Radke W, Müller AHE. Hyperbranched methacrylates by self-condensing group transfer polymerization. Macromol Rapid Commun 1997;18:865–73. doi:10.1002/marc.1997.030180915.

[89] Sakamoto K, Aimiya T, Kira M. Preparation of hyperbranched polymethacrylates by self-condensing group transfer polymerization. Chem Lett 1997;26:1245–6. doi:10.1246/cl.1997.1245.

[90] Goodwin A, Baskaran D. Inimer mediated synthesis of hyperbranched polyglycerol via self-condensing ring-opening polymerization. Macromolecules 2012;45:9657–65. doi:10.1021/ma301768k.

[91] Wilms D, Stiriba S-E, Frey H. Hyperbranched polyglycerols: from the controlled synthesis of biocompatible polyether polyols to multipurpose applications. Acc Chem Res 2010;43:129–41. doi:10.1021/ar900158p.

[92] Yan D, Hou J, Zhu X, Kosman JJ, Wu H-S. A new approach to control crystallinity of resulting polymers: Self-condensing ring opening polymerization. Macromol Rapid Commun 2000;21:557–61. doi:10.1002/1521-3927(20000601)21:9<557::AID-MARC557>3.0.CO;2-K.

[93] Liu M, Vladimirov N, Fréchet JMJ. A new approach to hyperbranched polymers by ring-opening polymerization of an AB monomer: 4-(2-hydroxyethyl)-ε-caprolactone. Macromolecules 1999;32:6881–4. doi:10.1021/MA990785X.

[94] Liu J, Huang W, Zhou Y, Yan D. Synthesis of hyperbranched polyphosphates by self-condensing ring-opening polymerization of HEEP without catalyst. Macromolecules 2009;42:4394–9. doi:10.1021/ma900798h.

[95] Hawker CJ, Frechet JMJ, Grubbs RB, Dao J. Preparation of hyperbranched polyacrylates by atom transfer radical polymerization. 1. acrylic AB* monomers in “living” radical polymerizations. J Am Chem Soc 1995;117:10763–4.

doi:10.1021/ja00148a027.

[96] Tao Y, He J, Wang Z, Pan J, Jiang H, Chen S, et al. Synthesis of branched polystyrene and poly(styrene- b -4-methoxystyrene) by nitroxyl stable radical controlled polymerization. Macromolecules 2001;34:4742–8. doi:10.1021/ma0100201.

[97] Niu A, Li C, Zhao Y, He J, Yang Y, Wu C. Thermal decomposition kinetics and structure of novel polystyrene clusters with MTEMPO as a branching agent. Macromolecules 2001;34:460–4. doi:10.1021/ma000569k.

[98] Grubbs RB. Nitroxide-mediated radical polymerization: limitations and versatility. Polym Rev 2011;51:104–37. doi:10.1080/15583724.2011.566405.

[99] Jung K, Abetz V, Stadler R. Thermodynamically controlled morphological disorder in a microphase-separated cylindrical block copolymer. Macromolecules 1996;29:1076–8. doi:10.1021/ma951307z.

[100] Huang C-F, Kuo S-W, Moravčíková D, Liao J-C, Han Y-M, Lee T-H, et al. Effect of variations of $Cu^{II}X_2$/L, surface area of Cu^0, solvent, and temperature on atom transfer radical polyaddition of 4-vinylbenzyl 2-bromo-2-isobutyrate inimers. RSC Adv 2016;6:51816–22. doi:10.1039/C6RA06186A.

[101] Matyjaszewski K, Gaynor SG. Preparation of hyperbranched polyacrylates by atom transfer radical polymerization. 3. Effect of reaction conditions on the self-condensing vinyl polymerization of 2-((2-bromopropionyl)oxy)ethyl acrylate. Macromolecules 1997;30:7042–9. doi:10.1021/ma970635r.

[102] Alfurhood JA, Bachler PR, Sumerlin BS. Hyperbranched polymers via RAFT self-condensing vinyl polymerization. Polym Chem 2016;7:3361–9. doi:10.1039/c6py00571c.

[103] Lu Y, Nemoto T, Tosaka M, Yamago S. Synthesis of structurally controlled hyperbranched polymers using a monomer having hierarchical reactivity. Nat Commun 2017;8:1863. doi:10.1038/s41467-017-01838-0.

[104] Peacock AJ. Handbook of polyethylene : structures, properties, and applications. New York: Marcel Dekker; 2000.

[105] McKnight AL, Waymouth RM. Group 4 ansa- cyclopentadienyl-amido catalysts for

olefin polymerization. Chem Rev 1998;98:2587–98. doi:10.1021/cr940442r.

[106] Stevens JC, Timmers FJ, Wilson DR, Schmidt GF, Nickias PN, Rosen RK, et al. Constrained geometry addition polymerization catalysts, processes for their preparation, precursors therefor, methods of use, and novel polymers formed therewith. EP416815-A2, 1991.

[107] Barnhart RW, Bazan GC, Mourey T. Synthesis of branched polyolefins using a combination of homogeneous metallocene mimics. J Am Chem Soc 1998;120:1082–3. doi:10.1021/ja9735867.

[108] Zhibin Guan, P. M. Cotts, E. F. McCord SJM. Chain walking: a new strategy to control polymer topologyitle. Science 1999;283:2059. doi:10.1126/science.283.5410.2059.

[109] Dong Z, Ye Z. Hyperbranched polyethylenes by chain walking polymerization: synthesis, properties, functionalization, and applications. Polym Chem 2012;3:286–301. doi:10.1039/C1PY00368B.

[110] Johnson LK, Killian CM, Brookhart M. New Pd(II)- and Ni(II)-based catalysts for polymerization of ethylene and alpha-olefins. J Am Chem Soc 1995;117:6414–5. doi:10.1021/ja00128a054.

[111] Schwerdtfeger ED, Irwin LJ, Miller SA. Highly branched polyethylene from ethylene alone via a single zirconium-based catalyst. Macromolecules 2008;41:1080–5. doi:10.1021/ma702213c.

[112] Matsumura Y, Maeda H. A new concept for macromolecular therapeutics in cancer chemotherapy: mechanism of tumoritropic accumulation of proteins and the antitumor agent smancs. Cancer Res 1986.

[113] Grayson SM, Godbey WT. The role of macromolecular architecture in passively targeted polymeric carriers for drug and gene delivery. J Drug Targeting 2008;16:329–56. doi:10.1080/10611860801969616.

[114] Fang J, Nakamura H, Maeda H. The EPR effect: Unique features of tumor blood vessels for drug delivery, factors involved, and limitations and augmentation of the effect. Adv Drug Deliv Rev 2011;63:136–51. doi:10.1016/J.ADDR.2010.04.009.

[115] Seymour LW, Duncan R, Strohalm J, Kopecek J. Effect of molecular weight (Mw) of N-

(2-hydroxypropyl)methacrylamide copolymers on body distribution and rate of excretion after subcutaneous, intraperitoneal, and intravenous administration to rats. J Biomed Mater Res 1987;21:1341–58. doi:10.1002/jbm.820211106.

[116] Soo Choi H, Liu W, Misra P, Tanaka E, Zimmer JP, Itty Ipe B, et al. Renal clearance of quantum dots. Nat Biotechnol 2007;25:1165–70. doi:10.1038/nbt1340.

[117] Longmire M, Choyke PL, Kobayashi H. Clearance properties of nano-sized particles and molecules as imaging agents: considerations and caveats. Nanomedicine 2008;3:703–17. doi:10.2217/17435889.3.5.703.

[118] Vicent MJ, Duncan R. Polymer conjugates: nanosized medicines for treating cancer. Trends Biotechnol 2006;24:39–47. doi:10.1016/j.tibtech.2005.11.006.

[119] Danhier F, Feron O, Préat V. To exploit the tumor microenvironment: Passive and active tumor targeting of nanocarriers for anti-cancer drug delivery. J Controlled Release 2010;148:135–46. doi:10.1016/j.jconrel.2010.08.027.

[120] Kurniasih IN, Keilitz J, Haag R. Dendritic nanocarriers based on hyperbranched polymers. Chem Soc Rev 2015;44:4145–64. doi:10.1039/C4CS00333K.

[121] Wang D, Zhao T, Zhu X, Yan D, Wang W. Bioapplications of hyperbranched polymers. Chem Soc Rev 2015;44:4023–71. doi:10.1039/C4CS00229F.

[122] Jaskula-Sztul R, Xu W, Chen G, Harrison A, Dammalapati A, Nair R, et al. Thailandepsin A-loaded and octreotide-functionalized unimolecular micelles for targeted neuroendocrine cancer therapy. Biomaterials 2016;91:1–10. doi:10.1016/j.biomaterials.2016.03.010.

[123] Luo K, Liu G, She W, Wang Q, Wang G, He B, et al. Gadolinium-labeled peptide dendrimers with controlled structures as potential magnetic resonance imaging contrast agents. Biomaterials 2011;32:7951–60. doi:10.1016/j.biomaterials.2011.07.006.

[124] Wang W, Ma J, Jin F, Liao J. Hyperbranched polymer drug delivery treatment for lung metastasis of salivary adenoid cystic carcinoma in nude mice. Exp Ther Med 2017;14:3105–11. doi:10.3892/etm.2017.4902.

[125] Yi X, Xu M, Zhou H, Xiong S, Qian R, Chai Z, et al. Ultrasmall hyperbranched

semiconducting polymer nanoparticles with different radioisotopes labeling for cancer theranostics. ACS Nano 2018;12:9142–51. doi:10.1021/acsnano.8b03514.

[126] Li Y, Beija M, Laurent S, Elst L vander, Muller RN, Duong HTT, et al. Macromolecular ligands for gadolinium MRI contrast agents. Macromolecules 2012;45:4196–204. doi:10.1021/ma300521c.

[127] Picco AS, Yameen B, Knoll W, Ceolín MR, Azzaroni O. Temperature-driven self-assembly of self-limiting uniform supraparticles from non-uniform unimolecular micelles. J Colloid Interface Sci 2016;471:71–5. doi:10.1016/j.jcis.2016.03.005.

[128] Zhou Y, Huang W, Liu J, Zhu X, Yan D. Self-assembly of hyperbranched polymers and its biomedical applications. Adv Mater 2010;22:4567–90. doi:10.1002/adma.201000369.

[129] Jin H, Huang W, Zhu X, Zhou Y, Yan D. Biocompatible or biodegradable hyperbranched polymers: from self-assembly to cytomimetic applications. Chem Soc Rev 2012;41:5986–97. doi:10.1039/c2cs35130g.

[130] Jiang W, Zhou Y, Yan D, Chen D, Fang J, Yu S, et al. Hyperbranched polymer vesicles: from self-assembly, characterization, mechanisms, and properties to applications. Chem Soc Rev 2015;44:3874–89. doi:10.1039/C4CS00274A.

[131] Zhou Y, Yan D, Zhou Y, Yan D, Pan C, Wang L, et al. Supramolecular self-assembly of amphiphilic hyperbranched polymers at all scales and dimensions: progress, characteristics and perspectives. Chem Commun 2009;10:1172. doi:10.1039/b814560c.

[132] Fan W, Fan X, Tian W, Zhang X, Wang G, Zhang W, et al. Phase transition dynamics and mechanism for backbone-thermoresponsive hyperbranched polyethers. Polym Chem 2014;5:4022. doi:10.1039/c4py00155a.

[133] Son S, Shin E, Kim B-S. Light-responsive micelles of spiropyran initiated hyperbranched polyglycerol for smart drug delivery. Biomacromolecules 2014;15:628–34. doi:10.1021/bm401670t.

[134] Steinhilber D, Witting M, Zhang X, Staegemann M, Paulus F, Friess W, et al. Surfactant free preparation of biodegradable dendritic polyglycerol nanogels by inverse nanoprecipitation for encapsulation and release of pharmaceutical

biomacromolecules. J Controlled Release 2013;169:289–95. doi:10.1016/j.jconrel.2012.12.008.

[135] Santra S, Kaittanis C, Perez JM. Cytochrome c encapsulating theranostic nanoparticles: a novel bifunctional system for targeted delivery of therapeutic membrane-impermeable proteins to tumors and imaging of cancer therapy. Mol Pharmaceutics 2010;7:1209–22. doi:10.1021/mp100043h.

[136] Irfan M, Seiler M. Encapsulation using hyperbranched polymers: from research and technologies to emerging applications. Ind Eng Chem Res 2010;49:1169–96. doi:10.1021/ie900216r.

[137] Etrych T, Strohalm J, Chytil P, Černoch P, Starovoytova L, Pechar M, et al. Biodegradable star HPMA polymer conjugates of doxorubicin for passive tumor targeting. Eur J Pharm Sci 2011;42:527–39. doi:10.1016/J.EJPS.2011.03.001.

[138] Zhang S, Hou Y, Chen H, Liao Z, Chen J, Xu BB, et al. Reduction-responsive amphiphilic star copolymers with long-chain hyperbranched poly(ε-caprolactone) core and disulfide bonds for trigger release of anticancer drugs. Eur Polym J 2018;108:364–72. doi:10.1016/J.EURPOLYMJ.2018.09.014.

[139] Hu X, Liu G, Li Y, Wang X, Liu S. Cell-penetrating hyperbranched polyprodrug amphiphiles for synergistic reductive Milieu-triggered drug release and enhanced magnetic resonance signals. J Am Chem Soc 2015;137:362–8. doi:10.1021/ja5105848.

[140] Qiu L, Liu Q, Hong C-Y, Pan C-Y. Unimolecular micelles of camptothecin-bonded hyperbranched star copolymers via β-thiopropionate linkage: synthesis and drug delivery. J Mater Chem B 2016;4:141–51. doi:10.1039/C5TB01905B.

[141] Xia Y, Wang Y, Wang Y, Tu C, Qiu F, Zhu L, et al. A tumor pH-responsive complex: Carboxyl-modified hyperbranched polyether and cis-dichlorodiammineplatinum(II). Colloids Surf, B 2011;88:674–81. doi:10.1016/J.COLSURFB.2011.07.059.

[142] Haxton KJ, Burt HM. Hyperbranched polymers for controlled release of cisplatin. Dalt Trans 2008:5872–5. doi:10.1039/b809949a.

[143] Ye L, Letchford K, Heller M, Liggins R, Guan D, Kizhakkedathu JN, et al. Synthesis and characterization of carboxylic acid conjugated, hydrophobically derivatized, hyperbranched polyglycerols as nanoparticulate drug carriers for cisplatin.

Biomacromolecules 2011;12:145–55. doi:10.1021/bm101080p.

[144] Wu H, Yin T, Li K, Wang R, Chen Y, Jing L. Encapsulation property of hyperbranched polyglycerols as prospective drug delivery systems. Polym Chem 2018;9:300–6. doi:10.1039/C7PY01419H.

[145] Liu G, Zhang G, Hu J, Wang X, Zhu M, Liu S. Hyperbranched self-immolative polymers (h SIPs) for programmed payload delivery and ultrasensitive detection. J Am Chem Soc 2015;137:11645–55. doi:10.1021/jacs.5b05060.

[146] Yang B, Dong X, Lei Q, Zhuo R, Feng J, Zhang X. Host–guest interaction-based self-engineering of nano-sized vesicles for co-delivery of genes and anticancer drugs. ACS Appl Mater Interfaces 2015;7:22084–94. doi:10.1021/acsami.5b07549.

[147] Cook AB, Peltier R, Zhang J, Gurnani P, Tanaka J, Burns JA, et al. Hyperbranched poly(ethylenimine- *co* -oxazoline) by thiol–yne chemistry for non-viral gene delivery: investigating the role of polymer architecture. Polym Chem 2019;10:1202–12. doi:10.1039/C8PY01648H.

[148] Duan S, Yu B, Gao C, Yuan W, Ma J, Xu F-J. A facile strategy to prepare hyperbranched hydroxyl-rich polycations for effective gene therapy. ACS Appl Mater Interfaces 2016;8:29334–42. doi:10.1021/acsami.6b11029.

[149] Peng Y-Y, Diaz-Dussan D, Vani J, Hao X, Kumar P, Narain R. Achieving safe and highly efficient epidermal growth factor receptor silencing in cervical carcinoma by cationic degradable hyperbranched polymers. ACS Appl Bio Mater 2018;1:961–6. doi:10.1021/acsabm.8b00371.

[150] Zhou X, Zheng Q, Wang C, Xu J, Wu J-P, Kirk TB, et al. Star-shaped amphiphilic hyperbranched polyglycerol conjugated with dendritic poly(l-lysine) for the codelivery of docetaxel and MMP-9 siRNA in cancer therapy. ACS Appl Mater Interfaces 2016;8:12609–19. doi:10.1021/acsami.6b01611.

[151] Zhou X, Xu L, Xu J, Wu J, Kirk TB, Ma D, et al. Construction of a high-efficiency drug and gene co-delivery system for cancer therapy from a pH-sensitive supramolecular inclusion between oligoethylenimine- graft -β-cyclodextrin and hyperbranched polyglycerol derivative. ACS Appl Mater Interfaces 2018;10:35812–29. doi:10.1021/acsami.8b14517.

[152] Mou Q, Ma Y, Jin X, Zhu X. Designing hyperbranched polymers for gene delivery. Mol Syst Des Eng 2016;1:25–39. doi:10.1039/C5ME00015G.

[153] Chen G, Jaskula–Sztul R, Harrison A, Dammalapati A, Xu W, Cheng Y, et al. KE108-conjugated unimolecular micelles loaded with a novel HDAC inhibitor thailandepsin-A for targeted neuroendocrine cancer therapy. Biomaterials 2016;97:22–33. doi:10.1016/j.biomaterials.2016.04.029.

[154] Popeney CS, Lukowiak MC, Böttcher C, Schade B, Welker P, Mangoldt D, et al. Tandem coordination, ring-opening, hyperbranched polymerization for the synthesis of water-soluble core–shell unimolecular transporters. ACS Macro Lett 2012;1:564–7. doi:10.1021/mz300083y.

[155] Donskyi IS, Achazi K, Wycisk V, Licha K, Adeli M, Haag R. Fullerene polyglycerol amphiphiles as unimolecular transporters. Langmuir 2017;33:6595–600. doi:10.1021/acs.langmuir.7b00183.

[156] Kolhe P, Khandare J, Pillai O, Kannan S, Lieh-Lai M, Kannan R. Hyperbranched polymer-drug conjugates with high drug payload for enhanced cellular delivery. Pharm Res 2004;21:2185–95. doi:10.1007/s11095-004-7670-x.

[157] Duro-Castano A, Movellan J, Vicent MJ. Smart branched polymer drug conjugates as nano-sized drug delivery systems. Biomater Sci 2015;3:1321–34. doi:10.1039/C5BM00166H.

[158] Liu J, Pang Y, Chen J, Huang P, Huang W, Zhu X, et al. Hyperbranched polydiselenide as a self assembling broad spectrum anticancer agent. Biomaterials 2012;33:7765–74. doi:10.1016/J.BIOMATERIALS.2012.07.003.

[159] Gandin V, Khalkar P, Braude J, Fernandes AP. Organic selenium compounds as potential chemotherapeutic agents for improved cancer treatment. Free Radical Biol Med 2018;127:80–97. doi:10.1016/J.FREERADBIOMED.2018.05.001.

[160] Álvarez-Pérez M, Ali W, Marć M, Handzlik J, Domínguez-Álvarez E, Álvarez-Pérez M, et al. Selenides and diselenides: A review of their anticancer and chemopreventive activity. Molecules 2018;23:628. doi:10.3390/molecules23030628.

[161] Harris JM, Chess RB. Effect of pegylation on pharmaceuticals. Nat Rev Drug Discov 2003;2:214–21. doi:10.1038/nrd1033.

[162] Tziveleka L-A, Kontoyianni C, Sideratou Z, Tsiourvas D, Paleos CM. Novel functional hyperbranched polyether polyols as prospective drug delivery systems. Macromol Biosci 2006;6:161–9. doi:10.1002/mabi.200500181.

[163] Sharma K, Zolotarskaya OY, Wynne KJ, Yang H. Poly(ethylene glycol)-armed hyperbranched polyoxetanes for anticancer drug delivery. J Bioact Compat Polym 2012;27:525–39. doi:10.1177/0883911512461470.

[164] Liu N, Vignolle J, Vincent J-M, Robert F, Landais Y, Cramail H, et al. One-pot synthesis and PEGylation of hyperbranched polyacetals with a degree of branching of 100%. Macromolecules 2014;47:1532–42. doi:10.1021/ma4026509.

[165] Kontoyianni C, Sideratou Z, Theodossiou T, Tziveleka L-A, Tsiourvas D, Paleos CM. A novel micellar PEGylated hyperbranched polyester as a prospective drug delivery system for paclitaxel. Macromol Biosci 2008;8:871–81. doi:10.1002/mabi.200800015.

[166] Zhu L, Shi Y, Tu C, Wang R, Pang Y, Qiu F, et al. Construction and application of a pH-sensitive nanoreactor via a double-hydrophilic multiarm hyperbranched polymer. Langmuir 2010;26:8875–81. doi:10.1021/la9046275.

[167] Xu S, Luo Y, Graeser R, Warnecke A, Kratz F, Hauff P, et al. Development of pH-responsive core–shell nanocarriers for delivery of therapeutic and diagnostic agents. Bioorg Med Chem Lett 2009;19:1030–4. doi:10.1016/J.BMCL.2008.01.043.

[168] Xu S, Luo Y, Haag R. Water-soluble pH-responsive dendritic core-shell nanocarriers for polar dyes based on poly(ethylene imine). Macromol Biosci 2007;7:968–74. doi:10.1002/mabi.200700066.

[169] Kurniasih IN, Liang H, Kumar S, Mohr A, Sharma SK, Rabe JP, et al. A bifunctional nanocarrier based on amphiphilic hyperbranched polyglycerol derivatives. J Mater Chem B 2013;1:3569–77. doi:10.1039/c3tb20366b.

[170] Bordat A, Boissenot T, Nicolas J, Tsapis N. Thermoresponsive polymer nanocarriers for biomedical applications. Adv Drug Deliv Rev 2019;138:167–92. doi:10.1016/J.ADDR.2018.10.005.

[171] Luo S, Hu X, Zhang Y, Ling C, Liu X, Chen S. Synthesis of thermoresponsive unimolecular polymeric micelles with a hydrophilic hyperbranched poly(glycidol) core. Polym J 2011;43:41–50. doi:10.1038/pj.2010.93.

[172] Zhao Y, Fan X, Liu D, Wang Z. PEGylated thermo-sensitive poly(amidoamine) dendritic drug delivery systems. Int J Pharm 2011;409:229–36. doi:10.1016/J.IJPHARM.2011.02.005.

[173] Gullotti E, Yeo Y. Extracellularly activated nanocarriers: a new paradigm of tumor targeted drug delivery. Mol Pharmaceutics 2009;6:1041–51. doi:10.1021/mp900090z.

[174] Bae YH. Drug targeting and tumor heterogeneity. J Controlled Release 2009;133:2–3. doi:10.1016/j.jconrel.2008.09.074.

[175] Farkhani SM, Valizadeh A, Karami H, Mohammadi S, Sohrabi N, Badrzadeh F. Cell penetrating peptides: efficient vectors for delivery of nanoparticles, nanocarriers, therapeutic and diagnostic molecules. Peptides 2014;57:78–94. doi:10.1016/j.peptides.2014.04.015.

[176] Ruoslahti E. Tumor penetrating peptides for improved drug delivery. Adv Drug Deliv Rev 2017;110–111:3–12. doi:10.1016/j.addr.2016.03.008.

[177] Soudy R, Byeon N, Raghuwanshi Y, Ahmed S, Lavasanifar A, Kaur K. Engineered peptides for applications in cancer targeted drug delivery and tumor detection. Mini Rev Med Chem 2017;17:1696–712. doi:10.2174/1389557516666160219121836.

[178] Zhang X-X, Eden HS, Chen X. Peptides in cancer nanomedicine: Drug carriers, targeting ligands and protease substrates. J Controlled Release 2012;159:2–13. doi:10.1016/j.jconrel.2011.10.023.

[179] Liu J, Wei T, Zhao J, Huang Y, Deng H, Kumar A, et al. Multifunctional aptamer-based nanoparticles for targeted drug delivery to circumvent cancer resistance. Biomaterials 2016;91:44–56. doi:10.1016/j.biomaterials.2016.03.013.

[180] Chen K, Liu B, Yu B, Zhong W, Lu Y, Zhang J, et al. Advances in the development of aptamer drug conjugates for targeted drug delivery. Wiley Interdiscip Rev : Nanomed Nanobiotechnol 2017;9:e1438. doi:10.1002/wnan.1438.

[181] Ray P, White RR. Aptamers for targeted drug delivery. Pharmaceuticals 2010;3:1761–78. doi:10.3390/ph3061761.

[182] Khoee S, Kavand A. Preparation, co-assembling and interfacial crosslinking of photocurable and folate-conjugated amphiphilic block copolymers for controlled and

targeted drug delivery: Smart armored nanocarriers. Eur J Med Chem 2014;73:18–29. doi:10.1016/j.ejmech.2013.11.033.

[183] Zhao X, Li H, Lee RJ. Targeted drug delivery via folate receptors. Expert Opin Drug Deliv 2008;5:309–19. doi:10.1517/17425247.5.3.309.

[184] Marchetti C, Palaia I, Giorgini M, De Medici C, Iadarola R, Vertechy L, et al. Targeted drug delivery via folate receptors in recurrent ovarian cancer: a review. Onco Targets Ther 2014;7:1223–36. doi:10.2147/OTT.S40947.

[185] Field LD, Delehanty JB, Chen Y, Medintz IL. Peptides for specifically targeting nanoparticles to cellular organelles: Quo Vadis ? Acc Chem Res 2015;48:1380–90. doi:10.1021/ar500449v.

[186] Sun H, Dong Y, Feijen J, Zhong Z. Peptide-decorated polymeric nanomedicines for precision cancer therapy. J Controlled Release 2018;290:11–27. doi:10.1016/j.jconrel.2018.09.029.

[187] Zong J, Cobb SL, Cameron NR. Peptide-functionalized gold nanoparticles: versatile biomaterials for diagnostic and therapeutic applications. Biomater Sci 2017;5:872–86. doi:10.1039/C7BM00006E.

[188] Deng T, Peng Y, Zhang R, Wang J, Zhang J, Gu Y, et al. Water-solubilizing hydrophobic ZnAgInSe/ZnS QDs with tumor-targeted cRGD-sulfobetaine-PIMA-histamine ligands via a self-assembly strategy for bioimaging. ACS Appl Mater Interfaces 2017;9:11405–14. doi:10.1021/acsami.6b16639.

[189] Richard S, Boucher M, Lalatonne Y, Mériaux S, Motte L. Iron oxide nanoparticle surface decorated with cRGD peptides for magnetic resonance imaging of brain tumors. Biochim Biophys Acta - Gen Subj 2017;1861:1515–20. doi:10.1016/j.bbagen.2016.12.020.

[190] Di Paola M, Quarta A, Conversano F, Sbenaglia EA, Bettini S, Valli L, et al. Human hepatocarcinoma cell targeting by glypican-3 ligand peptide functionalized silica nanoparticles: implications for ultrasound molecular imaging. Langmuir 2017;33:4490–9. doi:10.1021/acs.langmuir.7b00327.

[191] Lee Y, Kischuk E, Crist S, Ratliff TL, Thompson DH. Targeting and internalization of liposomes by bladder tumor cells using a fibronectin attachment protein-derived

peptide–lipopolymer conjugate. Bioconjugate Chem 2017;28:1481–90. doi:10.1021/acs.bioconjchem.7b00153.

[192] Zhang B, Wang H, Shen S, She X, Shi W, Chen J, et al. Fibrin-targeting peptide CREKA-conjugated multi-walled carbon nanotubes for self-amplified photothermal therapy of tumor. Biomaterials 2016;79:46–55. doi:10.1016/j.biomaterials.2015.11.061.

[193] Ma P, Yu H, Zhang X, Mu H, Chu Y, Ni L, et al. Increased active tumor targeting by an αvβ3-targeting and cell-penetrating bifunctional peptide-mediated dendrimer-based conjugate. Pharm Res 2017;34:121–35. doi:10.1007/s11095-016-2045-7.

[194] Fang Z, Sun Y, Xiao H, Li P, Liu M, Ding F, et al. Targeted osteosarcoma chemotherapy using RGD peptide-installed doxorubicin-loaded biodegradable polymeric micelle. Biomed Pharmacother 2017;85:160–8. doi:10.1016/j.biopha.2016.11.132.

[195] Liu T, Huang Q. Biodegradable brush-type copolymer modified with targeting peptide as a nanoscopic platform for targeting drug delivery to treat castration-resistant prostate cancer. Int J Pharm 2016;511:1002–11. doi:10.1016/j.ijpharm.2016.08.017.

[196] Lv J, Hao X, Li Q, Akpanyung M, Nejjari A, Neve AL, et al. Star-shaped copolymer grafted PEI and REDV as a gene carrier to improve migration of endothelial cells. Biomater Sci 2017;5:511–22. doi:10.1039/C6BM00856A.

[197] Wang S, Chen R. pH-responsive, lysine-based, hyperbranched polymers mimicking endosomolytic cell-penetrating peptides for efficient intracellular delivery. Chem Mater 2017;29:5806–15. doi:10.1021/acs.chemmater.7b00054.

[198] Dissanayake S, Denny WA, Gamage S, Sarojini V. Recent developments in anticancer drug delivery using cell penetrating and tumor targeting peptides. J Controlled Release 2017;250:62–76. doi:10.1016/j.jconrel.2017.02.006.

[199] Roveri M, Bernasconi M, Leroux J-C, Luciani P. Peptides for tumor-specific drug targeting: state of the art and beyond. J Mater Chem B 2017;5:4348–64. doi:10.1039/C7TB00318H.

[200] Liu R, Li X, Xiao W, Lam KS. Tumor-targeting peptides from combinatorial libraries. Adv Drug Deliv Rev 2017;110–111:13–37. doi:10.1016/j.addr.2016.05.009.

[201] Zhao N, Qin Y, Liu H, Cheng Z. Tumor-targeting peptides: ligands for molecular

imaging and therapy. Anticancer Agents Med Chem 2018;18:74–86. doi:10.2174/1871520617666170419143459.

[202] Humphries JD, Byron A, Humphries MJ. Integrin ligands at a glance. J Cell Sci 2006;119:3901–3. doi:10.1242/jcs.03098.

[203] Yu Y-P, Wang Q, Liu Y-C, Xie Y. Molecular basis for the targeted binding of RGD-containing peptide to integrin αVβ3. Biomaterials 2014;35:1667–75. doi:10.1016/j.biomaterials.2013.10.072.

[204] Qi Y, Chilkoti A. Growing polymers from peptides and proteins: a biomedical perspective. Polym Chem 2014;5:266–76. doi:10.1039/C3PY01089A.

[205] Becker ML, Liu J, Wooley KL. Peptide-polymer bioconjugates: hybrid block copolymers generated via living radical polymerizations from resin-supported peptides. Chem Commun 2003:180–1. doi:10.1039/b209557b.

[206] Mei Y, Beers KL, Byrd HCM, VanderHart DL, Washburn NR. Solid-phase ATRP synthesis of peptide−polymer hybrids. J Am Chem Soc 2004;126:3472–6. doi:10.1021/ja039583d.

[207] ten Cate MGJ, Rettig H, Bernhardt K, Börner HG. Sequence-defined polypeptide−polymer conjugates utilizing reversible addition fragmentation transfer radical polymerization. Macromolecules 2005;38:10643–9. doi:10.1021/ma0519415.

[208] Rettig H, Krause E, Börner HG. Atom transfer radical polymerization with polypeptide initiators: a general approach to block copolymers of sequence-defined polypeptides and synthetic polymers. Macromol Rapid Commun 2004;25:1251–6. doi:10.1002/marc.200400140.

[209] Hentschel J, Bleek K, Ernst O, Lutz J-F, Börner HG. Easy access to bioactive peptide−polymer conjugates via RAFT. Macromolecules 2008;41:1073–5. doi:10.1021/ma8000934.

[210] Chen C, Guo X, Du J, Choi B, Tang H, Feng A, et al. Synthesis of multifunctional miktoarm star polymers *via* an RGD peptide-based RAFT agent. Polym Chem 2019;10:228–34. doi:10.1039/C8PY01355A.

[211] Jackson AW. Octreotide end-functionalized diblock copolymers facilitated by RAFT

polymerization. J Polym Res 2017;24:64. doi:10.1007/s10965-017-1220-9.

[212] Wang Y, Wang L, Chen G, Gong S. Carboplatin-complexed and cRGD-conjugated unimolecular nanoparticles for targeted ovarian cancer therapy. Macromol Biosci 2017;17:1600292. doi:10.1002/mabi.201600292.

[213] Bencherif SA, Gao H, Srinivasan A, Siegwart DJ, Hollinger JO, Washburn NR, et al. Cell-Adhesive Star Polymers Prepared by ATRP. Biomacromolecules 2009;10:1795–803. doi:10.1021/bm900213u.

[214] Cho HY, Gao H, Srinivasan A, Hong J, Bencherif SA, Siegwart DJ, et al. Rapid Cellular Internalization of Multifunctional Star Polymers Prepared by Atom Transfer Radical Polymerization. Biomacromolecules 2010;11:2199–203. doi:10.1021/bm1006272.

[215] Chen C, Kong F, Wei X, Thang SH. Syntheses and effectiveness of functional peptide-based RAFT agents. Chem Commun 2017;53:10776–9. doi:10.1039/C7CC05316A.

[216] Chen C, Thang SH. RAFT polymerization of a RGD peptide-based methacrylamide monomer for cell adhesion. Polym Chem 2018;9:1780. doi:10.1039/c7py01887h.

[217] Shokeen M, Pressly ED, Hagooly A, Zheleznyak A, Ramos N, Fiamengo AL, et al. Evaluation of multivalent, functional polymeric nanoparticles for imaging applications. ACS Nano 2011;5:738–47. doi:10.1021/nn102278w.

[218] Maynard HD, Okada SY, Grubbs RH. Synthesis of norbornenyl polymers with bioactive oligopeptides by ring-opening Metathesis polymerization. Macromolecules 2000;33:6239–48. doi:10.1021/ma000460c.

[219] Parelkar SS, Chan-Seng D, Emrick T. Reconfiguring polylysine architectures for controlling polyplex binding and non-viral transfection. Biomaterials 2011;32:2432–44. doi:10.1016/J.BIOMATERIALS.2010.12.004.

[220] Kammeyer JK, Blum AP, Adamiak L, Hahn ME, Gianneschi NC. Polymerization of protecting-group-free peptides via ROMP. Polym Chem 2013;4:3929–33. doi:10.1039/c3py00526g.

[221] Gauthier MA, Gibson MI, Klok H-A. Synthesis of functional polymers by post-polymerization modification. Angew Chem Int Ed 2008;48:48–58. doi:10.1002/anie.200801951.

[222] Theato P, Klok H-A. Functional polymers by post-polymerization modification : concepts, guidelines, and applications. 1 edition. Weinheim: Wiley-VCH; 2012.

[223] Das A, Theato P. Activated ester containing polymers: opportunities and challenges for the design of functional macromolecules. Chem Rev 2016;116:1434–95. doi:10.1021/acs.chemrev.5b00291.

[224] Nair DP, Podgórski M, Chatani S, Gong T, Xi W, Fenoli CR, et al. The thiol-Michael addition click reaction: a powerful and widely used tool in materials chemistry. Chem Mater 2014;26:724–44. doi:10.1021/cm402180t.

[225] Singh MS, Chowdhury S, Koley S. Advances of azide-alkyne cycloaddition-click chemistry over the recent decade. Tetrahedron 2016;72:5257–83. doi:10.1016/J.TET.2016.07.044.

[226] Jewett JC, Bertozzi CR. Cu-free click cycloaddition reactions in chemical biology. Chem Soc Rev 2010;39:1272–9. doi:10.1039/b901970g.

[227] Sindhu KS, Anilkumar G. Recent advances and applications of Glaser coupling employing greener protocols. RSC Adv 2014;4:27867–87. doi:10.1039/C4RA02416H.

[228] Buck ME, Lynn DM. Azlactone-functionalized polymers as reactive platforms for the design of advanced materials: Progress in the last ten years. Polym Chem 2012;3:66–80. doi:10.1039/C1PY00314C.

[229] Riva R, Lenoir S, Jérôme R, Lecomte P. Functionalization of poly(ε-caprolactone) by pendant hydroxyl, carboxylic acid and epoxide groups by atom transfer radical addition. Polymer 2005;46:8511–8. doi:10.1016/J.POLYMER.2005.03.105.

[230] Radhakrishnan B, Chambon P, Cloutet E, Cramail H. Synthesis of hydroxy- and dihydroxy-end-capped poly(n-butyl acrylate)s and their use as reactive stabilizers for the preparation of polyurethane latexes. Colloid Polym Sci 2003;281:516–30. doi:10.1007/s00396-002-0800-2.

[231] Coiai S, Passaglia E, Cicogna F. Post-polymerization modification by nitroxide radical coupling. Polym Int 2019;68:27–63. doi:10.1002/pi.5664.

[232] Sanyal A. Diels-Alder cycloaddition-cycloreversion: a powerful combo in materials design. Macromol Chem Phys 2010;211:1417–25. doi:10.1002/macp.201000108.

[233] Ireson C, Kelland L. Discovery and development of anticancer aptamers. Mol Cancer Ther 2006;5:2957–62. doi:10.1158/1535-7163.MCT-06-0172.

[234] Shieh Y-A, Yang S-J, Wei M-F, Shieh M-J. Aptamer-based tumor-targeted drug delivery for photodynamic therapy. ACS Nano 2010;4:1433–42. doi:10.1021/nn901374b.

[235] Farokhzad OC, Karp JM, Langer R. Nanoparticle–aptamer bioconjugates for cancer targeting. Expert Opin Drug Deliv 2006;3:311–24. doi:10.1517/17425247.3.3.311.

[236] Zhou G, Latchoumanin O, Hebbard L, Duan W, Liddle C, George J, et al. Aptamers as targeting ligands and therapeutic molecules for overcoming drug resistance in cancers. Adv Drug Deliv Rev 2018;134:107–21. doi:10.1016/j.addr.2018.04.005.

[237] Alshaer W. Aptamer-guided nanomedicines for anticancer drug delivery. Adv Drug Deliv Rev 2018;134:122–37. doi:10.1016/J.ADDR.2018.09.011.

[238] Vandghanooni S, Eskandani M, Barar J, Omidi Y. Recent advances in aptamer-armed multimodal theranostic nanosystems for imaging and targeted therapy of cancer. Eur J Pharm Sci 2018;117:301–12. doi:10.1016/j.ejps.2018.02.027.

[239] Zwicke GL, Mansoori GA, Jeffery CJ. Utilizing the folate receptor for active targeting of cancer nanotherapeutics. Nano Rev 2012;3:18496. doi:10.3402/nano.v3i0.18496.

[240] Destito G, Yeh R, Rae CS, Finn MG, Manchester M. Folic acid-mediated targeting of cowpea mosaic virus particles to tumor cells. Chem Biol 2007;14:1152–62. doi:10.1016/j.chembiol.2007.08.015.

[241] Müller C, Schibli R. Folic acid conjugates for nuclear imaging of folate receptor-positive cancer. J Nucl Med 2011;52:1–4. doi:10.2967/jnumed.110.076018.

[242] Hillier SM, Maresca KP, Femia FJ, Marquis JC, Foss CA, Nguyen N, et al. Preclinical evaluation of novel glutamate-urea-lysine analogues that target prostate-specific membrane antigen as molecular imaging pharmaceuticals for prostate cancer. Cancer Res 2009;69:6932–40. doi:10.1158/0008-5472.CAN-09-1682.

[243] Fuchs A V., Tse BWC, Pearce AK, Yeh M-C, Fletcher NL, Huang SS, et al. Evaluation of polymeric nanomedicines targeted to PSMA: effect of ligand on targeting efficiency. Biomacromolecules 2015;16:3235–47. doi:10.1021/acs.biomac.5b00913.

[244] Pearce AK, Rolfe BE, Russell PJ, Tse BW-C, Whittaker AK, Fuchs A V., et al.

Development of a polymer theranostic for prostate cancer. Polym Chem 2014;5:6932–42. doi:10.1039/C4PY00999A.

[245] Pearce AK, Simpson JD, Fletcher NL, Houston ZH, Fuchs A V., Russell PJ, et al. Localised delivery of doxorubicin to prostate cancer cells through a PSMA-targeted hyperbranched polymer theranostic. Biomaterials 2017;141:330–9. doi:10.1016/j.biomaterials.2017.07.004.

[246] Bone-targeted delivery of nanodiamond-based drug carriers conjugated with alendronate for potential osteoporosis treatment. J Controlled Release 2016;232:152–60. doi:10.1016/J.JCONREL.2016.04.025.

[247] Chen H, Li G, Chi H, Wang D, Tu C, Pan L, et al. Alendronate-conjugated amphiphilic hyperbranched polymer based on Boltorn H40 and poly(ethylene glycol) for bone-targeted drug delivery. Bioconjugate Chem 2012;23:1915–24. doi:10.1021/bc3003088.

[248] Pinho SS, Reis CA. Glycosylation in cancer: mechanisms and clinical implications. Nat Rev Cancer 2015;15:540–55. doi:10.1038/nrc3982.

[249] Thurecht KJ, Blakey I, Peng H, Squires O, Hsu S, Alexander C, et al. Functional hyperbranched polymers: toward targeted in Vivo 19 F magnetic resonance imaging using designed macromolecules. J Am Chem Soc 2010;132:5336–7. doi:10.1021/ja100252y.

[250] Sun P, Deng H, Zhou L, Wu Y, Jin X, Tong G, et al. “Bottom-up” fabrication of BODIPY-functionalized fluorescent Hyperbranched glycopolymers for hepatoma-targeted imaging. Macromol Biosci 2018;18:1700381. doi:10.1002/mabi.201700381.

[251] Choudhury H, Pandey M, Chin PX, Phang YL, Cheah JY, Ooi SC, et al. Transferrin receptors-targeting nanocarriers for efficient targeted delivery and transcytosis of drugs into the brain tumors: a review of recent advancements and emerging trends. Drug Deliv Transl Res 2018;8:1545–63. doi:10.1007/s13346-018-0552-2.

[252] Xu Q, Liu Y, Su S, Li W, Chen C, Wu Y. Anti-tumor activity of paclitaxel through dual-targeting carrier of cyclic RGD and transferrin conjugated hyperbranched copolymer nanoparticles. Biomaterials 2012;33:1627–39. doi:10.1016/j.biomaterials.2011.11.012.

[253] Hyaluronic acid and its derivatives in drug delivery and imaging: Recent advances and challenges. Eur J Pharm Biopharm 2015;97:400–16. doi:10.1016/J.EJPB.2015.03.032.

[254] Nikitovic D, Tzardi M, Berdiaki A, Tsatsakis A, Tzanakakis GN. Cancer microenvironment and inflammation: role of hyaluronan. Front Immunol 2015;6:169. doi:10.3389/fimmu.2015.00169.

[255] Gu J, Chen X, Ren X, Zhang X, Fang X, Sha X. CD44-targeted hyaluronic acid-coated redox-responsive hyperbranched poly(amido amine)/plasmid DNA ternary nanoassemblies for efficient gene delivery. Bioconjugate Chem 2016;27:1723–36. doi:10.1021/acs.bioconjchem.6b00240.

[256] Li N, Jin Y, Xue L, Li P, Yan D, Zhu X. 188Re-labeled hyperbranched polysulfonamine as a robust tool for targeted cancer diagnosis and radioimmunotherapy. Chinese J Polym Sci 2013;31:530–40. doi:10.1007/s10118-013-1242-7.

[257] Ellis LM, Hicklin DJ. VEGF-targeted therapy: mechanisms of anti-tumour activity. Nat Rev Cancer 2008;8:579–91. doi:10.1038/nrc2403.

[258] Hetian L, Ping A, Shumei S, Xiaoying L, Luowen H, Jian W, et al. A novel peptide isolated from a phage display library inhibits tumor growth and metastasis by blocking the binding of vascular endothelial growth factor to its kinase domain receptor. J Biol Chem 2002;277:43137–42. doi:10.1074/jbc.M203103200.

[259] Lim E-K, Kim T, Paik S, Haam S, Huh Y-M, Lee K. Nanomaterials for theranostics: recent advances and future challenges. Chem Rev 2015;115:327–94. doi:10.1021/cr300213b.

[260] Pu Y, Leng J, Wang D, Wang J, Foster NR, Chen J. Recent progress in the green synthesis of rare-earth doped upconversion nanophosphors for optical bioimaging from cells to animals. Chinese J Chem Eng 2018;26:2206–18. doi:10.1016/J.CJCHE.2018.03.005.

[261] Bagheri A, Arandiyan H, Boyer C, Lim M. Lanthanide-doped upconversion nanoparticles: Emerging intelligent light-activated drug delivery systems. Adv Sci 2016;3:1–25. doi:10.1002/advs.201500437.

[262] Loening AM, Wu AM, Gambhir SS. Red-shifted Renilla reniformis luciferase variants for imaging in living subjects. Nat Methods 2007;4:641–3. doi:10.1038/nmeth1070.

[263] Day RN, Davidson MW. The fluorescent protein palette: tools for cellular imaging. Chem Soc Rev 2009;38:2887. doi:10.1039/b901966a.

[264] Wang F, Banerjee D, Liu Y, Chen X, Liu X. Upconversion nanoparticles in biological labeling, imaging, and therapy. Analyst 2010;135:1839–54. doi:10.1039/c0an00144a.

[265] Li Q, Liu L, Liu J-W, Jiang J-H, Yu R-Q, Chu X. Nanomaterial-based fluorescent probes for live-cell imaging. TrAC Trends Anal Chem 2014;58:130–44. doi:10.1016/J.TRAC.2014.03.007.

[266] Hardman R. A toxicologic review of quantum dots: toxicity depends on physicochemical and environmental factors. Environ Health Perspect 2006;114:165–72. doi:10.1289/ehp.8284.

[267] Gao X, Cui Y, Levenson RM, Chung LWK, Nie S. In vivo cancer targeting and imaging with semiconductor quantum dots. Nat Biotechnol 2004;22:969–76. doi:10.1038/nbt994.

[268] Nam SH, Bae YM, Park Y Il, Kim JH, Kim HM, Choi JS, et al. Long-Term Real-Time Tracking of Lanthanide Ion Doped Upconverting Nanoparticles in Living Cells. Angew Chem Int Ed 2011;50:6093–7. doi:10.1002/anie.201007979.

[269] Zhu X, Su Q, Feng W, Li F. Anti-Stokes shift luminescent materials for bio-applications. Chem Soc Rev 2017;46:1025. doi:10.1039/c6cs00415f.

[270] Chen G, Qiu H, Prasad PN, Chen X. Upconversion Nanoparticles: Design, Nanochemistry, and Applications in Theranostics. Chem Rev 2014;114:5161–214. doi:10.1021/cr400425h.

[271] Yao C, Wang W, Wang P, Zhao M, Li X, Zhang F. Near-Infrared Upconversion Mesoporous Cerium Oxide Hollow Biophotocatalyst for Concurrent pH-/H_2O_2-Responsive O_2-Evolving Synergetic Cancer Therapy. Adv Mater 2018;30:1704833. doi:10.1002/adma.201704833.

[272] Chen S, Weitemier AZ, Zeng X, He L, Wang X, Tao Y, et al. Near-infrared deep brain stimulation via upconversion nanoparticle-mediated optogenetics. Science 2018;359:679–84. doi:10.1126/science.aaq1144.

[273] Hilderbrand SA, Weissleder R. Near-infrared fluorescence: application to in vivo

molecular imaging. Curr Opin Chem Biol 2010;14:71–9. doi:10.1016/J.CBPA.2009.09.029.

[274] Chen J, Zhao JX. Upconversion Nanomaterials: Synthesis, Mechanism, and Applications in Sensing. Sensors 2012;12:2414–35. doi:10.3390/s120302414.

[275] Naccache R, Yu Q, Capobianco JA. The Fluoride Host: Nucleation, Growth, and Upconversion of Lanthanide-Doped Nanoparticles. Adv Opt Mater 2015;3:482–509. doi:10.1002/adom.201400628.

[276] Chua M, Tanner PA, Reid MF. Phonon-assisted energy transfer. J Lumin 1994;60–61:838–41. doi:10.1016/0022-2313(94)90291-7.

[277] Li D, Ågren H, Chen G. Near infrared harvesting dye-sensitized solar cells enabled by rare-earth upconversion materials. Dalt Trans 2018;47:8526–37. doi:10.1039/C7DT04461E.

[278] DaCosta M V., Doughan S, Han Y, Krull UJ. Lanthanide upconversion nanoparticles and applications in bioassays and bioimaging: A review. Anal Chim Acta 2014;832:1–33. doi:10.1016/J.ACA.2014.04.030.

[279] Dibaba ST, Xiaoqian Ge, Ren W, Sun L. Recent progress of energy transfer and luminescence intensity boosting mechanism in Nd3+-sensitized upconversion nanoparticles. J Rare Earths 2019;37:791–805. doi:10.1016/J.JRE.2019.02.001.

[280] Ge X, Sun L, Shi L, Wei R. The modified upconversion nanomaterials (UCNMs) for multimodal imaging and therapies. Biomed Spectrosc Imaging 2015;4:391–412. doi:10.3233/BSI-150120.

[281] Sun L, Ge X, Liu J, Qiu Y, Wei Z, Tian B, et al. Multifunctional nanomesoporous materials with upconversion (in vivo) and downconversion (in vitro) luminescence imaging based on mesoporous capping UCNPs and linking lanthanide complexes. Nanoscale 2014;6:13242–52. doi:10.1039/C4NR04258A.

[282] Ge X, Liu J, Sun L. Controlled optical characteristics of lanthanide doped upconversion nanoparticles for emerging applications. Dalt Trans 2017;46:16729. doi:10.1039/c7dt03049e.

[283] Yu M, Li F, Chen Z, Hu H, Zhan C, Yang H, et al. Laser Scanning Up-Conversion

Luminescence Microscopy for Imaging Cells Labeled with Rare-Earth Nanophosphors. Anal Chem 2009;81:930–5. doi:10.1021/ac802072d.

[284] Zijlmans HJMAA, Bonnet J, Burton J, Kardos K, Vail T, Niedbala RS, et al. Detection of Cell and Tissue Surface Antigens Using Up-Converting Phosphors: A New Reporter Technology. Anal Biochem 1999;267:30–6. doi:10.1006/ABIO.1998.2965.

[285] Ruggiero E, Alonso-de Castro S, Habtemariam A, Salassa L. Upconverting nanoparticles for the near infrared photoactivation of transition metal complexes: new opportunities and challenges in medicinal inorganic photochemistry. Dalt Trans 2016;45:13012–20. doi:10.1039/C6DT01428C.

[286] Weissleder R. A clearer vision for in vivo imaging. Nat Biotechnol 2001;19:316–7. doi:10.1038/86684.

[287] Zhao J. Exploring unique optical properties of upconversion nanocrystals towards a new library of molecular probes. Macquarie University, 2014.

[288] Dong H, Sun L-D, Yan C-H. Energy transfer in lanthanide upconversion studies for extended optical applications. Chem Soc Rev 2015;44:1608–34. doi:10.1039/C4CS00188E.

[289] Wang F, Liu X. Recent advances in the chemistry of lanthanide-doped upconversion nanocrystals. Chem Soc Rev 2009;38:976–89. doi:10.1039/b809132n.

[290] Wang G, Peng Q, Li Y. Lanthanide-Doped Nanocrystals: Synthesis, Optical-Magnetic Properties, and Applications. Acc Chem Res 2011;44:322–32. doi:10.1021/ar100129p.

[291] Speghini A, Piccinelli F, Bettinelli M. Synthesis, characterization and luminescence spectroscopy of oxide nanopowders activated with trivalent lanthanide ions: The garnet family. Opt Mater (Amst) 2011;33:247–57. doi:10.1016/J.OPTMAT.2010.10.039.

[292] O. Lehmann, H. Meyssamy, K. Kömpe, Schnablegger H, Haase M. Synthesis, Growth, and Er3+ Luminescence of Lanthanide Phosphate Nanoparticles. J Phys Chem B 2003;107:7449–53. doi:10.1021/JP030012H.

[293] Yang D, Ma P, Hou Z, Cheng Z, Li C, Lin J. Current advances in lanthanide ion (Ln^{3+})-based upconversion nanomaterials for drug delivery. Chem Soc Rev 2015;44:1416–

48. doi:10.1039/C4CS00155A.

[294] Chen G, Qiu H, Prasad PN, Chen X. Upconversion Nanoparticles: Design, Nanochemistry, and Applications in Theranostics. Chem Rev 2014;114:5161–214. doi:10.1021/cr400425h.

[295] Diamente PR, Raudsepp M, van Veggel FCJM. Dispersible Tm3+ Doped Nanoparticles that Exhibit Strong 1.47 µm Photoluminescence. Adv Funct Mater 2007;17:363–8. doi:10.1002/adfm.200600142.

[296] Wang D, Zhu L, Chen J-F, Dai L. Liquid Marbles Based on Magnetic Upconversion Nanoparticles as Magnetically and Optically Responsive Miniature Reactors for Photocatalysis and Photodynamic Therapy. Angew Chem Int Ed 2016;55:10795–9. doi:10.1002/anie.201604781.

[297] Chen D, Huang P, Yu Y, Huang F, Yang A, Wang Y. Dopant-induced phase transition: a new strategy of synthesizing hexagonal upconversion NaYF4 at low temperature. Chem Commun 2011;47:5801. doi:10.1039/c0cc05722c.

[298] Auzel F. Upconversion and Anti-Stokes Processes with f and d Ions in Solids. Chem Rev 2004;104:139–74. doi:10.1021/CR020357G.

[299] Haase M, Schäfer H. Upconverting Nanoparticles. Angew Chem Int Ed 2011;50:5808–29. doi:10.1002/anie.201005159.

[300] Wang F, Liu X. Multicolor Tuning of Lanthanide-Doped Nanoparticles by Single Wavelength Excitation. Acc Chem Res 2014;47:1378–85. doi:10.1021/ar5000067.

[301] Liu Q, Feng W, Li F. Water-soluble lanthanide upconversion nanophosphors: Synthesis and bioimaging applications in vivo. Coord Chem Rev 2014;273–274:100–10. doi:10.1016/J.CCR.2014.01.004.

[302] Chan EM. Combinatorial approaches for developing upconverting nanomaterials: high-throughput screening, modeling, and applications. Chem Soc Rev 2015;44:1653–79. doi:10.1039/C4CS00205A.

[303] Heer S, Kömpe K, Güdel H-U, Haase M. Highly Efficient Multicolour Upconversion Emission in Transparent Colloids of Lanthanide-Doped $NaYF_4$ Nanocrystals. Adv Mater 2004;16:2102–5. doi:10.1002/adma.200400772.

[304] Wang F, Liu X. Recent advances in the chemistry of lanthanide-doped upconversion nanocrystals. Chem Soc Rev 2009;38:976–89. doi:10.1039/b809132n.

[305] Heer S, Kömpe K, Güdel HU, Haase M. Highly efficient multicolour upconversion emission in transparent colloids of lanthanide-doped NaYF4 nanocrystals. Adv Mater 2004;16:2102–5. doi:10.1002/adma.200400772.

[306] Mackenzie LE, Goode JA, Vakurov A, Nampi PP, Saha S, Jose G, et al. The theoretical molecular weight of NaYF 4 :RE upconversion nanoparticles. Sci Rep 2018;8:1106. doi:10.1038/s41598-018-19415-w.

[307] Thoma RE, Insley H, Hebert GM. The Sodium Fluoride-Lanthanide Trifluoride Systems. Inorg Chem 1966;5:1222–9. doi:10.1021/ic50041a032.

[308] Krämer KW, Biner D, Frei G, Güdel HU, Hehlen MP, Lüthi SR. Hexagonal Sodium Yttrium Fluoride Based Green and Blue Emitting Upconversion Phosphors. Chem Mater 2004;16:1244–51. doi:10.1021/CM031124O.

[309] Wang F, Han Y, Lim CS, Lu Y, Wang J, Xu J, et al. Simultaneous phase and size control of upconversion nanocrystals through lanthanide doping. Nature 2010;463:1061–5. doi:10.1038/nature08777.

[310] Du P, Luo L, Yu JS. Facile synthesis of Er^{3+} /Yb^{3+} -codoped $NaYF_4$ nanoparticles: a promising multifunctional upconverting luminescent material for versatile applications. RSC Adv 2016;6:94539–46. doi:10.1039/C6RA22349D.

[311] Mai H-X, Zhang Y-W, Si R, Yan Z-G, Sun L, You L-P, et al. High-Quality Sodium Rare-Earth Fluoride Nanocrystals: Controlled Synthesis and Optical Properties. J Am Chem Soc 2006;128:6426–36. doi:10.1021/JA060212H.

[312] Aebischer A, Heer S, Biner D, Krämer K, Haase M, Güdel HU. Visible light emission upon near-infrared excitation in a transparent solution of nanocrystalline β-NaGdF4: Yb3+, Er3+. Chem Phys Lett 2005;407:124–8. doi:10.1016/J.CPLETT.2005.03.053.

[313] Mao C, Yang X, Zhao L. Simultaneous morphology control and upconversion fluorescence enhancement of NaYF4:Yb,Er crystals through alkali ions doping. Chem Eng J 2013;229:429–35. doi:10.1016/J.CEJ.2013.06.026.

[314] Liu Q, Sun Y, Yang T, Feng W, Li C, Li F. Sub-10 nm Hexagonal Lanthanide-Doped

NaLuF $_4$ Upconversion Nanocrystals for Sensitive Bioimaging in Vivo. J Am Chem Soc 2011;133:17122–5. doi:10.1021/ja207078s.

[315] Ostrowski AD, Chan EM, Gargas DJ, Katz EM, Han G, Schuck PJ, et al. Controlled Synthesis and Single-Particle Imaging of Bright, Sub-10 nm Lanthanide-Doped Upconverting Nanocrystals. ACS Nano 2012;6:2686–92. doi:10.1021/nn3000737.

[316] Shan J, Ju Y. Controlled synthesis of lanthanide-doped NaYF4 upconversion nanocrystals via ligand induced crystal phase transition and silica coating. Appl Phys Lett 2007;91:123103. doi:10.1063/1.2783476.

[317] Shan J, Ju Y. A single-step synthesis and the kinetic mechanism for monodisperse and hexagonal-phase NaYF $_4$:Yb, Er upconversion nanophosphors. Nanotechnology 2009;20:275603. doi:10.1088/0957-4484/20/27/275603.

[318] Liu D, Xu X, Du Y, Qin X, Zhang Y, Ma C, et al. Three-dimensional controlled growth of monodisperse sub-50 nm heterogeneous nanocrystals. Nat Commun 2016;7:10254. doi:10.1038/ncomms10254.

[319] Liu X, Zhang X, Tian G, Yin W, Yan L, Ruan L, et al. A simple and efficient synthetic route for preparation of NaYF $_4$ upconversion nanoparticles by thermo-decomposition of rare-earth oleates. CrystEngComm 2014;16:5650–61. doi:10.1039/C4CE00231H.

[320] Na H, Woo K, Lim K, Jang HS. Rational morphology control of β-NaYF4:Yb,Er/Tm upconversion nanophosphors using a ligand, an additive, and lanthanide doping. Nanoscale 2013;5:4242. doi:10.1039/c3nr00080j.

[321] Ye S, Xiao P, Liao H, Li S, Wang D. Fast synthesis of sub-10 nm β-NaYF4:Yb3+, Er3+@NaYF4 core-shell upconversion nanocrystals mediated by oleate ligands. Mater Res Bull 2018;103:279–84. doi:10.1016/J.MATERRESBULL.2018.03.011.

[322] Zhai X, Wang Y, Liu X, Liu S, Lei P, Yao S, et al. A Simple Strategy for the Controlled Synthesis of Ultrasmall Hexagonal-Phase NaYF $_4$:Yb,Er Upconversion Nanocrystals. ChemPhotoChem 2017;1:369–75. doi:10.1002/cptc.201700013.

[323] Zhang C, Lee JY. Prevalence of Anisotropic Shell Growth in Rare Earth Core–Shell Upconversion Nanocrystals. ACS Nano 2013;7:4393–402. doi:10.1021/nn4009214.

[324] Johnson NJJ, van Veggel FCJM. Sodium lanthanide fluoride core-shell nanocrystals: A

general perspective on epitaxial shell growth. Nano Res 2013;6:547–61. doi:10.1007/s12274-013-0333-7.

[325] Gai S, Li C, Yang P, Lin J. Recent Progress in Rare Earth Micro/Nanocrystals: Soft Chemical Synthesis, Luminescent Properties, and Biomedical Applications. Chem Rev 2014;114:2343–89. doi:10.1021/cr4001594.

[326] Dong H, Du S-R, Zheng X-Y, Lyu G-M, Sun L-D, Li L-D, et al. Lanthanide Nanoparticles: From Design toward Bioimaging and Therapy. Chem Rev 2015;115:10725–815. doi:10.1021/acs.chemrev.5b00091.

[327] Liang S, Liu Y, Tang Y, Xie Y, Sun H, … HZ-J of, et al. A user-friendly method for synthesizing high-quality NaYF 4: Yb, Er (Tm) nanocrystals in liquid paraffin. J Nanomater 2011:302364. doi:10.1155/2011/302364.

[328] Shan J, Qin X, Yao N, Ju Y. Synthesis of monodisperse hexagonal $NaYF_4$:Yb, Ln (Ln = Er, Ho and Tm) upconversion nanocrystals in TOPO. Nanotechnology 2007;18:445607. doi:10.1088/0957-4484/18/44/445607.

[329] Liu C, Gao Z, Zeng J, Hou Y, Fang F, Li Y, et al. Magnetic/Upconversion Fluorescent $NaGdF_4$:Yb,Er Nanoparticle-Based Dual-Modal Molecular Probes for Imaging Tiny Tumors *in Vivo*. ACS Nano 2013;7:7227–40. doi:10.1021/nn4030898.

[330] Wang J, Song H, Xu W, Dong B, Xu S, Chen B, et al. Phase transition, size control and color tuning of NaREF4:Yb3+, Er3+ (RE = Y, Lu) nanocrystals. Nanoscale 2013;5:3412. doi:10.1039/c3nr34282d.

[331] Rodrigues EM, Gálico DA, Lemes MA, Bettini J, T. Neto E, Mazali IO, et al. One pot synthesis and systematic study of the photophysical and magnetic properties and thermal sensing of α and β-phase $NaLnF_4$ and β-phase core@shell nanoparticles. New J Chem 2018;42:13393–405. doi:10.1039/C8NJ02471E.

[332] Pu Y, Lin L, Wang D, Wang J-X, Qian J, Chen J-F. Green synthesis of highly dispersed ytterbium and thulium co-doped sodium yttrium fluoride microphosphors for in situ light upconversion from near-infrared to blue in animals. J Colloid Interface Sci 2018;511:243–50. doi:10.1016/J.JCIS.2017.10.017.

[333] Wang F, Liu X. Upconversion Multicolor Fine-Tuning: Visible to Near-Infrared Emission from Lanthanide-Doped $NaYF_4$ Nanoparticles. J Am Chem Soc 2008;130:5642–3.

doi:10.1021/ja800868a.

[334] Qiu H, Chen G, Sun L, Hao S, Han G, Yang C. Ethylenediaminetetraacetic acid (EDTA)-controlled synthesis of multicolor lanthanide doped BaYF5 upconversion nanocrystals. J Mater Chem 2011;21:17202. doi:10.1039/c1jm12950c.

[335] Zeng J-H, Su J, Li Z-H, Yan R-X, Li Y-D. Synthesis and Upconversion Luminescence of Hexagonal-Phase NaYF4:Yb, Er3+ Phosphors of Controlled Size and Morphology. Adv Mater 2005;17:2119–23. doi:10.1002/adma.200402046.

[336] Wang L, Li P, Li Y. Down- and Up-Conversion Luminescent Nanorods. Adv Mater 2007;19:3304–7. doi:10.1002/adma.200700144.

[337] Wang F, Chatterjee DK, Li Z, Zhang Y, Fan X, Wang M. Synthesis of polyethylenimine/NaYF $_4$ nanoparticles with upconversion fluorescence. Nanotechnology 2006;17:5786–91. doi:10.1088/0957-4484/17/23/013.

[338] Zhou L, Li Z, Liu Z, Yin M, Ren J, Qu X. One-step nucleotide-programmed growth of porous upconversion nanoparticles: application to cell labeling and drug delivery. Nanoscale 2014;6:1445–52. doi:10.1039/c3nr04255c.

[339] Qiu P, Zhou N, Wang Y, Zhang C, Wang Q, Sun R, et al. Tuning lanthanide ion-doped upconversion nanocrystals with different shapes via a one-pot cationic surfactant-assisted hydrothermal strategy. CrystEngComm 2014;16:1859. doi:10.1039/c3ce42076k.

[340] Sun R, Qiu P, Yin T, Gao G, Fu H, Wang K, et al. Potassium sodium tartrate-assisted hydrothermal synthesis of BaLuF5:Yb3+/Er3+ nanocrystals. Particuology 2016;24:164–9. doi:10.1016/J.PARTIC.2015.02.005.

[341] Wang M, Liu J-L, Zhang Y-X, Hou W, Wu X-L, Xu S-K. Two-phase solvothermal synthesis of rare-earth doped NaYF4 upconversion fluorescent nanocrystals. Mater Lett 2009;63:325–7. doi:10.1016/J.MATLET.2008.10.028.

[342] Yi G, Lu H, Zhao S, Ge Y, Yang W, Chen D, et al. Synthesis, Characterization, and Biological Application of Size-Controlled Nanocrystalline NaYF4:Yb,Er Infrared-to-Visible Up-Conversion Phosphors. Nano Lett 2004;4:2191–6. doi:10.1021/NL048680H.

[343] Li Z, Zhang Y. An efficient and user-friendly method for the synthesis of hexagonal-

phase $NaYF_4$:Yb, Er/Tm nanocrystals with controllable shape and upconversion fluorescence. Nanotechnology 2008;19:345606. doi:10.1088/0957-4484/19/34/345606.

[344] Shah S, Liu J-J, Pasquale N, Lai J, McGowan H, Pang ZP, et al. Hybrid upconversion nanomaterials for optogenetic neuronal control. Nanoscale 2015;7:16571–7. doi:10.1039/c5nr03411f.

[345] Liu C, Wang H, Li X, Chen D. Monodisperse, size-tunable and highly efficient β-NaYF4:Yb,Er(Tm) up-conversion luminescent nanospheres: controllable synthesis and their surface modifications. J Mater Chem 2009;19:3546. doi:10.1039/b820254k.

[346] Liu C, Wang H, Zhang X, Chen D. Morphology- and phase-controlled synthesis of monodisperse lanthanide-doped $NaGdF_4$ nanocrystals with multicolor photoluminescence. J Mater Chem 2009;19:489–96. doi:10.1039/B815682D.

[347] Wang M, Abbineni G, Clevenger A, Mao C, Xu S. Upconversion nanoparticles: synthesis, surface modification and biological applications. Nanomedicine Nanotechnology, Biol Med 2011;7:710–29. doi:10.1016/j.nano.2011.02.013.

[348] Mao Z, Yang C. Micro-mixing in chemical reactors: A perspective. Chinese J Chem Eng 2017;25:381–90. doi:10.1016/J.CJCHE.2016.09.012.

[349] Wen S, Zhou J, Zheng K, Bednarkiewicz A, Liu X, Jin D. Advances in highly doped upconversion nanoparticles. Nat Commun 2018;9:2415. doi:10.1038/s41467-018-04813-5.

[350] Zhou B, Shi B, Jin D, Liu X. Controlling upconversion nanocrystals for emerging applications. Nat Nanotechnol 2015;10:924–36. doi:10.1038/nnano.2015.251.

[351] Sun Q-C, Ding YC, Sagar DM, Nagpal P. Photon upconversion towards applications in energy conversion and bioimaging. Prog Surf Sci 2017;92:281–316. doi:10.1016/J.PROGSURF.2017.09.003.

[352] Li K, Hong E, Wang B, Wang Z, Zhang L, Hu R, et al. Advances in the application of upconversion nanoparticles for detecting and treating cancers. Photodiagnosis Photodyn Ther 2019;25:177–92. doi:10.1016/J.PDPDT.2018.12.007.

[353] Duan C, Liang L, Li L, Zhang R, Xu ZP. Recent progress in upconversion luminescence

nanomaterials for biomedical applications. J Mater Chem B 2018;6:192. doi:10.1039/c7tb02527k.

[354] González-Béjar M, Francés-Soriano L, Pérez-Prieto J. Upconversion Nanoparticles for Bioimaging and Regenerative Medicine. Front Bioeng Biotechnol 2016;4:47. doi:10.3389/fbioe.2016.00047.

[355] Rafique R, Kailasa SK, Park TJ. Recent advances of upconversion nanoparticles in theranostics and bioimaging applications. TrAC Trends Anal Chem 2019:115646. doi:10.1016/J.TRAC.2019.115646.

[356] Cao T, Yang T, Gao Y, Yang Y, Hu H, Li F. Water-soluble NaYF4:Yb/Er upconversion nanophosphors: Synthesis, characteristics and application in bioimaging. Inorg Chem Commun 2010;13:392–4. doi:10.1016/J.INOCHE.2009.12.031.

[357] Liebherr RB, Soukka T, Wolfbeis OS, Gorris HH. Maleimide activation of photon upconverting nanoparticles for bioconjugation. Nanotechnology 2012;23:485103. doi:10.1088/0957-4484/23/48/485103.

[358] Meiser F, Cortez C, Caruso F. Biofunctionalization of Fluorescent Rare-Earth-Doped Lanthanum Phosphate Colloidal Nanoparticles. Angew Chem Int Ed 2004;43:5954–7. doi:10.1002/anie.200460856.

[359] Zhang Q, Song K, Zhao J, Kong X, Sun Y, Liu X, et al. Hexanedioic acid mediated surface–ligand-exchange process for transferring NaYF4:Yb/Er (or Yb/Tm) up-converting nanoparticles from hydrophobic to hydrophilic. J Colloid Interface Sci 2009;336:171–5. doi:10.1016/J.JCIS.2009.04.024.

[360] Yu J, Yin W, Peng T, Chang Y, Zu Y, Li J, et al. Biodistribution, excretion, and toxicity of polyethyleneimine modified $NaYF_4$:Yb,Er upconversion nanoparticles in mice via different administration routes. Nanoscale 2017;9:4497–507. doi:10.1039/C7NR00078B.

[361] Chatterjee DK, Rufaihah AJ, Zhang Y. Upconversion fluorescence imaging of cells and small animals using lanthanide doped nanocrystals. Biomaterials 2008;29:937–43. doi:10.1016/J.BIOMATERIALS.2007.10.051.

[362] Gu Y, Qiao X, Zhang J, Sun Y, Tao Y, Qiao S. Effects of surface modification of upconversion nanoparticles on cellular uptake and cytotoxicity. Chem Res Chinese

Univ 2016;32:474–9. doi:10.1007/s40242-016-6026-5.

[363] Boyer J-C, Manseau M-P, Murray JI, van Veggel FCJM. Surface Modification of Upconverting NaYF $_4$ Nanoparticles with PEG−Phosphate Ligands for NIR (800 nm) Biolabeling within the Biological Window. Langmuir 2010;26:1157–64. doi:10.1021/la902260j.

[364] Naccache R, Vetrone F, Mahalingam V, Cuccia LA, Capobianco JA. Controlled Synthesis and Water Dispersibility of Hexagonal Phase NaGdF $_4$:Ho $^{3+}$ /Yb $^{3+}$ Nanoparticles. Chem Mater 2009;21:717–23. doi:10.1021/cm803151y.

[365] Duong HTT, Chen Y, Tawfik SA, Wen S, Parviz M, Shimoni O, et al. Systematic investigation of functional ligands for colloidal stable upconversion nanoparticles. RSC Adv 2018;8:4842–9. doi:10.1039/c7ra13765f.

[366] Liu C, Wang Z, Wang X, Li Z. Surface modification of hydrophobic NaYF4:Yb,Er upconversion nanophosphors and their applications for immunoassay. Sci China Chem 2011;54:1292–7. doi:10.1007/s11426-011-4319-6.

[367] Bogdan N, Vetrone F, Roy R, Capobianco JA. Carbohydrate-coated lanthanide-doped upconverting nanoparticles for lectin recognition. J Mater Chem 2010;20:7543. doi:10.1039/c0jm01617a.

[368] Cao T, Yang Y, Gao Y, Zhou J, Li Z, Li F. High-quality water-soluble and surface-functionalized upconversion nanocrystals as luminescent probes for bioimaging. Biomaterials 2011;32:2959–68. doi:10.1016/J.BIOMATERIALS.2010.12.050.

[369] Chen Z, Chen H, Hu H, Yu M, Li F, Zhang Q, et al. Versatile synthesis strategy for carboxylic acid-functionalized upconverting nanophosphors as biological labels. J Am Chem Soc 2008;130:3023–9. doi:10.1021/ja076151k.

[370] Lemieux RU, Rudloff E Von. Periodate–permanganate oxidations: i. oxidation of olefins. Can J Chem 1955;33:1701–9. doi:10.1139/v55-208.

[371] Zhou H-P, Xu C-H, Sun W, Yan C-H. Clean and Flexible Modification Strategy for Carboxyl/Aldehyde-Functionalized Upconversion Nanoparticles and Their Optical Applications. Adv Funct Mater 2009;19:3892–900. doi:10.1002/adfm.200901458.

[372] Bogdan N, Rodríguez EM, Sanz-Rodríguez F, Iglesias de la Cruz MC, Juarranz Á, Jaque

D, et al. Bio-functionalization of ligand-free upconverting lanthanide doped nanoparticles for bio-imaging and cell targeting. Nanoscale 2012;4:3647. doi:10.1039/c2nr30982c.

[373] Liang S, Zhang X, Wu Z, Liu Y, Zhang H, Sun H, et al. Decoration of up-converting NaYF4:Yb,Er(Tm) nanoparticles with surfactant bilayer. A versatile strategy to perform oil-to-water phase transfer and subsequently surface silication. CrystEngComm 2012;14:3484. doi:10.1039/c2ce06578a.

[374] Li L-L, Zhang R, Yin L, Zheng K, Qin W, Selvin PR, et al. Biomimetic Surface Engineering of Lanthanide-Doped Upconversion Nanoparticles as Versatile Bioprobes. Angew Chem Int Ed 2012;51:6121–5. doi:10.1002/anie.201109156.

[375] Ren W, Tian G, Jian S, Gu Z, Zhou L, Yan L, et al. TWEEN coated NaYF4:Yb,Er/NaYF4 core/shell upconversion nanoparticles for bioimaging and drug delivery. RSC Adv 2012;2:7037. doi:10.1039/c2ra20855e.

[376] Budijono SJ, Shan J, Yao N, Miura Y, Hoye T, Austin RH, et al. Synthesis of Stable Block-Copolymer-Protected $NaYF_4$:Yb^{3+}, Er^{3+} Up-Converting Phosphor Nanoparticles. Chem Mater 2010;22:311–8. doi:10.1021/cm902478a.

[377] Nichkova M, Dosev D, Gee SJ, Hammock BD, Kennedy IM. Microarray Immunoassay for Phenoxybenzoic Acid Using Polymer Encapsulated Eu:Gd2O3 Nanoparticles as Fluorescent Labels. Anal Chem 2005;77:6864–73. doi:10.1021/AC050826P.

[378] Cheng L, Yang K, Zhang S, Shao M, Lee S, Liu Z. Highly-sensitive multiplexed in vivo imaging using pegylated upconversion nanoparticles. Nano Res 2010;3:722–32. doi:10.1007/s12274-010-0036-2.

[379] Wang L, Yan R, Huo Z, Wang L, Zeng J, Bao J, et al. Fluorescence Resonant Energy Transfer Biosensor Based on Upconversion-Luminescent Nanoparticles. Angew Chem Int Ed 2005;44:6054–7. doi:10.1002/anie.200501907.

[380] Bao Y, Luu Q, Lin C, Schloss J, … PM-J of materials, 2010 U. Layer-by-layer assembly of freestanding thin films with homogeneously distributed upconversion nanocrystals. J Mater Chem 2010;20:8356–61.

[381] Guller AE, Generalova AN, Petersen E V., Nechaev A V., Trusova IA, Landyshev NN, et al. Cytotoxicity and non-specific cellular uptake of bare and surface-modified

upconversion nanoparticles in human skin cells. Nano Res 2015;8:1546–62. doi:10.1007/s12274-014-0641-6.

[382] Zhang H, Li Y, Ivanov IA, Qu Y, Huang Y, Duan X. Plasmonic modulation of the upconversion fluorescence in NaYF4 :Yb/Tm hexaplate nanocrystals using gold nanoparticles or nanoshells. Angew Chem Int Ed Engl 2010;49:2865–8. doi:10.1002/anie.200905805.

[383] Guerrero-Martínez A, Pérez-Juste J, Liz-Marzán LM. Recent Progress on Silica Coating of Nanoparticles and Related Nanomaterials. Adv Mater 2010;22:1182–95. doi:10.1002/adma.200901263.

[384] Sedlmeier A, Gorris HH. Surface modification and characterization of photon-upconverting nanoparticles for bioanalytical applications. Chem Soc Rev 2015;44:1526–60. doi:10.1039/C4CS00186A.

[385] Xia A, Chen M, Gao Y, Wu D, Feng W, Li F. Gd3+ complex-modified NaLuF4-based upconversion nanophosphors for trimodality imaging of NIR-to-NIR upconversion luminescence, X-Ray computed tomography and magnetic resonance. Biomaterials 2012;33:5394–405. doi:10.1016/j.biomaterials.2012.04.025.

[386] Hlaváček A, Farka Z, Hübner M, Horňáková V, Němeček D, Niessner R, et al. Competitive Upconversion-Linked Immunosorbent Assay for the Sensitive Detection of Diclofenac. Anal Chem 2016;88:6011–7. doi:10.1021/acs.analchem.6b01083.

[387] Zhang C, Zhao K, Bu W, Ni D, Liu Y, Feng J, et al. Marriage of Scintillator and Semiconductor for Synchronous Radiotherapy and Deep Photodynamic Therapy with Diminished Oxygen Dependence. Angew Chem Int Ed 2015;54:1770–4. doi:10.1002/anie.201408472.

[388] Abdul Jalil R, Zhang Y. Biocompatibility of silica coated NaYF4 upconversion fluorescent nanocrystals. Biomaterials 2008;29:4122–8. doi:10.1016/J.BIOMATERIALS.2008.07.012.

[389] Liu Z, Yi G, Zhang H, Ding J, Zhang Y, Xue J. Monodisperse silicananoparticles encapsulating upconversion fluorescent and superparamagnetic nanocrystals. Chem Commun 2008:694–6. doi:10.1039/B715402J.

[390] Xing H, Bu W, Zhang S, Zheng X, Li M, Chen F, et al. Multifunctional nanoprobes for

upconversion fluorescence, MR and CT trimodal imaging. Biomaterials 2012;33:1079–89. doi:10.1016/J.BIOMATERIALS.2011.10.039.

[391] Sivakumar S, Diamente PR, van Veggel FCJM. Silica-Coated Ln3+-Doped LaF3 Nanoparticles as Robust Down- and Upconverting Biolabels. Chem - A Eur J 2006;12:5878–84. doi:10.1002/chem.200600224.

[392] Li Z, Zhang Y. Monodisperse Silica-Coated Polyvinylpyrrolidone/NaYF4 Nanocrystals with Multicolor Upconversion Fluorescence Emission. Angew Chemie 2006;118:7896–9. doi:10.1002/ange.200602975.

[393] Mansky P, Liu Y, Huang E, Russell TP, Hawker C. Controlling Polymer-Surface Interactions with Random Copolymer Brushes. Science 1997;275:1458–60. doi:10.1126/science.275.5305.1458.

[394] Balazs AC, Singh C, Zhulina E, Chern S-S, Lyatskaya Y, Pickett G. Theory of polymer chains tethered at interfaces. Prog Surf Sci 1997;55:181–269. doi:10.1016/S0079-6816(97)00026-9.

[395] Rühe J, Knoll W. FUNCTIONAL POLYMER BRUSHES. J Macromol Sci Part C Polym Rev 2002;42:91–138. doi:10.1081/MC-120003096.

[396] Liu S, Tian B, Wu S, Wang Y, Huang J, Gao B, et al. pH-sensitive polymer-gated multifunctional upconversion NaYF4:Yb/Er@mSiO2 nanocomposite for oral drug delivery. Microporous Mesoporous Mater 2018;264:151–8. doi:10.1016/J.MICROMESO.2018.01.029.

[397] Dai Y, Ma P, Cheng Z, Kang X, Zhang X, Hou Z, et al. Up-Conversion Cell Imaging and pH-Induced Thermally Controlled Drug Release from $NaYF_4$:Yb^{3+}/Er^{3+}@Hydrogel Core–Shell Hybrid Microspheres. ACS Nano 2012;6:3327–38. doi:10.1021/nn300303q.

[398] Tian J, Bai J, Peng Y, Qie Z, Zhao Y, Ning B, et al. A core–shell-structured molecularly imprinted polymer on upconverting nanoparticles for selective and sensitive fluorescence sensing of sulfamethazine. Analyst 2015;140:5301–7. doi:10.1039/C5AN00579E.

[399] Tian B, Liu S, Lu W, Jin L, Li Q, Shi Y, et al. Construction of pH-responsive and up-conversion luminescent NaYF4:Yb3+/Er3+@SiO2@PMAA nanocomposite for colon targeted drug delivery. Sci Rep 2016;6:21335. doi:10.1038/srep21335.

[400] Wang Y, Ren S, Jiang H, Peng Y, Bai J, Li Q, et al. A label-free detection of diethylstilbestrol based on molecularly imprinted polymer-coated upconversion nanoparticles obtained by surface grafting. RSC Adv 2017;7:22215–21. doi:10.1039/C6RA26999K.

[401] Carrot G, Rutot-Houzé D, Pottier A, Degée P, Hilborn J, Dubois P. Surface-Initiated Ring-Opening Polymerization: A Versatile Method for Nanoparticle Ordering. Macromolecules 2002;35:8400–4. doi:10.1021/MA020558M.

[402] Edmondson S, Osborne VL, Huck WTS. Polymer brushes via surface-initiated polymerizations. Chem Soc Rev 2004;33:14. doi:10.1039/b210143m.

[403] He B, Zhou L. Efficient tailoring of the surface of upconversion nanoparticles via surface-initiated cationic ring-opening polymerization. RSC Adv 2015;5:97764–72. doi:10.1039/C5RA18922E.

[404] Zhou L, He B, Huang J, Cheng Z, Xu X, Wei C. Multihydroxy Dendritic Upconversion Nanoparticles with Enhanced Water Dispersibility and Surface Functionality for Bioimaging. ACS Appl Mater Interfaces 2014;6:7719–27. doi:10.1021/am500980z.

[405] He B, Zhou L. Efficient tailoring of the surface of upconversion nanoparticles via surface-initiated cationic ring-opening polymerization. RSC Adv 2015;5:97764–72. doi:10.1039/C5RA18922E.

[406] Wang J-S, Matyjaszewski K. Controlled/"living" radical polymerization. atom transfer radical polymerization in the presence of transition-metal complexes. J Am Chem Soc 1995;117:5614–5. doi:10.1021/ja00125a035.

[407] Hui CM, Pietrasik J, Schmitt M, Mahoney C, Choi J, Bockstaller MR, et al. Surface-Initiated Polymerization as an Enabling Tool for Multifunctional (Nano-)Engineered Hybrid Materials. Chem Mater 2014;26:745–62. doi:10.1021/cm4023634.

[408] Zhang M, Herrera M, Patten TE, Augustine M, Sun L-D, Yan C-H, et al. Core/Shell/Shell Nanomaterials of NayF4: Yb, Er/Silica/Polystyrene with High Thermal Stability. Int J Nanoparticles Nanotechnol 2015;1:2–7. doi:10.35840/2631-5084/5503.

[409] Zhang W, Peng B, Tian F, Qin W, Qian X. Facile Preparation of Well-Defined Hydrophilic Core–Shell Upconversion Nanoparticles for Selective Cell Membrane Glycan Labeling and Cancer Cell Imaging. Anal Chem 2014;86:482–9.

doi:10.1021/ac402389w.

[410] Xiang J, Tong X, Shi F, Yan Q, Yu B, Zhao Y. Near-infrared light-triggered drug release from UV-responsive diblock copolymer-coated upconversion nanoparticles with high monodispersity. J Mater Chem B 2018;6:3531–40. doi:10.1039/C8TB00651B.

[411] John Chiefari, Y. K. (Bill) Chong, Frances Ercole, Julia Krstina, Justine Jeffery, Tam P. T. Le, et al. Living Free-Radical Polymerization by Reversible Addition−Fragmentation Chain Transfer: The RAFT Process. Macromolecules 1998;31:5559–62. doi:10.1021/MA9804951.

[412] Perrier S. *50th Anniversary Perspective* : RAFT Polymerization—A User Guide. Macromolecules 2017;50:7433–47. doi:10.1021/acs.macromol.7b00767.

[413] Tian X, Ding J, Zhang B, Qiu F, Zhuang X, Chen Y. Recent Advances in RAFT Polymerization: Novel Initiation Mechanisms and Optoelectronic Applications. Polymers 2018;10:318. doi:10.3390/polym10030318.

[414] Wu L, Glebe U, Böker A. Surface-initiated controlled radical polymerizations from silica nanoparticles, gold nanocrystals, and bionanoparticles. Polym Chem 2015;6:5143–84. doi:10.1039/c5py00525f.

[415] Braunecker WA. Controlled/living radical polymerization: Features, developments, and perspectives. Prog Polym Sci 2007;32:93–146. doi:10.1016/J.PROGPOLYMSCI.2006.11.002.

[416] Zoppe JO, Ataman NC, Mocny P, Wang J, Moraes J, Klok H-A. Surface-Initiated Controlled Radical Polymerization: State-of-the-Art, Opportunities, and Challenges in Surface and Interface Engineering with Polymer Brushes. Chem Rev 2017;117:1105–318. doi:10.1021/acs.chemrev.6b00314.

[417] Bagheri A, Sadrearhami Z, Adnan NNM, Boyer C, Lim M. Surface functionalization of upconversion nanoparticles using visible light-mediated polymerization. Polymer 2018;151:6–14. doi:10.1016/j.polymer.2018.07.054.

[418] Xie Z, Deng X, Liu B, Huang S, Ma P, Hou Z, et al. Construction of Hierarchical Polymer Brushes on Upconversion Nanoparticles via NIR-Light-Initiated RAFT Polymerization. ACS Appl Mater Interfaces 2017;9:30414–25. doi:10.1021/acsami.7b09124.

[419] Bagheri A, Arandiyan H, Adnan NNM, Boyer C, Lim M. Controlled Direct Growth of Polymer Shell on Upconversion Nanoparticle Surface via Visible Light Regulated Polymerization. Macromolecules 2017;50:7137–47. doi:10.1021/acs.macromol.7b01405.

[420] Li Y, Zhao L, Xiao M, Huang Y, Dong B, Xu Z, et al. Synergic effects of upconversion nanoparticles $NaYbF_4:Ho^{3+}$ and ZrO_2 enhanced the efficiency in hole-conductor-free perovskite solar cells. Nanoscale 2018;10:22003–11. doi:10.1039/C8NR07225F.

[421] Chen G, Qiu H, Prasad PN, Chen X. Upconversion nanoparticles: design, nanochemistry, and applications in theranostics. Chem Rev 2014;114:5161–214. doi:10.1021/cr400425h.

[422] Zhang Z, Shikha S, Liu J, Zhang J, Mei Q, Zhang Y. Upconversion Nanoprobes: Recent Advances in Sensing Applications. Anal Chem 2019;91:548–68. doi:10.1021/acs.analchem.8b04049.

[423] Kumar D, Verma K, Verma S, Chaudhary B, Som S, Sharma V, et al. Recent advances in enhanced luminescence upconversion of lanthanide-doped NaYF4 phosphors. Phys B Condens Matter 2018;535:278–86. doi:10.1016/J.PHYSB.2017.08.003.

[424] Renero-Lecuna C, Martín-Rodríguez R, Valiente R, González J, Rodríguez F, Krämer KW, et al. Origin of the High Upconversion Green Luminescence Efficiency in β-$NaYF_4$:2%Er^{3+},20%Yb^{3+}. Chem Mater 2011;23:3442–8. doi:10.1021/cm2004227.

[425] Shi F, Wang J, Zhai X, Zhao D, Qin W. Facile synthesis of β-NaLuF4 : Yb/Tm hexagonal nanoplates with intense ultraviolet upconversion luminescence. CrystEngComm 2011;13:3782. doi:10.1039/c1ce05092c.

[426] Liang X, Wang X, Zhuang J, Peng Q, Li Y. Synthesis of NaYF4 Nanocrystals with Predictable Phase and Shape. Adv Funct Mater 2007;17:2757–65. doi:10.1002/adfm.200600807.

[427] Radunz S, Schavkan A, Wahl S, Würth C, Tschiche HR, Krumrey M, et al. Evolution of Size and Optical Properties of Upconverting Nanoparticles during High-Temperature Synthesis. J Phys Chem C 2018;122:28958–67. doi:10.1021/acs.jpcc.8b09819.

[428] Mai HX, Zhang YW, Sun LD, Yan CH. Size- and Phase-Controlled Synthesis of Monodisperse NaYF4:Yb,Er Nanocrystals from a Unique Delayed Nucleation Pathway

Monitored with Upconversion Spectroscopy. J Phys Chem C 2007;111:13730–9. doi:10.1021/jp073919e.

[429] Komban R, Klare JP, Voss B, Nordmann J, Steinhoff H-J, Haase M. An Electron Paramagnetic Resonance Spectroscopic Investigation on the Growth Mechanism of NaYF4:Gd Nanocrystals. Angew Chem Int Ed 2012;51:6506–10. doi:10.1002/anie.201201025.

[430] Voß B, Nordmann J, Uhl A, Komban R, Haase M. Effect of the crystal structure of small precursor particles on the growth of β-NaREF $_4$ (RE = Sm, Eu, Gd, Tb) nanocrystals. Nanoscale 2013;5:806–12. doi:10.1039/C2NR33083K.

[431] Suter JD, Pekas NJ, Berry MT, May PS. Real-Time-Monitoring of the Synthesis of β-NaYF $_4$:17% Yb,3% Er Nanocrystals Using NIR-to-Visible Upconversion Luminescence. J Phys Chem C 2014;118:13238–47. doi:10.1021/jp502971j.

[432] Rinkel T, Nordmann J, Raj AN, Haase M. Ostwald-ripening and particle size focussing of sub-10 nm NaYF $_4$ upconversion nanocrystals. Nanoscale 2014;6:14523–30. doi:10.1039/C4NR03833A.

[433] May PB, Suter JD, May PS, Berry MT. The Dynamics of Nanoparticle Growth and Phase Change During Synthesis of β-NaYF $_4$. J Phys Chem C 2016;120:9482–9. doi:10.1021/acs.jpcc.6b01365.

[434] Palo E, Tuomisto M, Hyppänen I, Swart HC, Hölsä J, Soukka T, et al. Highly uniform up-converting nanoparticles: Why you should control your synthesis even more. J Lumin 2017;185:125–31. doi:10.1016/J.JLUMIN.2016.12.051.

[435] Ayyub P, Palkar VR, Chattopadhyay S, Multani M. Effect of crystal size reduction on lattice symmetry and cooperative properties. Phys Rev B 1995;51:6135–8. doi:10.1103/PhysRevB.51.6135.

[436] Thanh NTK, Maclean N, Mahiddine S. Mechanisms of Nucleation and Growth of Nanoparticles in Solution. Chem Rev 2014;114:7610–30. doi:10.1021/cr400544s.

[437] Zhai X, Wang Y, Liu X, Liu S, Lei P, Yao S, et al. A Simple Strategy for the Controlled Synthesis of Ultrasmall Hexagonal-Phase NaYF 4 :Yb,Er Upconversion Nanocrystals. ChemPhotoChem 2017;1:369–75. doi:10.1002/cptc.201700013.

[438] Zhang J, Huang F, Lin Z. Progress of nanocrystalline growth kinetics based on oriented attachment. Nanoscale 2010;2:18–34. doi:10.1039/B9NR00047J.

[439] Lee EJH, Ribeiro C, Longo E, Leite ER. Oriented Attachment: An Effective Mechanism in the Formation of Anisotropic Nanocrystals. J Phys Chem B 2005;109:20842–6. doi:10.1021/jp0532115.

[440] Na H, Woo K, Lim K, Jang HS. Rational morphology control of β-NaYF4:Yb,Er/Tm upconversion nanophosphors using a ligand, an additive, and lanthanide doping. Nanoscale 2013;5:4242. doi:10.1039/c3nr00080j.

[441] Yin Y, Alivisatos AP. Colloidal nanocrystal synthesis and the organic–inorganic interface. Nature 2005;437:664–70. doi:10.1038/nature04165.

[442] Xue X, Penn RL, Leite ER, Huang F, Lin Z. Crystal growth by oriented attachment: kinetic models and control factors. CrystEngComm 2014;16:1419. doi:10.1039/c3ce42129e.

[443] Liz-Marzán LM, Grzelczak M. Growing anisotropic crystals at the nanoscale. Science 2017;356:1120–1. doi:10.1126/science.aam8774.

[444] Hu H, Chen Z, Cao T, Al, Hui Zeng J, Hua Li Z, et al. Rapid microwave-enhanced hydrothermal synthesis and shape evolution of uniform NaGdF 4 :Yb, Er (Tm/Ho) nanocrystals with upconversion and paramagnetic properties Hydrothermal synthesis of hexagonal lanthanide-doped LaF3 nanoplates with bright upconversion. Nanotechnology 2012;23:22705. doi:10.1088/0957-4484/23/22/225705.

[445] Hood M, Mari M, Muñoz-Espí R. Synthetic Strategies in the Preparation of Polymer/Inorganic Hybrid Nanoparticles. Materials 2014;7:4057–87. doi:10.3390/ma7054057.

[446] Francis R, Joy N, Aparna EP, Vijayan R. Polymer Grafted Inorganic Nanoparticles, Preparation, Properties, and Applications: A Review. Polym Rev 2014;54:268–347. doi:10.1080/15583724.2013.870573.

[447] Jordan R, West N, Ulman A, Chou Y-M, Nuyken O. Nanocomposites by Surface-Initiated Living Cationic Polymerization of 2-Oxazolines on Functionalized Gold Nanoparticles. Macromolecules 2001;34:1606–11. doi:10.1021/MA001615J.

[448] Zirbs R, Binder W, Gahleitner M, Machl D. “Grafting From” -Living Cationic Polymerization of Poly(isobutylene) from Silica-Nanoparticle Surfaces. Macromol Symp 2007;254:93–6. doi:10.1002/masy.200750814.

[449] Zhou Q, Wang S, Fan X, Advincula R, Mays J. Living Anionic Surface-Initiated Polymerization (LASIP) of a Polymer on Silica Nanoparticles. Langmuir 2002;18:3324–31. doi:10.1021/LA015670C.

[450] Hübner E, Allgaier J, Meyer M, Stellbrink J, Pyckhout-Hintzen W, Richter D. Synthesis of Polymer/Silica Hybrid Nanoparticles Using Anionic Polymerization Techniques. Macromolecules 2010;43:856–67. doi:10.1021/ma902213p.

[451] von Werne T, Patten TE. Preparation of Structurally Well-Defined Polymer−Nanoparticle Hybrids with Controlled/Living Radical Polymerizations. J Am Chem Soc 1999;121:7409–10. doi:10.1021/JA991108L.

[452] Pyun J, Matyjaszewski K. Synthesis of Nanocomposite Organic/Inorganic Hybrid Materials Using Controlled/“Living” Radical Polymerization. Chem Mater 2001;13:3436–48. doi:10.1021/CM011065J.

[453] Zhang Z, Zhang P, Wang Y, Zhang W. Recent advances in organic–inorganic well-defined hybrid polymers using controlled living radical polymerization techniques. Polym Chem 2016;7:3950–76. doi:10.1039/C6PY00675B.

[454] Kango S, Kalia S, Celli A, Njuguna J, Habibi Y, Kumar R. Surface modification of inorganic nanoparticles for development of organic–inorganic nanocomposites—A review. Prog Polym Sci 2013;38:1232–61. doi:10.1016/J.PROGPOLYMSCI.2013.02.003.

[455] Neoh KG, Kang ET. Functionalization of inorganic nanoparticles with polymers for stealth biomedical applications. Polym Chem 2011;2:747–59. doi:10.1039/C0PY00266F.

[456] Wang X, Gao H. Recent Progress on Hyperbranched Polymers Synthesized via Radical-Based Self-Condensing Vinyl Polymerization. Polymers 2017;9:188. doi:10.3390/polym9060188.

[457] Liu P, Wang T. Surface-graft hyperbranched polymer via self-condensing atom transfer radical polymerization from zinc oxide nanoparticles. Polym Eng Sci 2007;47:1296–301. doi:10.1002/pen.20804.

[458] Schüll C, Frey H. Grafting of hyperbranched polymers: From unusual complex polymer topologies to multivalent surface functionalization. Polymer 2013;54:5443–55. doi:10.1016/J.POLYMER.2013.07.065.

[459] Kaiser E, Colescott RL, Bossinger CD, Cook PI. Color test for detection of free terminal amino groups in the solid-phase synthesis of peptides. Anal Biochem 1970;34:595–8. doi:10.1016/0003-2697(70)90146-6.

[460] Duan Z, Qu Z, Hu F, Yang Y, Chen G, Xu H. Quantification of surface-anchored RAFT chain transfer agent on silica particles. Appl Surf Sci 2014;300:104–10. doi:10.1016/J.APSUSC.2014.02.012.

[461] Liu C-H, Pan C-Y. Grafting polystyrene onto silica nanoparticles via RAFT polymerization. Polymer 2007;48:3679–85. doi:10.1016/J.POLYMER.2007.04.055.

[462] Duncan R. The dawning era of polymer therapeutics. Nat Rev Drug Discov 2003;2:347–60. doi:10.1038/nrd1088.

[463] Chytil P, Koziolová E, Etrych T, Ulbrich K. HPMA Copolymer-Drug Conjugates with Controlled Tumor-Specific Drug Release. Macromol Biosci 2018;18:1700209. doi:10.1002/mabi.201700209.

[464] Das S, Banik M, Chen G, Sinha S, Mukherjee R. Polyelectrolyte brushes: theory, modelling, synthesis and applications. Soft Matter 2015;11:8550–83. doi:10.1039/C5SM01962A.

[465] Turgman-Cohen S, Genzer J. Computer Simulation of Controlled Radical Polymerization: Effect of Chain Confinement Due to Initiator Grafting Density and Solvent Quality in “Grafting From” Method. Macromolecules 2010;43:9567–77. doi:10.1021/ma102046q.

[466] Wei Z, Hao X, Kambouris PA, Gan Z, Hughes TC. One-pot synthesis of hyperbranched polymers using small molecule and macro RAFT inimers. Polymer 2012;53:1429–36. doi:10.1016/J.POLYMER.2012.02.011.

[467] Skrabania K, Miasnikova A, Bivigou-Koumba AM, Zehm D, Laschewsky AE. Examining the UV-vis absorption of RAFT chain transfer agents and their use for polymer analysis. Polym Chem 2011;2:2074–83. doi:10.1039/c1py00173f.

[468] Alfurhood JA, Sun H, Bachler PR, Sumerlin BS. Hyperbranched poly(N-(2-hydroxypropyl) methacrylamide) via RAFT self-condensing vinyl polymerization. Polym Chem 2016;7:2099. doi:10.1039/c6py00111d.

[469] Hölter D, Burgath A, Frey H. Degree of branching in hyperbranched polymers. Acta Polym 1997;48:30–5. doi:10.1002/actp.1997.010480105.

[470] Alfurhood JA, Bachler PR, Sumerlin BS. Hyperbranched polymers via RAFT self-condensing vinyl polymerization. Polym Chem 2016;7:3361–9. doi:10.1039/C6PY00571C.

[471] Yan D, Müller AHE, Matyjaszewski K. Molecular Parameters of Hyperbranched Polymers Made by Self-Condensing Vinyl Polymerization. 2. Degree of Branching. Macromolecules 1997;30:7024–33. doi:10.1021/MA961919Z.

[472] Zhou D, Mastan E, Zhu S. Termination of Surface Radicals and Kinetic Analysis of Surface-Initiated RAFT Polymerization on Flat Surfaces. Macromol Theory Simul 2012;21:602–14. doi:10.1002/mats.201200043.

[473] Tsujii Y, Ejaz M, Sato K, Goto A, Fukuda T. Mechanism and kinetics of RAFT-mediated graft polymerization of styrene on a solid surface. 1. experimental evidence of surface radical migration. Macromolecules 2001;34:8872–8. doi:10.1021/MA010733J.

[474] Ohno K, Ma Y, Huang Y, Mori C, Yahata Y, Tsujii Y, et al. Surface-initiated reversible addition–fragmentation chain transfer (RAFT) polymerization from fine particles functionalized with trithiocarbonates. Macromolecules 2011;44:8944–53. doi:10.1021/ma202105y.

[475] Simon PFW, Müller AHE. Synthesis of Hyperbranched and Highly Branched Methacrylates by Self-Condensing Group Transfer Copolymerization. Macromolecules 2001;34:6206–13. doi:10.1021/MA002156P.

[476] Mori H, Chan Seng D, Lechner H, Zhang M, Müller AHE. Synthesis and Characterization of Branched Polyelectrolytes. 1. Preparation of Hyperbranched Poly(acrylic acid) via Self-Condensing Atom Transfer Radical Copolymerization. Macromolecules 2002;35:9270–81. doi:10.1021/MA021159U.

[477] Li C, C. Benicewicz B. Synthesis of well-defined polymer brushes grafted onto silica nanoparticles via surface Reversible addition−fragmentation chain transfer

polymerization. Macromolecules 2005;38:5929–36. doi:10.1021/ma050216r.

[478] Turgman-Cohen S, Genzer J. Simultaneous Bulk- and Surface-Initiated Controlled Radical Polymerization from Planar Substrates. J Am Chem Soc 2011;133:17567–9. doi:10.1021/ja2081636.

[479] Kwak Y, Goto A, Tsujii Y, Murata Y, Komatsu K, Fukuda T. A Kinetic study on the rate retardation in radical polymerization of styrene with addition−fragmentation chain transfer. Macromolecules 2002;35:3026–9. doi:10.1021/ma0118421.

[480] Li D, Luo Y, Li B-G, Zhu S. Effect of rate retardation in RAFT grafting polymerization from silicon wafer surface. J Polym Sci Part A Polym Chem 2008;46:970–8. doi:10.1002/pola.22440.

[481] Kelkar SS, Reineke TM. Theranostics: Combining Imaging and Therapy. Bioconjugate Chem 2011;22:1879–903. doi:10.1021/bc200151q.

[482] Sharma P, Brown S, Walter G, Santra S, Moudgil B. Nanoparticles for bioimaging. Adv Colloid Interface Sci 2006;123–126:471–85. doi:10.1016/j.cis.2006.05.026.

[483] Bao Y, Sherwood JA, Sun Z. Magnetic iron oxide nanoparticles as T_1 contrast agents for magnetic resonance imaging. J Mater Chem C 2018;6:1280–90. doi:10.1039/C7TC05854C.

[484] Bae SW, Tan W, Hong J-I. Fluorescent dye-doped silica nanoparticles: new tools for bioapplications. Chem Commun 2012;48:2270. doi:10.1039/c2cc16306c.

[485] Martynenko I V., Litvin AP, Purcell-Milton F, Baranov A V., Fedorov A V., Gun'ko YK. Application of semiconductor quantum dots in bioimaging and biosensing. J Mater Chem B 2017;5:6701–27. doi:10.1039/C7TB01425B.

[486] Wu X, Chen G, Shen J, Li Z, Zhang Y, Han G. Upconversion Nanoparticles: A Versatile Solution to Multiscale Biological Imaging. Bioconjugate Chem 2015;26:166–75. doi:10.1021/bc5003967.

[487] Sokolova V, Epple M. Inorganic Nanoparticles as Carriers of Nucleic Acids into Cells. Angew Chem Int Ed 2008;47:1382–95. doi:10.1002/anie.200703039.

[488] Jeong W, Bu J, Kubiatowicz LJ, Chen SS, Kim Y, Hong S. Peptide–nanoparticle conjugates: a next generation of diagnostic and therapeutic platforms? Nano Converg

2018;5:38. doi:10.1186/s40580-018-0170-1.

[489] Li S-D, Huang L. Stealth Nanoparticles: High Density but Sheddable PEG is a Key for Tumor Targeting. J Control Release 2010;145:178. doi:10.1016/J.JCONREL.2010.03.016.

[490] Arias J. Novel Strategies to Improve the Anticancer Action of 5-Fluorouracil by Using Drug Delivery Systems. Molecules 2008;13:2340–69. doi:10.3390/molecules13102340.

[491] Longley DB, Harkin DP, Johnston PG. 5-Fluorouracil: mechanisms of action and clinical strategies. Nat Rev Cancer 2003;3:330–8. doi:10.1038/nrc1074.

[492] Caballero GA, Ausman RK, Quebbeman EJ. Long-term, ambulatory, continuous IV infusion of 5-FU for the treatment of advanced adenocarcinomas. Cancer Treat Rep 1985;69:13–5.

[493] Shah A, MacDonald W, Goldie J, Gudauskas G, Brisebois B. 5-FU infusion in advanced colorectal cancer: a comparison of three dose schedules. Cancer Treat Rep 1985;69:739–42.

[494] Arıca B, Çalış S, Kaş H., Sargon M., Hıncal A. 5-Fluorouracil encapsulated alginate beads for the treatment of breast cancer. Int J Pharm 2002;242:267–9. doi:10.1016/S0378-5173(02)00172-2.

[495] BOISDRON-CELLE M, MENEI P, BENOIT JP. Preparation and Characterization of 5-Fluorouracil-loaded Microparticles as Biodegradable Anticancer Drug Carriers. J Pharm Pharmacol 1995;47:108–14. doi:10.1111/j.2042-7158.1995.tb05760.x.

[496] Arias JL, Ruiz MA, López-Viota M, Delgado Á V. Poly(alkylcyanoacrylate) colloidal particles as vehicles for antitumour drug delivery: A comparative study. Colloids Surf, B 2008;62:64–70. doi:10.1016/J.COLSURFB.2007.09.018.

[497] Elorza B, Elorza MA, Frutos G, Chantres JR. Characterization of 5-fluorouracil loaded liposomes prepared by reverse-phase evaporation or freezing-thawing extrusion methods: study of drug release. Biochim Biophys Acta - Biomembr 1993;1153:135–42. doi:10.1016/0005-2736(93)90398-J.

[498] Malet-Martino M, Martino R. Clinical Studies of Three Oral Prodrugs of 5-Fluorouracil

(Capecitabine, UFT, S-1): A Review. Oncologist 2002;7:288–323. doi:10.1634/theoncologist.7-4-288.

[499] Dong Z, Zheng W, Xu Z, Yin Z. Improved stability and tumor targeting of 5-fluorouracil by conjugation with hyaluronan. J Appl Polym Sci 2013;130:927–32. doi:10.1002/app.39247.

[500] Yan G-P, Zhuo R-X, Zheng C-Y. Study on the Anticancer Drug 5-Fluorouracil-Conjugated Polyaspartamide Containing Hepatocyte-Targeting Group. J Bioact Compat Polym 2001;16:277–93. doi:10.1106/M4LK-LWJQ-34CL-LR85.

[501] Chen B, Dai W, He B, Zhang H, Wang X, Wang Y, et al. Current Multistage Drug Delivery Systems Based on the Tumor Microenvironment. Theranostics 2017;7:538–58. doi:10.7150/thno.16684.

[502] Dong H, Pang L, Cong H, Shen Y, Yu B. Application and design of esterase-responsive nanoparticles for cancer therapy. Drug Deliv 2019;26:416–32. doi:10.1080/10717544.2019.1588424.

[503] Wong PT, Choi SK. Mechanisms of Drug Release in Nanotherapeutic Delivery Systems. Chem Rev 2015;115:3388–432. doi:10.1021/cr5004634.

[504] Huo M, Yuan J, Tao L, Wei Y. Redox-responsive polymers for drug delivery: from molecular design to applications. Polym Chem 2014;5:1519–28. doi:10.1039/C3PY01192E.

[505] Kovár M, Strohalm J, Etrych T, Ulbrich K, Říhová B. Star structure of antibody-targeted HPMA copolymer-bound doxorubicin: a novel type of polymeric conjugate for targeted drug delivery with potent antitumor effect. Bioconjugate Chem 2002;13:206–15.

[506] Islami M, Zarrabi A, Tada S, Kawamoto M, Isoshima T, Ito Y. Controlled quercetin release from high-capacity-loading hyperbranched polyglycerol-functionalized graphene oxide. Int J Nanomed 2018;13:6059–71. doi:10.2147/IJN.S178374.

[507] Perumal O, Khandare J, Kolhe P, Kannan S, Lieh-Lai M, Kannan RM. Effects of branching architecture and linker on the activity of hyperbranched polymer-drug conjugates. Bioconjugate Chem 2009;20:842–6. doi:10.1021/bc800526z.

[508] Duncan R. Development of HPMA copolymer–anticancer conjugates: Clinical experience and lessons learnt. Adv Drug Deliv Rev 2009;61:1131–48. doi:10.1016/J.ADDR.2009.05.007.

[509] Sun Z-J, Sun B, Sun C-W, Wang L-B, Xie X, Ma W-C, et al. A poly(glycerol-sebacate-(5-fluorouracil-1-acetic acid)) polymer with potential use for cancer therapy. J Bioact Compat Polym 2012;27:18–30. doi:10.1177/0883911511431876.

[510] Liu L, Yao W, Rao Y, Lu X, Gao J. pH-Responsive carriers for oral drug delivery: challenges and opportunities of current platforms. Drug Deliv 2017;24:569–81. doi:10.1080/10717544.2017.1279238.

[511] Li M, Liang Z, Sun X, Gong T, Zhang Z. A Polymeric Prodrug of 5-Fluorouracil-1-Acetic Acid Using a Multi-Hydroxyl Polyethylene Glycol Derivative as the Drug Carrier. PLoS One 2014;9:e112888. doi:10.1371/journal.pone.0112888.

[512] Sauraj, Kumar SU, Gopinath P, Negi YS. Synthesis and bio-evaluation of xylan-5-fluorouracil-1-acetic acid conjugates as prodrugs for colon cancer treatment. Carbohydr Polym 2017;157:1442–50. doi:10.1016/J.CARBPOL.2016.09.096.

[513] NIU R, JING H, CHEN Z, XU J, DAI J, YAN Z. Differentiating malignant colorectal tumor patients from benign colorectal tumor patients by assaying morning urinary arylsulfatase activity. Asia Pac J Clin Oncol 2012;8:362–7. doi:10.1111/j.1743-7563.2012.01545.x.

[514] McGoldrick CA, Jiang Y-L, Paromov V, Brannon M, Krishnan K, Stone WL. Identification of oxidized protein hydrolase as a potential prodrug target in prostate cancer. BMC Cancer 2014;14:77. doi:10.1186/1471-2407-14-77.

[515] Franklin MR. Phase I Biotransformation Reactions-Esterases, and Amidases. XPharm Compr Pharmacol Ref 2007:1–3. doi:10.1016/B978-008055232-3.60279-X.

[516] Saito G, Swanson JA, Lee K-D. Drug delivery strategy utilizing conjugation via reversible disulfide linkages: role and site of cellular reducing activities. Adv Drug Deliv Rev 2003;55:199–215. doi:10.1016/S0169-409X(02)00179-5.

[517] Sun H, Meng F, Cheng R, Deng C, Zhong Z. Reduction-sensitive degradable micellar nanoparticles as smart and intuitive delivery systems for cancer chemotherapy. Expert Opin Drug Deliv 2013;10:1109–22. doi:10.1517/17425247.2013.783009.

[518] Tao L, Liu J, Tan BH, Davis TP. RAFT Synthesis and DNA Binding of Biodegradable, Hyperbranched Poly(2-(dimethylamino)ethyl Methacrylate. Macromolecules 2009;42:4960–2. doi:10.1021/ma900865c.

[519] Brulikova L, Okorochenkova Y, Hlavac J. A solid-phase synthetic approach to pH-independent rhodamine-type fluorophores. Org Biomol Chem 2016;14:10437–43. doi:10.1039/C6OB01772J.

[520] Podgorski I, Sloane BF. Cathepsin B and its role(s) in cancer progression. Biochem Soc Symp 2003:263–76.

[521] Subr V, Strohalm J, Plocova D, Jelınkova M, Rıhova B. Polymeric drugs based on conjugates of synthetic and natural macromolecules I. Synthesis and physico-chemical characterisation. J Controlled Release 2000;64:63–79. doi:10.1016/S0168-3659(99)00141-8.

[522] Dukhno O, Przybilla F, Muhr V, Buchner M, Hirsch T, Mély Y. Time-dependent luminescence loss for individual upconversion nanoparticles upon dilution in aqueous solution. Nanoscale 2018;10:15904–10. doi:10.1039/C8NR03892A.

[523] Gnanasammandhan MK, Idris NM, Bansal A, Huang K, Zhang Y. Near-IR photoactivation using mesoporous silica–coated NaYF4:Yb,Er/Tm upconversion nanoparticles. Nat Protoc 2016;11:688–713. doi:10.1038/nprot.2016.035.

Université de Strasbourg

École doctorale Physique, chimie-physique ED 182 Université de Strasbourg

Alireza KAVAND

Development of a theranostic platform based on hyperbranched polymers grafted onto upconversion nanoparticles for the delivery of 5-fluorouracil

Résumé

La théranostique est un domaine de la biomédecine en plein essor qui combine le diagnostic et la thérapie en un même vecteur. L'approche développée lors de cette thèse combine les propriétés luminescentes des UCNPs et la capacité des polymères à encapsuler un principe actif de façon covalente ou non. Ce projet a conduit au développement et approfondissement de différentes compétences : 1) synthèse de nanocristaux de NaYF4:Yb^{3+},Er^{3+} dans des microtubes permettant de moduler la taille, la forme et la phase en fonction de différents paramètres opératoires, 2) la synthèse de nouveaux monomères et transmères en combinant la chimie organique et la synthèse peptidique en phase solide, 3) la préparation de polymères hyperramifiés par polymérisation radicalaire contrôlée de type RAFT depuis la surface des nanocristaux, 4) l'étude de l'encapsulation covalente et non covalente ainsi que le relargage de 5-fluorouracile et 5) l'étude de polymères répondant à un stimulus en terme de dégradation.

Mots-clés : UCNPs, traitement thermique, transition de phase, nanovecteur, encapsulation, polymères hyperrramifiés

Summary

Theranostics is a growing field in biomedicine because of its ability to combine diagnosis and therapy in a single vector. The approach developed in this thesis combines the luminescent properties of UCNPs and the ability of polymers to encapsulate covalently or not a drug. This doctoral project led to the development and/or deepening of different skills: 1) synthesis of NaYF4:Yb^{3+},Er^{3+} nanocrystals in microtubes with tunable size, shape and phase according to different operating parameters, 2) synthesis of new monomers and transmers by combining organic chemistry and solid-phase peptide synthesis, 3) the preparation of hyperbranched polymers by controlled radical polymerization under RAFT conditions from the surface of nanocrystals, 4) the study of covalent and non-covalent encapsulation and the release of 5-fluorouracil and 5) the study of polymers responding to a stimulus in terms of degradation.

Keywords: UCNPs, heat treatment, phase transition, nanocarrier, encapsulation, hyperbranched